UNIVERSITÉ DE LORRAINE | BIBLIOTHÈQUES UNIVERSITAIRES

AVERTISSEMENT

Ce document est le fruit d'un long travail approuvé par le jury de soutenance et mis à disposition de l'ensemble de la communauté universitaire élargie.

Il est soumis à la propriété intellectuelle de l'auteur. Ceci implique une obligation de citation et de référencement lors de l'utilisation de ce document.

D'autre part, toute contrefaçon, plagiat, reproduction illicite encourt une poursuite pénale.

Contact bibliothèque : ddoc-theses-contact@univ-lorraine.fr
(Cette adresse ne permet pas de contacter les auteurs)

LIENS

Code de la Propriété Intellectuelle. articles L 122. 4
Code de la Propriété Intellectuelle. articles L 335.2- L 335.10
http://www.cfcopies.com/V2/leg/leg_droi.php

Thèse

Présentée et soutenue publiquement pour l'obtention du titre de

DOCTEURE DE l'UNIVERSITE DE LORRAINE

Mention : Génie des Procédés, des Produits et des Molécules

par **Audrey MICHAUD**

Sous la direction de : **Rainier HREIZ**
Jean-François PORTHA

Conception optimale de réacteurs-échangeurs par minimisation de la création d'entropie

7 Novembre 2025

Membres du jury :

Directeur(s) de thèse :	PORTHA Jean-François	Maître de conférences, Université de Lorraine, LRGP, Nancy
	HREIZ Rainier	Maître de conférences, Université de Lorraine, LRGP, Nancy
Président du jury :	FERRASSE Jean-Henry	Professeur, Université d'Aix-Marseille, M2P2, Marseille
Rapporteurs :	BOUYER Denis	Professeur, Université de Montpellier 2, IEM, Montpellier
	SIROUX Monica	Professeure, INSA de Strasbourg, ICube, Strasbourg
Examinateurs :	THERY HÉTREUX Raphaele	Maîtresse de conférences, Toulouse INP, LGC, Toulouse
Membres invités :	COMMENGE Jean-Marc	Professeur, Université de Lorraine, LRGP, Nancy
	LASALA Silvia	Maîtresse de conférences, Université de Lorraine, LRGP, Nancy

Table of Contents

Acknowledgements **6**

Remerciements **8**

Abstract **10**

Résumé **11**

General introduction **12**

Chapter 1 ..... **20**

Abstract 23

1.1 Introduction 24

1.2 An historical introduction to the concept of irreversibilities 25

1.3 Entropy generation analysis 27

1.3.1 One dimensional entropy generation calculation 28

1.3.2 Two-dimensional entropy generation calculation (2D/3D modelling) 32

1.4 Equipartition of entropy production 36

1.5 Entropy generation minimization 39

1.5.1 Optimisation of heat exchangers 40

1.5.2 Optimisation of transient processes 42

1.5.3 Optimisation of processes with mass transfer 44

1.5.4 Optimisation of reactive systems 46

1.6 Conclusion 51

Chapter 2 ..... **57**

Abstract 62

2.1 Introduction 63

2.2 Acetic anhydride hydrolysis 64

2.3 Heat-exchanger reactor configuration 66

2.3.1 HER geometries: uniform and piecewise profiled configurations 66
2.3.2 Operating and geometric parameters 68
2.4 Systemic modelling 71
2.4.1 Mass and momentum balances 71
2.4.2 Heat balances 73
2.4.3 Species mass balances 75
2.4.4 Systemic modelling limitations 76
2.5 CFD model 79
2.5.1 Coupled hydrodynamics equations 79
2.5.2 One-dimensional reduced modelling 83
2.6 Multi-objective optimisation problem formulation 85
2.6.1 Objective functions 85
2.6.2 Multi-objective optimisation problem 89
2.6.3 Numerical procedure 91
2.7 Conclusion 92
Appendix A. Local friction coefficient calculation 96
Appendix B. Local heat transfer coefficient calculation 97
Appendix C. Nusselt number in a thermally developed laminar flow with uniform volumetric heat generation 99
Appendix D. Calculation of the chemical entropy generation rate 101
Appendix E. Pilot sizing 103
E.1 Pilot P&ID 105
E.2 Sizing methodology 109
Chapter 3 114
Abstract 117
3.1 Introduction 118
3.2 Comparison of the results of the 1D and CFD models 119
3.2.1 Entropy generation due to viscous dissipation 123
3.2.2 Entropy generation due to heat transfer 128
3.2.3 Entropy generation due to chemical reaction and mass transfer 134
3.2.4 Results comparison 143
3.3 1D Optimisation results and discussion 145

3.3.1 Reference case 147

3.3.2 Equipartition of entropy generation and driving forces: comparison between MPCEnt and a suboptimal geometry for the reference case 153

3.3.3 Influence of the inlet mixture temperature 158

3.3.4 Influence of the inlet heat carrier temperature 163

3.3.5 Influence of the mixture mass flow rate 167

3.3.6 Influence of the heat carrier mass flow rate 171

3.3.7 Summary of the 1D optimisation main results 173

3.4 CFD optimisation 175

3.5 Conclusion 180

Chapter 4 185

Abstract 190

4.1 Introduction 191

4.2 SO_2 oxidation reaction 192

4.3 Heat-exchanger reactor configuration 195

4.3.1 HER geometries: uniform and piecewise profiled configurations 195

4.3.2 Operating and geometric parameters 197

4.4 Systemic process model 200

4.4.1 Mass and momentum balances 200

4.4.2 Heat balances 203

4.4.3 Species mass balances 206

4.4.4 Systemic modelling limitations 207

4.5 CFD model 208

4.6 Multi-objective optimisation problem formulation 212

4.6.1 Objective functions 212

4.6.2 Multi-objective optimisation problem 214

4.6.3 Numerical procedure 216

4.7 Conclusion 217

Appendix A. Calculation of the friction coefficient in the annular space flow 221

Appendix B. Heat transfer in the packed bed: simplifying assumptions 222

B.1 Equivalent radial thermal conductivity of the packed bed 222

B.2 Equivalent axial thermal conductivity of the packed bed and axial thermal Péclet number 224
B.3 Prater criterion and pseudo-homogenous model assumption 225
Appendix C. Calculation of Nusselt number in the annular space flow 227
Appendix D. Mass transfer in the packed bed: simplifying assumptions 228
D.1 External mass transfer resistance 228
D.2 Calculation of the effective diffusivity in the catalyst pellets 229
D.3 Internal mass transfer resistance and Weisz criterion 231
Appendix E. Detailed characterization of the MPCEnt and MPCVol designs of the reference case study 232
E.1 Mass transfer limitation 232
E.1 Heat transfer limitation 234
Chapter 5 236
Abstract 238
5.1 Introduction 239
5.2 1D model optimisation results 240
5.2.1 Reference case study 241
5.2.2 Effects of the inlet pressure of the reactive mixture 248
5.2.3 Influence of the maximum allowable temperature constraint 253
5.2.4 Influence of the inlet heat carrier temperature 255
5.2.5 Influence of the inlet gas molar flowrate 259
5.2.6 Influence of the inlet gas temperature 264
5.2.7 Influence of the inlet gas O_2/SO_2 molar ratio 268
5.2.8 Influence of the required conversion 273
5.2.9 Summary of the 1D optimisation key results 277
5.3 2D model comparison 280
5.4 Conclusion 284
General conclusion and perspectives 289
Résumé en français 294

Acknowledgements

I would first like to thank the LRGP (Laboratoire Réactions et Génie des Procédés) and the CNRS for giving me the opportunity to carry out this PhD, as well as the ANR for funding the NACREE project in which this work is embedded.

I also wish to express my deep gratitude to the members of my jury, Denis Bouyer, Monica Siroux, Raphaele Héteux-Théry, and Jean-Henry Ferrasse, for agreeing to evaluate this work, as well as to Jean-Marc Commenge and Silvia Lasala, who showed a particular interest in my research.

I am especially grateful to my two supervisors, Jean-François Portha and Rainier Hreiz, for their support, guidance, and expertise. Thanks to you, this work reached a level it would never have attained without your mentoring. Your positivity, encouragement, and valuable advice made these three years both stimulating and enriching, professionally and personally.

My thanks also go to all those who contributed their expertise to this project: Emilien Girot, Charly Koening, as well as all the members of the SERM, whose discussions on the pilot development taught me a great deal. I am also indebted to Sabine Rode, whose rigor and scientific expertise impressed me on many occasions. I would like to express my sincere gratitude to Lucas Frapiccini and Mohammed Iqbal Sandoval, whom I had the pleasure of supervising during my PhD. Their dedication, scientific curiosity, and rigor greatly contributed to the progress of this work. I am truly thankful for their commitment, enthusiasm, and the quality of our discussions, all of which enriched this project throughout our collaboration.

I would also like to thank those who worked behind the scenes within the SAFIC, particularly Mrs. Florence Cherpitelle, as well as Mrs. Christine Fivet and Mrs. Nathalie Ohl, for their valuable help in dealing with administrative challenges.

I wish to thank my fellow PhD students, Noha-Lys Senoussaoui and Shuxin Zheng, as well as my colleagues in the NACREE project, Gilles Héteux and Olivier Boutin, whose discussions helped move this work forward.

I was also fortunate to work in such an inspiring environment thanks to the people who made it so. Many thanks to all my colleagues at Café PRIMO, who filled my Thursday lunches with laughter and good cheer, and to the members of the BJC – Ryma Benrabah, Élise Cabaset, Mathilde Lafont, Sephora Lahouari, Morgane Moinard, Laure Brice, Madi Moussa, Darrick Hillaby, Adrien Rizza, and many others – for making life at the lab more joyful. I am also deeply grateful to my fellow PhD students Désiré Damiba, Omar Aljasem Alhmiedy, Faicel Belgacem, and Omran Abushammala, whose company and conversations brightened so many days.

To my friends, who fled Nancy whenever they could – Delphine Michaux, Nicolas Reversat, Sébastien Mari, and Bertrand Goutelard – I owe an immense thank you. Our online evenings were the cornerstone of my mental health throughout these three years. Your friendship was a constant driving force that helped me through the difficult times. I also wish to thank Céline Glaud, my oldest friend, who showed me that distance and time are truly relative.

Finally, my heartfelt thanks go to my father, Fabrice Michaud, and my mother, Valérie Michaud, who have always given me the love and support I needed to keep moving forward and to overcome life's challenges. And, of course, I have saved for last my siblings, Adèle and Lucas Michaud, who have shaped the person I am in more ways than they could ever imagine. This thesis is the result of all these interactions and of all the people who, near or far, gave me the strength to persevere through difficult times. I am deeply grateful for each and every one of these encounters.

Remerciements

Je souhaite tout d'abord remercier le LRGP (Laboratoire Réactions et Génie des Procédés) ainsi que le CNRS pour m'avoir offert l'opportunité de réaliser cette thèse, ainsi que l'ANR pour le financement du projet NACREE dans lequel s'inscrit ce travail.

J'exprime également toute ma gratitude aux membres de mon jury, Denis Bouyer, Monica Siroux, Raphaele Héteux-Théry et Jean-Henry Ferrasse, pour avoir accepté d'évaluer ce travail, ainsi qu'à Jean-Marc Commenge et Silvia Lasala, qui ont manifesté un intérêt particulier pour mes recherches.

Je tiens à remercier chaleureusement mes deux directeurs de thèse, Jean-François Portha et Rainier Hreiz, pour leur écoute, leurs conseils et leur expertise. Grâce à vous, ce travail a pris une dimension qu'il n'aurait jamais atteinte sans votre accompagnement. Votre bonne humeur, vos encouragements et vos précieux conseils ont rendu ces trois années de thèse stimulantes et enrichissantes à la fois professionnellement et personnellement.

Mes remerciements vont également à toutes les personnes qui ont contribué à ce projet par leur expertise : Emilien Girot, Charly Koening, ainsi que l'ensemble des membres du SERM, dont les échanges autour du développement du pilote m'ont beaucoup appris. Je souhaite aussi exprimer ma reconnaissance à Sabine Rode, dont la rigueur et l'expertise scientifique m'ont impressionnée à de nombreuses reprises. Je tiens à exprimer ma profonde gratitude à Lucas Frapiccini et Mohammed Iqbal Sandoval, que j'ai eu le plaisir d'encadrer durant ma thèse. Leur engagement, leur curiosité scientifique et leur rigueur ont grandement contribué à l'avancée de nos travaux. Je les remercie sincèrement pour leur investissement, leur enthousiasme et la qualité de leurs échanges, qui ont enrichi ce projet tout au long de notre collaboration.

Je remercie aussi les personnes qui ont œuvré dans les coulisses au sein du SAFIC, notamment Mme Florence Cherpitelle, ainsi que Mme Christine Fivet et Mme Nathalie Ohl pour leur aide précieuse face aux problématiques que j'ai pu rencontrer.

Je souhaite adresser mes remerciements à mes collègues doctorantes, Noha-Lys Senoussaoui et Shuxin Zheng, ainsi qu'aux collègues du projet NACREE, Gilles Héteux et Olivier Boutin, dont les discussions ont permis de faire progresser ce travail.

J'ai également eu la chance d'évoluer dans un environnement de travail incroyable grâce aux personnes qui le composent. Merci à tous mes collègues du café PRIMO, qui ont apporté à mes jeudis midis plein de rire et de bonne humeur, ainsi qu'aux membres du BJC – Ryma Benrabah, Élise Cabaset, Mathilde Lafont, Sephora Lahouari, Morgane Moinard, Laure Brice, Madi Moussa, Darrick Hillaby, Adrien Rizza, et tant d'autres – pour avoir su rendre la vie au laboratoire plus joyeuse. Je tiens aussi à remercier chaleureusement mes collègues doctorants

Désiré Damiba, Omar Aljasem Alhmiedy, Faicel Belgacem et Omran Abushammala, dont la compagnie et les discussions ont éclairé bien des journées.

À mes amis, qui ont fui Nancy dès qu'ils le pouvaient – Delphine Michaux, Nicolas Reversat, Sébastien Mari et Bertrand Goutelard –, je tiens à dire un immense merci. Nos soirées en ligne ont été le pilier de ma santé mentale tout au long de ces trois années de thèse. Votre amitié a été un moteur constant qui m'a permis de traverser les moments difficiles. Je souhaite également remercier Céline Glaud, ma plus vieille amie, qui m'a montré que la distance et le temps étaient bel et bien relatifs.

Enfin, un grand merci à mon père, Fabrice Michaud, et à ma mère, Valérie Michaud, qui m'ont toujours offert l'amour et le soutien nécessaires pour avancer et surmonter les épreuves de la vie. Et, bien sûr, je garde pour la fin mon adelphie, Adèle et Lucas Michaud, qui ont façonné la personne que je suis dans bien plus d'aspects qu'ils ne pourront jamais l'imaginer. Cette thèse est le fruit de toutes ces interactions et de toutes ces personnes qui, de près ou de loin, m'ont donné la force de persévérer dans les moments difficiles. Je suis profondément reconnaissante pour chacune de ces rencontres.

Abstract

The chemical industry is a major contributor to global greenhouse gas emissions, highlighting the need for more energy-efficient and sustainable processes. This thesis focuses on process intensification through the optimisation of heat-exchanger reactors (HERs) using entropy generation minimization (EGM) as a guiding principle. EGM makes it possible to quantify and subsequently minimize irreversibilities in reactive systems, thereby providing a systematic approach to improving thermodynamic efficiency.

Two case studies are considered: the homogeneous hydrolysis of acetic anhydride in liquid phase and the heterogeneous catalytic oxidation of sulphur dioxide in a packed-bed HER. Both one-dimensional (1D) systemic models and two-dimensional (2D) axisymmetric computational fluid dynamics (CFD) simulations are employed to capture global trends and local effects, respectively. Entropy generation is analysed from viscous, thermal, chemical, and mass transfer contributions.

Multi-objective optimisation combining reactor volume reduction and entropy generation minimization were carried out. Results show that heat transfer and chemical reaction dominate entropy generation, while viscous and mass transfer contributions remain secondary. Profiled reactor geometries can significantly reduce irreversibilities in highly exothermic systems, whereas simple tubular designs are sufficient for reactions with low thermicity. Comparison between 1D and CFD models highlights that 1D approaches are suitable for preliminary screening, while CFD is essential for accurate prediction of radial effects and hot spots.

This work demonstrates that coupling 1D and CFD models with EGM enables the design of compact, energy-efficient HERs. Perspectives include experimental validation, improved AI-driven surrogate models, improved correlations for heat and mass transfer, and global process-level optimisation. Overall, this thesis establishes EGM as a practical framework for sustainable reactor design, contributing to reduced energy consumption and lower environmental impact in the chemical industry.

Keywords: CFD, Entropy generation, Modelling, Second law, Simulation, Heat exchanger reactor, Dynamic optimization, Intensification

Résumé

L'industrie chimique est un contributeur majeur aux émissions mondiales de gaz à effet de serre, soulignant la nécessité de développer des procédés plus économes en énergie et durables. Cette thèse s'intéresse à l'intensification des procédés par l'optimisation des réacteurs-échangeurs de chaleur (HER) en utilisant la minimisation de la génération d'entropie (EGM) comme principe directeur. L'EGM permet de quantifier puis minimiser les irréversibilités dans les systèmes réactifs, et constitue ainsi une approche systématique pour améliorer l'efficacité thermodynamique.

Deux cas d'étude sont considérés : l'hydrolyse homogène de l'anhydride acétique en phase liquide et l'oxydation catalytique hétérogène du dioxyde de soufre dans un HER à lit fixe. Des modèles systémiques unidimensionnels (1D) et des simulations CFD (Mécanique des fluides numérique) axisymétriques bidimensionnelles (2D) sont utilisés pour rendre compte respectivement des tendances globales et des effets locaux. La génération d'entropie est analysée en tenant compte des contributions visqueuses, thermiques, chimiques et de transfert de masse.

Des optimisations multi-objectifs combinant la réduction du volume du réacteur et la minimisation de l'entropie créée ont été réalisées. Les résultats montrent que le transfert de chaleur et la réaction chimique dominent la génération d'entropie, tandis que les contributions visqueuses et liées au transfert de masse restent secondaires. Les géométries de réacteurs profilées permettent de réduire sensiblement les irréversibilités dans les systèmes fortement exothermiques, tandis que des conceptions tubulaires simples suffisent pour des réactions de faible thermicité. La comparaison entre les modèles 1D et CFD montre que les approches 1D sont adaptées pour un criblage préliminaire, tandis que la CFD est essentielle pour la prédiction précise des effets radiaux et des points chauds.

Ce travail démontre que le couplage des modèles 1D et CFD avec l'EGM permet de concevoir des HER compacts et économes en énergie. Les perspectives de ce travail incluent la validation expérimentale, le développement de modèles de substitution assistés par intelligence artificielle, l'amélioration des corrélations de transfert de chaleur et de matière, ainsi que l'optimisation à l'échelle globale du procédé. Cette thèse établit finalement l'EGM comme un cadre pratique pour la conception de réacteurs durables, contribuant à la réduction de la consommation énergétique et de l'impact environnemental de l'industrie chimique.

Mots-clés : CFD, Création d'entropie, Modélisation, Second principe, Simulation, Réacteur-échangeur de chaleur, Optimisation dynamique, Intensification

General introduction

The Intergovernmental Panel on Climate Change (IPCC) regularly publishes comprehensive assessments on the state of the global climate. In its Sixth Assessment Report (AR6) (IPCC, 2023), the IPCC unequivocally confirmed that human activities have a significant and measurable impact on global warming. Several future scenarios are outlined in the report, ranging from the most optimistic—limiting global temperature rise to 2°C (with the 1.5°C threshold expected to be reached by around 2030, even under the most favourable conditions)—to the most pessimistic, projecting a temperature increase of up to 4°C by the end of the century (Figure 0.1).

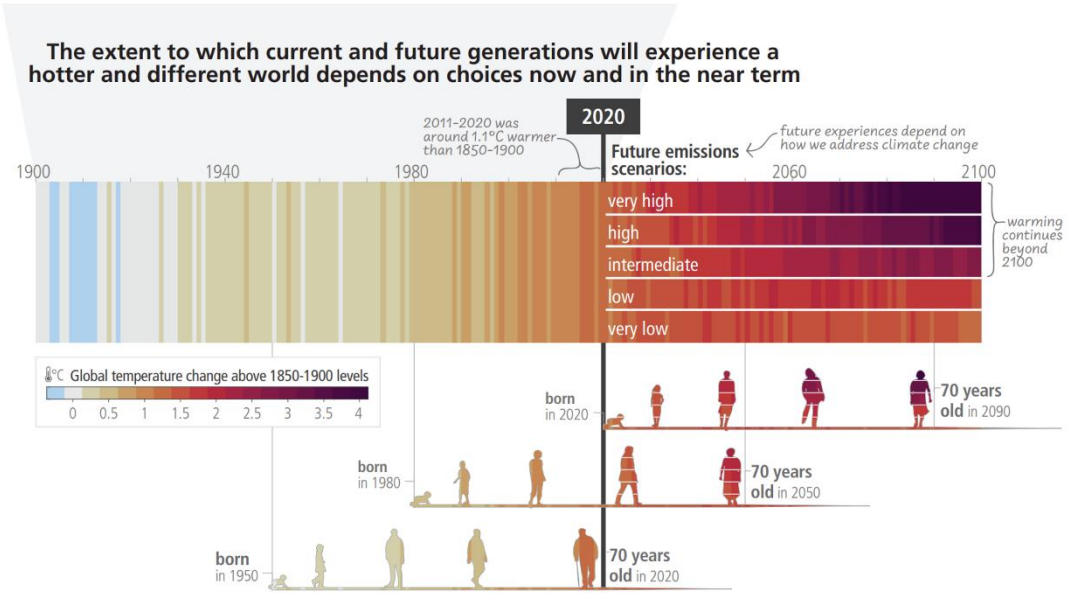

Figure 0.1: Observed (1900–2020) and projected (2021–2100) changes in global surface temperature (relative to 1850-1900), which are linked to changes in climate conditions and impacts (IPCC, 2023).

As human activities intensify, their visible consequences on the environment and biodiversity become more pronounced. These include the retreat of glaciers, melting of the Greenland ice sheet, ocean acidification, rising sea levels—threatening the existence of low-lying islands—and the increasing frequency of extreme weather events such as hurricanes, wildfires, floods, and droughts.

Beyond these environmental impacts, the effects on human and animal life are also undeniable. Climate change contributes to food insecurity (through declining crop yields, soil degradation, water scarcity and contamination) and large-scale population displacement. Vulnerable groups such as the elderly, pregnant women, and children are particularly at risk from extreme heatwaves. By 2100, it is estimated that between half and three-quarters of the world's population could be exposed to deadly temperature and humidity conditions.

These consequences, though inevitable to some extent, will depend in their severity on the effectiveness of current and future climate policies. While a certain degree of warming can no longer be avoided, it is essential to limit it as much as possible in order to mitigate its impact on both current and future generations.

The primary driver of this temperature increase is the accumulation of greenhouse gases (GHGs) in the atmosphere, particularly carbon dioxide (CO_2), methane (CH_4), and nitrous oxide (N_2O). These gases are partially absorbed by natural sinks such as oceans, terrestrial ecosystems, and polar ice caps. Prior to industrialization, these reservoirs were able to absorb and degrade GHGs over timescales of decades to centuries, preventing significant atmospheric build-up. However, due to current emission levels, these natural systems have become saturated, leading to an ever-increasing concentration of GHGs in the atmosphere and a reinforcing cycle of warming and diminished natural absorption capacity.

GHG emissions are distributed across various economic sectors. In France (including both metropolitan and overseas territories within the European Union), the industrial sector was responsible for 17.4% of national GHG emissions in 2023. Within this sector, the chemical industry alone accounted for nearly 24%, making it the largest source of CO_2 emissions (CITEPA, 2024).

Several strategies exist to mitigate CO_2 emissions, including carbon capture, utilization and storage; optimisation of supply chains and circular economy practices (e.g., short supply loops, material reuse); substitution of raw materials; the use of renewable energy; and, importantly, the improvement of industrial processes to reduce energy demand—thereby decreasing associated CO_2 emissions. This thesis focuses on the latter approach by using entropy generation minimization as a method for intensifying chemical processes. This thermodynamic method aims to quantify energy degradation within a system and uses it as an objective function to be minimized, thereby improving the energy efficiency of the process.

Process intensification is a modern approach in chemical engineering that aims to make chemical processes significantly more efficient by fundamentally rethinking how they are designed and operated. Instead of relying on traditional large-scale equipment and sequential unit operations, process intensification encourages the development of compact, integrated systems that perform multiple functions at once—with much higher performance, such as in the case of heat exchanger reactors (HER). The goal is to achieve substantial increases in efficiency, safety, and sustainability (Stankiewicz and Moulijn, 2002). The central idea of intensification is that "smaller can be better." By reducing the size and complexity of process equipment, engineers can achieve faster reaction rates, better control, reduced energy consumption, and lower environmental impact. This is particularly significant in a world where industrial processes must use less land, reduce emissions, and operate more flexibly.

One of the most promising examples of intensified technology is the HER. Heat exchanger reactors are a class of multifunctional process intensification devices that integrate heat transfer

and chemical reaction within a single compact system (Anxionnaz et al., 2008). This integration enables improved thermal control, enhanced safety, and higher reaction selectivity compared to conventional stirred tank or tubular reactors. The development and optimisation of heat exchanger reactors respond to growing industrial needs for smaller, safer, cleaner, and more energy-efficient processes—particularly in exothermic or endothermic systems where precise thermal control is critical. These benefits are not merely theoretical; industrial case studies have shown that HERs can reduce reaction times from hours to minutes and significantly cut down on by-product formation (Stankiewicz and Moulijn, 2002).

A wide variety of HER types exist, each offering specific advantages depending on the targeted application (Anxionnaz et al., 2008). These include spinning disk reactors (Figure 0.2a), which generate high heat and mass transfer rates through thin-film formation under centrifugal force; microchannel reactors, known for their high surface-area-to-volume ratio and rapid transient response; static mixers (Figure 0.2b), which create plug-flow-like behaviour and improve thermal homogeneity without additional energy needs; and oscillatory flow reactors, which decouple mixing intensity from net flow rate to allow better control of residence time and selectivity (Anxionnaz et al., 2008).

(a)

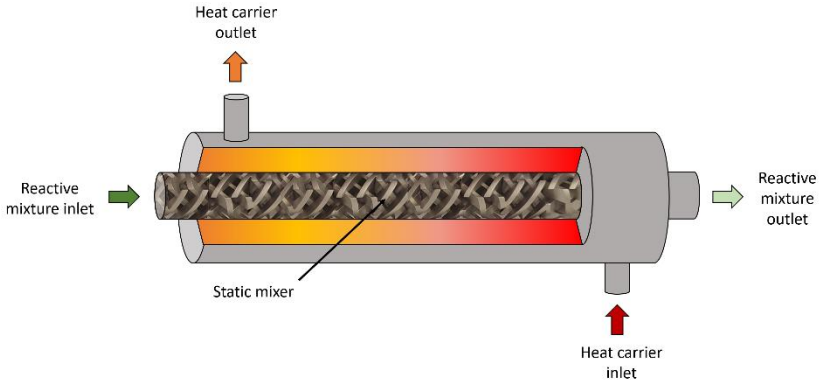

(b)

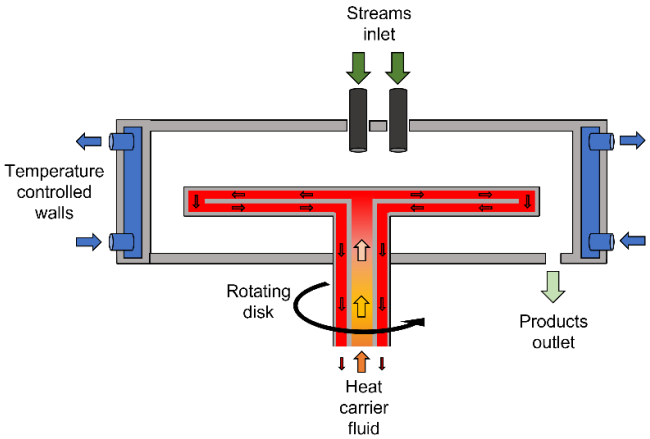

Figure 0.2: HERs operating principles: (a) Static mixer reactor, (b) Spinning disk reactor.

In particular, compact HERs—whose geometries are derived from classical heat exchangers such as plate-fin or shell-and-tube designs and adapted for reactive applications—may incorporate internal structures like offset strip fins, metallic foams, vortex generators, or catalytic inserts. These features improve micromixing and heat management even under laminar flow regimes, thus intensifying transport phenomena without significantly increasing pressure drop or reactor size. Working on HERs is particularly relevant due to their ability to (Anxionnaz et al., 2008):

- Improve reaction control, especially for fast or hazardous reactions;
- Reduce energy consumption through better thermal coupling and reduced heat loss;
- Minimize by-product formation thanks to improved selectivity from isothermal conditions;
- Allow fast and continuous production with smaller amounts of reactive chemicals, thereby enhancing safety and flexibility;
- Support modular design and ease of scale-up via numbering-up strategies;
- Adapt to additive manufacturing techniques, enabling custom geometries that further enhance performance.

In this thesis, the optimisation is performed on a concentric double-pipe HER in which two exothermic chemical reactions are carried out—one in the liquid phase (acetic anhydride hydrolysis) and one in the gas phase in a packed bed (SO_2 oxidation). The exothermicity of both reactions motivated the selection of a HER, as such systems, as described above, allow for effective heat management and compact design. The HER intensification will be carried out through a shape optimisation approach based on entropy generation minimization (EGM).

It is worth noting that shape optimisation has also been explored independently of entropy generation considerations. For example, Grundtvig et al. (2017) applied shape optimisation to the design of biocatalytic microreactors (Figure 0.3). Their objective was to maximize the product concentration at the reactor outlet by modifying the geometry of a YY-type microreactor to enhance mixing between two parallel laminar streams—one containing an enzyme (amine transaminase) and the other containing the substrates (acetophenone and isopropylamine). The optimisation was carried out using a random search algorithm, a gradient-free method well-suited for discontinuous objective functions and complex, non-convex domains. The optimal shape obtained exhibited complex undulations on the channel walls, resembling passive mixing structures, and led to an 8.4-fold increase in product yield, mainly due to improved convective mixing in the reaction zone. However, the final shape was deemed too complex for practical fabrication, highlighting the need for a balance between performance and manufacturability in shape optimisation.

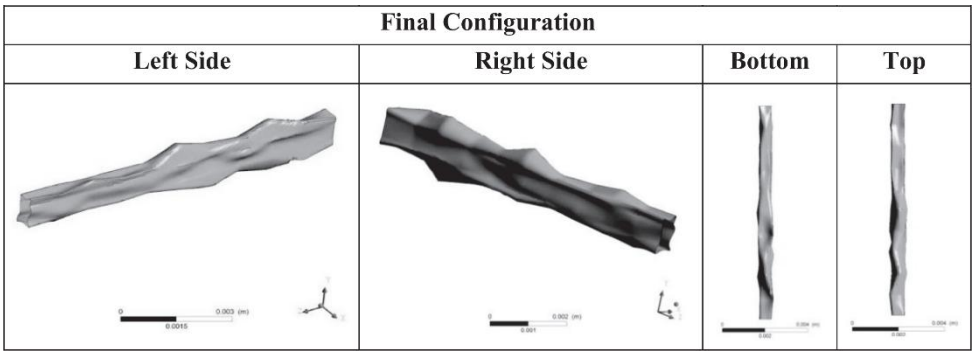

Figure 0.3: Optimised configuration (Grundtvig et al., 2017).

This issue was addressed by Courtais et al. (2023), who optimised a packed-bed reactor through a multi-objective optimisation framework, aiming to achieve the best trade-off between a high conversion rate—by minimizing the average reactant concentration at the reactor outlet—and low fluid energy dissipation. Their approach, which relied on a CFD-based model combined with the Hadamard boundary variation method (a gradient-based optimisation technique), preserved manufacturability while allowing general domain deformations. To select the most suitable optimised geometry, the multi-attribute utility theory was applied. The resulting reactor shapes were manufactured via 3D printing (Figure 0.4) and validated experimentally.

(a)

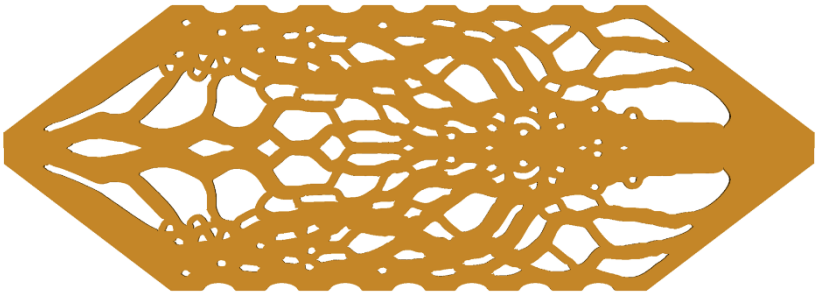

(b)



Figure 0.4: Optimised reactor configuration: (a) numerical model, (b) manufactured prototype (Courtais et al., 2023).

In contrast, the optimisation approach developed in this thesis explicitly aims to minimize total entropy generation by considering not only viscous dissipation but also the irreversibilities associated with heat transfer and chemical reactions. Furthermore, as explained in the following sections, the reactor shapes optimised in this thesis consist of a succession of easily manufacturable conical segments with varying slopes.

This thesis is structured into five chapters.

Chapter 1 introduces the concept of entropy generation, offering a historical overview and presenting the fundamental equations for both local modelling—allowing spatial visualization of entropy generation from distinct sources—and global modelling based on the entropy balance. It also introduces the principle of equipartition of entropy generation, which states that optimal systems are those in which entropy generation is uniformly distributed in space and time. A literature review on entropy generation minimization is included, with a focus on chemical reactors.

Chapter 2 focuses on the modelling of a concentric double-pipe HER where the hydrolysis of acetic anhydride—a homogeneous liquid-phase reaction—takes place. It establishes the governing equations for a systemic one-dimensional (1D) model, representing temperature, pressure, and concentration by single values along the axial position, as well as a more complex two-dimensional (2D) axisymmetric model, computed using Computational Fluid Dynamics (CFD), capturing axial and radial gradients. This chapter describes the system, modelling assumptions, and the methodology for optimising reactors geometries by minimizing entropy generation. It also details an experimental pilot reactor designed during the thesis, intended to assess the influence of reactor diameter on entropy generation and to validate the numerical simulations. Unfortunately, its long manufacturing and construction time prevented its use within the timeline of this thesis.

Chapter 3 provides a detailed comparison of the two modelling approaches (1D and CFD) in terms of their impact on computed entropy generation under identical operating conditions and reactors geometries. The influence of the modelling approach is examined through three case studies, each highlighting discrepancies related to the three main sources of entropy in a chemical reactor: viscous dissipation, heat transfer, and chemical reaction. The chapter then focuses on the shape optimisation results, exploring the influence of various operating conditions through multi-objective optimisation using Pareto fronts. These results identify reactor geometries that achieve a balance between low entropy generation and compact volume.

Chapter 4 presents the modelling of the catalytic oxidation of SO_2 in a concentric double-pipe HER with a fixed bed in the inner pipe. This chapter addresses a heterogeneous catalytic reaction using both 1D and CFD approaches, introducing additional physical phenomena, such as radiative heat transfer and catalyst behaviour modelling, not considered in the previous chapters.

Finally, Chapter 5 details the multi-objective shape optimisation of the SO_2 oxidation reactor. It analyses the impact of various operating conditions and emphasizes how the choice of modelling approach influences optimisation results. This chapter aims to provide meaningful guidelines for designing compact and efficient gaseous catalytic systems by minimizing entropy generation, while also offering insights into how modelling strategies affect optimisation results—serving as guidance for future research in this field.

List of Figures

Figure 0.1: Observed (1900–2020) and projected (2021–2100) changes in global surface temperature (relative to 1850-1900), which are linked to changes in climate conditions and impacts (IPCC, 2023). 12

Figure 0.2: HERs operating principles: (a) Static mixer reactor, (b) Spinning disk reactor. 14

Figure 0.3: Optimised configuration (Grundtvig et al., 2017). 16

Figure 0.4: Optimised reactor configuration: (a) numerical model, (b) manufactured prototype (Courtais et al., 2023) 16

Bibliography

Anxionnaz, Z., Cabassud, M., Gourdon, C., & Tochon, P. (2008). Heat exchanger/reactors (HEX reactors): concepts, technologies: state-of-the-art. Chemical Engineering and Processing: Process Intensification, 47(12), 2029-2050.

CITEPA. (2024). Émissions de gaz à effet de serre en France : estimation de l'année 2023 avec les données Secten du Citepa. Consulté le 15 avril 2024, sur https://www.citepa.org/emissions-de-gaz-a-effet-de-serre-en-france-nouvelle-estimation-lannee-2023-avec-les-donnees-secten-du-citepa/.

Courtais, A., Lesage, F., Privat, Y., Pelaingre, C., & Latifi, A. M. (2023). CFD-based geometrical shape optimization of a packed-bed reactor combining multi-objective and adjoint system methods. Chemical Engineering Science, 275, 118728.

Grundtvig, I. P. R., Daugaard, A. E., Woodley, J. M., Gernaey, K. V., & Krühne, U. (2017). Shape optimization as a tool to design biocatalytic microreactors. Chemical Engineering Journal, 322, 215-223.

IPCC, 2023: Climate Change 2023: Synthesis Report. Contribution of Working Groups I, II and III to the Sixth Assessment Report of the Intergovernmental Panel on Climate Change

[Core Writing Team, H. Lee and J. Romero (eds.)]. IPCC, Geneva, Switzerland, pp. 35-115, doi: 10.59327/IPCC/AR6-9789291691647.

Stankiewicz, A., & Moulijn, J. A. (2002). Process intensification. Industrial & Engineering Chemistry Research, 41(8), 1920-1924.

Chapter 1

Entropy generation minimization: The path to thermodynamic perfection

Table of Contents

Chapter 1 20

Abstract 23

1.1 Introduction 24

1.2 An historical introduction to the concept of irreversibilities 25

1.3 Entropy generation analysis 27

1.3.1 One dimensional entropy generation calculation 28

1.3.2 Two-dimensional entropy generation calculation (2D/3D modelling) 32

1.4 Equipartition of entropy production 36

1.5 Entropy generation minimization 39

1.5.1 Optimisation of heat exchangers 40

1.5.2 Optimisation of transient processes 42

1.5.3 Optimisation of processes with mass transfer 44

1.5.4 Optimisation of reactive systems 46

1.6 Conclusion 51

Nomenclature

$\boldsymbol{A}$	Chemical affinity (J mol^{-1})
$\mathfrak{D}$	Mass diffusivity (m^2 s^{-1})
$\vec{\boldsymbol{J}}$	Molar flux density vector (mol m^{-2} s^{-1})
L	HER total length (m)
M	Molecular weight (kg mol^{-1})
$\dot{m}$	Mass flow rate (kg s^{-1})
$\vec{\boldsymbol{n}}$	Local unit normal vector (-)
$\mathrm{N_s}$	Modified entropy generation number (-)
p	Pressure (Pa)
$\dot{Q}$	Heat transfer rate (W)
R_{gas}	Universal Gas Constant (J mol^{-1} K^{-1})
r_{vol}	Global rate of reaction (mol m^{-3} s^{-1})
S	Entropy generation (J K^{-1})
$\dot{S}$	Entropy generation rate (W K^{-1})
$\dot{s}'$	Rate of entropy generation per unit length (W K^{-1} m^{-1})
$\dot{s}'''$	Volumetric entropy generation rate (W K^{-1} m^{-3})
$\bar{s}$	Specific entropy (J kg^{-1} K^{-1})
s_{pure}	Molar entropy of pure (J mol^{-1} K^{-1})
T	Absolute temperature (K)
T_0	Environment temperature (K)
$\vec{\boldsymbol{u}}$	Velocity vector (m s^{-1})
$\dot{V}$	Volume flow rate (m^3 s^{-1})
V	Volume (m^3)
V_{HER}	Total volume of the heat exchanger reactor (m^3)
$\dot{W}$	Work rate (W)
x	Molar fraction (-)
$\vec{x}$	Molar fraction vector (-)
Y	Mass fraction (-)
z	Axial position along the system (m)

Greek letters

$\Delta_R G$	Gibbs free energy of reaction (J mol^{-1})
ε	Second law efficiency (-)
η	Dynamic viscosity (Pa s)
λ	Thermal conductivity (W m^{-1} K^{-1})
μ	Chemical potential (J mol^{-1})
ρ	Density (kg m^{-3})
$\overline{\overline{\boldsymbol{\tau}}}$	Viscous shear stress tensor (Pa)
$\vec{\boldsymbol{\varphi}}$	Heat flux density vector (W m^{-2})
ψ	Sensible heat flux per unit length (W m^{-1})
Ω	Flow section area (m^2)

Subscripts

ch	Refers to the chemical reaction
h	Refers to the heat transfer
hc	Refers to the heat carrier
inl	Refers to the inlet of the HER
irr	Refers to an irreversible transformation
j	Refers to the species j
k	Refers to the reaction k
M	Refers to the mixing-cup
m	Refers to the mth outlet
n	Refers to the nth inlet
out	Refers to outlet of the HER
rev	Refers to reversibility
tot	Refers to the total
tr	Refers to transient process
w	Refers to the wall
η	Refers to the viscous dissipation
μ	Refers to the mass transfer

Abbreviations

CAPEX	Capital expenditure
CFD	Computational Fluid Dynamics
EGA	Entropy Generation Analysis
EGM	Entropy Generation Minimization
EoDF	Equipartition of Driving Forces
EoEP	Equipartition of Entropy Production
ETS	Equal Thermodynamic Speed
GHG	Greenhouse Gas
HER	Heat Exchanger Reactor
IPCC	Intergovernmental Panel on Climate Change
LHTES	Latent Heat Thermal Energy Storage
OPEX	Operational Expenditure

Abstract

This chapter reviews the principles and applications of entropy generation minimization (EGM) in reactive systems. Starting from an historical perspective on thermodynamic irreversibilities, it presents both one-dimensional and multi-dimensional methods for calculating entropy generation, and discusses the principle of equipartition of entropy production. The chapter further explores optimisation strategies for heat exchangers, transient processes, mass transfer systems, and chemical reactors, highlighting dominant sources of entropy generation, such as heat transfer and chemical reactions. Particular attention is given to the limitations of conventional approaches, including the neglect of entropy generation in the heat carrier stream. By synthesising recent studies, the chapter underscores the relevance of EGM in improving process efficiency, providing the theoretical foundation for the numerical investigations and optimisation approaches presented in the following chapters.

1.1 Introduction

The design and optimisation of reactive systems are fundamentally constrained by thermodynamic irreversibilities. Over the past century, the analysis of entropy generation has emerged as a powerful tool to quantify these irreversibilities and guide the improvement of process efficiency. Chapter 1 provides a comprehensive review of the historical development of the concept of irreversibilities and the methodological advances in entropy generation analysis.

The chapter begins with an historical introduction to the concept of irreversibilities and its role in thermodynamic systems (Section 1.2), followed by a detailed discussion of entropy generation analysis methods, ranging from one-dimensional analytical calculations (Section 1.3.1) to two- and three-dimensional modelling approaches (Section 1.3.2). The principle of equipartition of entropy generation (Section 1.4) is presented as a key concept that drives optimal reactor design.

Section 1.5 focuses on the concept of entropy generation minimization (EGM) and its application to a wide variety of processes, including heat exchangers, transient processes, mass transfer systems, and reactive systems (Sections 1.5.1–1.5.4). Throughout the chapter, emphasis is placed on identifying the dominant sources of entropy generation, the strategies employed to mitigate them, and the trade-offs involved in multi-objective optimisation.

Overall, this chapter sets the stage for the subsequent work by summarising the theoretical and practical foundations of EGM, demonstrating how it can be applied to enhance the design and performance of reactive systems, and highlighting the challenges that arise when extending these concepts to more complex, real-world processes.

1.2 An historical introduction to the concept of irreversibilities

Multiple examples and definitions have been proposed for entropy. One of the most frequently cited—yet often misunderstood by newcomers— equates entropy to the notion of disorder. From a thermodynamic standpoint, entropy can be described as the extensive property associated with heat transfer. Indeed, every form of energy can be expressed as the product of a driving force and an extensive variable. In the case of gravitational energy, for example, the force is the elevation difference, and the extensive property is mass. Analogously, for thermal energy, temperature difference acts as the driving force, while entropy plays the role of the extensive property.

However, unlike other extensive properties, entropy is unique in that it is not conserved: it can be created but never destroyed. This fundamental distinction explains why all forms of energy can be entirely transformed into heat, but not the other way around.

Entropy generation stems from irreversibilities in a process. If a transformation was entirely reversible—meaning that running it backward would not seem surprising, much like watching a movie in reverse where nothing appears unnatural—no entropy would be created, as energy could be fully converted back into its original form. However, in reality, no process is truly reversible. Friction, mixing, thermal gradients, and other dissipative phenomena are present in all real systems, making the creation of entropy inevitable.

The utility of a given form of energy is directly related to its ability to be converted into another. Energy can be divided into two components: exergy and anergy. Exergy represents the usable fraction of energy—the available work—that can be entirely converted into another form. In contrast, anergy corresponds to the lost work, relative to the theoretical maximum available work for a given type of energy. As a result, exergy cannot be created, only destroyed, due to process irreversibilities (Jin, 2017).

The value of energy depends on how well it is transformed from one form to another: the less exergy is lost, the higher its value. Such observations have led to the development of specialized analytical fields that quantify energy degradation. For example, thermo-economics, introduced by J.H. Keenan in 1932 (Tsatsaronis, 1993), assigns an economic value to energy based on its quality. Similarly, exergo-environmental analysis (or thermo-environmental analysis) combines exergy analysis with assessments of environmental impact, enabling a more holistic evaluation of energy systems (Ordonez, 2022).

Exergy destruction is directly related to entropy generation through the Gouy–Stodola theorem, which expresses the relationship as follows (Moran et al., 2010):

$$\dot{W}_{rev} - \dot{W} = T_0 \dot{S}_{tot} \qquad 1.2.1$$

This equation shows that the difference between the reversible (theorical maximum) work output $\dot{W}_{rev}$ and the actual work output $\dot{W}$ is proportional to the entropy generation rate $\dot{S}_{tot}$, multiplied by the ambient temperature T_0. Thus, entropy generation is directly linked to lost work, and minimizing it becomes a clear path toward improving process efficiency.

The concept of irreversibility dates back to Sadi Carnot, who in his 1824 work "Réflexions sur la puissance motrice du feu et sur les machines propres à développer cette puissance" (Carnot, 1924), introduced the notion of a perfectly reversible cycle. He demonstrated that this idealized cycle represented a theoretical limit of efficiency that could never be achieved in practice. These foundational insights laid the groundwork for other scientists as Gibbs, Clausius and Kelvin to explore the limits of energy conversion and the potential for improving process efficiency (Chen, 1999).

A shift in perspective came with Josiah Willard Gibbs, who focused on the thermodynamic study of equilibrium systems undergoing transformations over infinitely long timeframes. This approach made it possible to analyse internal equilibria without significant exchanges with the environment and without increases in total entropy. Such reversible processes, while theoretically insightful, are unattainable in real-world applications (Chen, 1999).

From the 1970s onward, the study of real, constrained processes gained momentum. In physics, this gave rise to Finite Time Thermodynamics—also known as Endoreversible Thermodynamics—which analyses process efficiency over finite durations. In engineering, Bejan and Tsatsaronis extended this concept into what is now known as Entropy Generation Minimization (EGM) (Bejan, 1996). This methodology treats entropy generation as a criterion for optimisation and was popularized by Bejan in his influential 1982 work "Entropy Generation through Heat and Fluid Flow" (Bejan, 1982). In this work, he identified key contributors to entropy generation—primarily heat transfer and pressure drop—while omitting, at that stage, contributions from concentration gradients as heat exchangers were the main focus. Bejan demonstrated that entropy generation could be minimized through thoughtful design and optimisation within the real constraints of the process.

The common thread across these methodologies is the integration of fluid mechanics, heat transfer, and thermodynamics to identify and reduce sources of irreversibility. This not only improves process efficiency, but also reduces environmental impact (Chen, 1999). The field expanded rapidly in the wake of the 1970s energy crisis, the lifting of the Iron Curtain, and the convergence of previously isolated schools of thought. The evolution of “finite time” thermodynamics and the growing need for sustainable energy use further fuelled its development (Bejan, 1996). To use this powerful optimisation tool efficiently, a thorough understanding of how to calculate entropy generation is needed, which will be the focus of the next section.

1.3 Entropy generation analysis

As with any model-based optimisation approach, the practical optimality of the design identified by EGM depends heavily on the model accuracy as well as on the statement of the optimisation problem, particularly the formulation of the objective function, the entropy generation. Indeed, to properly optimised a system by reducing its entropy generation, it is necessary to accurately estimate this generation. This issue is covered by the Entropy Generation Analysis (EGA) which focuses on accurately modelling entropy generation in real processes, i.e., the identification and expression of entropy sources based on the velocity, temperature and/or concentration profiles, predicted by the process model. Indeed, entropy generation arises from velocity gradients which cause mechanical energy dissipation into heat, as well as heterogeneities in temperature and concentration since the resulting heat and mass transfer leads to a deterioration of the mechanizable part of energy. Therefore, EGA constitutes a diagnostic tool allowing to investigate the sources of irreversibility in an equipment (Awad, 2015) and thus, to assess its energy efficiency.

There are several possible sources of entropy generation inside a chemical reactor such as viscous dissipation, heat transfer, mass transfer and chemical reaction. Entropy is created when the flowing fluid degrades its kinetic energy or pressure into heat by friction with the reactor walls or with the catalyst in the case of fixed bed, or when the heat is released during the chemical reaction. Entropy can also be created inside a reactor from the coupling of mass and heat transfer, through the Soret and Dufour effects. The Soret effect, also known as thermal diffusion, refers to the phenomenon whereby a temperature gradient in a multicomponent mixture induces a mass flux, causing species to migrate from hotter to colder regions (or vice versa, depending on the substance). The Dufour effect is the reciprocal phenomenon of the Soret effect. It describes the generation of a heat flux due to a concentration gradient in a multicomponent system. The Soret and Dufour effects can usually be neglected as the Fickian mass diffusion predominates (Carrington and Sun, 1991).

Two main approaches are used in the literature to model entropy generation, depending on the complexity of the system model. For simplicity and time-saving reasons, systemic models are often employed to estimate entropy generation within a 1D framework. For more comprehensive cases, CFD has been used to simulate the system and calculate entropy generation in two- or three-dimensional models (2D axisymmetric, in this thesis). However, while the use of CFD generally allows for more precise modelling, this approach is also more time-consuming. Both local entropy formulations are presented in this chapter.

1.3.1 One dimensional entropy generation calculation

When a systemic model, e.g. a plug flow reactor model, is used to describe a process, only a single representative value of velocity, pressure, temperature and/or concentration is determined at each flow section. Thus, only the axial variations of the process variables are directly simulated, while radial profiles are assumed to be uniform (or quasi-uniform). The velocities predicted by 1D process models are based on the mass conservation equation and therefore represent the average velocity at each flow section. The temperatures and concentrations are calculated based on the energy conservation and species transport equations respectively and thus, represent the mixing-cup (i.e., mass flow rate or volume flow rate weighted averages) temperatures and concentrations at each axial position. 1D process models are much more computationally efficient than CFD, but they are obviously less accurate since they neglect radial gradients.

There are two main methods for estimating entropy generation in a system. The first one is the local approach, which evaluates the local entropy generation rate at each axial position for each source of irreversibility. This method not only provides a total entropy generation value (after integration over the reactor length), but also gives a spatially resolved insight into where entropy generation is the most significant along the system. The second method is based on an entropy balance, which estimates the entropy generated within the system by calculating the difference between the entropy fluxes at the inlet and outlet. While this approach does not offer spatial detail about where entropy is generated, it has the advantage of being simpler to implement. Both entropy estimation methods, as applied within the context of 1D systemic modelling, are presented below.

a. Local entropy generation calculation

The local approach consists of evaluating the local entropy generation rates (per unit length) based on local entropy balances. Integrating this source term throughout the system's length gives the total entropy generation of the process.

As aforementioned, the entropy generation inside a system can stem from different sources. Consequently, $\dot{s}'_{tot}$ [W K m^{-1}], the total entropy generation rate by unit length, is the sum of the following contributions:

$$\dot{s}'_{tot} = \dot{s}'_{\eta} + \dot{s}'_{h} + \dot{s}'_{ch} \qquad 1.3.1$$

where $\dot{s}'_{\eta}$, $\dot{s}'_{h}$ and $\dot{s}'_{ch}$ represent the rates of entropy generation per unit length that are respectively due to viscous dissipation, heat transfer and chemical reactions. It is noteworthy that, to the best of the authors' knowledge, no 1D formulation for entropy generation by mass transfer has been reported so far in the literature for non-separation process.

The rate of entropy generation per unit length due to viscous dissipation in a flowing fluid, $\dot{s}'_{\eta}$, can be calculated as follows (De Groot and Mazur, 1984; Johannessen and Kjelstrup, 2004):

$$\dot{s}'_{\eta} = -\frac{1}{T_M}\dot{V}\left(\frac{dp_M}{dz}\right)_{irr} \qquad 1.3.2$$

where T_M [K] and $\dot{V}$ [m^3 s^{-1}] represent respectively the mixing-cup temperature and the volumetric flowrate of the fluid, and z the axial position along the system. The irreversible term considered in this equation is the volumetric mechanical energy (the sum of pressure, dynamic head and gravitational head) to express the fact that the generation of entropy is due to mechanical energy dissipation and not simply to pressure variation. Indeed, in the case of inclined tubes or pipes with a varying flow section, gravitational and Venturi effects also induce pressure variations in the flow, but these variations correspond to reversible conversion of pressure into potential or kinetic energies that are not solely due to viscous dissipation, and therefore, should not be accounted for in the entropy generation source term.

In the case of heat transfer between a flowing fluid and a wall, in absence of phase transition, the resulting entropy generation rate within the fluid phase (i.e., it does not include the wall zone) is expressed as follows (Bejan, 1996; Johannessen and Kjelstrup, 2004):

$$\dot{s}'_{h} = \psi\left(\frac{1}{T_M} - \frac{1}{T_w}\right) \qquad 1.3.3$$

where ψ [W m^{-1}] is the sensible heat flux per unit length that is transferred between the fluid and the wall (considered positive when the heat flux is received by the fluid), T_w [K] the wall temperature and T_M [K] the fluid mixing-cup temperature.

In the absence of phase transition, for heat transfer between two fluid flows separated by a wall, irreversible thermodynamics allows expressing the linear entropy generation rate within the entire system (i.e., encompassing the two fluid phases as well as the wall) as follows (Johannessen and Kjelstrup, 2004):

$$\dot{s}'_{h} = \left|\psi\left(\frac{1}{T_{M,1}} - \frac{1}{T_{M,2}}\right)\right| \qquad 1.3.4$$

where ψ [W m^{-1}] here represents the heat flux per unit length that is transferred between the two flows through the wall and $T_{M,1}$ and $T_{M,2}$ [K] the mixing-cup temperatures of the two fluids.

In any case, the derivation of Equations 1.3.3 and 1.3.4 is based on the hypothesis that the temperatures of the fluids are quasi-uniform over the flow sections (an assumption rarely verified in practice apart for thermally developed laminar flows in narrow tubes or highly turbulent flows) and that the heat transfer occurs perpendicularly to the wall (assumption that is not valid neither in narrow metallic tubes where wall axial conduction becomes significant

nor in conditions of low thermal Péclet number where axial conduction in the fluid is not negligible). Therefore, compared to the CFD modelling approaches, Equations 1.3.3 and 1.3.4 are expected to poorly estimate entropy generation rates in most practical processes as radial gradients are not directly considered.

Concerning the rate of entropy generation by chemical reactions, it is expressed as follows (equation adapted from Nummedal et al. (2003) and Johannessen and Kjelstrup (2004)):

$$\dot{s}'_{ch} = -\Omega \sum r_{vol,k} \frac{(\Delta_R G)_k}{T_M} \qquad 1.3.5$$

where $r_{vol,k}$ [mol m^{-3} s^{-1}] is the global reaction rate of reaction k, Ω [m^2] is the flow cross-section and $(\Delta_R G)_k$ [J mol^{-1}] its Gibbs free energy of reaction k, both evaluated at the fluid mixing-cup temperature.

Equation 1.3.5 assumes that fluid temperature and species concentrations are uniform across the reactor cross-section, leading to uniform reactions rates and Gibbs free energies. Therefore, temperature and concentration gradients in the cross-stream direction limit the accuracy of Equation 1.3.5.

Integrating $\dot{s}'_{tot}$ throughout the system's length gives $\dot{S}_{tot}$ [W K^{-1}], the total entropy generation rate of the process:

$$\dot{S}_{tot} = \int_0^L \dot{s}'_{tot}\, dz \qquad 1.3.6$$

where L [m] represents the system's length.

b. Global entropy generation calculation

As aforementioned, the global approach consists of evaluating the total entropy generation of the process through an entropy balance over the system boundaries, instead of calculating and integrating the entropy source terms as with the local approach. Considering that the system boundaries consist of inlets/outlets and impermeable inert walls, and that the heat and mass transfer Péclet numbers are large, the global approach estimates the entropy generation rate under steady-state conditions as follows (Bejan, 1996):

$$\dot{S}_{tot} = \sum_{out} \dot{m}_m \bar{s}_m - \sum_{inl} \dot{m}_n \bar{s}_n - \int_{wall} \frac{\psi}{T} dz \qquad 1.3.7$$

where $\dot{m}$ [kg s^{-1}] denotes the mass flow rate, the subscripts m and n refer to the mth outlet and the nth inlet respectively, and $\bar{s}$ [J kg^{-1} K^{-1}] is the specific entropy of the fluid at the inlet/outlet. By convention, ψ, the heat flux per unit length, is considered positive (i.e., entropy inlet) when received by the system. The summation terms in Equation 1.3.7 represent advective transport

of entropy through the system inlets/outlets, while the integral term corresponds to entropy flux due to heat transfer between the fluid and the wall. Thus, this last term vanishes in the case of an adiabatic wall.

To solve Equation 1.3.7, the specific entropy, $\bar{s}$, needs to be expressed in terms of the state variables calculated by the 1D systemic model, i.e., the mixing-cup temperature and mole fractions (or concentrations), T_M and $x_{M,j}$, at the inlets and outlets. Without information on the radial profiles which are not simulated, the temperature and concentrations are supposed to be uniform at the inlets and outlets, as assumed by the systemic model. Therefore, if an ideal mixture is considered, the specific entropy expresses as follows (Foussard et al., 2015):

$$\bar{s}\left(T_M, p_M, \vec{x}_{M,j}\right) = \frac{\sum\left(x_{M,j} s_{j,pure}\left(T_M, p_M\right)\right)}{\sum\left(x_{M,j} M_j\right)} - R_{gas} \frac{\sum\left(x_{M,j} \ln\left(x_{M,j}\right)\right)}{\sum\left(x_{M,j} M_j\right)} \qquad 1.3.8$$

where $s_{j,pure}$ [J mol^{-1} K^{-1}] is the specific entropy of the pure component j, M_j [kg mol^{-1}] its molecular mass and R_{gas} [J mol^{-1} K^{-1}] the universal gas constant.

Finally, it is worthy to note that the local and global modelling approaches, both based on irreversible thermodynamics formulations, theoretically lead to the same results. The local method, however, has the advantage of making it possible to identify the phenomena and to locate the areas of the process which contribute the most to entropy generation.

1.3.2 Two-dimensional entropy generation calculation (2D/3D modelling)

a. Local entropy generation calculation

CFD simulations are more time-consuming than 1D models, however, they allow determining the velocity, temperature and species concentrations at each point in the computational domain (by solving the mass, momentum and energy equations). Thus, unlike 1D approaches, they allow a precise evaluation of the radial inhomogeneities in the system, which makes them suitable for describing real-world processes where velocity, temperature and/concentration are rarely uniform over the flow sections. Compared to the 1D approach, the formulation of each entropy generation term undergoes slight modifications to take into account this additional complexity.

Once the velocity, temperature and concentration fields are calculated, local entropy generation rates can be easily derived using the framework of "non-equilibrium thermodynamics" or "irreversible thermodynamics" (De Groot and Mazur, 1984). The basis of irreversible thermodynamics lies in the assumption that the local equilibrium hypothesis remains valid in non-equilibrium systems. Thus, in systems presenting macroscopic heterogeneities in composition/temperature (and therefore, generating entropy), local thermodynamic equilibrium is supposed to hold in each infinitesimal volume. Based on this assumption, under steady state conditions, the transport equation of the specific entropy within the framework of continuum theory gives (Sciacovelli et al., 2015):

$$div(\rho\vec{\boldsymbol{u}}\bar{s}) = -div\left(\frac{\vec{\boldsymbol{\varphi}}}{T} - \frac{1}{T}\sum \mu_j\vec{\boldsymbol{J}}_j\right) + \dot{s}'''_{tot} \qquad 1.3.9$$

where ρ [kg m^{-3}] denotes fluid density, $\vec{\boldsymbol{u}}$ [m s^{-1}] the velocity vector, $\bar{s}$ [J kg^{-1} K^{-1}] the specific entropy, $\vec{\boldsymbol{\varphi}}$ [W m^{-2}] the heat flux density vector, T [K] the absolute temperature, μ_j [J mol^{-1}] the chemical potential of species j, $\vec{\boldsymbol{J}}_j$ [mol m^{-2} s^{-1}] the molar flux density vector of species j and $\dot{s}'''_{tot}$ [W K^{-1} m^{-3}] the total entropy generation rate per unit volume. This equation expresses the second law of thermodynamics in its local differential form for non-equilibrium systems. It states that the rate of change of specific entropy within a fluid element (left-hand side of the equation) is the result of entropy flux divergence (first term on the right-hand side of the equation) and the local entropy generation due to irreversible processes (last term on the right-hand side of the equation).

In the simplest situations, the heat flux density vector, $\vec{\boldsymbol{\varphi}}$, consists of the conductive heat transfer only, but in more general cases, it also includes radiative heat transfer and Soret-Dufour effects terms. Also, in the most common situations, the molar flux density vector, $\vec{\boldsymbol{J}}$, simply accounts for ordinary (i.e., Fickian) diffusion, although in its most generic formulation, diffusion due to thermal or pression gradients should be accounted for. The reader may refer to Sciacovelli et al. (2015) for addition theoretical details.

The local entropy generation term for multi-dimensional modelling, $\dot{s}'''_{tot}$, includes the same entropy sources as the one-dimensional model, with the addition of entropy generation due to mass transfer, which is captured thanks to the capabilities of CFD modelling. Accordingly, the entropy generation term is the sum of the following contributions:

$$\dot{s}'''_{tot} = \dot{s}'''_{\eta} + \dot{s}'''_{h} + \dot{s}'''_{\mu} + \dot{s}'''_{ch} \qquad 1.3.10$$

where $\dot{s}'''_{\eta}$, $\dot{s}'''_{h}$, $\dot{s}'''_{\mu}$ and $\dot{s}'''_{ch}$ represent the volumetric entropy generation rates which are respectively due to viscous dissipation, heat transfer, mass transfer and chemical reaction. It should be noted that in some particular situations which are beyond the scope of this thesis, additional contributions need to be considered in Equation 1.3.10, namely electromagnetic sources in the case of magneto-hydrodynamics for example (Torabi et al., 2017), coupled heat and mass transfer terms in the presence of Soret and/or Dufour effects (Sciacovelli et al., 2015), ohmic losses in the presence of electric current (Sciacovelli and Verda, 2010), etc.

As noted previously, $\dot{s}'''_{\eta}$ represents rate of entropy generation due to viscous dissipation, i.e., to mechanical energy dissipation into heat by viscous stresses. This irreversibility occurs whenever the process includes a flowing fluid (apart from the theoretical cases of the forced vortex and the plug flow where no shear stress develops) and it can be calculated as follows (Sciacovelli et al., 2015):

$$\dot{s}'''_{\eta} = -\frac{1}{T}\bar{\bar{\tau}} : \bar{\bar{\nabla}}\vec{u} \qquad 1.3.11$$

where $\bar{\bar{\tau}}$ [Pa] and $\bar{\bar{\nabla}}\vec{u}$ [s^{-1}] respectively represent the shear stress and velocity gradient tensors. In the case of a Newtonian fluid, the shear stress tensor is expressed as follows:

$$\bar{\bar{\tau}} = -\eta\left[\bar{\bar{\nabla}}\vec{u} + \bar{\bar{\nabla}}^{T}\vec{u} - \frac{2}{3}div(\vec{u})\bar{\bar{1}}\right] \qquad 1.3.12$$

where η [Pa s] is the fluid dynamic viscosity.

$\dot{s}'''_{h}$ represents the rate of entropy generation due to heat transfer, i.e., to temperature inhomogeneities within the system. When the conductive heat transfer follows the Fourier's law and if radiation and phase transition are not involved, this term expresses as follows (Sciacovelli et al., 2015):

$$\dot{s}'''_{h} = \frac{\lambda}{T^2}\left(\vec{\nabla}T\right)^2 \qquad 1.3.13$$

where λ [W m^{-1} K^{-1}] is the thermal conductivity. This irreversibility occurs whenever the system involves heat transfer, which includes heat exchangers and reactors with endothermic/exothermic chemical reactions as they lead to temperature gradients. More

theoretically, since fluid flows lead to viscous dissipation as noted previously, they also involve heat transfer phenomena, although the resulting temperature variations remain negligible in most practical processes.

$\dot{s}_{\mu}'''$ represents the rate of entropy generation due to mass transfer, i.e., to concentration gradients within the system. When the reactive mixture can be treated as ideal, and if diffusion phenomena are solely described by Fick's law (i.e., absence of electrophoretic diffusion, Soret effect, etc.) this term is expressed as follows (Sciacovelli et al., 2015):

$$\dot{s}_{\mu}''' = \rho\, R_{gas} \sum \frac{\mathfrak{D}_{j,m}}{M_j x_j} \vec{\nabla} Y_j . \vec{\nabla} x_j \qquad 1.3.14$$

where R_{gas} [J mol^{-1} K^{-1}] is the universal ideal gas constant, $\mathfrak{D}_{j,m}$ [m^2 s^{-1}] the mass diffusion coefficient of species j in the mixture, M_j [kg mol^{-1}] its molecular weight, Y_j and x_j its mass and molar fractions respectively. Mass transfer contributes to entropy generation in multispecies mixtures involving concentration heterogeneities and in reactive flows since chemical reactions (except in very specific situations) lead to concentration gradients.

$\dot{s}_{ch}'''$ represents the rate of entropy generation due to chemical reactions. It is expressed as follows (Sciacovelli et al., 2015):

$$\dot{s}_{ch}''' = -\frac{1}{T} \sum \mu_j\, r_{vol,j} \qquad 1.3.15$$

where $r_{vol,j}$ [mol m^{-3} s^{-1}] represents the rate of creation of species j and μ_j [J mol^{-1}] its chemical potential.

CFD simulations allow obtaining the fields of velocity, temperature, concentrations and rate of reactions at each axial and radial position. The entropy generation rates, expressed by Equations 1.3.11, 1.3.13, 1.3.14 and 1.3.15 can be easily postprocessed then and summed up (Equation 1.3.10) to determine $\dot{s}_{tot}'''$, the local entropy source term. The total entropy generation rate of the system, $\dot{S}_{tot}$ [W K^{-1}], can be deduced by volume integration over the numerical domain (the total volume of the HER):

$$\dot{S}_{tot} = \iiint \dot{s}_{tot}'''\, dV \qquad 1.3.16$$

where dV represents an infinitesimal volume (usually approximated as the volume of the CFD mesh cells).

This local approach has the advantage of making it possible to identify the phenomena which contribute the most to irreversibility generation in the process, as well as providing a spatial (and temporal if needed) vision of the zones involving high entropy generation. This

information allows engineers to set their priorities and determine the transfer phenomena to be enhanced and the parts of the equipment whose design must be improved first.

b. Global entropy generation calculation

The CFD global entropy generation modelling approach consists in performing CFD simulation and using a global entropy balance to compute entropy generation rate. Volume integration of Equation 1.3.9 with the divergence theorem (i.e., Ostogradsky's theorem) lead to:

$$\dot{S}_{tot} = \iint \left(\rho \vec{u} \bar{s} + \frac{\vec{\varphi}}{T} - \frac{1}{T} \sum \mu_j \vec{J}_j \right) . \vec{n} \, d\Omega \qquad 1.3.17$$

where $\vec{n}$ is the local unit normal vector and $d\Omega$ [m^2] the infinitesimal surface area. The first term in the double integral represents advective transport of entropy and the second and third ones respectively represent heat and mass transfer effects.

The global approach evaluates the total entropy generation rate through surface integration of Equation 1.3.17 over the system's boundary. If these boundaries consist only of open inlets/outlets and impermeable inert walls (i.e., no permeable walls such as porous media or selective membranes and no reactive walls where heterogeneous reactions occur), Equation 1.3.17 can be further simplified. Indeed, impermeable inert wall boundaries allow heat transfer while preventing flow and mass transfer phenomena. When the heat and mass transfer Péclet numbers are large, which is the case in most practical processes, axial heat conduction and axial diffusion in the system, particularly at the inlets and outlets, can be neglected compared to advective transport. If all these assumptions are verified, Equation 1.3.17 can be simplified as follows:

$$\dot{S}_{tot} = \iint_{inl/out} \rho \vec{u} . \vec{n} \, \bar{s} d\Omega + \iint_{wall} \frac{\vec{\varphi}}{T} . \vec{n} \, dA \qquad 1.3.18$$

1.4 Equipartition of entropy production

The principle of Equipartition of Entropy Production (EoEP) suggests that, in transfer and separation processes, the total entropy generation is minimized when the local entropy generation is uniformly distributed across space and time. This concept, formulated by Tondeur and Kvaalen (1987), applies under conditions of fixed transfer duty and transfer area. In essence, the process is optimised when entropy is generated at a constant rate per unit of space or time.

This principle is particularly valuable from an engineering-economic perspective. For a system constrained by a fixed geometrical or dimensional criterion—interpretable as a fixed capital expenditure (CAPEX)—minimizing entropy generation aligns with reducing operational expenditure (OPEX). Since entropy generation represents lost useful energy, minimizing it translates to enhanced energetic efficiency and reduced operating costs, even though some entropy generation is thermodynamically unavoidable.

Building on this framework, Balkan (2005) proposed a methodology to select the most appropriate utility fluid to satisfy this equipartition principle. His work, grounded in the original analysis by Tondeur and Kvaalen (1987), emphasizes that variations in temperature profiles within heat exchangers can lead to deviations from equipartition. In particular, Balkan (2005) pointed out that using a constant and uniform heat transfer coefficient during the optimisation process, where the overall heat transfer coefficient is bound to change, may result in suboptimal performance. Instead, he advocates for the use of variable heat transfer coefficients during the optimisation process to better align with local thermodynamic conditions and maintain uniform entropy production. His work was based on a simple case, where he recalculated a uniform overall heat transfer coefficient for each optimised case (the optimisation was based on operating conditions). As the optimisation cases were tested, the fluid temperature and flow rates changed, which meant the overall heat transfer coefficient, assumed to be uniform in his study, had to be updated as well. He also concluded that the best optimisation choice is the one that results in the highest overall heat transfer coefficient. This study provides a foundation and shows the importance of accurately estimating the heat transfer coefficient. This work could be further developed by considering a heat transfer coefficient that varies along the length of the reactor, as implemented in this thesis, in contrast to the uniform Balkan (2005) coefficient used throughout the reactor.

In articles focusing on EGM, another equipartition principle is often mentioned, the Equipartition of Driving Forces (EoDF). While both aim to distribute physical quantities uniformly across a system, they differ in concept and application. EoEP asserts that local entropy production remains uniform throughout the system, often leading to the true minimum in total entropy production when full control over driving forces is available. This principle does not require constant transport coefficients and remains robust even when control is incomplete. In contrast, EoDF assumes uniform thermodynamic driving forces across the system, offering a simpler implementation but relying on more restrictive assumptions, such as

constant transport properties and uncoupled transport pathways. While EoDF can approximate the optimal configuration under ideal conditions, it may yield suboptimal results when those conditions are not met (Magnanelli et al., 2017).

Further contributions on this topic were made by Austbø and Gundersen (2015), who reviewed optimal distributions of driving forces in heat exchange systems under the assumption of constant heat transfer coefficients. Their analysis compares four main design strategies and confirms that irreversibilities are minimized, for a given heat exchanger size, when a uniform entropy generation per unit area is observed. They also observed that maintaining a uniform temperature difference across the exchanger, as usually considered as a design guideline, leads to higher irreversibilities and less efficient utilization of the transfer area.

The EoDF has also been extended beyond classical heat and mass transfer phenomenon to apply to chemical reactors. Sauar et al. (1997) generalized the concept by stating that, for a rate-controlled chemical reaction in a reactor of fixed volume and fixed overall reaction rate (and hence, fixed conversion), the energetically optimal configuration is the one in which the quantity $\frac{\Delta_R G}{T}$ is uniform across the reactor's spatial and temporal dimensions. Interestingly, Sauar et al. (1997) also points out that the maximum total conversion would be obtained if the entropy production and reaction time were fixed and the quantity $\frac{\Delta_R G}{T}$ was kept uniform in space and time.

This finding was reinforced by Johannessen and Kjelstrup (2004), who introduced the notion of a "highway in space"—a pathway in the space of operating conditions along which energy-efficient operation consistently occurs. Using optimal control theory, they explored thousands of reactor configurations controlled via heat carrier temperature and found that all energy-efficient solutions follow this highway. These trajectories are characterized by nearly constant entropy production and driving forces, even though flux–force relationships remain nonlinear. For processes operating under moderate intensities (desired conversion), this highway provides a powerful framework for identifying energy-optimal reactor designs.

Table 1.1 shows each driving force associated with its corresponding source of entropy generation in the case of a heat exchanger reactor, for both modelling approaches. This table highlights that the driving forces behind entropy generation, viscous dissipation, heat transfer, mass transfer and chemical reaction are related to gradients: pressure or velocity gradients for viscous dissipation, temperature gradients for heat transfer, and chemical potential gradients for mass transfer. For chemical reactions, the driving force is the deviation from equilibrium, expressed through the Gibbs free energy of reaction.

Table 1.1: Entropy sources driving forces for both modelling approaches.

	1D driving forces (Nummedal et al., 2005)	**2D/3D driving forces (Torabi et al., 2017)**
Viscous dissipation	$-\frac{1}{T_M}\left(\frac{dp_M}{dz}\right)_{irr}$	$\bar{\bar{\nabla}}\vec{u}$
Heat transfer	$\frac{1}{T_M}-\frac{1}{T_{M,hc}}$	$-\vec{\nabla}T$
Mass transfer		$-\vec{\nabla}\mu_i$
Chemical reaction	$-\frac{\Delta_r G}{T_M}$	$\boldsymbol{A}$

where $\boldsymbol{A}$ [J mol^{-1}] the chemical reaction affinity.

1.5 Entropy generation minimization

The minimization of entropy generation in a system is an approach that requires a thorough understanding of the studied process, its constraints, and the parameters over which the engineer has control. The application of EGM involves several steps. To apply this approach, a reference situation must first be defined—this corresponds to the initial, non-optimised process. Once the reference state is adequately described through reliable mathematical models, it becomes possible to calculate the generated entropy and attempt to reduce its generation. Entropy minimization can then be carried out numerically using an optimisation algorithm, such as genetic algorithms. The minimized function, subject to the imposed process constraints, enables the engineer to operate or modify the process in a way that reduces exergy losses (Sciacovelli et al., 2015).

EGM differs from exergy analysis, which relies solely on thermodynamics—specifically the first and second laws—and on reference values for the thermodynamic properties of the components. In contrast, entropy minimization must take into account the inherent non-idealities of real processes and thus draws on fluid mechanics, thermodynamics, and heat transfer. Furthermore, the analysis of entropy generation also incorporates the time and geometric constraints of processes (Bejan, 1996). This establishes EGM as a discipline, offering an explicit connection between system irreversibilities, operating conditions, and process geometry (Sciacovelli et al., 2015).

Because entropy is defined as the product of a flux and a driving force, entropy production analysis and optimisation allow the attribution of generated entropy to its specific source—something that other energy-based approaches cannot provide. This ability to obtain a qualitative, spatial, and temporal view of irreversibilities enables the identification of the most critical elements of the process, thereby enhancing the optimisation potential. However, this type of analysis is highly sensitive to the engineer's assumptions. It is essential to be discerning when deciding which sources of irreversibility to include in the study—and even more cautious regarding those neglected or considered perfectly reversible (Bejan, 1996). Additionally, the engineer's decisions will influence the optimisation outcome, as it takes into account both the real process constraints and those defined by the engineer.

The ultimate goal of a process is to produce a specific product with maximum efficiency, minimum cost and minimum environmental impact. However, due to non-idealities such as temperature or concentration gradients, entropy is inevitably generated in a process. These gradients cause energy dissipation as heat (or the destruction of available work). The EGM approach allows entropy generation to be considered explicitly as an objective function during process optimisation. By reducing entropy production, energy efficiency, product quality, environmental impact and costs can all be improved.

1.5.1 Optimisation of heat exchangers

Several researchers have applied the EGM method to a wide variety of systems, showing its potential to improve efficiency by optimising geometry and operating conditions. In the field of heat exchangers, for example, Chowdhury (Chowdhury and Sarangi, 1983) and Sarangi (Sarangi and Chowdhury, 1982) considered counterflow configurations and incorporated axial heat conduction to determine the most suitable material for the exchanger, which would enhance radial thermal conductivity and limit axial conduction. Their work demonstrated how thermophysical properties, flow conditions, and capacity rate ratios (defined as the ratio of the minimum to the maximum product of heat capacity and mass flow rate between the two streams) influence the optimal thermal conductivity of the exchanger internal walls. They considered a classical concentric tube exchanger with a large heat transfer unit number. They found that high conductivity materials are optimal for heat exchangers involving high velocities, while low thermal conductivities material are better at low velocities.

This emphasis on geometric optimisation has also been explored by Sciubba (1996), who investigated the optimal spacing of fins in a heat exchanger to minimize entropy generation. Similarly, Wang et al. (2011) applied EGM to improve the design of a centrifugal fan, confirming that performance gains can be achieved even in rotating machinery.

Miniaturized systems, particularly those used for electronic component cooling, have also benefited from the EGM approach. Researchers such as Culham and Muzychka (2001), Iyengar and Bar-Cohen (2003), and Zhang et al. (2010) used this method to enhance the performance of compact cooling devices under strict spatial constraints. In the same context, Eger et al. (2017) applied EGM to the heat sinks of electrical machines, identifying inefficient heat transfer zones and enabling the redesign of geometries for improved thermal behaviour.

Awad (2015) proposed further enhancements for microchannel heat sinks by suggesting innovative channel shapes, such as elliptical or triangular cross-sections, and the use of advanced working fluids like nanofluids or magnetic nanofluids. These fluids, combined with the flexibility of EGM to account for new geometries and thermophysical behaviours, open promising avenues for performance optimisation, especially at the microscale.

The adaptability of EGM has also been highlighted by Bejan (1996), who applied the method to a wide range of systems including thermal storage, solar power plants, nuclear and fossil fuel facilities, and refrigeration systems. He showed that EGM could help define optimal heating and cooling durations, and in the case of solar power, determine the ideal operating temperatures to reduce thermal losses. For conventional power plants, it proved useful in optimising heat exchanger design and operating strategies.

Finally, Guo et al. (2009) applied EGM to shell-and-tube heat exchangers. They used a modified entropy generation number to reduce pumping power and enhance heat transfer:

$$N_S = \frac{\dot{S}_{tot} T_{hc}}{\dot{Q}} \qquad 1.5.1$$

where N_S is the modified entropy generation number, $\dot{S}_{tot}$ [W K^{-1}] is the total entropy generation rate, $\dot{Q}$ [W] is the actual heat transfer rate and T_{hc} [K] is the temperature of the cold stream. This number is different from the one originally stated by Bejan (1982) (which consist of the total entropy generation rate over the maximal capacity rate ratio) because it allows to bypass the "entropy generation paradox". Indeed, as originally reported by Bejan, when the entropy generation rate is non-dimensionalized using the heat capacity rate of the stream the resulting function exhibits a non-monotonic behaviour: entropy generation reaches a maximum at intermediate effectiveness values (which is the actual heat transfer rate over the maximum possible heat transfer rate, which occurs when the heat exchanger has an infinite surface area (ideal case)) and tends to zero both when the effectiveness approaches zero and one. This is counterintuitive, as one would expect entropy generation to decrease monotonically with increasing exchanger performance. This paradox arises because the normalization does not account for the heat actually transferred. To resolve this issue, Hesselgreaves (2000) proposed a more consistent formulation by normalizing the entropy generation with the heat flow rate, leading to a revised entropy generation number. This approach aligns with exergy analysis principles and ensures that the entropy generation number decreases continuously with increasing heat exchanger effectiveness, thereby avoiding the paradox and providing a more reliable metric for optimisation.

1.5.2 Optimisation of transient processes

One of the main limitations in the current application of EGM lies in its scarce use for the analysis and optimisation of transient processes. Most studies available in the literature focus on steady-state conditions, mainly due to the complexity of accounting for time-dependent effects. Unlike stationary systems, transient processes require optimisation over a specific time interval, and the optimal configuration may vary depending on the chosen period. This issue becomes particularly relevant in systems operating in cycles, such as energy storage technologies.

Among these, latent heat thermal energy storage (LHTES) systems—based on phase change materials—have attracted significant scientific interest. While their general behaviour is well documented in reviews such as that of Jegadheeswaran et al. (2010), the optimisation efforts in this field have largely been limited to operating parameters, with very few studies addressing geometry optimisation. Jegadheeswaran et al. emphasized the potential of entropy generation analysis to improve both the design and operational performance of LHTES systems, yet concrete applications remain rare.

In this context, the work of Guelpa et al. (2013) stands out as one of the few examples where local entropy generation calculations were used to propose optimised fin arrangements for a shell-and-tube LHTES configuration. Their study employed a CFD model to simulate phase change and heat transfer between the heat transfer fluid and the phase change material. They found that entropy generation due to heat transfer dominated over that from fluid friction. Two design strategies were explored: increasing the number of fins while reducing their thickness and redistributing them more densely in some parts of the LHTES system. The former reduced solidification time by 16%, and the latter improved second-law efficiency by 5%. Notably, they observed that a non-uniform fin distribution could reduce the time-averaged entropy generation by 17%, underlining the importance of geometry in dynamic performance. Their transient analysis also revealed critical periods where these geometric modifications had the greatest impact.

Furthermore, for transient processes, a second law efficiency criterion was established in order to better characterize the time-dependent entropy generation. Several authors have also explored the interplay between entropy generation and second-law efficiency.

The second law efficiency ε is a criterion established for transient processes and can be described as (Erek and Dincer, 2008):

$$\varepsilon = 1 - N_{s,transient} \qquad 1.5.2$$

with

$$N_{s,transient} = \frac{T_0 S_{tot}}{Ex_{in}} \quad 1.5.3$$

where $N_{s,transient}$ is the entropy generation number for transient processes, T_0 [K] is the ambient temperature, S_{tot} [J K^{-1}] is the entropy generation and Ex_{in} [J] is the total exergy inlet. This criterion can be assimilated to the maximum potential associated with the incoming thermal energy (Erek and Dincer, 2008). It represents the destroyed exergy over the exergy that was given to the system over a certain time period.

Sciacovelli et al. (2014), working on LHTES systems, optimised Y-shaped fins through a multi objective optimisation, using global entropy generation and surface integral of heat flux —two strongly correlated metrics— as the objective functions. They found that a configuration with 30° secondary branches accelerated the solidification of the phase change material by 30%. Although this led to increased entropy generation, the overall second-law efficiency remained unchanged due to a higher exergy flux.

Domanski and Fellah (1996) also evaluated the second-law efficiency of thermal energy storage using phase change materials in a two-unit series system. Their results showed that the use of multiple units—each with a tailored melting point—can improve efficiency, with the upstream unit requiring a higher melting material and the downstream one closer to ambient temperature. However, they also highlighted that increasing the number of units excessively can lead to efficiency losses due to increased friction, indicating that an optimal configuration must be found to balance these opposing effects.

Despite these contributions, the optimisation of transient processes using EGM remains largely underexplored, particularly when it comes to the geometry of the system. The few studies that exist point to the significant potential of this approach, especially for storage systems operating under intermittent or cyclic regimes.

1.5.3 Optimisation of processes with mass transfer

Processes involving mass transfer and chemical reactions have been less extensively studied compared to those focused solely on thermal exchanges, such as heat exchangers. In particular, the formulation of local entropy generation terms due to chemical reactions, mass transfer, and the coupling effects from the Soret and Dufour phenomena remains an area of limited research. Teng et al. (1998) proposed a formulation to account for these local terms.

In the field of cooling towers, several studies have aimed to optimise their performance. Narayan and Zubair (2010) focused on minimizing entropy generation in heat and mass exchanger devices without chemical reactions, particularly in cooling towers and humidification-dehumidification desalination systems. They introduced a new "modified heat capacity rate ratio", which, when optimised, helped to minimize entropy generation. The modified heat capacity rate ratio is defined as the ratio of the maximum enthalpy change of the cold stream over the maximum enthalpy change of the hot stream, considering both sensible and latent heat effects in combined heat and mass transfer processes, such as those involving phase change. Unlike the conventional heat capacity rate ratio used for heat exchangers without mass transfer—which only accounts for sensible enthalpy changes—, the modified ratio incorporates the additional energy associated with phase transition, thereby providing a more accurate representation of the thermal behaviour in such systems.

Smrekar et al. (2005) also studied cooling towers, specifically optimising water distribution in natural draft cooling towers. Their work demonstrated that improving heat transfer homogeneity through optimised water distribution reduces entropy generation and minimizes exergy loss, highlighting again the entropy generation equipartition principle. Maintaining a constant and minimal water/air mass flow ratio further contributed to lowering water outlet temperatures, ultimately improving the efficiency of condensers and power plants.

Desalination technologies also benefited from entropy generation analysis. Mistry et al. (2011) focused on reverse osmosis desalination and found that entropy generation was not only caused by separation irreversibilities, but also by the thermal disequilibrium of discharge and irreversible brine mixing with seawater. They emphasized that better management of the discharged stream could reduce entropy generation, thus improving system efficiency.

Furthermore, research in distillation towers by Ratkje et al. (1995) and Johannessen and Røsjorde (2007) further explored the application of entropy minimization. Ratkje et al. (1995) demonstrated that the principle of equipartition of forces minimizes entropy production in distillation columns by uniformly distributing separation driving forces. Their numerical simulations showed up to a 7% reduction in entropy production per cubic meter of product when distributed heating was applied, though this involves a higher equipment cost. Similarly, Johannessen and Røsjorde (2007) found that the equipartition principle closely approximates optimal entropy production in diabatic tray distillation, particularly when large heat transfer

areas and more trays are involved, despite the challenges of independently controlling all driving forces.

Finally, entropy generation minimization has also been applied in membrane separation systems. Magnanelli et al. (2017) investigated this concept using a membrane unit designed for CO_2 separation from natural gas, where CO_2 and CH_4 are treated as ideal gases. The process involved a counter-current configuration between the feed and permeate flows, with permeation driven by partial pressure differences across the membrane. They performed an entropy generation minimization in order to compare multiple principles such as EoEP, EoDF and Equal Thermodynamic Speed (ETS). The thermodynamic speed represents how quickly a system responds or evolves in thermodynamic terms when driven away from equilibrium. For each case, they controlled the permeate partial or total pressure at any position.

Multiple optimisations were carried out under different additional constraints to assess their impact on system performance. Specifically, the local entropy production was constrained to remain constant for the EoEP case, the thermodynamic driving forces were held constant for the EoDF, and the thermodynamic speed was maintained constant for the ETS strategy. These constrained strategies were systematically compared against a baseline optimisation aimed at minimizing total entropy generation, without any of the additional constraints imposed in the other scenarios.

Two configurations were considered: a continuous membrane system and a discrete-stage system. The purified system consisted of natural gas with a CO_2 mole fraction reduced to 2% at the outlet. The permeate stream was designed to flow in counter-current to the feed, and the separation relied on differences in the permeation rates of CO_2 and CH_4, governed by state-dependent transport coefficients.

One key finding was that when all driving forces can be independently controlled, the EoEP condition exactly reproduces the numerical optimum. However, when control is limited (e.g., only total permeate pressure can be adjusted and not the partial pressures), the EoEP and ETS strategies still provided very good approximations of the minimum entropy production, while EoDF was less accurate under these constraints.

Importantly, the authors highlighted that equipartition principles simplify the design process by reducing the dimensionality of the optimisation problem, sometimes to a single scalar variable. However, they also warned that equipartition does not guarantee uniqueness of the solution unless the number of constraints equals the number of degrees of freedom. Therefore, while these principles can guide efficient design, full numerical optimisation remains necessary in under-constrained scenarios.

1.5.4 Optimisation of reactive systems

The optimisation of chemical reactors through entropy generation minimization is a relatively recent area of investigation. As with other non-reactive process equipment, several strategies can be employed to reduce entropy production. Numerous studies have explored this objective using various optimisation approaches, including thermal boundary control, geometric modifications and operating conditions adjustments and reactor shape design. An overview of these studies, along with their respective methodologies, outcomes, and conclusions, is presented below. This literature review aims to support the interpretation of the results obtained in this thesis, whose overarching objective is to propose a shape optimisation methodology applicable to both liquid- and gas-phase reactions. Additionally, it seeks to provide insights into entropy generation behaviour in reactive systems and the effect of variable operating conditions on the optimised shapes.

A significant number of studies have focused on optimising thermal boundary conditions to reduce entropy generation. Li et al. (2019) conducted a study on methanol synthesis reactors, successfully reducing total entropy generation by 20.5% through optimisation of the exterior wall temperature along the reactor's length. By applying EGM, they achieved a more uniform local entropy generation rate, emphasizing how a balanced distribution of the driving forces along the reactor can effectively minimize entropy production. This concept of optimising thermal and mass transfer in reactors is echoed in various other studies, highlighting the importance of understanding and controlling the thermodynamic forces in reaction systems.

Furthermore, Kjelstrup et al. (2000) examined the impact of catalyst distribution and combustion conditions on entropy generation, where the cooling temperature was chosen as the control variable in a plug flow methanol reactor. They showed that increasing the catalyst weight and optimising its distribution could significantly reduce entropy generation in such reactors. They also found out that heat transfer was the main contribution to entropy generation, followed by the chemical reaction.

The optimisation of entropy generation through thermal boundary conditions was also sometimes coupled with other levers. For example, Johannessen and Kjelstrup (2004) studied the optimisation of a SO_2 oxidation reactor, where they reduced the reactor length (shape optimisation) and adjusted the wall temperature. They observed a 25% reduction in entropy generation, further reinforcing the idea that reactor geometry, temperature control, and the distribution of thermodynamic forces are key to minimizing irreversibilities.

Additionally, Zhang et al. (2019) studied hydrocarbon synthesis from CO_2 and hydrogen in fixed-bed reactors. The control variables chosen were the temperature profile at the plug reactor wall and the inlet conditions such as the inlet reactant ratio (operating conditions optimisation). The EoEP and EoDF were not observed very obviously in the optimised configurations. Instead, the primary source of irreversibilities in their system came from the chemical reactions themselves, highlighting that in certain cases, the application of

equipartition must be carefully evaluated, particularly in reactors operating predominantly under reaction mode (where chemical reaction is the dominant contribution to the total entropy creation).

Nummedal et al. (2003) also optimised operating conditions and coolant temperature profiles and demonstrated how ammonia reaction systems could be optimised to reduce entropy generation by adjusting inlet conditions (operating conditions optimisation) and coolant temperature profiles. Their results illustrated a manageable range of entropy generation reduction, but they also reminded that preheating and specific system constraints could impact the optimisation process.

Using the operating conditions as control variable in EGM was also carried out in other studies. Indeed, a similar approach was adopted by Nummedal et al. (2005) in their study of a multi-reaction tubular steam reformer reactor. By optimising the inlet conditions and the flow rates, they achieved a 60% reduction in entropy generation, underscoring the impact of careful design modifications on reactor efficiency. However, their results also point out a trade-off between reducing entropy generation and the need for preheating, which in itself introduces additional irreversibility.

Arjmandi and Amani (2015) worked on turbulent combustion of a mixed bluff-body swirl stabilized flame in a gas turbine. They studied the effect of different operating conditions in a system subject to a maximal temperature constraint and a flame height constraint. The two entropy calculation methods, global balance vs. local rate, show an acceptable 6.4% deviation, which has been attributed to the simplified modelling of turbulence effects in the entropy source terms, the averaging procedure of mean variables and the turbulence model. Chemical reactions and heat transfer are the dominant and opposing contributors, and their trade-off defines optimal conditions.

Sun et al. (2020) explored sulphuric acid decomposition in a tubular reactor. They used inlet temperature, inlet pressure, and inlet total mole flow rate as control variables to optimise a tubular plug-flow sulphuric acid decomposition reactor. Their multi-objective optimisation study resulted in a 9% reduction in entropy generation alongside a 14% increase in SO_2 yield, underscoring the trade-offs between entropy minimization and performance objectives in reaction-based systems.

Additional to operating conditions, the reactor itself was considered in the EGM framework. Jejurkar and Mishra (2011) focused on the impact of the reactor material by investigating the effects of wall thermal conductivity in an annular micro-combustor. Their results show that while chemical reactions and heat conduction were constant contributors to entropy production, irreversibility due to mass transfer decreases when the wall thermal conductivity is increased. This study emphasizes the complex interplay between different sources of irreversibilities.

Another way for reducing entropy generation is through shape optimisation of the reactor, an optimisation lever that is the main focus of this thesis. Several authors took interest into shape optimisation and applied it to reactors where different chemical reactions are carried out.

Magnanelli et al. (2019) built upon Johannessen and Kjelstrup (2004) SO_2 oxidation study and proposed a "reindeer nose" optimal geometry, which demonstrated an 11% reduction in total entropy production. When the reactor length was also considered as an optimisation parameter, entropy generation was further decreased of 16% compared to the reference reactor case, illustrating how geometric modifications can significantly enhance reactor performance by aligning the flow with the principle of uniform entropy distribution. These findings are aligned with those of Kizilova et al. (2024), who, in their CFD analysis of heat exchanger plug flow reactors, studied 9 nature-inspired geometries and found that uniform entropy production along the reactor tube was the optimal solution for minimizing irreversibilities.

Chen et al. (2018) examined CO_2 hydrogenation to light olefins in a fixed tubular reactor, reporting remarkable entropy generation reductions of up to 24.78% through modifications of the reactor diameter and the catalyst bed density, with an observed trade-off between the irreversibilities stemming from heat transfer and chemical reaction.

Finally, Sciacovelli and Verda (2009) worked on solid oxide fuel cell geometry, where coupled heat-mass transfer was found to play a significant role in entropy generation, and redesigning the geometry resulted in a 6% increase in power density. These findings underscore the importance of considering all contributing factors to entropy production, as they interact within the system. All the studies are summed up in Table 1.2.

Table 1.2: Summary of EGM optimisations on systems involving chemical reactions.

Authors	Studied system	System modelling	Objective function	Findings
Kjelstrup et al. (2000)	Methanol production	Systemic model	Single-objective	Multi-reaction reactor. Increasing catalyst weight significantly reduces entropy generation.
Nummedal et al. (2003)	Ammonia reaction	Systemic model	Single-objective	Highlights the critical role of the overall heat transfer coefficient.
Johannessen and Kjelstrup (2004)	SO_2 oxidation reactor	Systemic model	Single-objective	Entropy production reduced by 10.4% with optimised cooling, reaching 24.7% when reactor length was also adjusted. Thermodynamic forces remain nearly constant.
Nummedal et al. (2005)	Tubular steam reformer	Systemic model	Single-objective	Multi-reaction reactor. Entropy production reduced by over 60% along the optimal path.
Sciacovelli and Verda (2009)	Solid oxide fuel cell (SOFC)	CFD	Single-objective	Major irreversibilities stem from mass transfer and coupled heat–mass transfer in SOFC.

Jejurkar and Mishra (2011)	H_2–air combustion	CFD	Single-objective	Optimal thermal conductivity range (0.1–1.75 W m^{-1} K^{-1}) ensures stable operation and high energetic efficiency. Mass diffusion irreversibility decreased with higher thermal conductivity.
Arjmandi and Amani (2015)	Combustion chamber	CFD	Single-objective	Chemical reactions and heat transfer are opposing contributors; their trade-off defines optimal conditions. Deviation between local and global entropy generation calculation.
Magnanelli et al. (2019)	SO_2 oxidation reactor	Systemic model	Single-objective	Optimal "reindeer nose" geometry leads to about 16% entropy reduction.
Zhang et al. (2019)	Hydrocarbon synthesis	Systemic model	Single-objective	Multi-reaction reactor. Equipartition of entropy generation does not always yield optimal results; chemical reaction irreversibility is dominant.
Li et al. (2019)	Methanol synthesis via CO_2 hydrogenation	Systemic model	Single-objective	Optimised design reduces total entropy generation by 20.5%. Guidelines on optimal inlet molar flowrate and component subtraction.
Chen et al. (2018)	CO_2 hydrogenation to light olefins	Systemic model	Single-objective	Multi-reaction reactor. Up to 24.78% entropy reduction through changes in reactor diameter and catalyst bed density. Trade-off observed between irreversibilities from heat transfer and chemical reaction.
Sun et al. (2020)	Sulphuric acid decomposition	Systemic model	Multi-objective	A trade-off exists between minimizing entropy generation rate and maximizing SO_2 yield.
Kizilova et al. (2024)	SO_2 oxidation reactor	CFD	Multi-objective	Nature-inspired design enhances exergy efficiency. Comparison of different geometries and Pareto fronts of hydraulic resistivity, thermal resistivity, thermal inlet length and entropy production through 9 geometries.

This literature review has provided an overview of the different levers employed in recent years to optimise reactive systems through EGM. Several types of control variables have been investigated, including thermal boundary control, geometric modifications, operating condition adjustments, and reactor shape design. It is important to highlight that thermal boundary control—namely, the optimisation of wall temperature in plug flow reactors—is not always a practical solution from an industrial standpoint, as the temperature of the reactor wall is difficult (if not impossible) to regulate precisely. Moreover, while the temperature of the heat carrier is often considered as a control variable, the entropy generated within that carrier stream is frequently neglected. This thesis addresses that limitation by explicitly accounting for the entropy generated outside the reactive domain, i.e., in the heat carrier stream.

Most of literature studies focused on gas-phase reactions occurring in plug flow reactors. These reactions generally operate at high temperatures, often exceeding 200 °C, which intensifies the role of thermal and chemical phenomena. Overall, the studies consistently identified heat transfer and chemical reaction as the dominant sources of entropy generation, with the latter usually being the most significant. Finally, nearly all studies reported the observance of the EoEP principle as an outcome of the optimisation process, reinforcing its relevance as a guiding principle for thermodynamic optimisation in reactive systems.

1.6 Conclusion

This literature review shows the important role of EGM in improving the design and performance of heat-exchanger reactors. Many studies, from methanol synthesis to biomass gasification, have shown that reducing entropy generation is a complex task. It requires careful adjustment of operating conditions and reactor design to optimise both thermal and chemical processes. One key idea from these studies is the benefit of keeping the entropy generation evenly distributed inside the reactor. This is reflected in the principle of equipartition of entropy generation.

This thesis focuses on the optimisation of the geometry of a plug flow heat-exchanger-reactor, using two case studies: the hydrolysis of acetic anhydride and the catalytic oxidation of sulphur dioxide. The approach combines numerical simulations based on two complementary modelling frameworks: a one-dimensional systemic model implemented in MATLAB, and a two-dimensional axisymmetric model developed using ANSYS Fluent. These tools are employed to investigate the reactor's performance in terms of fluid flow, heat and mass transfer, and chemical kinetics, starting from a baseline geometry and progressing toward more optimised, complex configurations. Special attention is given to the modelling of entropy generation, which serves as the optimisation criterion throughout the study. By comparing results obtained from both the 1D and 2D models, this work aims to identify the sources of discrepancy between modelling approaches and to better interpret the optimisation outcomes. The analysis is carried out for both homogeneous and heterogeneous systems, with a final multi-objective optimisation phase that highlights the trade-offs between entropy generation and the reactor compacity.

List of Tables

Table 1.1: Entropy sources driving forces for both modelling approaches. 38
Table 1.2: Summary of EGM optimisations on systems involving chemical reactions. . 48

Bibliography

Arjmandi, H. R., & Amani, E. (2015). A numerical investigation of the entropy generation in and thermodynamic optimization of a combustion chamber. Energy, 81, 706-718.

Austbø, B., & Gundersen, T. (2015). Optimal distribution of temperature driving forces in low-temperature heat transfer. AIChE Journal, 61(8), 2447-2455.

Awad, Mohamed M. « A Review of Entropy Generation in Microchannels ». Advances in Mechanical Engineering, vol. 7, no 12, décembre 2015, p. 1687814015590297. DOI.org (Crossref), https://doi.org/10.1177/1687814015590297.

Balkan, F. (2005). Application of EoEP principle with variable heat transfer coefficient in minimizing entropy production in heat exchangers. Energy conversion and management, 46(13-14), 2134-2144.

Bejan, Adrian. Entropy generation minimization: the method of thermodynamic optimization of finite-size systems and finite-time processes. CRC Press, 1996.

Bejan, Adrian. Entropy generation through heat and fluid flow. Wiley, 1982.

Carrington, C. G., & Sun, Z. F. (1991). Second law analysis of combined heat and mass transfer phenomena. International Journal of Heat and Mass Transfer, 34(11), 2767-2773.

Carnot Sadi, Réflexions sur la puissance motrice du feu et sur les machines propres à développer cette puissance, Paris, Bachelier, coll. « (Landmarks of science) », 1824

Chen, L., Wu, C., & Sun, F. (1999). Finite time thermodynamic optimization or entropy generation minimization of energy systems.

Chen, L., Zhang, L., Xia, S., & Sun, F. (2018). Entropy generation minimization for CO2 hydrogenation to light olefins. Energy, 147, 187-196.

Chowdhury, K., et S. Sarangi. « A Second Law Analysis of the Concentric Tube Heat Exchanger: Optimisation of Wall Conductivity ». International Journal of Heat and Mass Transfer, vol. 26, no 5, mai 1983, p. 783 86. DOI.org (Crossref), https://doi.org/10.1016/0017-9310(83)90029-7.

Culham, J. R., et Y. S. Muzychka. « Optimization of plate fin heat sinks using entropy generation minimization ». IEEE Transactions on Components and Packaging Technologies, vol. 24, no 2, juin 2001, p. 159 65. DOI.org (Crossref), https://doi.org/10.1109/6144.926378.

De Groot, S. R. de, et P. Mazur. Non-equilibrium thermodynamics. Dover ed, Dover Publications, 1984.

Domański, Roman, et Giuma Fellah. « Exergy Analysis for the Evaluation of a Thermal Storage System Employing PCMS with Different Melting Temperatures ». Applied Thermal Engineering, vol. 16, no 11, novembre 1996, p. 907 19. DOI.org (Crossref), https://doi.org/10.1016/1359-4311(96)00003-8.

Eger, T., Bol, T., Thanu, A. R., Daróczy, L., Janiga, G., Schroth, R., & Thévenin, D. (2017). Application of entropy generation to improve heat transfer of heat sinks in electric machines. Entropy, 19(6), 255.

Erek, A., & Dincer, I. (2008). An approach to entropy analysis of a latent heat storage module. International Journal of Thermal Sciences, 47(8), 1077-1085.

Foussard, J.-N., Julien, E., Mathé, S., & Debellefontaine, H. (2015). Thermodynamique: Applications aux systèmes physicochimiques. Dunod.

Guelpa, E., Sciacovelli, A., & Verda, V. (2013). Entropy generation analysis for the design improvement of a latent heat storage system. Energy, 53, 128-138.

Guo, J., Cheng, L., & Xu, M. (2009). Optimization design of shell-and-tube heat exchanger by entropy generation minimization and genetic algorithm. Applied Thermal Engineering, 29(14-15), 2954-2960.

Hesselgreaves, J. E. (2000). Rationalisation of second law analysis of heat exchangers. International Journal of Heat and Mass Transfer, 43(22), 4189-4204.

Iyengar, M., et A. Bar-Cohen. « Least-Energy Optimization of Forced Convection Plate-Fin Heat Sinks ». IEEE Transactions on Components and Packaging Technologies, vol. 26, no 1, mars 2003, p. 62 70. DOI.org (Crossref), https://doi.org/10.1109/TCAPT.2003.811484.

Jegadheeswaran, S., Pohekar, S. D., & Kousksou, T. (2010). Exergy based performance evaluation of latent heat thermal storage system: a review. Renewable and Sustainable Energy Reviews, 14(9), 2580-2595.

Jejurkar, S. Y., & Mishra, D. P. (2011). Effects of wall thermal conductivity on entropy generation and exergy losses in a H2-air premixed flame microcombustor. International Journal of Hydrogen Energy, 36(24), 15851-15859.

Jin, Yan. « Second-Law Analysis: A Powerful Tool for Analyzing Computational Fluid Dynamics (CFD) Results ». Entropy, vol. 19, no 12, décembre 2017, p. 679. DOI.org (Crossref), https://doi.org/10.3390/e19120679.

Johannessen, E., & Kjelstrup S. « Minimum Entropy Production Rate in Plug Flow Reactors: An Optimal Control Problem Solved for SO_2 Oxidation ». Energy, vol. 29, no 12 15, décembre 2004, p. 2403 23. DOI.org (Crossref), https://doi.org/10.1016/j.energy.2004.03.033.

Johannessen, E., & Røsjorde, A. (2007). Equipartition of entropy production as an approximation to the state of minimum entropy production in diabatic distillation. Energy, 32(4), 467-473.

Kizilova, N., Shankar, A., & Kjelstrup, S. (2024). A Minimum Entropy Production Approach to Optimization of Tubular Chemical Reactors with Nature-Inspired Design. Energies, 17(2), 432.

Kjelstrup, S., Johannessen, E., Rosjorde, A., Nummedal, L., & Bedeaux, D. (2000). Minimizing the entropy production of the methanol producing reaction in a methanol reactor. International Journal of Thermodynamics, 3(4), 147-153.

Li, P., Chen, L., Xia, S., & Zhang, L. (2019). Entropy generation rate minimization for methanol synthesis via a CO2 hydrogenation reactor. Entropy, 21(2), 174.

Magnanelli, E., Johannessen, E., & Kjelstrup, S. (2017). Entropy production minimization as design principle for membrane systems: Comparing equipartition results to numerical optima. Industrial & Engineering Chemistry Research, 56(16), 4856-4866.

Magnanelli, E., Solberg, S. B. B., & Kjelstrup, S. (2019). Nature-inspired geometrical design of a chemical reactor. Chemical Engineering Research and Design, 152, 20-29.

Mistry, K. H., McGovern, R. K., Thiel, G. P., Summers, E. K., Zubair, S. M., & Lienhard V, J. H. (2011). Entropy generation analysis of desalination technologies. Entropy, 13(10), 1829-1864.

Moran, M. J., Shapiro, H. N., Boettner, D. D., & Bailey, M. B. (2010). Fundamentals of engineering thermodynamics. John Wiley & Sons.

Narayan, G. P., & Zubair, S. M. (2010). Entropy generation minimization of combined heat and mass transfer devices. International Journal of Thermal Sciences, 49(10), 2057-2066.

Nummedal, L., Kjelstrup, S., & Costea, M. (2003). Minimizing the entropy production rate of an exothermic reactor with a constant heat-transfer coefficient: the ammonia reaction. Industrial & engineering chemistry research, 42(5), 1044-1056.

Nummedal, L., Røsjorde, A., Johannessen, E., & Kjelstrup, S. (2005). Second law optimization of a tubular steam reformer. Chemical Engineering and Processing: Process Intensification, 44(4), 429-440.

Ordonez, J. C., Cavalcanti, E. J., & Carvalho, M. (2022). Energy, exergy, entropy generation minimization, and exergoenvironmental analyses of energy systems-a mini-review. Frontiers in Sustainability, 3, 902071.

Ratkje, S. K., Sauar, E., Hansen, E. M., Lien, K. M., & Hafskjold, B. (1995). Analysis of entropy production rates for design of distillation columns. Industrial & engineering chemistry research, 34(9), 3001-3007.

Sarangi, S., et K. Chowdhury. « On the Generation of Entropy in a Counterflow Heat Exchanger ». Cryogenics, vol. 22, no 2, février 1982, p. 63 65. DOI.org (Crossref), https://doi.org/10.1016/0011-2275(82)90095-9.

Sauar, E., Kjelstrup, S., & Lien, K. M. (1997). Equipartition of forces—Extension to chemical reactors. Computers & chemical engineering, 21, S29-S34.

Sciacovelli, A., & al. « Entropy Generation Analysis as a Design Tool—A Review ». Renewable and Sustainable Energy Reviews, vol. 43, 2015, p. 1167 81. DOI.org (Crossref), https://doi.org/10.1016/j.rser.2014.11.104

Sciacovelli, A., & Verda, V. (2009). Entropy generation analysis in a monolithic-type solid oxide fuel cell (SOFC). Energy, 34(7), 850-865.

Sciacovelli, A., & Verda, V. (2010). Entropy generation minimization in a tubular solid oxide fuel cell.

Sciacovelli, A., Guelpa, E., & Verda, V. (2014). Second law optimization of a PCM based latent heat thermal energy storage system with tree shaped fins. International Journal of Thermodynamics, 17(3), 145-154.

Sciubba, Enrico. « A Minimum Entropy Generation Procedure for the Discrete Pseudo-Optimization of Finned-Tube Heat Exchangers ». Revue Générale de Thermique, vol. 35, no 416, septembre 1996, p. 517 25. DOI.org (Crossref), https://doi.org/10.1016/S0035-3159(99)80079-8.

Smrekar, J., Oman, J., & Širok, B. (2006). Improving the efficiency of natural draft cooling towers. Energy conversion and management, 47(9-10), 1086-1100.

Sun, M., Xia, S., Chen, L., Wang, C., & Tang, C. (2020). Minimum entropy generation rate and maximum yield optimization of sulfuric acid decomposition process using NSGA-II. Entropy, 22(10), 1065.

Teng, H., Kinoshita, C. M., Masutani, S. M., & Zhou, J. (1998). Entropy generation in multicomponent reacting flows.

Tondeur, Daniel, et Eric Kvaalen. « Equipartition of Entropy Production. An Optimality Criterion for Transfer and Separation Processes ». Industrial & Engineering Chemistry Research, vol. 26, no 1, janvier 1987, p. 50 56. DOI.org (Crossref), https://doi.org/10.1021/ie

Torabi, M., Torabi, M., & Peterson, G. P. (2017). Entropy generation of double diffusive forced convection in porous channels with thick walls and soret effect. Entropy, 19(4), 171. https://doi.org/10.3390/e19040171

Tsatsaronis, George. « Thermoeconomic Analysis and Optimization of Energy Systems ». Progress in Energy and Combustion Science, vol. 19, no 3, janvier 1993, p. 227 57. DOI.org (Crossref), https://doi.org/10.1016/0360-1285(93)90016-8.

Wang, S., Zhang, L., Zhang, Q., & Ye, X. (2011). Numerical investigation of entropy generation and optimization on a centrifugal fan. Advanced Science Letters, 4(6-7), 2240-2245.

Zhang, L., Yang, C., & Zhou, J. (2010). A distributed parameter model and its application in optimizing the plate-fin heat exchanger based on the minimum entropy generation. International Journal of Thermal Sciences, 49(8), 1427-1436.

Zhang, L., Xia, S., Chen, L., Ge, Y., Wang, C., & Feng, H. (2019). Entropy generation rate minimization for hydrocarbon synthesis reactor from carbon dioxide and hydrogen. International Journal of Heat and Mass Transfer, 137, 1112-1123.

Chapter 2

Modelling of a heat-exchanger reactor for a homogenous reaction: acetic anhydride hydrolysis case study

Table of Contents

Chapter 2 57

Abstract 62

2.1 Introduction 63

2.2 Acetic anhydride hydrolysis 64

2.3 Heat-exchanger reactor configuration 66

2.3.1 HER geometries: uniform and piecewise profiled configurations 66

2.3.2 Operating and geometric parameters 68

2.4 Systemic modelling 71

2.4.1 Mass and momentum balances 71

2.4.2 Heat balances 73

2.4.3 Species mass balances 75

2.4.4 Systemic modelling limitations 76

2.5 CFD model 79

2.5.1 Coupled hydrodynamics equations 79

2.5.2 One-dimensional reduced modelling 83

2.6 Multi-objective optimisation problem formulation 85

2.6.1 Objective functions 85

2.6.2 Multi-objective optimisation problem 89

2.6.3 Numerical procedure 91

2.7 Conclusion 92

Appendix A. Local friction coefficient calculation 96

Appendix B. Local heat transfer coefficient calculation 97

Appendix C. Nusselt number in a thermally developed laminar flow with uniform volumetric heat generation 99

Appendix D. Calculation of the chemical entropy generation rate 101

Appendix E. Pilot sizing 103

E.1 Pilot P&ID 105

E.2 Sizing methodology 109

Nomenclature

a	Activity (-)
A_h	Heat transfer surface area (m^2)
C	Concentration (mol m^{-3})
CoV_r	Coefficient of variation reduction (-)
$\bar{c}_p$	Specific heat capacity (J kg^{-1} K^{-1})
$c^o_{p,j}$	Standard state constant pressure molar heat capacity of species j at constant pressure (J mol^{-1} K^{-1})
C_{fz}	Local apparent friction coefficient (-)
Da	Damköhler number (-)
$\mathfrak{D}$	Molecular diffusivity (m^2 s^{-1})
D_H	Hydraulic diameter (m)
d_i	Inner diameter of the inner tube (m)
d_o	Inner diameter of the outer tube (m)
e	Thickness or width (m)
$\vec{F}$	Vector of objective functions (-)
F	Molar flow rate (mol s^{-1})
Gz	Graetz number (-)
H	Overall heat transfer coefficient (W m^{-2} K^{-1})
h	Local heat transfer coefficient (W m^{-2} K^{-1})
$\bar{h}$	Specific enthalpy (J kg^{-1})
k	Hydrolysis kinetic constant (m^3 mol^{-1} s^{-1})
K_i	Static mixer coefficient (-)
L	HER total length (m)
M	Molecular weight (kg mol^{-1})
$\dot{m}$	Mass flow rate (kg s^{-1})
m	Number of HER sections (-)
$\vec{n}$	Local unit normal vector (-)
Nu	Nusselt number (-)
p	Pressure (Pa)
Pr	Prandtl number (-)
q'''	Uniform volumetric heat source (W m^{-3})
R_{gas}	Universal Gas Constant (J mol^{-1} K^{-1})
R_i	Inner pipe radius (m)
Re	Reynolds number (-)
r	Radial position (m)
r_{vol}	Global rate of reaction (mol m^{-3} s^{-1})
$\bar{r}_{vol,j}$	Volumetric formation rate of species j (kg m^{-3} s^{-1})
$r_{vol,j}$	Formation rate of species j (mol m^{-3} s^{-1})

r^*	Shape factor of the annulus space (-)
$\dot{S}$	Entropy generation rate (W K^{-1})
$\dot{s}'$	Rate of entropy generation per unit length (W K^{-1} m^{-1})
$\dot{s}'''$	Volumetric entropy generation rate (W K^{-1} m^{-3})
$\bar{s}_j$	Specific entropy of component j (J kg^{-1} K^{-1})
s°	Standard state entropy (J mol^{-1} K^{-1})
T	Absolute temperature (K)
$\vec{u}$	Velocity vector (m s^{-1})
u	Velocity of the fluid (m s^{-1})
u_z	Local axial velocity (m s^{-1})
u'''	Volumetric heat generation (W m^{-3})
$\dot{V}$	Volumetric flow rate (m^3 s^{-1})
V_{HER}	Total volume of the heat exchanger reactor (m^3)
$\vec{v}$	Vector of decision variables (-)
$\vec{X}$	Vector of process variables (-)
x	Molar fraction (-)
Y	Mass fraction (-)
z	Axial position along the system (m)
z^+	Dimensionless axial distance (-)

Greek letters

α	Local slope of the diameter profile (-)
α_m	Slope of the mth HER section (-)
$\Delta_R G$	Gibbs free energy of reaction (J mol^{-1})
$\Delta_R G^\circ$	Standard Gibbs free energy of reaction (J mol^{-1})
$\Delta_f h^\circ$	Standard enthalpy of formation (J mol^{-1})
$\Delta_R h$	Heat of reaction (J mol^{-1})
$\Delta_R h^\circ$	Standard enthalpy of reaction (J mol^{-1})
$\Delta_R s^\circ$	Standard entropy of reaction (J mol^{-1} K^{-1})
ε_{AR}	Nominal aspect ratio (-)
η	Dynamic viscosity (Pa s)
λ	Thermal conductivity (W m^{-1} K^{-1})
μ	Chemical potential (J mol^{-1})
ν	Stoichiometric coefficient (-)
ξ	Conversion (-)
ρ	Density (kg m^{-3})
$\bar{\bar{\tau}}$	Viscous shear stress tensor (Pa)
ϕ	Heat flux (W m^{-2})
ψ	Sensible heat flux per unit length (W m^{-1})
Ω	Flow section area (m^2)

Subscripts

an	Refers to the fluid circulating in the annulus
ch	Refers to the chemical reaction
f	Refers to the fluid phase
h	Refers to the heat transfer
i	Refers to the fluid circulating in the inner pipe
inl	Refers to the inlet of the HER
j	Refers to the species j
liq	Refers to liquid phase
M	Refers to the mixing-cup
min	Refers to the minimum
tot	Refers to the total
w	Refers to the wall
η	Refers to the viscous dissipation
μ	Refers to the mass transfer

Abbreviations

CFD	Computational Fluid Dynamics
DOE	Design of Experiments
HER	Heat Exchanger Reactor
MOGA	Multi-Objective Genetic Algorithm
P&ID	Piping and Instrumentation Diagram
PLIF	Planar Laser-Induced Fluorescence
UHF	Uniform Heat Flux
UWT	Uniform Wall Temperature

Abstract

This chapter develops and applies a modelling framework for the simulation and optimisation of Heat-Exchanger Reactors (HERs), using the hydrolysis of acetic anhydride into acetic acid as a representative liquid-phase homogeneous reaction. Two reactor configurations were considered: a conventional tubular double-pipe HER and a piecewise diameter-varying configuration, which are later analysed and optimised.

Two complementary modelling strategies were established. First, a one-dimensional systemic model was derived from mass, momentum, energy, and species balances. This approach provides a simplified yet computationally efficient description of the reactor, enabling rapid parametric studies. However, its accuracy is limited by simplifying assumptions such as the plug-flow hypothesis and the lack of direct consideration of radial gradients. To address these limitations, a Computational Fluid Dynamics (CFD) model was developed by solving the coupled hydrodynamic, energy and mass transfer equations. This model yields detailed velocity, temperature, and concentration fields, providing local insights into entropy generation mechanisms. From CFD results, a reduced-order one-dimensional formulation was also constructed, bridging the gap between the systemic and CFD models that will be discussed in Chapter 3.

On this modelling basis, a multi-objective optimisation problem was formulated. Entropy generation minimisation and reactor volume reduction were chosen as objective functions, while the geometric parameters of the HER (inlet diameter, total length, and segment slopes) were selected as design variables. A genetic algorithm was implemented to explore the trade-offs between objectives and construct Pareto fronts, thus guiding the design of more compact and thermodynamically efficient HERs.

Finally, the chapter also presents the design of a pilot-scale unit aimed at validating the CFD results. Although time constraints prevented the realisation of experimental campaigns, the complete sizing methodology is provided as a reference for future work in Appendix E. The methodological framework developed here—integrating systemic modelling, CFD modelling, and multi-objective optimisation—serves as the foundation for the next chapter, where the predictive capabilities of the different modelling strategies will be compared and exploited for reactor optimisation.

2.1 Introduction

This chapter presents the modelling framework used to simulate and analyse the behaviour of a Heat-Exchanger Reactor (HER) for the hydrolysis of acetic anhydride into acetic acid. Two models are developed: a one-dimensional (1D) model and a Computational Fluid Dynamics (CFD) model. Each model has its own advantages and limitations when applied to optimisation. The 1D model provides a simplified description of the system with very short computation times, while the CFD model offers greater accuracy but requires much longer simulations. To assess whether the 1D model alone can deliver sufficiently reliable results for optimisation, both models are studied and compared. Their detailed descriptions are presented in the following sections.

Section 2.2 introduces the chemical reaction and provides the associated kinetic parameters. Section 2.3 describes the design and operational principles of the HER, detailing the reactor configuration and reference operating conditions used throughout the study.

Section 2.4 outlines a 1D systemic modelling approach, including the governing equations for mechanical energy conservation, enthalpy balance, and species mass balance. The limitations of this approach are also discussed, notably the reliance on mixing-cup averages and the inaccurate estimation of the heat transfer coefficients.

Section 2.5 presents a CFD modelling strategy for the HER, encompassing both full 2D/3D simulations and a reduced 1D formulation used for comparison and simplified analyses.

Finally, Section 2.6 defines the multi-objective optimisation problem addressed in this work. It introduces the selected objective functions and describes the numerical methods used—genetic algorithm—to identify optimal trade-offs between reactor volume and entropy generation.

2.2 Acetic anhydride hydrolysis

As mentioned in Chapter 1, the acetic anhydride hydrolysis is a homogeneous liquid phase reaction involving water, acetic anhydride and acetic acid. This reaction was chosen for its rather simple application in experimental set up and the fact that it is a well-known reaction due to its use in calorimeter calibration. In industrial applications, however, this reaction is generally regarded as undesirable, since acetic anhydride hydrolyses into acetic acid in the presence of ambient moisture or under inadequate storage conditions. Furthermore, as acetic anhydride is widely used as a reactant in various processes, such as the synthesis of aspirin (Olmsted, 2009) and the production of cellulose acetate for textile applications (Biswas et al., 2006), unintended hydrolysis is detrimental and therefore must be strictly avoided.

This reaction is exothermic, with a standard enthalpy of reaction at 298.15 K of approximately –57 kJ · mol^{-1}. At this temperature, the adiabatic temperature rise, i.e., the temperature increase that would occur if all the heat released by the reaction remained in the liquid phase (no heat exchange with the environment) is estimated to be approximately 12K. This reaction occurs via three main irreversible steps: addition, elimination, and proton transfer. As such, it is considered irreversible in this study.

$$H_2O + (CH_3CO)_2O \rightarrow 2\,CH_3COOH$$

The reaction kinetics were taken from the article of Asprey et al. (1996), who provide a second-order kinetic expression for the rate of hydrolysis:

$$r_{vol} = kC_{H_2O}C_{(CH_3CO)_2O} \qquad 2.2.1$$

where k [m^3 mol^{-1} s^{-1}], the second order kinetic constant, varies with the temperature following an Arrhenius type equation:

$$k = 2.12\,exp\left(\frac{-4.56\,10^4}{R_{gas}T}\right) \qquad 2.2.2$$

where r_{vol} [mol m^{-3} s^{-1}] is the global hydrolysis reaction rate, C_j [mol m^{-3}] the molar concentration of species j, R_{gas} [J mol^{-1} K^{-1}] is the universal gas constant and T [K] the reactive mixture temperature. The kinetics parameters were determined experimentally using temperature scanning method, where the temperature of the feed is gradually increased to measure several isothermal rates (using conductivity to follow the kinetic of the reaction) and subsequently, determine the constants of the Arrhenius equation. The temperature scanning experiments used to established the reaction kinetics were conducted under isothermal conditions (a controlled-temperature water bath was used) in three reactors: a plug flow reactor, a continuous stirred tank reactor and a batch reactor. The operating conditions of each reactor are summarized in Table 2.1.

Table 2.1: Operating setup for each reactor configuration (Asprey et al., 1996).

	Plug flow reactor	**Continuous stirred tank reactor**	**Batch reactor**
Temperature range (K)	302-334	298-334	284-327
Apparatus	¼-in. OD polyvinyl tube	1.44 L glass vessel	1.44 L glass vessel
Inlet mass fraction of acetic anhydride	0.1	0.1	0.1
Residence time (s)	not reported	800	

The reaction was carried out under atmospheric pressure. As a first step, the reaction was assumed to follow pseudo-first-order kinetics, with the water (the only other reactant added at the inlet along with the acetic anhydride) concentration maintained constant for regression purposes, thus obtaining a pseudo first-order rate constant. Subsequently, using the initial water concentration, regression of the second-order kinetics parameters was performed. The values obtained and their average are shown in Table 2.2.

Table 2.2: Arrhenius kinetics parameters obtained for each experimental configuration (Asprey et al., 1996).

	Activation energy (J mol^{-1})	**Pre-exponential factor (m^3 mol^{-1} s^{-1})**
Plug flow reactor	4.58×10^4	2.78
Continuous stirred tank reactor	4.56×10^4	1.88
Batch reactor	4.52×10^4	1.83
Average	4.56×10^4	2.12

These average values were used in the present work, as the experimental conditions (temperature range) match those used in the article from Asprey et al. (1996). Although more complex kinetic models exist—such as that of Garcia-Hernandez et al. (2019), which accounts for the autocatalytic effect of acetic acid—the simpler model from Asprey et al. (1996) was preferred for ease of implementation in early CFD simulations.

2.3 Heat-exchanger reactor configuration

2.3.1 HER geometries: uniform and piecewise profiled configurations

As previously stated, this thesis aims to optimise the geometry of a HER using acetic anhydride hydrolysis as a model reaction. The process is carried out in a double-pipe reactor, where the reacting liquid flows through the inner pipe while an inert heat carrier circulates in the annular space. Two reactor configurations are investigated in this work. The first configuration consists of a conventional tubular reactor with a constant inner diameter, as illustrated in Figure 2.1.

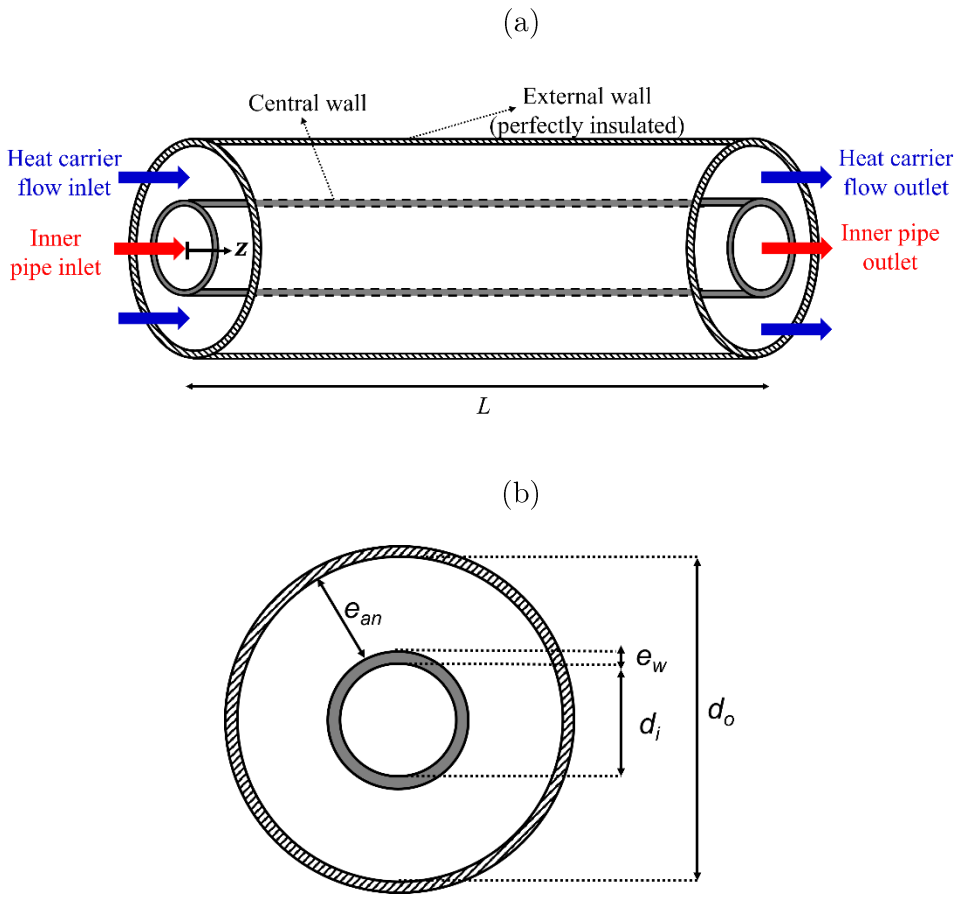

Figure 2.1: Schematic representation of the double pipe HER: (a) Side view, (b) Front view.

The second configuration is a piecewise profiled reactor, in which the inner tube is divided into ten equal-length sections. Each section is defined by a linear slope α, thereby allowing the inner diameter to vary progressively along the reactor length. The wall thickness and annular gap are maintained constant across all sections. A schematic illustration of this piecewise variable-diameter concept is provided in Figure 2.2.

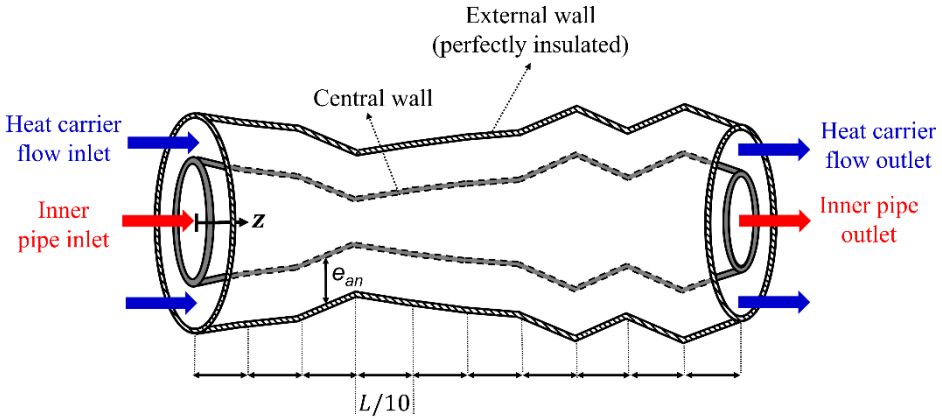

Figure 2.2: Schematic representation of the double pipe HER piecewise profiled configuration.

A schematic representation of the slope α is presented in Figure 2.3. It is equal to the ratio of Δr over Δz and to the tangent of the angle θ.

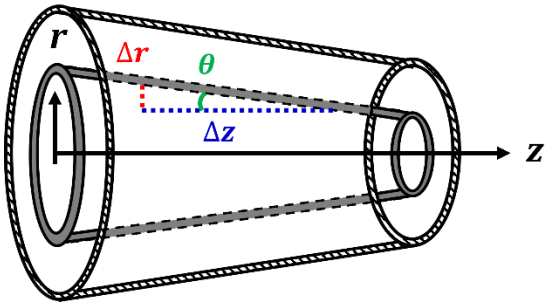

Figure 2.3: Schematic representation of the slope a of an HER segment.

Both configurations are subjected to a multi-objective optimisation process, as described in Section 2.6. In the case of the uniform tubular reactor, the optimisation is performed with respect to the inner diameter and the total length. For the piecewise profiled reactor, the optimisation is extended to include not only the total length and the inlet inner diameter, but also the ten consecutive slopes defining the variable-diameter profile. This approach enables a comprehensive assessment of how reactor geometry influences both heat management and reaction performance. The operating and geometrical parameters of this study are presented below.

2.3.2 Operating and geometric parameters

For both setups, the wall thickness, e_w, and annulus thickness, e_{an}, are kept constant and are set to 1 mm and 1 cm, respectively. The HER is assumed to be perfectly insulated and is therefore considered adiabatic. The reactor is made of aluminium, with a thermal conductivity of λ_w= 220 W m^{-1} K^{-1}.

The HER operates in co-current mode, with both fluid streams entering from the left side ($z = 0$, Figure 2.1a) of the system with uniform velocity profiles.

To investigate the effects of different operating and geometric parameters on the HER performance, a reference case was defined and summarized in Table 2.3.

Table 2.3: Reference case operating conditions.

Parameter	Symbol	Reference Case
Fluid circulating in the inner pipe	/	Reactive mixture
Fluid circulating in the annulus	/	Water
Inlet mole fraction of anhydride acetic in the inner pipe fluid	$x_{anh,inl}$	0.023
Inlet temperature of the inner pipe fluid (K)	$T_{M,i,inl}$	298.15
Inlet temperature of the heat carrier fluid (K)	$T_{M,an,inl}$	358.15
Inlet mass flow rate of the inner pipe fluid (kg s^{-1})	$\dot{m}_{i,inl}$	5.53 10^{-3}
Inlet mass flow rate of the heat carrier fluid (kg s^{-1})	$\dot{m}_{an,inl}$	4.83 10^{-2}

The reactive mixture is injected into the inner pipe at a uniform temperature $T_{M,i,inl}$ = 298.15 K and at uniform velocity $u_{M,i,inl}$ [m s^{-1}] (subscript "i" refers to the fluid circulating in the inner pipe). In this situation, the Reynolds number of the inner pipe flow equals 1600 for a diameter d_i of 5 mm, which corresponds to a laminar flow regime since it is significantly lower than 2 300. Liquid water, used as the heat carrier fluid, is injected into the annular space at a uniform temperature $T_{M,an,inl}$ = 358.15 K and at uniform velocity $u_{M,an,inl}$ [m s^{-1}] (subscripts "an" and "inl" respectively refer to the fluid circulating in the annular space and to the variables at the inlet of the HER, i.e., at $z = 0$). Water is treated as an incompressible fluid with constant properties that are reported in Table 2.4. The hydraulic diameter of the annulus, $D_{H,an}$, equals $d_o - (d_i + 2e_w)$ = 2 cm where d_o is the inner diameter of the outer pipe. The flow Reynolds number in the annular section is about 2 030 for an inner diameter d_i of 5 mm, which corresponds to a laminar flow regime as it is lower than 2 900, the approximate value above which transitional regime occurs in such annulus (Foster, 1965). Therefore, in all optimised configurations (with a minimum inner pipe diameter set to 5 mm), the flow of both fluids remains in the laminar regime.

The mixture initially consists of 97.7 mol% of water and 2.3 mol% of acetic anhydride, and the species concentration profiles are considered uniform at the inlet section. As previously mentioned, a homogeneous exothermic reaction occurs in this reactive mixture, the hydrolysis of acetic anhydride. The heat capacities were taken temperature dependent and calculated using correlations reported in Yaws (1999). The thermophysical properties of the involved species are reported in Table 2.4.

Table 2.4: Thermophysical properties of the species (Yaws,1999; Linstrom and Mallard, 2001).

Parameter	Symbol	Water	Acetic anhydride	Acetic acid
Density (kg m^{-3}) (*Yaws, 1999*)	ρ	997	1 077	1 043
Thermal conductivity (W m^{-1} K^{-1}) (*Yaws, 1999*)	λ	0.6	0.164	0.158
Viscosity (Pa s) (*Yaws, 1999*)	η	8.90 10^{-4}	8.06 10^{-4}	1.132 10^{-3}
Molecular weight (g mol^{-1}) *(Linstrom and Mallard, 2001)*	M	18	102	60
Standard State Entropy (298.15K) (J mol^{-1} K^{-1}) (*Linstrom and Mallard, 2001*)	$s^{\circ}_{j,liq}$	6.99 10^{1}	2.62 10^{2}	2.36 10^{2}
Standard State Enthalpy (298.15K) (J mol^{-1}) (*Linstrom and Mallard, 2001*)	$\Delta_f h^{\circ}_{j,liq}$	-2.86 10^{5}	-6.25 10^{5}	-4.84 10^{5}

The local thermal conductivity of the mixture, its dynamic viscosity and specific heat capacity are determined using mass fraction averaging of the properties of the pure species properties (Table 2.4). The mass diffusivities of water, acetic anhydride and acetic acid in the solution are assumed to be constant and equivalent, equal to 10^{-9} m^2 s^{-1} (classical order of magnitude for diffusivities in aqueous solutions at room temperature, verified using the Wilke-Chang (1955) correlation). The density of the reactive mixture is supposed to be independent of pressure (incompressibility assumption) and temperature, but varies with the local composition as follows:

$$\rho_i = \left(\sum \frac{Y_j}{\rho_j} \right)^{-1} \qquad 2.3.1$$

where ρ_i [kg m^{-3}] is the mixture (inner pipe flow) density, Y_j the mass fraction of species j and ρ_j [kg m^{-3}] its density at pure state (see Table 2.4).

Given the chemical reaction, the composition of the reactive mixture, and therefore its density, vary along the axial position. However, the product of the density by the average axial velocity remains constant since it corresponds to the conservation of the mass flux density of the mixture. Consequently, the Reynolds number of the inner pipe flow remains constant and for the operating conditions investigated here, which corresponds to laminar flow.

2.4 Systemic modelling

The hydrolysis was chosen to be carried in a continuous plug flow HER operating in steady state. The systemic process model used to simulate transport phenomena in the anhydride acetic case consists of a one-dimensional ideal plug flow (without axial dispersion) model for of each fluid stream, i.e., all flow variables are assumed to vary in the axial direction only and are considered uniform across the flow section of each fluid. The full set of system equations used for the one-dimensional modelling is presented below.

2.4.1 Mass and momentum balances

a. Reactive fluid

Pressure variations along the HER can be determined using mechanical energy balances. Since the flow section area of each stream is uniform, axial pressure variations are only due to pressure drop, i.e., to viscous dissipation and Venturi effect (the kinetic contribution was considered negligible). Therefore, the mechanical energy conservation equation for the inner pipe fluid is expressed as follows:

$$\frac{dp_{M,i}}{dz} = -\frac{1}{\cos(\alpha/2)}\frac{C_{fz,i}\,\rho_i}{2\,d_i}u_{M,i}^2 \qquad 2.4.1$$

$$p_{M,i}(z=0) = p_{M,i,inl} \qquad 2.4.2$$

where z [m] is the axial position, C_{fz} the local apparent friction coefficient (following the Darcy-Weisbach definition), $p_{M,i}$ [Pa] the mean pressure of the inner fluid at the flow section, $p_{M,i,inl}$ [Pa] the inlet mean pressure of the inner fluid at the flow section set to 1 bar, ρ [kg m^{-3}] the fluid density, u_M [m s^{-1}] the average axial velocity and d_i [m] the inner pipe diameter.

In profiled shapes, in the centre of the inner pipe, the average fluid flow aligns with the z-axis. However, near the central wall, the flow tends to follow the wall, resulting in a flow at an angle α with respect to the z-axis. Consequently, an angle of $\alpha/2$ is expected to provide a better estimation of the average mixture flow direction within a profiled reactor compared to an angle of α.

Concerning the inner pipe fluid, the reactive mixture density depends on the local composition (Equation 2.3.1) so its mean velocity varies along the axial direction as follows (mass conservation equation):

$$u_{M,i} = \frac{\rho_{i,inl}\,u_{M,i,inl}}{\rho_i \cos\left(\frac{\alpha}{2}\right)} \qquad 2.4.3$$

where subscript "i" refers to the fluid circulating in the inner pipe.

b. Heat carrier fluid

The mechanical energy conservation equation for the heat carrier is:

$$\frac{dp_{M,an}}{dz} = -\frac{1}{\cos(\alpha)}\frac{C_{fz,an}\,\rho_{an}}{2\,D_{H,an}}u_{M,an}^2 = -\frac{1}{\cos(\alpha)}\frac{C_{fz,an}\,\rho_{an}}{2\,(d_o-(d_i+2e_w))}u_{M,an}^2 \quad 2.4.4$$

$$p_{M,an}(z=0) = p_{M,an,inl} \quad 2.4.5$$

where D_H [m] is the hydraulic diameter, α the slope of the HER profile (α is zero in the case of the tubular configuration), $p_{M,an}$ [Pa] the heat carrier fluid pressure, $p_{M,an,inl}$ [Pa] the heat carrier pressure at the inlet, u_M [m s^{-1}] the average axial velocity and d_o [m] the outer pipe diameter. The two local friction coefficients are calculated using the correlation of Muzychka and Yavanovich (2009), detailed in Appendix A, which is valid for both developing and fully developed axial laminar flows in straight pipes of different cross-section geometries.

In the case of the tubular HER configuration, the average velocity of the heat carrier fluid, treated as incompressible, remains constant along the axial direction. In the 'profiled configuration', the modification of the flow cross-sectional area along the HER leads to additional variations in the velocities. Thus, at each axial position, the local average velocity of the heat carrier flow is calculated as follows:

$$u_{M,an} = \frac{\dot{V}_{an}}{\frac{\pi}{4}\left[(d_i+2e_w+2e_{an})^2-(d_i+2e_w)^2\right]\cos\alpha} \quad 2.4.6$$

where $\dot{V}_{an}$ [m^3 s^{-1}] is the annular fluid volumetric flow rate. The cosine term in Equation 2.4.6 accounts for the fact that the flow cross-section is inclined at an angle α relative to the z-axis.

2.4.2 Heat balances

a. Reactive fluid

The heat equation must take into consideration the heat of reaction and account for the variations of the fluid properties depending on the local mixture composition. Thus, the heat equation of the inner pipe fluid is:

$$\rho_i \dot{V}_i \frac{d\left(\bar{c}_{p,i} T_{M,i}\right)}{dz} = H\left(T_{M,an} - T_{M,i}\right)\frac{dA_h}{dz} - \frac{dp_{M,i}}{dz}\dot{V}_i + \Omega_i r_{vol}\, \Delta_R h^{\circ} \qquad 2.4.7$$

$$T_{M,i}(z = 0) = T_{M,i,inl} \qquad 2.4.8$$

where $\dot{V}$ [m^3 s^{-1}] is the volume flow rate, $\bar{c}_p$ [J kg^{-1} K^{-1}] the specific heat capacity at constant pressure, H [W m^{-2} K^{-1}] the overall heat transfer coefficient between the two flows, A_h [m^2] the heat transfer surface area, r_{vol} [mol m^{-3} s^{-1}] the reaction rate determined based on the local temperature and species concentration as detailed in Section 2.2, Ω_i [m^2] is the cross section of the inner pipe and $T_{M,i,inl}$ [K] the inlet reactive mixture temperature set to 298.15 K unless otherwise specified.

The product $H\, dA_h$ is calculated using the approach of thermal resistances in series:

$$\frac{1}{H\, dA_h} = \frac{\cos(\alpha)}{h_i\, \pi\, d_i\, dz} + \frac{ln\left(\frac{d_i + 2e_w}{d_i}\right)}{2\, \pi\, \lambda_w\, dz} + \frac{\cos(\alpha)}{h_{an}\, \pi\, (d_i + 2e_w)\, dz} \qquad 2.4.9$$

where h_i [W m^{-2} K^{-1}] is the convective heat transfer coefficient between the inner pipe flow and the central wall and h_{an} the heat transfer coefficient between the heat carrier fluid and the central wall. h_i and h_{an} are calculated using the correlations of Bennett (2019) (for laminar pipe flows) and Hirbodi et al. (2022) (valid for laminar flows in annular spaces) as detailed in Appendix B.

As with any situation, the use of correlations leads to inevitable inaccuracies compared to CFD. In particular, the aforementioned correlations were established for thermally developing flows (and not simultaneously developing) and uniform boundary conditions (which is rarely the case in practical processes, namely in the HERs considered in this thesis). Therefore, they can be expected to underestimate heat transfer efficiency in the entrance zones. Moreover, the correlations of Bennett (2019) were developed for inert incompressible fluids, thus, additional inaccuracies are expected in reactive systems where an exothermic reaction occurs in the reactive mixture.

b. Heat carrier fluid

Neglecting axial conduction phenomena, the energy equation of the heat carrier fluid expresses as follows:

$$\rho_{an}\dot{V}_{an}\bar{c}_{p,an}\frac{dT_{M,an}}{dz} = H\left(T_{M,i} - T_{M,an}\right)\frac{dA_h}{dz} - \dot{V}_{an}\frac{dp_{M,an}}{dz} \qquad 2.4.10$$

$$T_{M,an}(z = 0) = T_{M,an,inl} \qquad 2.4.11$$

where $T_{M,an,inl}$ [K] is the inlet heat carrier temperature set to 358.15 K unless otherwise specified.

Equation 2.4.10 expresses the local enthalpy balance over an infinitesimal axial section of the reactor: the left-hand side represents the change of the enthalpy of the annular fluid, while the first term on the right-hand side corresponds to the heat exchanged with the reactive mixture through the heat transfer surface, and the second term accounts for viscous heating. Although its effect is negligible on the temperature field, as discussed later, it is necessary to include it in the systemic model to account for entropy generation by pressure drop in the 1D entropy balance methodology.

2.4.3 Species mass balances

a. Reactive fluid

When a multispecies reactive mixture is involved, the mass conservation equations of the species are solved to determine the axial variations of concentrations. Assuming axial diffusion effects can be neglected so the mass balances express as follows:

$$\frac{dF_j}{dz} = \Omega_i \nu_j r_{vol} \qquad 2.4.12$$

$$F_j(z = 0) = F_{j,inl} \qquad 2.4.13$$

where F_j [mol s^{-1}] is the molar flux of species j, $F_{j,inl}$ [mol s^{-1}] the inlet molar flux of species j and ν_j its stoichiometric coefficient in the hydrolysis reaction. Unless otherwise specified, $F_{(CH_3CO)_2O,inl} = 1.25\ 10^{-3}$ mol s^{-1}, $F_{H_2O,inl} = 3.00\ 10^{-1}$ mol s^{-1} and $F_{CH_3COOH,inl} = 0$ mol s^{-1}, since no acetic acid is injected at the inlet.

b. Heat carrier fluid

The heat carrier fluid consists solely of water; therefore, no transformation occurs. The species mass balance can thus be written as:

$$\frac{dF_{an}}{dz} = 0 \qquad 2.4.14$$

$$F_{an}(z = 0) = F_{an,inl} \qquad 2.4.15$$

where F_{an} [mol s^{-1}] is the molar flux of the heat carrier fluid and $F_{an,inl}$ [mol s^{-1}] its inlet molar flux. Unless otherwise specified, $F_{an,inl} = 2.68$ mol s^{-1}.

2.4.4 Systemic modelling limitations

As previously mentioned, the heat transfer coefficient was initially estimated as the average of two correlations established for non-reactive fluids in tubular (rather than conical) geometries (described in Appendix B). A preliminary attempt to predict the heat transfer coefficient was carried out using CFD through numerical experiments in a simplified configuration. This internal study was performed by Lucas Frapiccini under the supervision of the PhD author.

The goal was to assess whether a preliminary correlation could be established and whether further development of such a correlation would be worthwhile. This work aims to explore the formulation of correlations linking the Nusselt number to classical dimensionless parameters such as the Reynolds Re (Equation 2.4.16), Prandtl Pr (Equation 2.4.17), Damköhler Da (Equation 2.4.18, adapted from Chao et al. (1973)), and Graetz Gz (Equation 2.4.19) numbers using neural networks.

$$Re = \frac{\rho u_{M,i} d_i}{\eta} \tag{2.4.16}$$

$$Pr = \frac{\eta \bar{c}_p}{\lambda} \tag{2.4.17}$$

$$Da = \frac{d_i^2 q'''}{\lambda (T_{M,i,inl} - T_w)} \tag{2.4.18}$$

$$Gz = \frac{L}{zRePr} \tag{2.4.19}$$

where T_w [K] is the inner wall temperature at the inlet q''' [W m^{-3}] is a uniform volumetric heat source within the fluid. These dimensionless numbers characterize various physical phenomena within the system. The Reynolds number reflects the balance between inertial and viscous forces, thereby defining the flow regime. The Prandtl number characterizes the relative rates of momentum and thermal diffusion. The Damköhler number describes the competition between internal heat generation and conductive dissipation and the Graetz number accounts for the thermal development of the flow, highlighting the influence of the entrance length on heat transfer correlations.

The numerical approach adopted is motivated by the inherent complexity of the phenomena involved in exothermic chemical reactions coupled with heat transfer. The temperature dependence of reaction kinetics makes it particularly challenging to simultaneously analyse the evolution of thermal and chemical parameters, which are further influenced by factors such as reaction progress and species diffusion. As a result, a comprehensive

understanding of the simulations requires preliminary investigations under simplified assumptions.

In particular two simplified approaches were chosen:

- First, the study of a well-documented benchmark case in the literature: the laminar flow of a fluid through a cylindrical pipe with a uniform wall temperature without a chemical reaction.
- The introduction of an additional term representing a uniform volumetric heat source within the fluid, denoted by q'''.

This heat generation term is intended to approximate the exothermic nature of a chemical reaction occurring within the fluid. The hypothesis of uniformity assumes temperature-independent reaction kinetics and negligible axial concentration gradients. This allows the exclusion of species diffusion and reaction conversion from the model.

This study investigates heat transfer in laminar flow through cylindrical pipes with fixed wall temperature, aiming to develop correlations between the Nusselt number and key dimensionless parameters: Reynolds (Re), Prandtl (Pr), Damköhler (Da), and Graetz (Gz) numbers. The Brinkman number was not considered in this regression step, as viscous heating effects is negligible in this study (laminar flow). CFD simulations (using ANSYS Fluent, version 2019 R3) allowed generating local Nusselt number data which were regressed using neural network (via MATLAB).

In the case without heat generation, a neural network was trained to predict Nusselt number as a function of Re, Pr, and Gz, achieving excellent agreement with reference literature values. Analytical expressions were also derived for thermally fully developed flows, confirming theoretical Nusselt number values (e.g., Nu = 3.66 at uniform wall temperature without heat generation).

Simulations involved a variety of fluids, both gaseous and liquid, covering wide ranges of Reynolds, Prandtl, and Damköhler numbers. Neural networks were then trained using MATLAB's nnstart toolbox to correlate the Nusselt number to the other dimensionless parameters. The structure of the networks (number of hidden layers) was optimised through trial-and-error, and outliers (e.g., from numerical singularities) were removed to ensure training robustness.

When a uniform internal heat generation term was introduced, additional physical phenomena such as singularities (points where the fluid temperature equals wall temperature) were observed wich lead to a divergence of the Nusselt number. This divergence may occur under two distinct conditions. The first corresponds to the presence of a volumetric heat source (positive internal heating) combined with an inlet fluid temperature lower than the temperature of the wall. In this case, the internal heating progressively increases the fluid

temperature until it matches the initially higher wall temperature. The second condition arises in the case of a volumetric heat sink (internal cooling), when the inlet fluid temperature is higher than the wall temperature. Here, the cooling effect decreases the fluid temperature until it reaches the lower wall temperature. Thus, in both scenarios, the system exhibits a singularity.

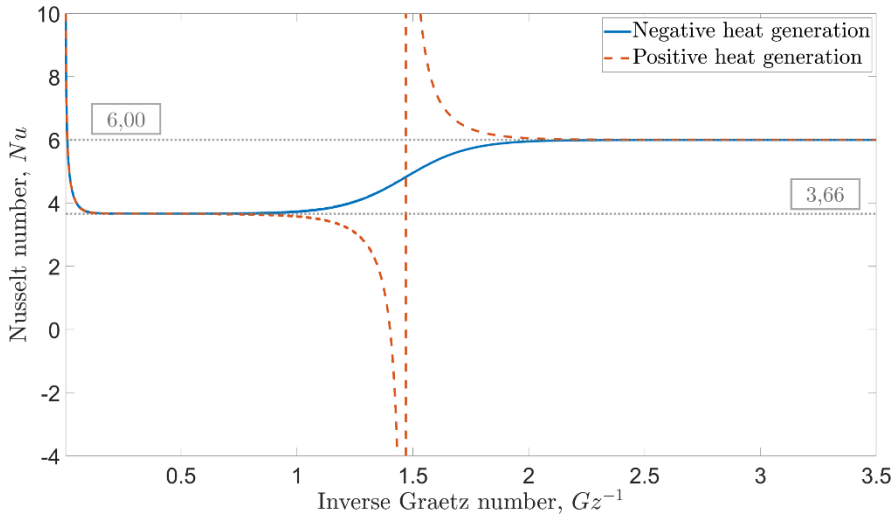

Figure 2.4: $Nu = f(Gz^{-1})$ for a positive heat generation (dotted red line) and for a negative heat generation (solid blue line).

Figure 2.4 illustrates an example of such behaviour for a case in which the inlet fluid temperature is lower than the wall temperature. In Figure 2.4, two scenarios are presented: one with a moderate positive heat source of 100 $W \cdot m^{-3}$ (red curve), and one with a moderate negative heat source of -100 $W \cdot m^{-3}$ (blue curve). These curves correspond to Damköhler numbers of 4.2 10^{-4} and -4.2 10^{-4}, respectively, which are low values consistent with the moderate heat source intensities.

The results show an initial plateau at Nu ≈ 3.656, which is consistent with the theoretical value for fully developed laminar flow without internal heat generation. A discontinuity then occurs (temperature crossing), followed by a second plateau approaching Nu ≈ 6 in the presence of a heat source. The detailed calculation for this last value is presented in Appendix C.

Although these complex behaviours provide valuable insight into the influence of internal heat generation on the Nusselt number, a more detailed investigation was considered beyond the scope of this thesis due to time constraints, as dealing with such discontinuity was found challenging, even with the use of neural networks. Moreover, even with the adapted correlations, the predictive accuracy remains inferior to that of CFD simulations.

2.5 CFD model

CFD is an attractive modelling tool that allows precise determination of velocity, temperature and concentration fields in the HER. Since the width of the annular space and the diameter of the inner pipe are both sufficiently small, and the temperature and concentration differences are moderate, gravity effects can be omitted. Indeed, hydrostatic pressure build-up is negligible and thermal and/or solutal natural convections do not develop. Therefore, the flow, temperature and concentration fields are assumed to be axisymmetric and a 2D (instead of a 3D) CFD modelling approach is adopted. Thus, the numerical domain used consists of half of a longitudinal slice of the HER (the example of a tubular geometry is presented in Figure 2.5) including the annular space, the central wall and the internal pipe. The outer wall, supposed to be perfectly insulated, is not integrated to the numerical domain and is simply considered via an adiabatic wall boundary condition.

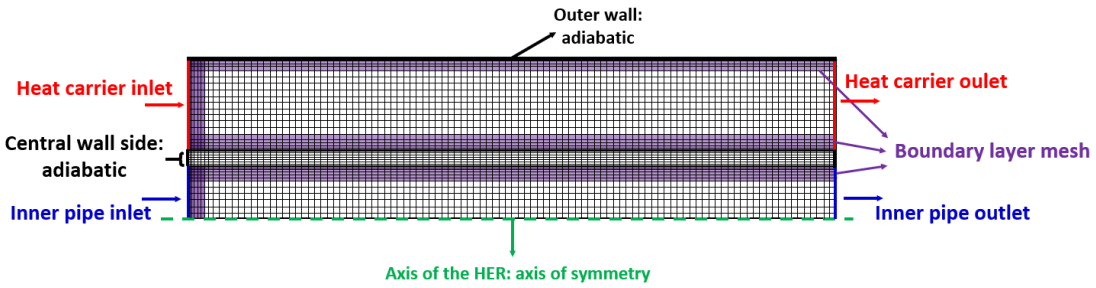

Figure 2.5: Schematic representation of numerical domain and mesh used to perform the 2D CFD simulations.

2.5.1 Coupled hydrodynamics equations

The steady-state velocity, temperature and concentration fields are determined by solving the coupled hydrodynamics (i.e., mass conservation and Navier-Stokes), heat and species transport equations using the commercial CFD code Ansys Fluent (version 2019 R3).

a. Reactive fluid

When a reactive mixture is injected in the inner pipe, in addition to mass and momentum conservation, species transport and reaction equations are solved. The conservation equations get more complex than for a pure fluid since the mixture properties are not uniform but depend on the local composition, and moreover, the energy equation must account for the heat released by the reaction and for enthalpy transport through species diffusion:

$$div(\rho_i \vec{u}) = 0 \qquad 2.5.1$$

$$\overrightarrow{div}\left(\rho_i \vec{u} \otimes \vec{u}\right) = -\vec{\nabla} p - \overrightarrow{div}(\bar{\bar{\tau}}) \qquad 2.5.2$$

$$div\left(\rho_i\left(\bar{h}+\frac{u^2}{2}\right)\vec{\boldsymbol{u}}\right)=div(\lambda_i\vec{\nabla}T)-div(\bar{\bar{\tau}}.\vec{\boldsymbol{u}})-\mathfrak{D}div\left(\rho_i\sum\vec{\nabla}(Y_j)\bar{h}_j\right)-r_{vol}\sum\frac{\Delta_f h^\circ}{M_j} \quad 2.5.3$$

$$div\left(\rho_i Y_j\vec{\boldsymbol{u}}\right)=\mathfrak{D}div\left(\rho_i\vec{\nabla}(Y_j)\right)+\bar{r}_{vol,j} \quad 2.5.4$$

where $\mathfrak{D}$ [$m^2\ s^{-1}$] is the mass diffusivity of the species in the mixture and ρ_i [$kg\ m^{-3}$] the mixture local density. Y_j is the mass fraction of species j, $\bar{h}_j$ [$J\ kg^{-1}$] its specific enthalpy, $\Delta_f h^\circ$ [$J\ mol^{-1}$] its molar enthalpy of formation at local temperature and $\bar{r}_{vol,j}$ [$kg\ m^{-3}\ s^{-1}$] its volumetric formation rate. Details on the modelling of the volumetric rate of creation are reported in Section 2.2.

Equation 2.5.1 is the continuity equation which expresses the conservation of mass. Physically, it states that, the mass flowrate at the inlet is equal to the outlet mass flowrate, meaning that no mass is lost or accumulated within the system. Equation 2.5.2 is the momentum conservation equation. The left-hand side corresponds to the advective transport of momentum, while the right-hand side accounts for the driving pressure gradient and the resistance due to viscous stresses. Equation 2.5.3 is the energy balance equation. The left-hand side describes the advective transport of energy. The first term on the right-hand side represents conductive heat transfer, while the second accounts for viscous dissipation, i.e., the irreversible transformation of mechanical energy into heat. The third term the transport of energy carried by diffusing species. The last term accounts for chemical reaction heat effects, i.e., heat released or absorbed due to reaction enthalpies. Finally, Equation 2.5.4 is the species conservation equation, which ensures the local mass balance of each chemical component *j*. The left-hand side describes advective transport, while the first term on the right-hand side represents molecular diffusion driven by concentration gradients (i.e., Fickian diffusion). The last term accounts for the source or sink of species due to chemical reactions.

b. Heat carrier fluid

For the heat carrier fluid (i.e., water circulating in the annular space) whose density is considered constant, these equations express as follows:

$$div(\vec{\boldsymbol{u}})=0 \quad 2.5.5$$

$$\overrightarrow{div}\left(\rho_{an}\vec{\boldsymbol{u}}\otimes\vec{\boldsymbol{u}}\right)=-\vec{\nabla}p+\eta_{an}\vec{\Delta}(\vec{\boldsymbol{u}}) \quad 2.5.6$$

$$div\left(\rho_{an}\left(\bar{h}+\frac{u^2}{2}\right)\vec{\boldsymbol{u}}\right)=\lambda_{an}\Delta T-div(\bar{\bar{\tau}}.\vec{\boldsymbol{u}}) \quad 2.5.7$$

with

$$\bar{\bar{\tau}} = -\eta\left[\bar{\bar{\nabla}}\vec{u} + \bar{\bar{\nabla}}^{T}\vec{u} - \frac{2}{3}div(\vec{u})\bar{\bar{1}}\right] \quad 2.5.8$$

where $\bar{h}$ [J kg^{-1}] is the specific enthalpy of the fluid. The viscous shear stress tensor, $\bar{\bar{\tau}}$, is calculated using Equation 2.5.8 (Newtonian fluid) which can be further simplified since its last term is nil (Equation 2.5.5) as the flow is considered incompressible (Equation 2.5.5).

Equation 2.5.5 represents the continuity equation for an incompressible flow. As for the mixture, it ensures the mass flow conservation. Equation 2.5.6 is the momentum conservation equation for the annular fluid, where the advective transport of momentum is balanced by the driving pressure gradient and the viscous stresses. Equation 2.5.7 corresponds to the energy conservation equation. The advective transport of enthalpy and kinetic energy is described on the left-hand side, while the right-hand side accounts for conductive heat transfer through the thermal conductivity of the annular fluid, as well as viscous dissipation associated with the irreversible transformation of mechanical energy into heat. This equation does not account for any species diffusion or chemical reactions as the utility fluid consists of pure water.

In the solid region (i.e., the central wall), only the steady-state energy equation is solved:

$$\lambda_w \Delta T = 0 \quad 2.5.9$$

Equation 2.5.9 is a steady-state heat conduction equation, ensuring that the heat flux entering and leaving the solid remains balanced. All the calculations described in this section were performed on a non-uniform Cartesian grid of about 8.5×10^5 square elements generated using Ansys Meshing software. Boundary layer meshes were applied at the fluid side of the liquid/solid interfaces for accurate calculation of the steep gradients prevailing in these areas. Moreover, a boundary layer mesh was also implemented at the HER's inlets region for accurate description of transport phenomena in the developing flows at the entrance zones where high entropy generation rates are expected.

Concerning the boundary conditions, uniform velocity, pressure, and temperature profiles as well as uniform species concentrations are imposed at the annular space and internal pipe inlets:

$$u_z(z=0) = u_{M,inl} \quad 2.5.10$$

$$u_r(z=0) = 0 \quad 2.5.11$$

$$T(z=0) = T_{M,inl} \quad 2.5.12$$

$$Y_j(z = 0) = Y_{j,inl} \quad 2.5.13$$

At both pipes' outlets, pressure, temperature and mass fractions values are extrapolated from the interior.

$$p(z = L) = p_{atm} \quad 2.5.14$$

$$\frac{dT}{dz}(z = L) = 0 \quad 2.5.15$$

$$\frac{dY_j}{dz}(z = L) = 0 \quad 2.5.16$$

A symmetry condition is imposed at the HER axis. At the walls, a no-slip boundary condition is applied. The outer wall and the left and right sides of the central pipe are treated as adiabatic. At the inner and outer surfaces of the central pipe which are internal boundaries, conjugate heat transfer conditions are applied, i.e., the heat flux is continuous and the fluid and solid share the same temperature at the interface.

Mesh-independence study was carried out by repeating the simulations on a much finer grid consisting of about 2.2×10^6 computational cells. The results obtained with both meshes were very similar, which proves that the coarse mesh density was already sufficient for reaching mesh-insensitive results.

2.5.2 One-dimensional reduced modelling

CFD simulations lead to a 2D representation of the flow field. To enable comparison of the axial profiles of temperature, pressure, concentrations, etc., predicted by CFD and those obtained by the systemic process model, CFD data need to be reduced to a single dimension by averaging or integrating these variables over the cross sections. Concerning the temperature, its representative value at each axial position is called the mixing-cup temperature, T_M. It corresponds to the mass flow rate weighted average of specific enthalpies and is calculated as follows:

$$T_M = \frac{\int_\Omega \rho\, \bar{c}_p\, u_z\, T\, r\, dr}{\int_\Omega \rho\, \bar{c}_p\, u_z\, r\, dr} \qquad 2.5.17$$

where Ω [m^2] is the cross section of the given flow, $\bar{c}_p$ [J kg^{-1} K^{-1}] the specific heat capacity of the fluid (which is assumed constant except in the reactive mixture), u_z [m s^{-1}] and T [K] are respectively the local axial velocity and temperature determined by CFD. This definition leads to temperature values which satisfy the energy balance. In other words, if the heat transfer correlations used in the systemic model were perfectly accurate, the predicted temperature obtained by the 1D model would match the mixing-cup results.

Similarly, for the reactive mixture, the representative values of the species concentrations at each cross section are determined following a volume flow rate-based mixing-cup formulation:

$$C_{M,j} = \frac{\int_\Omega x_j\, C_{tot}\, u_z\, r\, dr}{\int_\Omega u_z\, r\, dr} \qquad 2.5.18$$

where the denominator in Equation 2.5.18 corresponds to the local volume flow rate. C_{tot} [mol m^{-3}] is the total concentration of all molecules in the solution:

$$C_{tot} = \frac{\rho}{\sum\left(x_{M,j} M_j\right)} \qquad 2.5.19$$

where ρ [kg m^{-3}] is the fluid density and the denominator of Equation 2.5.19 corresponds to the local average molar mass of the mixture. Concentration values determined using the mixing-cup formulation satisfy the species mass conservation equations. In other words, if the reaction rate calculation in the systemic model was perfectly accurate, the predicted concentration values obtained by the systemic model would correspond to the mixing-cup results.

Following the same procedure, for each fluid, the representative average pressure at a flow section is calculated as follows:

$$p_M = \frac{\int_\Omega p\, u_z\, r\, dr}{\int_\Omega u_z\, r\, dr} \qquad 2.5.20$$

2.6 Multi-objective optimisation problem formulation

As previously outlined, the objective of this thesis is to optimise the design of HERs. In this section, attention is given to the multi-objective optimisation of two configurations presented in Section 2.3: a purely tubular geometry and a profiled geometry. This optimisation is applied to both reactive systems in order to construct Pareto fronts, thereby evaluating the trade-off between entropy generation and reactor volume.

Indeed, these two objective functions are inherently conflicting, as can be observed from the mathematical expressions of the local entropy generation terms. Viscous dissipation increases with higher velocity gradients; consequently, reducing it requires a larger reactor diameter, which increases the total reactor volume. Similarly, heat transfer-induced entropy generation is driven by steep temperature gradients. Larger diameters allow for a more uniform temperature distribution and a greater heat transfer surface area, thereby lowering the associated entropy production. The presence of exothermic chemical reactions further complicates the picture, as the heat released must be efficiently removed to avoid hotspots while maintaining fast reaction kinetics, introducing an additional trade-off between thermal management and entropy minimization.

Ultimately, reactor design involves balancing these competing effects: reducing irreversibilities while keeping the system economically and physically feasible, highlighting the relevance of multi-objective optimisation approaches Minimizing entropy generation and maintaining a compact reactor volume are inherently conflicting objectives (Bejan, 1996; Magnanelli et al., 2019). The detailed formulation of the multi-objective optimisation problem is presented below.

2.6.1 Objective functions

For each reactive case, the Pareto front illustrating the trade-off between two objective functions is determined, using the systemic modelling as a preliminary study before comparing the results to CFD modelling. The first objective function to minimize is the total volume of the HER, V_{HER}. For the tubular configuration, V_{HER} corresponds to the volume of a cylinder with a length L and a diameter equal to d_o. In the profiled configuration, the HER is divided into 10 segments of equal length, each measuring $L/10$ (where L is the total length of the HER). Within these segments, the inner pipe internal diameter d_i varies according to piecewise-linear functions that are continuously connected. Consequently, the total volume of the HER, V_{HER}, is the sum of the volumes of the 10 conical pipes.

The second objective function to be minimized is the total entropy generation rate in the HER, denoted as $\dot{S}_{tot}$ [W K^{-1}]. As presented in Chapter 1, two methods can be employed to determine $\dot{S}_{tot}$. The first method, referred to as the global method, calculates the entropy generation rate based on an entropy balance over the system boundaries. The second method, known as the local method, computes the total entropy generation by integrating the local

entropy generation rates throughout the system. Both methods theoretically yield the same results as detailed in Chapter 3 (Michaud et al., 2024 and Stanciu et al., 2001). The entropy generation equations for both the systemic and CFD modelling approaches, previously introduced in Chapter 1, are recalled below.

a. Local entropy generation approach: 1D model

Using the local method, the total entropy generation rate per unit length of the HER, denoted as $\dot{s}_{tot}$ [W K^{-1} m^{-1}], is the sum of different contributions (Johannessen and Kjelstrup, 2004) as presented in Chapter 1:

$$\dot{s}_{tot}^{'} = \dot{s}_{\eta,i}^{'} + \dot{s}_{\eta,an}^{'} + \dot{s}_{h}^{'} + \dot{s}_{ch}^{'} \qquad 2.6.1$$

The first two terms on the right hand-side of Equation 2.6.1, $\dot{s}_{\eta,i}$ and $\dot{s}_{\eta,an}$ [W K^{-1} m^{-1}], represent the viscous dissipation contributions to entropy generation in the reactive mixture and the heat carrier flow, respectively. They are calculated as follows:

$$\dot{s}_{\eta,i}^{'} = -\frac{1}{T_{M,i}}\dot{V}_i\left(\frac{dp_{M,i}}{dz}\right)_{irr} \qquad 2.6.2$$

$$\dot{s}_{\eta,an}^{'} = -\frac{1}{T_{M,an}}\dot{V}_{an}\left(\frac{dp_{M,an}}{dz}\right)_{irr} \qquad 2.6.3$$

The third term on the right hand-side of Equation 2.6.1, $\dot{s}_h$ [W K^{-1} m^{-1}], represents the heat transfer contribution to entropy generation from the reactive mixture, heat carrier flow, and the central wall. It is calculated as follows:

$$\dot{s}_{h}^{'} = \psi\left(\frac{1}{T_{M,an}} - \frac{1}{T_{M,i}}\right) \qquad 2.6.4$$

The last term on the right hand-side of Equation 2.6.1, $\dot{s}_{ch}$ [W K^{-1} m^{-1}], represents the chemical reaction contribution to entropy generation and is calculated as follows for the acetic anhydride hydrolysis:

$$\dot{s}_{ch}^{'} = -\frac{\pi d_i^2}{4} r_{vol}\frac{\Delta_R G}{T_{M,i}} \qquad 2.6.5$$

where $\Delta_R G$ [J mol^{-1}] is the reaction Gibbs energy, which is evaluated at the local temperature $T_{M,i}$ [K], as follows:

$$\Delta_R G(T_{M,i}) = \Delta_R G^{\circ}(T_{M,i}) + R_{gaz} T_{M,i} \ln\left(\prod (a_j)^{\nu_j}\right) \qquad 2.6.6$$

where $\Delta_R G^\circ$ [J mol^{-1}] is the standard Gibbs energy of reaction and a_j [-] is the activity of species j. The detailed calculation of $\Delta_R G^\circ$ is detailed in Appendix D.

In the acetic anhydride hydrolysis case, the activities coefficients are considered equal to unity (ideal solution assumption) which leads to the activities being equal to the molar fraction of the constituents.

Finally, the total entropy generation rate, $\dot{S}_{tot}$, is computed by integrating the local entropy source terms along the length of the HER:

$$\dot{S}_{tot} = \int_0^L \dot{s}'_{tot}\, \mathrm{d}z \qquad 2.6.7$$

b. Local entropy generation approach: CFD model

For the CFD modelling, the entropy generation term is the sum of the following contributions:

$$\dot{s}'''_{tot} = \dot{s}'''_{\eta} + \dot{s}'''_{h} + \dot{s}'''_{\mu} + \dot{s}'''_{ch} \qquad 2.6.8$$

where $\dot{s}'''_{\eta}$, $\dot{s}'''_{h}$, $\dot{s}'''_{\mu}$ and $\dot{s}'''_{ch}$ represent the volumetric entropy generation rates which are respectively due to viscous dissipation, heat transfer, mass transfer and chemical reaction.

As noted previously, $\dot{s}'''_{\eta}$ represents rate of entropy generation due to viscous dissipation, i.e., to mechanical energy dissipation into heat by viscous stresses. This irreversibility occurs whenever the process includes a flowing and is calculated as follows (Sciacovelli et al., 2015):

$$\dot{s}'''_{\eta} = -\frac{1}{T}\bar{\bar{\boldsymbol{\tau}}} : \bar{\bar{\nabla}}\vec{\boldsymbol{u}} \qquad 2.6.9$$

where $\bar{\bar{\boldsymbol{\tau}}}$ and $\bar{\bar{\nabla}}\vec{\boldsymbol{u}}$ respectively represent the shear stress and velocity gradient tensors.

$\dot{s}'''_{h}$ represents the rate of entropy generation due to heat transfer, i.e., to temperature inhomogeneities within the system. This term expresses as follows (Sciacovelli et al., 2015):

$$\dot{s}'''_{h} = \frac{\lambda}{T^2}\left(\vec{\nabla}T\right)^2 \qquad 2.6.10$$

where λ [W m^{-1} K^{-1}] is the thermal conductivity.

$\dot{s}'''_{\mu}$ represents the rate of entropy generation due to mass transfer, i.e., to concentration gradients within the system. When the reactive mixture can be treated as ideal, and if diffusion phenomena are solely described by Fick's law (i.e., absence of electrophoretic diffusion, Soret effect, etc.) this term is expressed as follows (Sciacovelli et al., 2015):

$$\dot{s}_{\mu}^{'''} = \rho\, R_{gas} \sum \frac{\mathfrak{D}_{j,m}}{M_j x_j} \vec{\nabla} Y_j . \vec{\nabla} x_j \qquad 2.6.11$$

where R_{gas} [J mol^{-1} K^{-1}] is the universal ideal gas constant, $\mathfrak{D}_{j,m}$ [m^2 s^{-1}] the mass diffusion coefficient of species j in the mixture, M_j [kg mol^{-1}] its molecular weight, Y_j and x_j its mass and molar fractions respectively.

$\dot{s}_{ch}^{'''}$ represents the rate of entropy generation due to chemical reactions. It is expressed as follows (Sciacovelli et al., 2015):

$$\dot{s}_{ch}^{'''} = -\frac{1}{T} \sum \mu_j\, r_{vol,j} \qquad 2.6.12$$

where $r_{vol,j}$ [mol m^{-3} s^{-1}] represents the rate of creation of species j and μ_j [J mol^{-1}] its chemical potential. The detailed calculation and implementation of this term is detailed in Appendix D.

CFD simulations allow obtaining the fields of velocity, temperature, concentrations and rate of reactions at each axial and radial position. The entropy generation rates, expressed by Equations 2.6.9, 2.6.10, 2.6.11 and 2.6.12 can be easily postprocessed then and summed up (Equation 2.6.8) to determine $\dot{s}_{tot}^{'''}$, the local entropy source term. The total entropy generation rate of the system, $\dot{S}_{tot}$ [W K^{-1}], can be deduced by volume integration over the numerical domain (the total volume of the HER):

$$\dot{S}_{tot} = \iiint \dot{s}_{tot}^{'''}\, dV \qquad 2.6.13$$

where dV represents an infinitesimal volume (usually approximated as the volume of the CFD mesh cells).

2.6.2 Multi-objective optimisation problem

The multi-objective optimisation problem is stated as follows:

$$\underset{\vec{v}}{\text{Min}}\,\vec{F} = \underset{\vec{v}}{\text{Min}}[\dot{S}_{tot}, V_{HER}]^T \quad 2.6.14$$

where $\vec{F}$ is the vector of objective functions and $\vec{v}$ represents the vector of decision variables. For the tubular HER, the decision variables include two variables, the total length of the HER, L, and the internal diameter of the inner tube, d_i. In the case of the profiled HER, there are 12 decision variables: the total length, L, the internal diameter of the packed bed at the inlet, $d_{i,inl}$ and the slopes of the 10 sections, denoted as α_m (where $1 \leq m \leq 10$). A positive slope indicates a divergent section of the HER, while a negative one to a convergent section.

This minimization multi-objective problem is subject to:

a- The process model equations, described in Section 2.4, which constitutes a differential system of equations:

$$\vec{f}\left(z, \vec{X}, \frac{d\vec{X}}{dz}, \vec{v}\right) = \vec{0} \quad 2.6.15$$

where $\vec{X}$ represents the set of process variables, including the temperature and pressure of the reactive mixture and the heat carrier, and the composition of the reactive mixture. Solving this system of equations for a given vector of decision variables allows for the computation of the objective functions.

b- The boundary conditions listed in Section 2.3, which remain unchanged across the various case studies conducted except if other conditions are specified:

$$\vec{X}(z = 0) = \vec{X}_{inl} \quad 2.6.16$$

c- End point or terminal inequality constraints. They correspond to constraints which must be satisfied at the end of the integration domain, i.e., at $z = L$:

$$\xi(z = L) \geq \xi_{min} \quad 2.6.17$$

The variable ξ [-] represents the chemical reaction conversion. Imposing a minimum conversion rate is essential to achieve HER designs of practical interest that meet the target conversion rate. Without this constraint, the optimisation process would yield HER designs of minimal length, as they would aim to minimize volume and entropy generation. The minimal conversion to achieve, denoted as ξ_{min}, is set to 0.8 across the various case studies conducted, unless otherwise specified. In practice, all Pareto optimal solutions achieve a conversion efficiency nearly equal to the target conversion.

Indeed, additional conversion beyond the minimum imposed conversion results in an increase in both the HER volume and total entropy generation. Therefore, mathematically, it would have been better to express Equation 2.6.17 as an equality rather than as an inequality constraint. However, the optimisation problem is solved using a genetic algorithm as explained later in this section, and equality constraints pose challenges for this type of algorithm by preventing it from identifying feasible solutions within an acceptable computational time. Thus, from a numerical perspective, Equation 2.6.17 is formulated as an inequality constraint to enable the algorithm to identify feasible solutions, which are refined from generation to generation until they converge toward a conversion practically equal to the imposed one.

d- Path constraints. They correspond to constraints which must be satisfied at each of the integration domain, i.e., $\forall\, z \in [0, L]$:

$$0.5\ \text{cm} \leq d_i \leq 10\ \text{cm} \tag{2.6.18}$$

e- Decision variables bounds. These inequality constraints establish the permissible values for the decision variables, thereby defining the feasible region in which the optimal solutions can be identified:

$$0.1\ \text{m} \leq L \leq 10\ \text{m} \tag{2.6.19}$$

$$-\frac{\pi}{2} < \alpha_m < \frac{\pi}{2} \ \text{for}\ 1 \leq m \leq 10 \tag{2.6.20}$$

The constraints outlined in Equation 2.6.19 define the permissible length for the HER, while those in Equation 2.6.20 apply exclusively to the profiled configuration. All slopes of diameter profiles, except for vertical sections, are permitted. In practice, the bounds established for the decision variables remained unreached throughout the optimisation process, meaning they did not influence any of the optimal designs.

2.6.3 Numerical procedure

For the systemic model optimisation, the process model presented in Section 2.4, which constitutes a differential system of equations, is implemented and solved using MATLAB software. The integration of the differential equations is carried out using a variable-step solver based on backward differentiation formulas. At each integration step, equations are solved using the Levenberg-Marquardt method.

The multi-objective optimisation problem (Section 2.6.2) was addressed using the Non-Dominated Sorting Genetic Algorithm 2 (NSGA-II), implemented in MATLAB. Such algorithms are classified as global optimisation methods because, unlike gradient-based techniques, they are not prone to getting trapped in local minima, making them particularly suitable for complex, nonlinear optimisation problems, although there is no guarantee that the global minimum will be found. For each case study, the genetic algorithm generates the Pareto front, illustrating the trade-off between minimal HER volume and minimal entropy generation rate.

For the CFD-based optimisation, the physical model is implemented and simulated using ANSYS Fluent (version 2019 R3). The governing equations, namely the Navier-Stokes equations along with energy and species transport equations, are numerically solved using the finite volume method. The multi-objective optimisation is performed using the Multi-Objective Genetic Algorithm (MOGA), coupled with response surface methodology. This approach enables an efficient exploration of the design space by approximating the CFD results with surrogate models. First, a design of experiments (DOE) is generated, and CFD simulations are run for each configuration. Based on these results, a response surface is constructed using the Kriging interpolation method to estimate objective functions as functions of selected design parameters. MOGA is then applied to this surrogate model to identify Pareto-optimal solutions, balancing multiple competing objectives. This method significantly reduces computational cost while maintaining acceptable accuracy. The optimisation process is conducted within the ANSYS Workbench environment, which ensures the integration and automation of Fluent simulations, parameter updates, and objective evaluation.

2.7 Conclusion

In this chapter, the hydrolysis of acetic anhydride in a HER was selected as a representative case study to investigate entropy generation in liquid-phase homogenous reactive systems. Two reactor configurations were introduced and characterized: a purely tubular double-pipe HER and a piecewise diameter-varying configuration, which will later be compared and optimised.

A systemic modelling framework was first developed by formulating the mass, momentum, energy, and species balances. This approach provides fast and valuable insights into the global reactor behaviour and overall performance indicators. However, the underlying assumptions—such as ideal plug-flow and the absence of radial gradients—limit its applicability when capturing local non-idealities. To overcome these limitations, CFD modelling was carried out by solving the coupled hydrodynamic and thermal fields, yielding detailed spatial information on velocity, concentration, and temperature profiles. A one-dimensional reduced modelling framework was then derived from CFD results, serving as a link between the two modelling. Together, these modelling approaches provide complementary perspectives as it will be detailed in the next chapter.

Building on these modelling foundations, the multi-objective optimisation problem was formulated. Entropy generation minimization and total reactor volume were defined as the objective functions, while the reactor's geometric parameters, namely the inlet diameter, the total length and the slopes of each segment, were introduced as decision variables.

Finally, a pilot-scale design was proposed to allow future validation of the CFD results. Although time constraints prevented the execution of experimental campaigns, the complete design methodology is provided in Appendix E as a reference for future work.

Overall, this chapter has established a comprehensive methodological framework that integrates systemic modelling, CFD simulations, and multi-objective optimisation. This framework constitutes the basis for the next chapter, where the different modelling strategies will be compared in terms of their predictive capabilities for HER performance and entropy generation estimation. Subsequently, these models will be applied within a multi-objective optimisation procedure to construct Pareto fronts, thereby highlighting design trade-offs and guiding the search for more compact and efficient heat-exchanger reactors.

List of Figures

Figure 2.1: Schematic representation of the double pipe HER: (a) Side view, (b) Front view. 66
Figure 2.2: Schematic representation of the double pipe HER piecewise profiled configuration 67
Figure 2.3: Schematic representation of the slope α of an HER segment 67
Figure 2.4: $Nu = f(Gz^{-1})$ for a positive heat generation (dotted red line) and for a negative heat generation (solid blue line) 78
Figure 2.5: Schematic representation of numerical domain and mesh used to perform the 2D CFD simulations. 79

List of Tables

Table 2.1: Operating setup for each reactor configuration (Asprey et al., 1996). 65
Table 2.2: Arrhenius kinetics parameters obtained for each experimental configuration (Asprey et al., 1996). 65
Table 2.3: Reference case operating conditions. 68
Table 2.4: Thermophysical properties of the species (Yaws,1999; Linstrom and Mallard, 2001). 69

Bibliography

Asprey, S. P., Wojciechowski, B. W., Rice, N. M., & Dorcas, A. (1996). Applications of temperature scanning in kinetic investigations: The hydrolysis of acetic anhydride. Chemical Engineering Science, 51(20), 4681–4692. https://doi.org/10.1016/0009-2509(96)00306-5

Bejan, Adrian. Entropy generation minimization: the method of thermodynamic optimization of finite-size systems and finite-time processes. CRC Press, 1996.

Bennett, T. D. (2019). Correlations for the Graetz problem in convection – Part 1: For round pipes and parallel plates. International Journal of Heat and Mass Transfer, 136, 832–841. https://doi.org/10.1016/j.ijheatmasstransfer.2019.03.006

Biswas, A., Saha, B. C., Lawton, J. W., Shogren, R. L., & Willett, J. L. (2006). Process for obtaining cellulose acetate from agricultural by-products. Carbohydrate polymers, 64(1), 134-137.

Chao, R. E., Caban, R. A., & Irizarry, M. M. (1973). Wall heat transfer to chemical reactors. The Canadian Journal of Chemical Engineering, 51(1), 67-70.

Foster, A. W. (1965). Friction factor characteristics for flow regime transition in concentric annuli. https://doi.org/10.14288/1.0059286

Foussard, J.-N., Julien, E., Mathé, S., & Debellefontaine, H. (2015). Thermodynamique: Applications aux systèmes physicochimiques. Dunod.

Garcia-Hernandez, E. A., Souza, C. R., Vernières-Hassimi, L., & Leveneur, S. (2019). Kinetic modeling using temperature as an on-line measurement: Application to the hydrolysis of acetic anhydride, a revisited kinetic model. Thermochimica Acta, 682, 178409.

Hirbodi, K., Yaghoubi, M., & Warsinger, D. M. (2022). New Nusselt number correlations for developing and fully developed laminar flows in concentric circular annular ducts. International Communications in Heat and Mass Transfer, 134, 105936. https://doi.org/10.1016/j.icheatmasstransfer.2022.105936

Johannessen, E., & Kjelstrup, S. (2004). Minimum entropy production rate in plug flow reactors: An optimal control problem solved for SO_2 oxidation. Energy, 29(12–15), 2403–2423.

Linstrom, P. J., & Mallard, W. G. (2001). The NIST chemistry webbook: A chemical data resource on the internet. Journal of Chemical & Engineering Data, 46(5), 1059–1063. https://doi.org/10.1021/je000236i

Michaud, A., Hreiz, R., & Portha, J. F. (2024). Entropy generation analysis for designing efficient and sustainable heat exchangers and chemical reactors: From 1D modelling to detailed CFD simulations. Chemical Engineering Science, 300, 120615.

Muzychka, Y. S., & Yovanovich, M. M. (2009). Pressure drop in laminar developing flow in noncircular ducts: A scaling and modeling approach. Journal of Fluids Engineering, 131(11), 111105. https://doi.org/10.1115/1.4000377

Olmsted III, J. A. (1998). Synthesis of aspirin: A general chemistry experiment. Journal of chemical education, 75(10), 1261.

Paul, E. L., Atiemo-Obeng, V. A., & Kresta, S. M. (2004). Handbook of industrial mixing (pp. 1–143). Wiley-Blackwell.

Sciacovelli, A., & al. « Entropy Generation Analysis as a Design Tool—A Review ». Renewable and Sustainable Energy Reviews, vol. 43, 2015, p. 1167 81. DOI.org (Crossref), https://doi.org/10.1016/j.rser.2014.11.104

Stanciu, D., Isvoranu, D., Marinescu, M., & Gogus, Y. (2001). Second law analysis of diffusion flames. International Journal of Thermodynamics, 4(1), 1–18.

Wilke, C. R., & Chang, P. (1955). Correlation of diffusion coefficients in dilute solutions. AIChE journal, 1(2), 264-270.

Yaws, C. L. (1999). Chemical properties handbook: Physical, thermodynamic, environmental, transport, safety, and health related properties for organic and inorganic chemicals. McGraw-Hill.

Appendix A. Local friction coefficient calculation

Local friction coefficients (employed in the systemic model) in both inner pipe and annular space are calculated using the correlation of Muzychka and Yavanovich (2009). This correlation is valid for both developing and fully developed internal laminar flows, and applies for different cross-section geometries, namely round and annular pipes. The correlation is expressed as follows:

$$C_{fz} = \frac{4}{Re_{\sqrt{\Omega}}}\left[\left(\frac{C_1}{z^+}\right)^n + \left(\frac{12}{\sqrt{\varepsilon_{AR}}(1+\varepsilon_{AR})\left[1-\frac{192\varepsilon_{AR}}{\pi^5}\tanh\left(\frac{\pi}{2\varepsilon_{AR}}\right)\right]}\right)^n\right]^{\frac{1}{n}} \quad \text{A.1}$$

where C_{fz} is the local apparent friction coefficient. $Re_{\sqrt{\Omega}}$ is a modified Reynolds number, based on Ω, the cross-section area of the flow, instead of the hydraulic diameter, and expresses as follows:

$$Re_{\sqrt{\Omega}} = \frac{\rho u_m \sqrt{\Omega}}{\eta} \quad \text{A.2}$$

z^+ is a dimensionless axial distance defined as follows:

$$z^+ = \frac{z}{\sqrt{\Omega} Re_{\sqrt{\Omega}}} \quad \text{A.3}$$

ε_{AR} is the nominal aspect ratio of the cross-section geometry and C_1 and n are correlation parameters that depend on the shape of the flow section. The values of these coefficients (Muzychka and Yavanovich, 2009) are reported in Table A1.

Table A1: Friction coefficient correlation parameters (Muzychka and Yavanovich, 2009).

	Inner round pipe	**Annular space**
$\boldsymbol{\varepsilon}$	1	$\frac{1-r^*}{\pi(1-r^*)}$ $r^* = \frac{d_i + 2e_w}{d_o}$ In the present study, $r^* = 0.375$ which leads to $\varepsilon = 0.145$
$\boldsymbol{n}$	2.01	2.092
$\boldsymbol{C_1}$	1.72	3.44
$\boldsymbol{\Omega}$	$\Omega_i = \frac{\pi d_i^2}{4}$ In the present study, $d_i = 10$ mm which leads to $\Omega_i = 7.85\ 10^{-5}$ m^2	$\Omega_{an} = \frac{\pi}{4}[d_o^2 - (d_i + 2e_w)^2]$

In the present study, $e_w = 1$ mm and $d_o = 32$ mm which leads to $\Omega_{an} = 6.91\ 10^{-4}$ m^2

Appendix B. Local heat transfer coefficient calculation

The systemic model requires local heat transfer coefficients to calculate the heat flux between the two flows. The calculation of the heat transfer coefficient between the inner pipe flow and the central wall is based on the results of Bennett (2019) who focused on thermally developing laminar flows in round pipes. Bennett (2019) proposed two correlations for the two limiting cases of boundary conditions. The first corresponds to Uniform Wall Temperature (UWT) and the second to Uniform Heat Flux (UHF) boundary conditions:

$$Nu_i^{UWT} = ((5.079Gz_i^{1.13} + 146.9)^{0.295} - 0.701) \times \left(1 - \frac{(Gz_i^{1.13}/3)/(Gz_i^{1.13} + 28.92)}{1 - 0.4338/(Gz_i^{1.13} + 28.92)^{0.295}}\right) \quad \text{B.1}$$

$$Nu_i^{UHF} = ((6.664Gz_i^{1.146} + 240.1)^{0.2908} - 0.559) \times \left(1 - \frac{(Gz_i^{1.146}/3)/(Gz_i^{1.146} + 36.03)}{1 - 0.3222/(Gz_i^{1.146} + 36.03)^{0.2908}}\right) \quad \text{B.2}$$

where Nu_i and Gz_i are respectively the Nusselt and Graetz numbers of the inner pipe flow. The Graetz number and the Nusselt number are expressed as follows:

$$Gz = \frac{D_H}{z} Re\ Pr \quad \text{B.3}$$

$$Nu = \frac{hd_i}{\lambda} \quad \text{B.4}$$

where D_H [m] is the hydraulic diameter, Re the Reynolds number and Pr the Prandtl number.

In the HER, neither the central wall temperature nor the heat flux is uniform. Therefore, for simplicity, the Nusselt number of the inner pipe flow was calculated as the average of the two limiting cases (UWT and UHF) described by Equations B.1 and B.2. It is noteworthy that the correlations of Bennett (2019) were developed for inert fluids. Thus, they are expected to lead to some inaccuracies in the case of the reactive mixture where the heat released by the reaction leads to a distortion of the temperature profiles.

Calculation of the heat transfer coefficient between the heat carrier fluid and the central wall is based on the results of Hirbodi et al. (2022) who focused on thermally developing laminar flows in pipes of annular cross-section. The outer wall of the HER being adiabatic, the two limiting cases correspond to situations where the inner wall of the annulus is respectively at

uniform temperature (UWT) or subjected to a uniform heat flux (UHF). The correlations of Hirbodi et al. (2022) express as follows:

$$Nu_{an} = a_1 r^{*a_2} + a_3 r^{*a_4} + a_5 + \frac{\left(b_1 r^{*b_2} + b_3\right)}{Gz_{an}^{\left(c_1 r^{*c_2} + c_3\right)}} exp\left(\frac{d_1 r^{*d_2} + d_3}{Gz_{an}}\right) \quad \text{B.5}$$

where r^*, the shape factor of the annulus, is equal to $(d_i + 2e_w)/d_o$, the ratio of the inner diameter to the outer diameter of the annular space. The values of parameters 'a' and 'b' depend on the boundary condition at the inner wall of the annulus and are reported in Table B1. Again, since in the HER, neither the central wall temperature nor the heat flux is uniform, the Nusselt number of the heat carrier fluid was simply estimated as the average of the two limiting cases (UWT and UHF):

$$Nu = \frac{Nu^{UHF} + Nu^{UWF}}{2} \quad \text{B.6}$$

Table B1: Values of the parameters used in the correlation of Hirbodi et al. (2022).

Boundary condition							
UWT	a_1	a_2	a_3	a_4	a_5	b_1	b_2
	1.263	-0.766	0.055	-1.061	3.543	0.029	-0.948
	b_3	c_1	c_2	c_3	d_1	d_2	d_3
	0.407	0.004	-0.709	-0.430	-33.160	0.181	-51.710
UHF	a_1	a_2	a_3	a_4	a_5	b_1	b_2
	1.217	-0.781	0.035	-1.091	4.133	0.029	-0.948
	b_3	c_1	c_2	c_3	d_1	d_2	d_3
	0.407	0.004	-0.709	-0.430	-33.160	0.181	-51.710

Appendix C. Nusselt number in a thermally developed laminar flow with uniform volumetric heat generation

In this section, an analytical expression for the Nusselt number is derived for the case of a steady, thermally fully developed laminar flow within a cylindrical duct, under the presence of a uniform internal heat generation source. All fluid thermophysical properties are assumed to be uniform, i.e., independent of temperature and pressure.

Starting from the radial energy balance in cylindrical coordinates, axisymmetric conditions with negligible axial conduction, the differential form of the energy equation becomes:

$$-\lambda_f \frac{d}{dr}\left(2\pi r L \frac{dT}{dr}\right) + 2\pi r L u''' = 0 \tag{C.1}$$

where λ_f [W m^{-1} K^{-1}] is the fluid thermal conductivity, r [m] the radial coordinate, L [m] the HER length, T [K] the absolute temperature and u''' [W m^{-3}] the volumetric heat generation.

Simplifying, we obtain the following ordinary differential equation:

$$\frac{d}{dr}\left(r\frac{dT}{dr}\right) = -\frac{u'''}{\lambda_f} r \tag{C.2}$$

Integrating once:

$$r\frac{dT}{dr} = -\frac{u'''}{2\lambda_f} r^2 + C_1 \tag{C.3}$$

Integrating again:

$$T(r) = -\frac{u'''}{4\lambda_f} r^2 + C_1 \ln(r) + C_2 \tag{C.4}$$

where C_1 and C_2 are integration constants.

To avoid a singularity at $r = 0$, we set $C_1 = 0$. Applying the boundary condition $T(r) = T_w$, we obtain:

$$T(r) = T_w + \frac{u'''}{4\lambda_f}(R_i^2 - r^2) \tag{C.5}$$

where R_i [m] is the inner pipe radius.

Using the mixing cup temperature defined by Equation 2.5.17 and assuming a parabolic velocity profile such as:

$$u(r) = u_{max}\left(1 - \frac{r^2}{R_i^2}\right) \tag{C.6}$$

The fluid mean temperature can be defined as:

$$T_M = T_w + \frac{u'''}{6\lambda_f} R_i^2 \tag{C.7}$$

The heat flux at the wall ϕ is:

$$\phi = -\lambda_f \left.\frac{dT}{dr}\right|_{r=R_i} = \frac{u'''}{2} R_i \tag{C.8}$$

The heat transfer coefficient h is then defined as:

$$h = \frac{\phi}{T_M - T_w} = \frac{3\lambda_f}{R_i} \tag{C.9}$$

Finally, by definition, this led to:

$$Nu = \frac{hd_i}{\lambda_f} = \frac{3\lambda_f}{R_i}\frac{2R_i}{\lambda_f} = 6 \tag{C.10}$$

Thus, the analytical solution confirms that the Nusselt number in this thermally fully developed laminar flow with uniform internal heat generation is $Nu = 6$.

Appendix D. Calculation of the chemical entropy generation rate

To implement the entropy source terms due to chemical reactions $\dot{s}_c'''$ [W m^{-3} K^{-1}] (Equation D.1) in the CFD software, the value of the chemical potential in each computational cell is required:

$$\dot{s}_c''' = -\frac{1}{T}\sum \mu_j r_{vol,j} \qquad \text{D.1}$$

where $r_{vol,j}$ [mol m^{-3} s^{-1}] represents the rate of reaction of species j, μ_j [J mol^{-1}] its chemical potential and T [K] the temperature of the reactive mixture. For calculating this entropy generation source, it should be expressed in terms the Gibbs free energy of reaction.

First, the species creation rates can be formulated using the global reaction rate as follows:

$$r_{vol,j} = \nu_j r_{vol} \qquad \text{D.2}$$

where ν_j represents the stoichiometric coefficient of species j and r_{vol} [mol m^{-3} s^{-1}] the global reaction rate of the hydrolysis reaction considered in the work. The stoichiometric sum of chemical potential corresponds to the Gibbs free energy of reaction (Foussard et al., 2015):

$$\Delta_R G = \sum \nu_j \mu_j \qquad \text{D.3}$$

By combining Equations D.1, D.2 and D.3, the local chemical entropy generation term is obtained in a similar form than that used in the 1D approach:

$$\dot{s}_c''' = -\frac{\Delta_R G}{T} r_{vol} \qquad \text{D.4}$$

The variation of Gibbs free energy can be expressed as the sum of a standard Gibbs free energy of reaction evaluated at the mixture temperature and a contribution depending on component activities (Foussard et al., 2015) as follows:

$$\Delta_R G = \Delta_R G°(T) + R_{gaz} T \ln\left(\prod (a_j)^{\nu_j}\right) \qquad \text{D.5}$$

where $\Delta_R G°(T)$ [J mol^{-1}] is the standard Gibbs free energy of the reaction, R_{gaz} [J K^{-1} mol^{-1}] the universal ideal gas constant and a_j the activity of species j. In this study, the activities coefficients are considered equal to unity (ideal solution assumption) which leads to the activities being equal to the molar fraction of the constituents:

$$\Delta_R G = \Delta_R G°(T) + R_{gaz} T \ln\left(\prod\left(x_j\right)^{\nu_j}\right) \quad \text{D.6}$$

The standard Gibbs free energy of reaction change was calculated using Equation D.7 as follows:

$$\Delta_R G°(T) = \Delta_R h°(T) - T\Delta_R s°(T) \quad \text{D.7}$$

where $\Delta_R h°$ [J mol^{-1}] is the standard enthalpy of reaction and $\Delta_R s°$ [J mol^{-1} K^{-1}] the standard entropy of reaction. They are respectively calculated using Equation D.8 and Equation D.9 and the data presented in Table C1 as follows:

$$\Delta_R h°(T) = \Delta_R h°(298.15) + \int_{298.15}^{T}\left[\sum\left(\nu_j c_{p,j}^{o}\right)\right] dT \quad \text{D.8}$$

$$\Delta_R s°(T) = \Delta_R s°(298.15) + \int_{298.15}^{T}\left[\frac{\sum\left(\nu_j c_{p,j}^{o}\right)}{T}\right] dT \quad \text{D.9}$$

where $c_{p,j}^{o}$ [J mol^{-1} K-1] is the standard molar heat capacity at constant pressure of species *j*. The $c_{p,j}^{o}$ are estimate from the species heat capacities reported in Table 2.4.

Appendix E. Pilot sizing

A pilot unit was designed to acquire experimental data for calculating total entropy generation during chemical reactions to confirm the numerical results. It was applied to the hydrolysis of acetic anhydride as a test reaction. The setup is modular and consists of concentric cylinders of varying diameters (reactive fluid in the inner tube, utility fluid in the annular space), allowing the validation of simulated temperature and concentration profiles. Non-reactive experiments will also be performed to decouple the coupled transport phenomena. Online measurements (temperature and concentration) will enable direct comparison with numerical models. Pressure gradient measurements were abandoned, as the expected values were too low to be detected without significantly disturbing the internal flow using available intrusive instrumentation.

The pilot principle is illustrated in Figure E1.

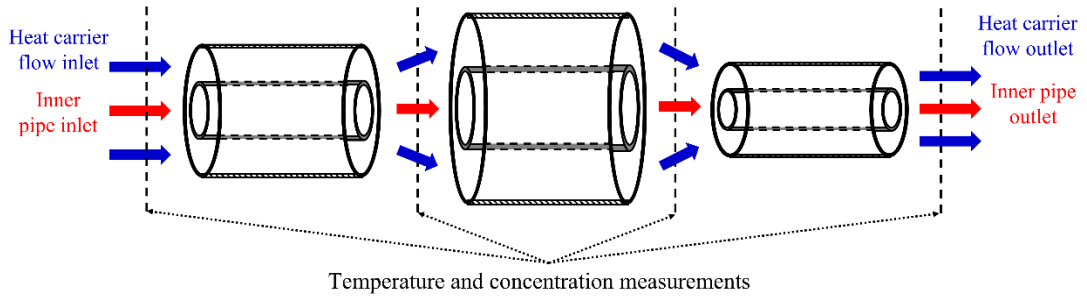

Figure E1: Pilot principle.

To study the effects of the reactor design on entropy generation, the pilot was designed to allow testing different combination of segments (straight pipe in a first approach) of different diameter in order to characterize their impact on the entropy generation rate and validate the simulation results. The quantification of the entropy generation is possible by measuring pressure, temperature and concentration values at the inlet and outlet of the reactor. Measuring temperature, pressure and concentration at the inlet and outlet of each segment will allow estimating entropy generation profiles along the HER.

It is noteworthy that the pilot was specifically sized to measure temperature and concentration gradients for the purpose of calculating entropy generation. Therefore, the design was not primarily aimed at achieving high conversion rates, but rather at producing significant gradients that could be experimentally quantified under different configurations. In practice, the observed conversions typically ranged from 10 to 25% for residence times between 30 and 360 s, depending on the diameter tested.

Although the pilot was designed and constructed during this thesis work, it could not be fully utilized due to time constraints. A 3D scheme of the designed HER is presented in Figure E2.



Figure E2: Pilot 3D view.

E.1 Pilot P&ID

The pilot Piping and Instrumentation Diagram (P&ID) of the HER carrying out the acetic anhydride hydrolysis is presented in Figure E3.

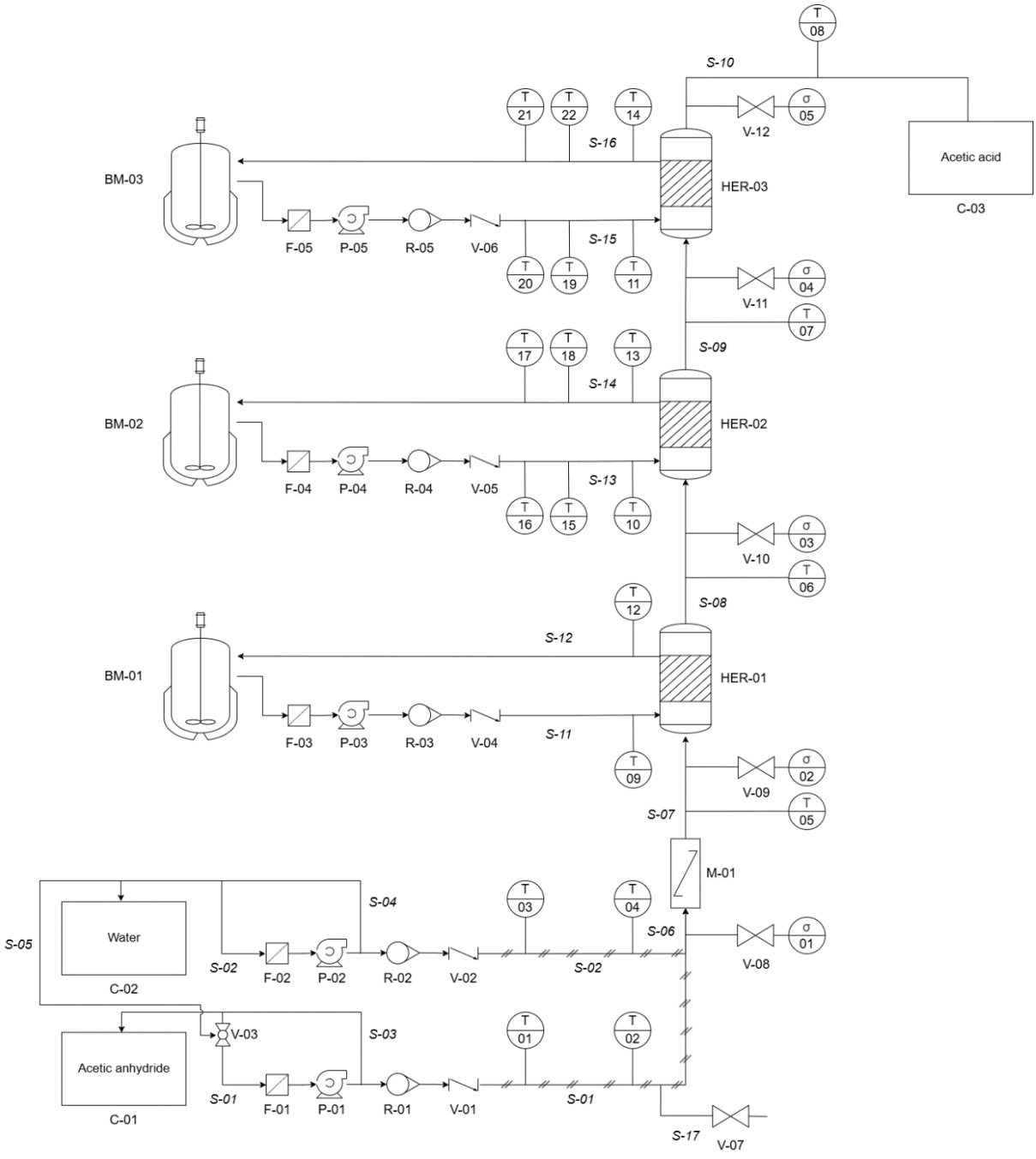

Figure E3: Pilot Piping and Instrumentation Diagram.

Feed and pre-treatment system

As illustrated in Figure E3, the pilot process begins with the delivery of two liquid reactants: acetic anhydride and water, stored in vessels C-01 and C-02, respectively. Each

reactant is pumped using independent gerotor pumps (P-01 for acetic anhydride and P-02 for water) after passing through inline filters (F-01 and F-02) to eliminate potential solid impurities. The pumped streams then pass through rotameters (R-01 and R-02) for flow rate monitoring. To prevent fluid backflow toward the feed tanks, non-return valves (V-01 and V-02) are installed downstream of the rotameters.

Preheating and inlet temperature control

Before mixing, each reactant stream is preheated using electrical heating cords wrapped around the feed lines. The heating cords are regulated by thermocouples (T-01 for S-01 and T-03 for S-02). Simultaneously, temperature probes (T-02 and T-04) are installed to measure the actual fluid temperature in each line, ensuring appropriate thermal conditions prior to reaction.

Mixing and pre-reaction monitoring

The two preheated streams, S-01 (acetic anhydride) and S-02 (water), are combined in a static mixer (M-01). It is noteworthy to point out that the heating was carried out before the mixing to guarantee that the two reactants mix well in one homogenous phase. A sampling point is installed just upstream of the mixer, accessible via valve V-08, and equipped with a conductivity sensor (σ-01). This allows for monitoring of reactant concentration at the mixer inlet.

Immediately downstream of the static mixer, a second temperature sensor (T-05) and conductivity probe (σ-02) allow quantifying the mixing effect and the concentration variation that occurred in the mixer, i.e., before entering the HER.

Recirculation and cleaning system

To enable precise flow control, recirculation loops are integrated downstream of each pump. Additionally, a cleaning loop (S-05) allows water from the S-02 line to be redirected into the acetic anhydride line (S-01) via valve V-03. This configuration enables in-place cleaning of the entire pilot unit, minimizing the risk of fouling or corrosion caused by residual acidic compounds. A dedicated purge line (S-17) and valve V-07 allow full drainage of the system when maintenance or shutdown is required.

Reaction and heat exchange modules

The partially reacted stream (S-07) then enters the first of the three heat exchanger reactors (HER-01, HER-02, and HER-03), each configured as a concentric double-pipe tubular reactor. The annular section of HER-01 is supplied with a utility fluid (S-11)—water, chosen for its safety and ease of use—pumped from a boiling water bath (BM-01) using P-03. The utility stream is filtered (F-03), monitored by a rotameter (R-03), and protected by a non-return valve (V-04) to avoid backflow to the boiler.

To evaluate entropy generation, the temperature of the utility fluid is measured both before (T-09) and after (T-12) the heat exchanger. It is noteworthy that T-09 also serves as the regulation point for controlling the heating bath BM-01. Meanwhile, the main process stream is monitored after each reactor using temperature and conductivity probes. It is important to note that the conductivity probes are not set up for on-stream measurement. Instead, a sample is drawn via a sample valve (V-08 to V-12), subsequently cooled, and then mixed before its conductivity is measured.

The same setup is replicated in HER-02 and HER-03, ensuring a progressive, thermally controlled conversion along the full reactor length. The only modification in the utility side of HER-02 and HER-03 lies in the temperature measurement system: Wheatstone bridge configurations are installed between S-13 and S-14 (using sensors T-15 to T-18) and between S-15 and S-16 (using T-19 to T-22). These Wheatstone bridges enable more accurate detection of smaller temperature differences, which become increasingly relevant in the second and third reactor stages, where heat transfer rates are lower than in the first (due to the co-current flow configuration).

Final product collection

The final product stream (S-10) is directed to collection vessel C-03, where the reaction can proceed to completion, yielding acetic acid as the final product.

The different components of the pilot and their purpose are described in Table E1.

Table E1: Description of P&ID equipment and their functions.

ID	Component Type	Description / Function
BM-01 to BM-03	Utility boilers	Supply hot water to the HERs.
C-01	Storage vessel	Contains acetic anhydride.
C-02	Storage vessel	Contains water.
C-03	Final collection vessel	Collects the final product (acetic acid).
F-01 to F-05	Inline filters	Remove solid impurities from each process stream.
HER-01 to HER-03	Heat exchanger reactors	Double-pipe concentric tubular reactors for combined reaction and heat exchange.
M-01	Static mixer	Ensures homogeneous mixing of the two reactants.
P-01 to P-02	Pumps	Deliver the reactants from vessels C-01 and C-02.
P-03 to P-05	Pumps	Circulate the utility fluid through the system.

R-01 to R-02	Rotameters	Monitor the flow rate of the reactant feeds.
R-03 to R-05	Rotameters	Monitor the flow rate of utility fluids.
σ-01 to σ-05	Conductivity sensors	Measure conductivity to estimate conversion rate.
T-01 - T-03	Temperature controllers	Regulate the power supplied to the heating cords.
T-02 - T-04	Temperature sensors	Monitor fluid temperature before mixing.
T-05 to T-08	Temperature sensors	Monitor temperature between each heat exchanger reactor (HER).
T-09 to T-11	Temperature controllers	Regulate boiler output to maintain desired utility temperature.
T-12 to T-14	Temperature sensors	Indicate utility fluid outlet temperature.
T-15 to T-21	Temperature sensors (Wheatstone bridge)	High-accuracy temperature measurements using Wheatstone bridge circuits.
V-01 to V-06	Non-return valves	Prevent backflow within the system.
V-03	Valve	Enables cleaning operations in the acetic anhydride loop.
V-07	Purge valve	Allows purging of the line.
V-08 to V-12	Sampling valves	Allow fluid sampling for conductivity analysis.
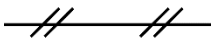	Heating cords	Electrical heaters used to preheat streams S-01 and S-02.

The pilot and its operating conditions were selected to enable the observation of axial temperature and concentration profiles in both the reactive mixture and the heat carrier. Although these conditions will likely be adjusted during the actual testing phase, they were initially chosen to match those listed in Table 2.3 and served as the reference for the pilot's design. Each configuration was simulated under these conditions and subsequently refined to ensure observable gradients in each segment, while remaining within the constraints of the equipment. Notably, concentration and temperature differences were more easily observed in the first segment, whereas the last segment posed certain challenges. This highlighted the necessity of implementing a Wheatstone bridge for accurate estimation of small temperature differences.

The sizing of the different equipment is explicated in the following section.

E.2 Sizing methodology

a. Reactors

Six reactor diameters were chosen with an internal pipe inner diameter ranging from 4 to 20 mm. Their length was fixed to 40 cm to allow the pilot fit into the laboratory hood. For each configuration, the ratio of the internal diameter of the outer tube to that of the inner tube was set to 2. This criterion was chosen for its applicability as finding configuration with fixed annular thickness was challenging with the available commercial pipes. The different configurations are summarized in Table E2.

Table E2: Dimensions of concentric double-pipe reactors (inner diameter ratio =2).

Configuration	Inner pipe (Outer diameter × thickness, mm)	Outer pipe (Outer diameter × thickness, mm)
1	6x1	10x1
2	8x1.5	12x1
3	10x1.5	16x1
4	12x1	23x1.5
5	18x1.5	33x1.5
6	23x1.5	43x1.5

The reactors were manufactured by the SERM service at the "Laboratoire Réactions et Génie des Procédés (LRGP), Nancy". The schematic representation of the reactors can be found in Figure E4.

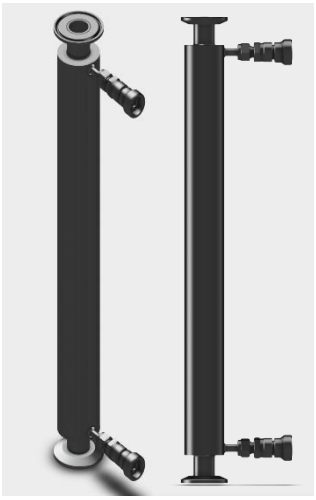

Figure E4: 3D model used to manufacture pilot reactors.

b. Flowmeters

The flowmeters were selected to fit the low operating flowrates required to obtain a laminar flow along the 3 HERs (Table E3).

Table E3: Pilot flow rates ranges.

Fluid	**Minimum flowrate (mL min^{-1})**	**Maximum flowrate (mL min^{-1})**
Acetic anhydride	4.5	25
Water (reactant)	35	200
Water (heat carrier)	50	500

The acetic anhydride will be delivered using a mini-CORI-FLOW M14V14I mass flow controller. This flowmeter, made of 316 stainless steel and equipped with Kalrez seals and an immersion probe, is chosen for his corrosion resistance as it will remain in constant contact with the acetic anhydride. It is more sensitive to temperature variations, with a maximum operating temperature of 40 °C, which aligns with the simulated case conditions.

For the water reactant, the selected device is the mini-CORI-FLOW M14 mass flow meter, capable of handling flow rates ranging from 4 to 200 mL min^{-1}.

Both flowmeters are of Coriolis type. This measurement technique relies on detecting the Coriolis force generated when a fluid flows through vibrating tubes. As the fluid passes through, the resulting mass flow induces a measurable phase shift due to the twisting of the tubes, allowing for direct and highly accurate mass flow measurement. In pumping systems, Coriolis flowmeters provide precise dosing and flow control, regardless of fluid properties such as viscosity, density, or temperature, making them ideal for demanding applications.

For the heat transfer fluid, Swagelok rotameters (VAF-G4-B2M-1-0-G) were selected, offering a flow capacity from 50 to 650 L/h. Coriolis flowmeters were not used for utility fluids, as the required precision for these streams is lower than for the reactants, making rotameters a more cost-effective choice.

c. Pumps

The gerotor mzr-4665-cy-f M2.1 pump was selected for the acetic anhydride stream. It offers a flow rate range of 0.12 to 72 mL min^{-1}, with a differential pressure capability of 0 to 5 bar depending on the fluid properties (e.g., viscosity). The operating temperature range is – 15°C to +60 °C, making it suitable for handling acetic anhydride under the conditions considered in this study.

The HNP mzr-7205 micro pump was chosen for the water reactant stream. It operates within a volumetric flow range of 0.048 to 288 mL min^{-1}, with a differential pressure range up to 40 bar, and is compatible with fluid temperatures between –5 °C and +60 °C.

For the utility fluid (heat carrier), the TCS Micropumps MGD1000S-PK-V (S-type) was selected. These pumps operate over a temperature range of 0 to 100 °C, and can deliver flow rates between 130 and 580 mL min^{-1}. These pumps are also capable of generating sufficient pressure (up to 8 bar) to overcome pressure losses downstream, particularly those introduced by the rotameter used in the heat carrier loop.

d. Utility boiler

Julabo F32-HL heating baths were available in the laboratory and used as the utility boiler. The heating baths are capable of operating within a temperature range from –35°C to 200°C, with a heating power of 2 kW. This kind of equipment allows precise temperature control of the heat carrier fluid and supports a wide operating temperature range and heating capacity, making it suitable for the thermal requirements of the pilot.

e. Static mixer

An SMX-type static mixer was selected, as this type was already available in the laboratory and adapted to the study. Several SMX variants were accessible, and the specific model chosen had a length (L) of 12.2 cm and a diameter (D) of 1.2 cm, resulting in a length-to-diameter ratio (L/D) of approximately 10.

The quality of mixing can be assessed using the coefficient of variation reduction ($\mathrm{CoV_r}$), which quantifies the degree of homogeneity. A $\mathrm{CoV_r}$ value below 0.05 is generally considered indicative of sufficient mixing. For laminar flows, $\mathrm{CoV_r}$ can be estimated using the following correlation (Paul et al., 2004):

$$\mathrm{CoV_r} = K_i^{L/D} \qquad 0.1$$

where $\mathrm{K_i}$ is a characteristic coefficient depending on the type of static mixer. For SMX mixers operating under laminar flow, $\mathrm{K_i} = 0.63$.

Applying this correlation to the selected mixer yields a $\mathrm{CoV_r}$ of approximately 7.5 10^{-3}, confirming that the chosen static mixer is adequate.

f. Conductivity captor

To monitor the reaction kinetics, conductivity measurement was selected as a practical and reliable method for tracking concentration changes between reactors, and was already used in literature (Asprey et al., 1996). The Hamilton Conducell 4UxF Arc 120 conductivity probe was chosen for this purpose.

This sensor is suitable for the expected operating conditions, with a measurement range from 1 µS cm^{-1} to 300 mS cm^{-1} and compatibility with temperatures between 25 °C and 70 °C.

To avoid interference from metal surfaces which can distort the measurements, conductivity measurements are performed externally in a refrigerated glass beaker, into which the fluid sample is transferred immediately after collection. This setup minimizes perturbations of the electric field and allows the probe to remain in optimal measurement conditions.

Indeed, as specified by the manufacturer, proper sensor operation requires a minimum clearance of 3 cm around the probe, and a spherical space with a radius of 10 mm must be kept free around the sensor tip to avoid distortions of the electric field. Implementing this configuration directly in-line would have required significant pipe enlargements between reactors, resulting in connection volumes larger than the reactors themselves for some configurations.

To overcome this issue, sampling valves were installed inline, and the conductivity measurements were carried out externally. This approach allowed the use of glass equipment and included immediate cooling at the outlet of the sampling valve to bring the sample within the optimal temperature range for measurement.

g. Heat cords

To preheat the reactants and maintain the same inlet temperature across all the studied experiments, heating cords were chosen. These cords, wrapped around the pipes, heat the fluid streams. They operate based on Joule heating principle, where electrical energy is converted into thermal energy as current flows through a resistive wire. The heat is transferred by conduction and convection from the cord to the fluid inside the tubing.

On the pilot setup, temperature regulation is achieved using thermocouples (T-01 for S-01 and T-03 for S-02) coupled with a feedback control system, ensuring the fluid reaches and maintains the desired temperature before mixing. In this study, a heating cord with a capacity of 40 W/m was selected. The required length was determined based on the maximum heating power needed to ensure that, under all operating conditions, the fluid temperature at the inlet of the static mixer reaches 25 °C. This accounts for the fact that the ambient temperature in the laboratory can drop to as low as 11 °C during winter.

h. Pressure sensors

As aforementioned, the goal of this pilot was to evaluate the total entropy generation, including viscous dissipation effects. However, preliminary studies show that in this case, given the laminar flow regime, the pressure drop in each heat exchanger segment is lower than 70 Pa (except for the narrowest tubing).

The available pressure captors were investigated (notably the one provided by the Kobold company) and it was found that the most precise captor would need at least detect a pressure loss of 70 Pa. Moreover, given that the mixture is acidic, to install this captor, a membrane of at least a dozen of centimetres is required to isolate the captor and transmit the pression value through inert fluid, which would greatly perturb the flow. These two constraints, in addition to the fact that the entropy generated by pressure drop was observed to be negligeable in preliminary studies in the case of laminar hydrolysis of acetic anhydride, lead to the choice to not implemented pressure captors in order to not invest in useless and damageable equipment for the pilot flow

Chapter 3

Entropy Generation Minimization Results for the Liquid-Phase Hydrolysis of Acetic Anhydride

Table of Contents

Chapter 3 114

Abstract 117

3.1 Introduction 118

3.2 Comparison of the results of the 1D and CFD models 119

3.2.1 Entropy generation due to viscous dissipation 123

3.2.2 Entropy generation due to heat transfer 128

3.2.3 Entropy generation due to chemical reaction and mass transfer 134

3.2.4 Results comparison 143

3.3 1D Optimisation results and discussion 145

3.3.1 Reference case 147

3.3.2 Equipartition of entropy generation and driving forces: comparison between MPCEnt and a suboptimal geometry for the reference case 153

3.3.3 Influence of the inlet mixture temperature 158

3.3.4 Influence of the inlet heat carrier temperature 163

3.3.5 Influence of the mixture mass flow rate 167

3.3.6 Influence of the heat carrier mass flow rate 171

3.3.7 Summary of the 1D optimisation main results 173

3.4 CFD optimisation 175

3.5 Conclusion 180

Nomenclature

c_p	Molar heat capacity (J mol^{-1} K^{-1})
d_i	Inner diameter of the inner tube (m)
L	HER total length (m)
M	Molecular weight (kg mol^{-1})
$\dot{m}$	Mass flow rate (kg s^{-1})
$\vec{n}$	Local unit normal vector (-)
r(without subscript)	Radial position (m)
$\dot{s}'$	Rate of entropy generation per unit length (W K^{-1} m^{-1})
$\dot{s}'''$	Volumetric entropy generation rate (W K^{-1} m^{-3})
$\bar{s}$	Specific entropy (J kg^{-1} K^{-1})
$\dot{S}$	Entropy generation rate (W K^{-1})
T	Absolute temperature (K)
$\vec{u}$	Velocity vector (m s^{-1})
u	Fluid velocity (m s^{-1})
u_z	Local axial velocity (m s^{-1})
V_{HER}	Total volume of the heat exchanger reactor (m^3)
x	Molar fraction (-)

Greek letters

ξ	Conversion (-)
ρ	Density (kg m^{-3})
Ω	Flow section area (m^2)

Subscripts

an	Refers to the fluid circulating in the annulus
anh	Refers to the acetic anhydride
ch	Refers to the chemical reaction
h	Refers to the heat transfer
i	Refers to the fluid circulating in the inner pipe
inl	Refers to the inlet of the HER
M	Refers to the mixing-cup
out	Refers to outlet of the HER
tot	Refers to the total
η	Refers to the viscous dissipation
μ	Refers to the mass transfer

Abbreviations

AI	Artificial intelligence
CFD	Computational Fluid Dynamics
EGMod	Entropy Generation Modelling
HER	Heat Exchanger Reactor
MPCEnt	Minimal Profiled Configuration Entropy generation rate
MPCVol	Minimal Profiled Configuration Volume

Abstract

Accurate quantification of entropy generation is essential for process intensification in heat exchanger reactors (HERs). In this chapter, the hydrolysis of acetic anhydride is studied using two complementary modelling approaches: a systemic 1D model, based on an ideal plug-flow model along with empirical correlations, and a CFD model, which resolves the two-dimensional velocity, temperature and concentration fields within the reactor. Entropy generation was assessed using both global and local formulations, enabling identification of the dominant irreversibility sources.

Three successive case studies allow characterizing the influence of viscous dissipation, heat transfer, and chemical reaction on entropy generation. The results confirm that chemical reaction is the predominant contribution, while viscous dissipation remains negligible under laminar liquid-phase conditions. Optimisation studies showed that entropy generation minimization often favours large-diameter tubular geometries, with only limited benefits from more complex, diameter-varying designs. This highlights that, in some cases, the additional cost of manufacturing optimised geometries may outweigh the modest thermodynamic improvements they provide.

The comparison between modelling frameworks reveals that 1D models are efficient tools for preliminary optimisation and parametric studies, whereas CFD provides a more accurate description of radial profiles and local entropy distributions, particularly important for reactive systems with significant heat generation effects.

Overall, this chapter demonstrates how combining 1D systemic models and CFD simulations offers a powerful methodology for entropy generation minimization and the design of intensified reactor systems.

3.1 Introduction

Accurate entropy generation calculation is crucial in process intensification (for both reactive and non-reactive systems). The appropriate entropy modelling approach has to be chosen by considering the modelling complexity and calculation time. This work presents, applies and compares entropy calculation approaches to a heat exchanger reactor in which the hydrolysis of acetic anhydride is carried out. Entropy generation is calculated in two different ways: local entropy generation modelling (local EGMod), allowing to link each fraction of entropy generated to its physical source and a global entropy balance to calculate the total entropy generated in the system (global EGMod). These calculation methods were applied to two process models: a systemic model, which describes the process using 1D equations that account for axial variations of pressure, temperature, and concentration, and a more precise CFD model that allows for the determination of 2D/3D fields within the HER.

The present chapter compares the discrepancies arising both from the dimensionality of the models and from the alternative formulations of entropy generation. Furthermore, it explores optimisation results based on both models, in order to assess which framework offers the best compromise between accuracy and computational efficiency for reactor optimisation.

In Section 3.2, the predictions of the two models are compared through three case studies of increasing complexity, progressively introducing viscous dissipation, heat transfer, and finally, the chemical reaction. This stepwise approach makes it possible to attribute the observed discrepancies between the models either to intrinsic differences arising from the formulation of entropy generation, or to modelling inaccuracies.

Section 3.3 focuses on an in-depth exploration of the 1D model, aiming to assess the influence of various operating conditions on the optimal designs of the HER. A multi-objective optimisation is carried out, and the resulting Pareto front highlights how the optimal geometries evolve with respect to the changing operating conditions.

Finally, Section 3.4 presents the results of the CFD-based optimisation and compares them with those obtained from the 1D optimisation, enabling a critical evaluation of the consistency and complementarity between both approaches.

3.2 Comparison of the results of the 1D and CFD models

Before presenting the results of the different shape optimisations carried out in this thesis, it is important to quantify the impact of the various modelling choices on our results, whether they stem from the entropy modelling approach (1D entropy generation calculation or 2D/3D entropy generation calculation, respectively presented in Section 1.3.1 and 1.3.2 of Chapter 1) or from the system-level modelling itself. Indeed, these differences have two distinct causes. The first is the limited precision (inherent to any correlation) in the calculation of the friction coefficient and Nusselt number used in the 1D modelling approach which leads to different axial profiles of pressure and temperature and consequently different profiles of concentration, etc. As highlighted in the previous chapter, the 1D systemic model does not provide access to radial distributions, since it relies on mass-flow-weighted values at each section (mixing-cup approach). These errors are expected to increase in the case of the reactive mixture since most of the correlations used were originally developed for inert fluids. The second source of discrepancy between the results lies in the mathematical formulation of entropy generation in the case of one-dimensional modelling. Indeed, as detailed in Chapter 2, both "1D local" and "1D global" EGMod (see Table 3.1) approaches assume that pressure, temperature and concentration are uniform in the cross-stream direction, and that their average or mixing-cup values are sufficient to evaluate entropy generation throughout the reactor.

To identify the sources of difference, six EGMod approaches were compared. The first two EGMod were applied to the 1D systemic model described in Chapter 2, Section 2.4. For this system, both the local and global (Chapter 1, Section 1.3.1) entropy generation were estimated using the 1D formulation. Two additional EGMod were tested using the 2D/3D CFD model presented in Chapter 2, Section 2.5.1. This 2D axisymmetric CFD model enables the estimation of entropy generation through both local (Chapter 1, Section 1.3.2.a) and global (Chapter 1, Section 1.3.2.b) calculations based on the 2D/3D formulation. Finally, the last two EGMod were based on the 1D reduced CFD model (Chapter 2, Section 2.5.2), which represents a 1D projection of the CFD results obtained by averaging the relevant variables (temperature, pressure, concentration, etc.) over each section. For this model, the 1D formulation of local and global entropy generation was applied.

The six EGMod approaches compared are presented in Table 3.1.

Table 3.1: Presentation of the six EGMod approaches.

EGMod approach designation	**Process model**	**Procedure for calculating the rate of entropy generation rate in the system**
1D global	Systemic model (e.g. plug flow)	Global entropy balance over the system boundaries
1D local	Systemic model (e.g. plug flow)	Integration of the local entropy generation term (obtained by considering the 1D entropy generation formulation) over the domain
CFD global	2D/3D CFD model	Global entropy balance over the system boundaries
CFD local	2D/3D CFD model	Integration of the local entropy generation term (obtained by considering the 2D entropy generation formulation) over the domain
1D reduced global	Reduced 2D/3D CFD model	Global entropy balance over the system boundaries
1D reduced local	Reduced 2D/3D CFD model	Integration of the local entropy generation term (obtained by considering the 1D entropy generation formulation) over the domain

The comparison of these six EGMod approaches allows for a precise identification of the sources of differences. Firstly, systematically comparing the local and global entropy generation calculations confirms that, when applied to the same system model, both approaches yield identical results. This validation is important for optimisation purposes, as in most cases, it is more practical to implement a simple entropy balance rather than a detailed local calculation of entropy generation.

Secondly, comparing the 1D systemic model with the detailed CFD model quantifies the impact of radial profiles of temperature, pressure, and concentration on the resulting entropy generation. The 1D systemic model relies on section-averaged values and does not account for radial distributions of these variables, which can significantly affect the entropy generation.

Thirdly, comparing the 1D reduced model with the CFD model allows the quantification of errors associated with the two formulations of entropy generation (1D versus 2D/3D). The 1D reduced model incorporates the influence of radial profiles on the final axial profiles. Since both the 2D axisymmetric and the 1D reduced CFD models share the same axial profiles, any differences in their entropy generation rates can be attributed to the mathematical formulation of the 1D entropy generation approach and its underlying assumptions.

Finally, comparing the 1D systemic model with the 1D reduced model enables the evaluation of errors arising from the correlations (e.g., Nusselt number, friction factor), which have known limitations, particularly in reactive systems. Since both EGMod approaches (1D and 2D/3D formulations) rely on the same fundamental hypotheses, the differences in entropy generation rates between the systemic model and the 1D reduced CFD data can be attributed to the assumptions of the systemic model and the limited precision of the correlations, which result in variations in pressure, temperature, and concentration values.

To compare the different entropy generation calculation methods, three case study (Table 3.2) were designed to compared systemic modelling and CFD simulation and their influence on entropy calculation. To simplify both analysis and discussion in this section, constant heat capacities were assumed for all species.

The first case, which will be referred as “first case study”, consists in injecting liquid water into the inner pipe at a uniform temperature $T_{M,i,inl}$ = 358.15 K and a uniform velocity $u_{M,i,inl}$ = 7 cm s^{-1} (subscript “i” refers to the fluid circulating in the inner pipe). In this situation, the Reynolds number of the inner pipe flow equals 700, which corresponds to a laminar flow regime since it is significantly lower than 2 300. Liquid water, used as the heat carrier fluid, is also injected into the annular space at a uniform temperature $T_{M,an,inl}$ = 358.15 K and a uniform velocity $u_{M,an,inl}$ = 7 cm s^{-1} (subscripts “an” and “inl” respectively refer to the fluid circulating in the annular space and to the variables at the inlet of the HER, i.e., at z = 0). The flow Reynolds number in the annular section is about 1 400, which corresponds to a laminar flow regime as it is significantly lower than 2 900, the approximate value above which transitional regime occurs in such annulus (Foster, 1965). This first case study aims to focus on entropy generation by viscous dissipation which will be the main source of irreversibility. Indeed, since the two fluids enter at the same temperature (358.15 K), the heat transfer will be negligible and only due to viscous heating.

The second case, which will be referred as “second case study”, corresponds to a classical co-current tubular heat exchanger (i.e., without chemical reaction). Its operating conditions are similar to those of the first case study, except that water is injected in the internal pipe at a lower temperature, $T_{M,i,inl}$ = 298.15 K. Since the two fluids streams are introduced at significantly different temperatures, heat transfer will be meaningful and should be the primary source of entropy generation.

The third case, which will be referred as “third case study”, corresponds to a HER, i.e., chemical reactor with heat exchange (the reaction occulting in the inner pipe flow). Its operating conditions are similar to those in the second case study except that an aqueous liquid mixture of acetic anhydride is injected in the inner pipe instead of water.

This third case is the most general situation investigated in this thesis since it involves all the entropy generation sources, namely chemical reaction and mass transfer (which were not considered in the two previous case studies), as well as heat transfer and viscous dissipation.

Table 3.2: Summary of the operating conditions considered for each case study.

Parameter	Symbol	Case 1	Case 2	Case 3
Fluid circulated in the inner pipe	/	Water	Water	Reactive mixture
Inlet mole fraction of anhydride acetic in the inner pipe fluid	$x_{anh,inl}$	/	/	0.023
Inlet temperature of the inner pipe fluid (K)	$T_{M,i,inl}$	358.15	298.15	298.15
Inlet temperature of the heat carrier fluid (K)	$T_{M,an,inl}$	358.15	358.15	358.15
Inlet velocity of the inner pipe fluid (m s^{-1})	$u_{M,i,inl}$	0.07	0.07	0.07
Inlet velocity of the heat carrier fluid (m s^{-1})	$u_{M,an,inl}$	0.07	0.07	0.07

3.2.1 Entropy generation due to viscous dissipation

a. Entropy generation due to viscous dissipation

As indicated previously, the first case study (Table 3.2) simply corresponds to a fluid transport system where the two flows are introduced at identical temperatures. In such situation, entropy generation is mainly due to viscous dissipation of mechanical energy which results in a pressure drop. However, the degradation of mechanical energy into heat (viscous heating) leads to a local increase in temperature, which however remains negligible in most industrial applications. In any case, viscous heating results in temperature gradients and thus, in heat transfer phenomena, which constitute a secondary source of entropy generation. As discussed later in this section, although heat transfer contribution remains negligible, global EGMod approaches require an accurate assessment of this infinitesimal heating to be able to determine the rate of total entropy generation in the system.

Figure 3.1 illustrates the CFD-calculated contour plot of gauge pressure on a midplane of the system. The grey areas correspond to the central wall. It should be noted that, given the axisymmetric assumption, the CFD solution is computed only over the system radius. However, for clarity, the contour plots are displayed across the entire midplane (using a mirror plane). Additionally, given the elongated shape of the system (3.2 cm outer diameter and 6 m long), in Figure 3.1 as well as in all the contour plots reported in the rest of this section, different scales are used in the axial and radial directions to enable clear display of the flow variables fields.

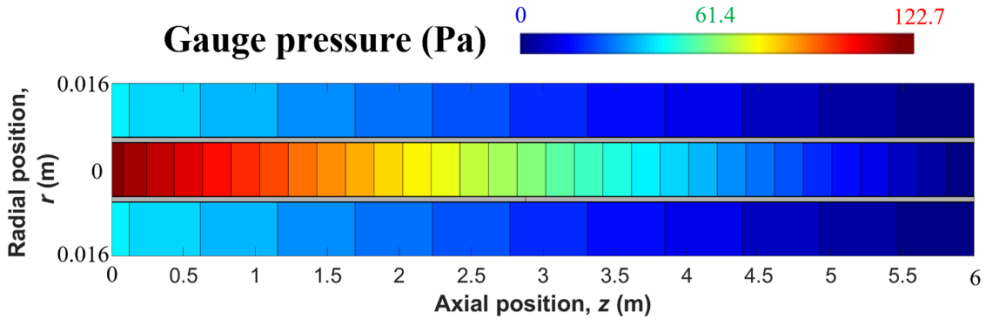

Figure 3.1: Case study 1: CFD contour plot of the gauge pressure (flow direction from left to right, as illustrated in Figure 2.1 of Chapter 2).

Figure 3.1 shows that for both flows, pressure is almost uniform over the cross sections as expected for axial parallel flows. Pressure drop (i.e., the rate of pressure decrease per unit length) is greater in the entrance regions where higher wall friction occurs (resulting in local head losses in addition to the regular head losses) and becomes uniform once the flow fully develops.

Thereafter, CFD results are 1D reduced (Chapter 2, Section 2.5.2) and compared to the systemic process model predictions in Figure 3.2. As already displayed in Figure 3.1, pressure

drop is the highest at the inlet and decreases until becoming uniform once the flow fully develops. Figure 3.2 reveals an excellent agreement between the systemic model predictions and CFD, although the friction factor correlations appear to slightly overestimate the pressure drop at the entrance zones, in particular for the inner pipe flow.

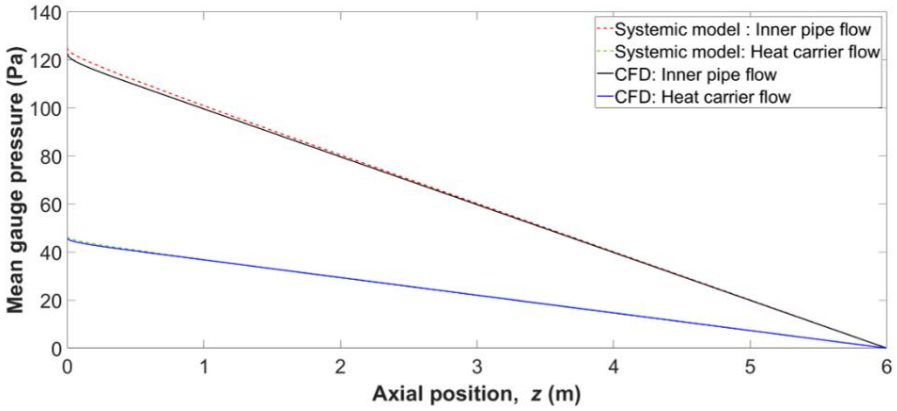

Figure 3.2: Case study 1: comparison of the axial profiles of gauge pressure between the systemic process model and CFD. Note that for the inner pipe flow, the results of the two models are practically similar and are therefore difficult to differentiate visually.

Figure 3.3 illustrates the CFD-calculated (CFD local EGMod approach) contour plot of $\dot{s}_{\eta}'''$, the local entropy generation rate by viscous dissipation. Entropy generation is extremely large near the walls at the inlets where velocity abruptly decreases from 0.07 m s^{-1} (velocity value imposed at the inlets, Table 3.2) to 0 because of no-slip condition at the wall. Therefore, to enable differentiating the entropy generation degrees across the domain, a logarithmic scale is used for the contour levels. Figure 3.3 shows that entropy generation is the highest in the near wall zones, especially in the developing hydrodynamic boundary layers at the entrances, where high velocity gradients predominate. Therefore, a fine CFD mesh is required in these areas to properly capture the entropy generation rates. In contrast, mechanical energy dissipation is the lowest at the pipe axis and in the "inviscid cores" at the entrances (i.e., fluid zones outside the developing boundary layers) where viscous stresses are low, or even zero.

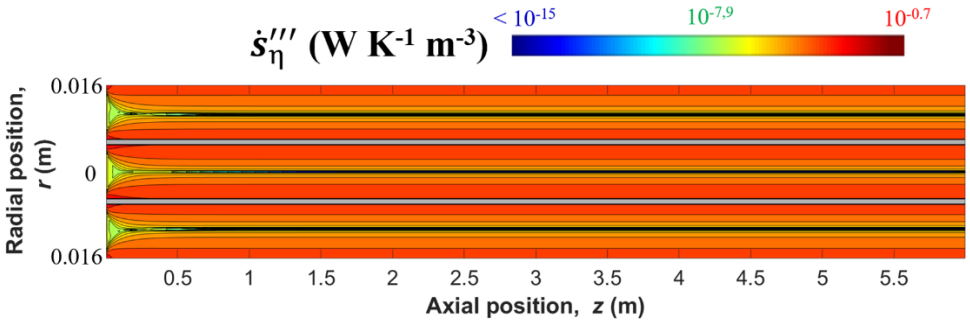

Figure 3.3: Case study 1: CFD contour plots of $\dot{s}_{\eta}'''$, the local entropy generation rate by viscous dissipation. Note that a logarithmic scale is used for the colorbar.

To allow comparison with 1D approaches, the mechanical entropy generation per unit length, $\dot{s}'_\eta$ [W K^{-1} m^{-1}], is determined by integrating $\dot{s}'''_\eta$ [W K^{-1} m^{-3}], the volumetric source term, on each cross-section and the results are shown in Figure 3.4. All three approaches agree that, consistent with Figure 3.1 and Figure 3.2, mechanical entropy generation is highest at the entrance of the system, where high velocity gradients occur, and gradually decreases to become uniform once the flow is fully developed. Note that, since the local entropy rates at the entrance are extremely high, for clarity purposes, the first 1 mm of the system has not been represented in Figure 3.4 (i.e., the minimum axial position is $z = 1$ mm and not zero).

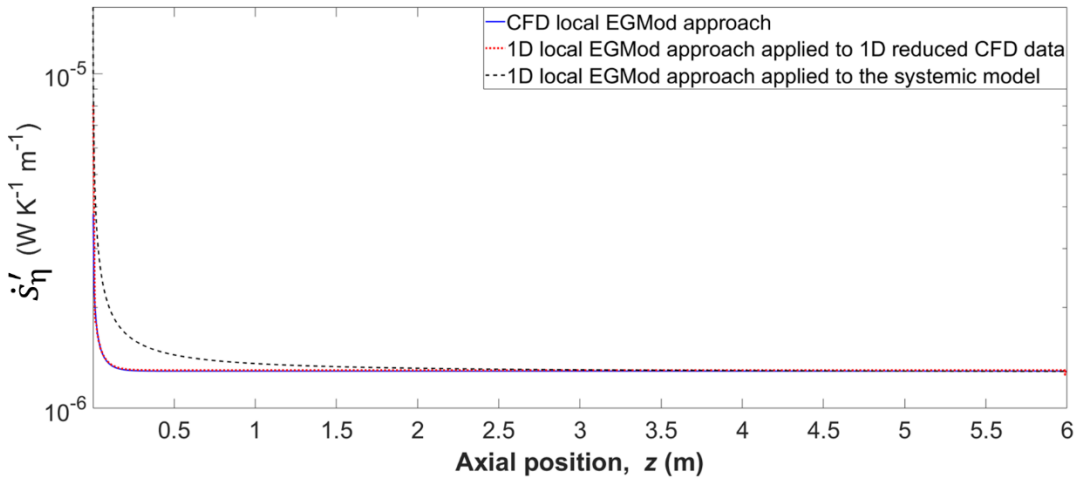

Figure 3.4: Case study 1, local rate of entropy generation by viscous dissipation: comparison between the "CFD local" EGMod approach (continuous blue curve) and the "1D local" EGMod approach applied to the 1D systemic model (dashed black curve) and to the 1D reduced CFD data (dotted red curve).

As discussed earlier, differences between the "1D local" EGMod approach applied to the 1D reduced CFD data and the "CFD local" EGMod approach are due to the formulation of the 1D EGMod of entropy terms and to its underlying assumption of uniform pressure in the transverse direction. Figure 3.4 shows that for mechanical entropy generation, both methods are in excellent agreement and exhibit practically identical results. Indeed, as shown in Figure 3.1, pressure is indeed uniform over the cross sections. Therefore, under such conditions, Equation 1.3.2 is perfectly valid and leads to results as accurate as those provided by Equation 1.3.11. The theoretical validity of Equation 1.3.11 is supposed to hold whenever the pressure field is uniform in the transverse direction, which is generally the case in developed parallel flows.

Comparison between the mechanical entropy generation rate predicted by the "1D local" EGMod applied to the 1D reduced CFD data (dotted red curve in Figure 3.4) and to the systemic process model (dashed black curve) reveals that, except in the entrance zone, the two methodologies are in very good agreement (with a maximal deviation less than 0.1%). At the entrance region however, the systemic model overpredicts the rate of local entropy generation

by viscous dissipation. The differences between the results of these two methodologies are due to the inherent imprecisions of the systemic model, particularly the limited accuracy of the friction coefficient correlations) which slightly overestimates the mechanical energy dissipation in the developing flow zone as already revealed by Figure 3.2.

As noted previously, in this first case study, although the two flows are injected at the same temperature, mechanical energy dissipation into heat by viscous forces (viscous heating) gives rise to some temperature gradients and therefore to heat transfer which constitutes here a secondary source of entropy generation.

In this first case study for example, the mixing-cup temperature of the inner flow increases of about 2.06×10^{-5} K between the inlet and outlet according to CFD simulations, while the systemic model predicts a temperature increase of about 2.38×10^{-5} K. For the heat carrier flow, CFD simulations and the 1D model predict an increase of mixing-temperature of about 1.16×10^{-5} K and 1.19×10^{-5} K respectively. The systemic model overpredicts the temperature elevation due to the limited accuracy of the friction coefficient correlations which, as noted previously, slightly overestimate the pressure drop.

The temperature variations induced by viscous heating are negligible as it could have been expected theoretically. However, the calculation of this infinitesimal heating is necessary to be able to determine the entropy generation using a global approach. Indeed, both CFD and 1D global EGMod approaches calculate the entropy generation rate in the system as the difference between the inlet and outlet entropy fluxes. However, for pure incompressible fluids as it is the case here, the specific entropy is independent of pressure and varies only with temperature. As a result, both global EGMod approaches would assume zero entropy generation in isothermal flows, regardless of the occurrence of pressure losses. Therefore, consideration of viscous heating, although its effects on temperature variation are generally minor, is necessary for global EGMod approaches to be able to determine mechanical entropy generation in incompressible flows.

b. Total entropy generation

The total rates of entropy generation predicted by the different EGMod approaches are summarized in Table 3.3. Unlike the global methodology, local EGMod methods allow quantifying the contribution of each source of irreversibility and reveal that heat transfer contribution to entropy generation is several orders of magnitude lower than that of mechanical energy dissipation by viscous stresses. Therefore, although the predicted rate of entropy generation by heat transfer has significant differences depending on the process model used, the sources of these differences will not be discussed further here. They will be discussed in details in Section 3.2.2 which deals with the second case study, i.e., the heat exchanger, where heat transfer constitutes the main source of entropy generation.

Table 3.3 shows that, for a same process model, the local and global EGMod approaches lead to similar entropy generation rates, with relative differences less than 1%, as might be expected theoretically. In the case of the CFD model, a sufficiently fine near-wall mesh was nonetheless required for accurate estimation of the entropy source terms in these zones where intense velocity gradients prevail, and thus, for accurate evaluation of entropy generation using the local EGMod approach.

Finally, given that mechanical entropy generation is the main source of irreversibility in this first case study and that this term is correctly evaluated by all three process models (Figure 3.4), the total rate of entropy generation predicted by the different EGMod approaches (Table 3.3) are quite similar. However, as already shown in Figure 3.1, due to the limited precision of the friction coefficient correlations, the 1D systemic model slightly overestimates the pressure drop in the developing flow region and thus, predicts a slightly higher rate of entropy generation than CFD-based approaches.

Table 3.3: Case study 1: comparison of the total entropy generation rate predicted by the different EGMod approaches.

EGMod approach	**Total generated entropy, $\dot{S}_{tot}$ (W K^{-1})**	**Relative difference between global and local EGMod approaches applied to a same process model (%)**
"CFD local" approach	$\dot{S}_{tot}$ = 7.815 10^{-6} W K^{-1} ➢ $\dot{S}_{\eta}$ = 7.815 10^{-6} W K^{-1} ➢ $\dot{S}_{h}$ = 7.800 10^{-14} W K^{-1}	0.55%
"CFD global" approach	$\dot{S}_{tot}$ = 7.858 10^{-6} W K^{-1}	
"1D local" approach applied to the systemic model	$\dot{S}_{tot}$ = 8.203 10^{-6} W K^{-1} ➢ $\dot{S}_{\eta}$ = 8.203 10^{-6} W K^{-1} ➢ $\dot{S}_{h}$ = 9.293 10^{-15} W K^{-1}	0.049%
"1D global" approach applied to the systemic model	$\dot{S}_{tot}$ = 8.207 10^{-6} W K^{-1}	
"1D local" approach applied to the 1D reduced CFD data	$\dot{S}_{tot}$ = 7.865 10^{-6} W K^{-1} ➢ $\dot{S}_{\eta}$ = 7.865 10^{-6} W K^{-1} ➢ $\dot{S}_{h}$ = 9.095 10^{-15} W K^{-1}	0.013%
"1D global" approach applied to the 1D reduced CFD data	$\dot{S}_{tot}$ = 7.864 10^{-6} W K^{-1}	

3.2.2 Entropy generation due to heat transfer

a. Entropy generation due to heat transfer

The second case study (Table 3.2) corresponds to a co-current double pipe heat exchanger operating under laminar flow conditions. Entropy is generated in the system by viscous dissipation of mechanical energy and heat transfer. Therefore, the remainder of this section will focus primarily on entropy generation through heat transfer. Mechanical energy dissipation effects are identical to those occurring in the first case study (and discussed in Section 3.2.1) and thus, will not be addressed in detail.

Figure 3.5 illustrates the CFD-calculated contour plot of temperature on a midplane of the heat exchanger. Under laminar flow conditions, radial transport of heat is carried out by thermal conduction only, which leads to significant temperature heterogeneities along the radial direction. However, axial heat transfer occurs primarily through advection, as the fluid motion along the tube transports energy in the flow direction (high thermal Péclet). Figure 3.5 shows that the inner pipe flow becomes thermally developed at 1 to 1.5 m from the inlet where the thermal boundary layer fills the entire flow area, while the annular flow remains thermally developing over the entire heat exchanger length.

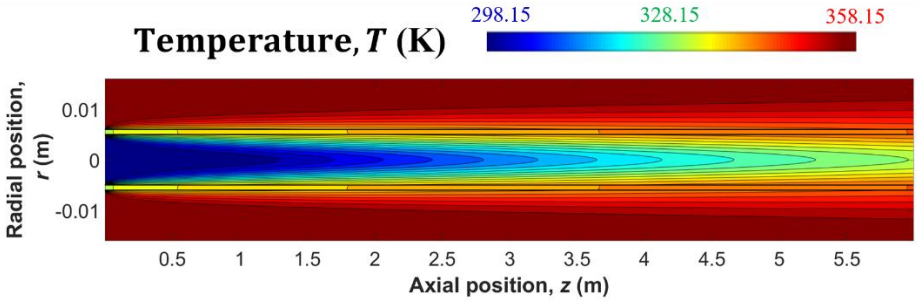

Figure 3.5: Case study 2: CFD contour plot of temperature on a midplane of the heat exchanger.

CFD results are 1D reduced and compared to the systemic process model predictions in Figure 3.6. Going downstream, the temperature difference between the two streams continuously decreases as the heat carrier fluid cools and the inner pipe flow heats up. Axial variations of temperature are greater in the inner pipe stream because its mass flow rate is higher. Although the temperature field exhibits significant non-uniformity in the radial direction (Figure 3.5), Figure 3.6 reveals excellent agreement between the systemic model predictions and CFD, proving the relevance of the mixing-cup averaging for calculating the representative temperature value at each cross-section. As could be expected, some minor differences are observed between the results, particularly for the inner pipe flow, and are due to the limited precision of the Nusselt number correlations for a thermally developing laminar flow which appear to slightly underestimate the heat transfer rates.

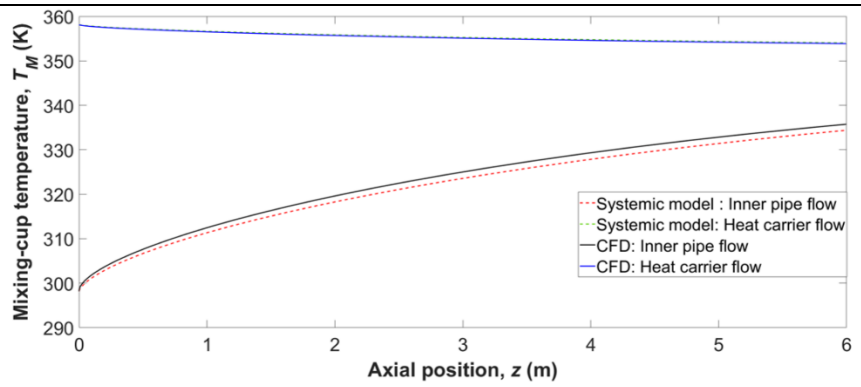

Figure 3.6: Case study 2: comparison of the axial profiles of mixing-cup temperature between the systemic process model and CFD. Note that for the inner pipe flow, the results of the two models are practically similar and are therefore difficult to differentiate visually.

Figure 3.7 illustrates the CFD-calculated (CFD local EGMod approach) contour plot of $\dot{s}_h'''$ (determined using Equation 1.3.13), the local rate of entropy generation by heat transfer. It is noteworthy that entropy generation by heat transfer occurs in the two fluid streams as well as in in the central wall. Entropy generation is extremely important near the central wall at the inlets where temperature gradients are maximum. Therefore, to enable differentiating the entropy generation degrees across the domain, a logarithmic scale is used for the contour levels. Figure 3.7 shows that entropy generation is the highest alongside the central wall, especially in the developing thermal boundary layers at the entrances, where high temperature gradients predominate. Therefore, a fine CFD mesh is required in these areas to properly capture the entropy generation rates. Going downstream, since the heat exchanger is operated co-currently, the temperature difference between the two flows decreases leading to lower temperature gradients and therefore reduced entropy generation.

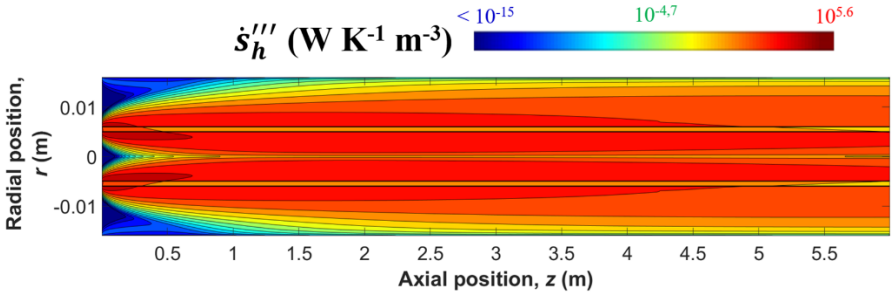

Figure 3.7: Case study 2: CFD contour plots of $\dot{s}_h'''$, the local entropy generation rate through heat transfer. Note that a logarithmic scale is used for the colorbar.

To allow comparison with 1D approaches, the thermal entropy generation rate per unit length, $\dot{s}_h'$ [W K^{-1} m^{-1}], is determined by integrating $\dot{s}_h'''$ [W K^{-1} m^{-3}], the volumetric source term, on each cross-section and the results are shown in Figure 3.8. Note that, since the local entropy rates at the entrance are extremely high, for clarity purposes, the first 1 mm of the heat exchanger has not been represented (i.e., the minimum axial position is $z = 1$ mm and not zero). All three approaches reveal high entropy generation rates in the entrance zone which

rapidly decrease, up to several orders of magnitude, when going downstream. This rapid decrease is due to two factors. The first is that the convective heat transfer coefficients rapidly decrease along the developing thermal boundary layers (before reaching asymptotic values in the thermally developed flows), which reduces the heat flux density between the two streams, and thus, the rate of entropy generation along the thermal boundary layers. The second factor is that, given the co-current operation of the heat exchanger, temperature difference between the two flows decreases in the axial direction, which contributes to the rapid decline of the local heat flux density in the entrance region and leads to a continuous decrease of entropy generation in the thermally developed zone.

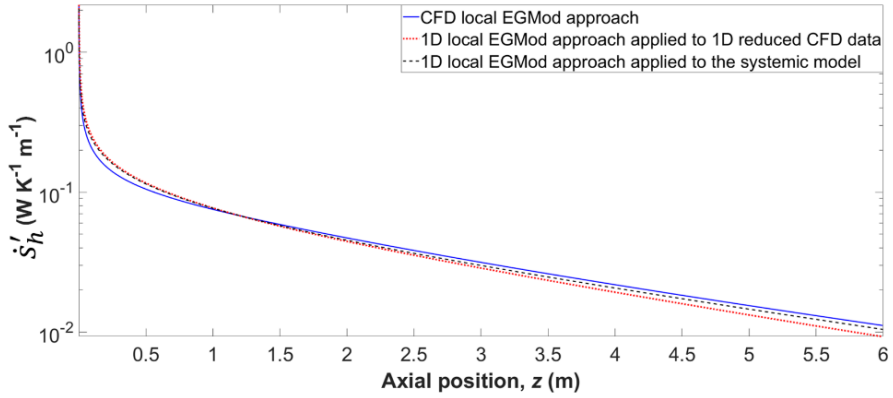

Figure 3.8: Case study 2, local rate of entropy generation by heat transfer: comparison between the "CFD local" EGMod approach (continuous blue curve) and the "1D local" EGMod approach applied to the 1D systemic model (dashed black curve) and to the 1D reduced CFD (dotted red curve).

As discussed earlier, differences between the results provided by the 1D EGMod approach when applied to the 1D reduced CFD data (dotted red curve in Figure 3.8) or the systemic process model (dashed black curve) are due to the limited accuracy of the Nusselt number correlations. Indeed, both methodologies rely on the same assumption that, at each axial position, thermal entropy generation can be determined using a single representative temperature value for each fluid, namely the mass flow rate weighted mixing-cup temperature. Therefore, the difference between their results is only due to the limited accuracy of the Nusselt numbers correlations used in the systemic model that leads to different heat flux densities and temperature profiles (Figure 3.6). In any case, the precision of these correlations reveals to be sufficient since a very good agreement is obtained in the temperature profiles (Figure 3.6), and therefore, in the predicted entropy generation rates (Figure 3.8).

In addition, CFD simulations and the 1D reduced data obviously share the same axial profiles of mixing-cup temperatures, local heat flux, etc. Therefore, the differences between the entropy generation rates they predict (Figure 3.8) are solely due to the formulation of the 1D EGMod approach which assumes that the mixing-cup temperature values, alone, allow determining entropy generation, whatever the radial inhomogeneities of temperatures. However, from a theoretical point of view, this assumption is incorrect unless temperature is

radially uniform (which implies the absence of heat transfer phenomena) and leads to an inevitable error in the calculation of the entropy generation rate.

b. Impact of radial temperature variations on 1D EGMod

To illustrate the theoretical limits of the one-dimensional EGMod approaches, a following demonstration will focus on the global methodology of entropy generation calculation to highlight that 1D models inherently misestimate thermal entropy generation because they evaluate specific entropy at section-averaged (mixing-cup) temperatures, whereas CFD approaches account for radial temperature variations, capturing the exact distribution of entropy fluxes and therefore the impact of non-uniform temperature fields on entropy generation. It should be recalled that global and local methodologies lead to the same results given the divergence theorem (i.e., Ostogradsky's theorem). When a 1D process model is used, enthalpy balances are solved in each fluid phase and allow obtaining the local mixing-cup temperatures which constitute the only information available on the temperature field. Therefore, to solve the entropy balance reported in Equation 1.3.7 (where the heat transfer through the exterior wall is not considered, given our adiabatic reactor), the specific entropies are evaluated at the mixing-cup temperatures at the inlets and outlets. In the case of a pure and incompressible fluid with constant thermophysical properties, combining Equations 1.3.7 and 1.3.8, the entropy balance employed in the 1D approach becomes:

$$\begin{aligned}\dot{S}_{tot} &= \dot{m}_i\left[\bar{s}_{i,out} - \bar{s}_{i,inl}\right] + \dot{m}_{an}\left[\bar{s}_{an,out} - \bar{s}_{an,inl}\right] \\ &= \dot{m}_i\left[\bar{s}\left(T_{M,i,out}\right) - \bar{s}\left(T_{M,i,inl}\right)\right] + \dot{m}_{an}\left[\bar{s}\left(T_{M,an,out}\right) - \bar{s}\left(T_{M,an,inl}\right)\right] \\ &= \dot{m}_i \frac{c_{p,i}}{M_i}\left[\frac{1}{T_{M,i,out}} - \frac{1}{T_{M,i,inl}}\right] + \dot{m}_{an} \frac{c_{p,an}}{M_{an}}\left[\frac{1}{T_{M,an,out}} - \frac{1}{T_{M,an,inl}}\right]\end{aligned} \qquad 3.2.1$$

Furthermore, when CFD is used to model the process, the complete temperature and velocity fields are simulated, i.e., radial profiles of temperature and velocity are obtained over the entire numerical domain. Therefore, the "CFD global" EGMod approach makes use of these detailed profiles for precise determination of the entropy fluxes at the inlets and outlets. Thus, combining Equations 1.3.8 and 1.3.18, the entropy balance used in the "CFD global" EGMod approach becomes:

$$\begin{aligned}\dot{S}_{tot} &= 2\pi \int_{out} \rho\, \vec{\boldsymbol{u}}.\vec{\boldsymbol{n}}\, \bar{s}\, r\, dr + 2\pi \int_{inlets} \rho\, \vec{\boldsymbol{u}}.\vec{\boldsymbol{n}}\, \bar{s}\, r\, dr \\ &= \int_{outlets} \rho\, u_z\, \bar{s}\, r\, d\Omega - \int_{inlets} \rho\, u_z\, \bar{s}\, d\Omega \\ &= \rho_i \frac{c_{p,i}}{M_i}\left[\int_{out,i} \frac{u_z}{T}\, d\Omega - \int_{inl,i} \frac{u_z}{T}\, d\Omega\right] \\ &\quad + \rho_{an} \frac{c_{p,an}}{M_{an}}\left[\int_{out,an} \frac{u_z}{T}\, d\Omega - \int_{inl,an} \frac{u_z}{T}\, d\Omega\right]\end{aligned} \qquad 3.2.2$$

Equation 3.2.1, which represents the entropy balance in 1D EGMod approaches, and Equation 3.2.2, which represents the entropy balance in CFD EGMod approaches, lead to different values of entropy generation rates unless temperature is radially uniform (since T, being constant over each flow section, can be moved out of the integrals) which is rarely the case at the outlet of heat exchangers. In other terms, 1D EGMod approaches evaluate the specific entropy at the mass flow weighted average temperature (i.e., the mixing-cup temperature), while CFD approaches allow determining the exact mass flow weighted average value of specific entropy. Therefore, 1D approaches lead to unavoidable errors in the calculation of the generation rate of thermal entropy.

The results provided in this section prove that 1D approaches inherently lead to two sources of errors. The first concern inaccuracies in the prediction of the axial temperature profiles and is mainly due to the limited precision of Nusselt number correlations. The second source concerns the method used to calculate entropy generation: in 1D models, the specific entropy at each position is evaluated using mixing-cup temperature only. This simplification neglects radial temperature variations, which can be significant in regions with strong thermal gradients, such as near the walls or in laminar flows with limited radial mixing. As a result, the estimated entropy generation may deviate from the true value, since local contributions from hotter or cooler zones within the section are not fully captured. Nonetheless, these errors may remain acceptable as shown in Figure 3.8, which explains the widespread use of 1D approaches given their computational efficiency.

c. Total entropy generation

Finally, Table 3.4 summarizes the results obtained using the different EGMod approaches in the second case study. Local approaches reveal that entropy generation is mainly due to heat transfer whose contribution is several orders of magnitudes higher than that of mechanical energy dissipation. Given that the two streams are introduced at significantly different temperatures, high heat transfer rates occur leading to a large contribution to entropy generation. For a same process model, the local and global EGMod approaches lead to similar entropy generation rates, with relative differences less than about 1%, as might be expected theoretically. Despite the simplifications inherent to 1D modelling that have been discussed previously, the results obtained using different process models are also in good agreement with only slight differences. However, these differences can be expected to become larger in the case of a more complex flow where the available correlations would be less precise and where the temperature field would exhibit higher radial gradients.

Table 3.4: Case study 2: comparison of the total entropy generation rate predicted by the different EGMod approaches.

EGMod approach	**Total generated entropy, $\dot{S}_{tot}$ (W K^{-1})**	**Relative difference between global and local EGMod approaches applied to a same process model (%)**
"CFD local" approach	$\dot{S}_{tot}$ = 2.890 10^{-1} W K^{-1} ➢ $\dot{S}_h$ = 2.890 10^{-1} W K^{-1} ➢ $\dot{S}_\eta$ = 8.039 10^{-6} W K^{-1}	0.77%
"CFD global" approach	$\dot{S}_{tot}$ = 2.868 10^{-1} W K^{-1}	
"1D local" approach applied to the systemic model	$\dot{S}_{tot}$ = 2.959 10^{-1} W K^{-1} ➢ $\dot{S}_h$ = 2.959 10^{-1} W K^{-1} ➢ $\dot{S}_\eta$ = 8.470 10^{-6} W K^{-1}	0.24%
"1D global" approach applied to the systemic model	$\dot{S}_{tot}$ = 2.966 10^{-1} W K^{-1}	
"1D local" approach applied to the 1D reduced CFD data	$\dot{S}_{tot}$ = 2.990 10^{-1} W K^{-1} ➢ $\dot{S}_h$ = 2.990 10^{-1} W K^{-1} ➢ $\dot{S}_\eta$= 8.115 10^{-6} W K^{-1}	0.37%
"1D global" approach applied to the 1D reduced CFD data	$\dot{S}_{tot}$ = 2.979 10^{-1} W K^{-1}	

3.2.3 Entropy generation due to chemical reaction and mass transfer

The third case study (Table 3.2) corresponds to a co-current HER where the reactive mixture is fed into the inner pipe and the utility fluid (water) in the annular zone. Both flows are laminar and are introduced in the system at significantly different temperatures leading to high heat transfer rates. The reactive mixture is considered to be ideal. Its inlet composition is close to the saturation point and consists of 97.7 mol% of water and 2.3 mol% of acetic anhydride. Entropy is generated in the HER by viscous dissipation, heat transfer, chemical reaction and mass transfer. These different contributions will be evaluated and compared, and as shown later in this section, the chemical reaction constitutes the main source of entropy in this third case study.

a. Entropy generation due to viscous dissipation

Concerning viscous dissipation, its effects are identical to those occurring in the previous case studies (and discussed in details in Section 3.2.1), and both the systemic model and the CFD simulations lead to similar predictions of the mechanical entropy generation rate (as detailed later in Table 3.5). However, it is noteworthy that, as the molar volume generally varies in the presence of a chemical reaction, reacting mixtures undergo volumetric expansion/contraction, that is, an increase/decrease of the volume flow rate along the reactor. For example, with the reaction considered in this study, as the acetic anhydride is hydrolysed into acetic acid, the mixture density decreases and leads to an increase of the volume flow rate. Friction coefficient correlations available in the literature are generally developed for flows with constant and uniform density. Therefore, they may lead to significant errors when applied to reacting mixtures involving significant volumetric expansion/contraction, limiting the accuracy of 1D modelling approaches compared to CFD. In this third case study, the reactive solution being diluted, volumetric expansion effects remain negligible and the 1D systemic model correctly captures the pressure drops along the reactor (which are very similar to those encountered in the first case study and shown in Figure 3.2). However, it should be emphasized that 1D modelling may lead to significant errors in the case of concentrated and/or gaseous mixtures where variations in the volume flow rate can become significant.

b. Entropy generation due to heat transfer

Concerning the temperature field, the results in this third case study are generally similar to those observed in the second case study (illustrated in Figure 3.5). Both the systemic model and the CFD simulations predict comparable trends in the axial profiles of mixing-cup temperatures, although the presence of a chemical reaction in the third case leads to moderately higher temperatures compared to the second case.

Indeed, the reactive mixture being diluted and the reaction enthalpy of acetic anhydride hydrolysis being moderate, the heat released by the exothermic reaction is significantly lower

than that transferred by the heat carrier fluid to the reactive mixture. Indeed, at the inlet temperature of the reactive mixture, the adiabatic temperature rise of the reaction is 12 K, corresponding to the temperature increase that would occur if the reaction proceeded under perfectly adiabatic conditions, without any heat loss to the surroundings. Therefore, reaction effects on the temperature field are negligible, and compared to the second case study, the accuracy of the systemic model is nearly unchanged. As detailed later in Table 3.5, the entropy generation rates predicted by the 1D and CFD EGMod approaches exhibit some slight differences, which are mainly due to the causes that have been already discussed. However, it should be emphasized that in the case of a concentrated solution and/or a high enthalpy of reaction, the chemical reaction, especially if it is fast, can significantly affect the temperature field and alter the accuracy of 1D modelling approaches. Indeed, the Nusselt number correlations (presented in Chapter 2) available in the literature are generally developed for inert flows in the absence of volumetric heat generation phenomena such as viscous heating or heat released by an exothermic reaction, etc. Therefore, if any of these effects is significant, Nusselt correlations are expected to lead to significant errors and reduce the accuracy of 1D modelling approaches compared to CFD.

The remainder of this section will mainly focus on entropy generation by chemical reaction and mass transfer, the two source terms that have not been encountered in the previous case studies.

c. Entropy generation due to chemical reaction

Figure 3.9a illustrates the CFD-calculated contour plot of the reaction rate on a midplane of the inner pipe. It should be noted that, compared to the previous contour plots (Figure 3.1 and Figure 3.5 for example), only the inner pipe zone is displayed in Figure 3.9, since no reaction occurs in the heat carrier fluid or in the central wall. Figure 3.9a shows that, at the inlet, the hydrolysis reaction mainly takes place near the wall where the mixture temperature is the highest (as already shown in Figure 3.5 for the second case study). Thus, acetic anhydride is rapidly consumed in this zone leading to a significant decrease of its local concentration as shown in Figure 3.9b. Going downstream, the reactive mixture temperature increases due to heating by the heat carrier fluid (in addition to the exothermicity of the hydrolysis reaction), an effect which accelerates the reaction rate. However, because of the poor mixing in laminar flows and the low mass diffusivity of liquid mixtures, the rate of reaction is higher than the rate of reactants transport, leading to a depletion of acetic anhydride in the near wall zone (Figure 3.9b). Therefore, as could be seen from Figure 3.9a, going downstream, the position at which the reaction rate is the highest gradually shifts from the near wall zone towards the pipe centre.

(a)

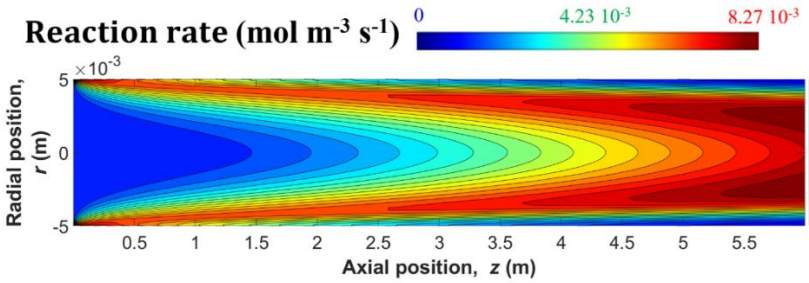

(b)

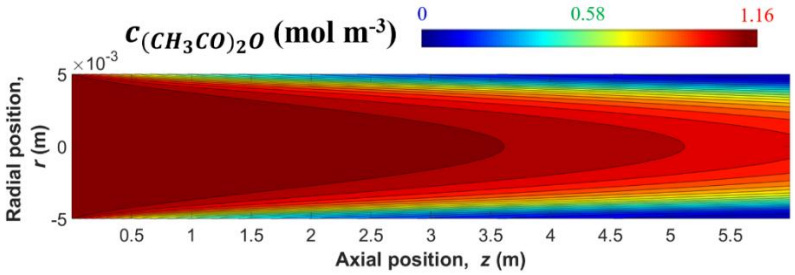

Figure 3.9: Case study 3, CFD contour plots on a midplane of the inner pipe of the: (a) global reaction rate of hydrolysis (b) acetic anhydride molar concentration.

The predictions of the systemic model are compared to the 1D reduced CFD data in Figure 3.10a compares the axial profiles of the mixing-cup temperature of the reactive mixture that are predicted by the 1D systemic model and by CFD. CFD temperature data were 1D reduced to determine the local mixing-cup temperatures. As noted previously, since the heat released by the reaction is significantly lower than the heat transferred from the utility fluids, the systemic process model, although based on Nusselt number correlations developed for inert flows, remain sufficiently accurate and correctly captures temperature variations of the reactive mixture along the HER.

(a) (b)

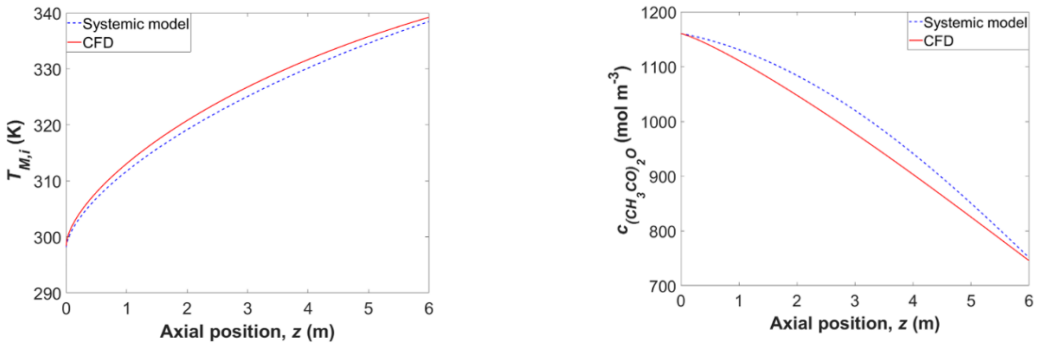

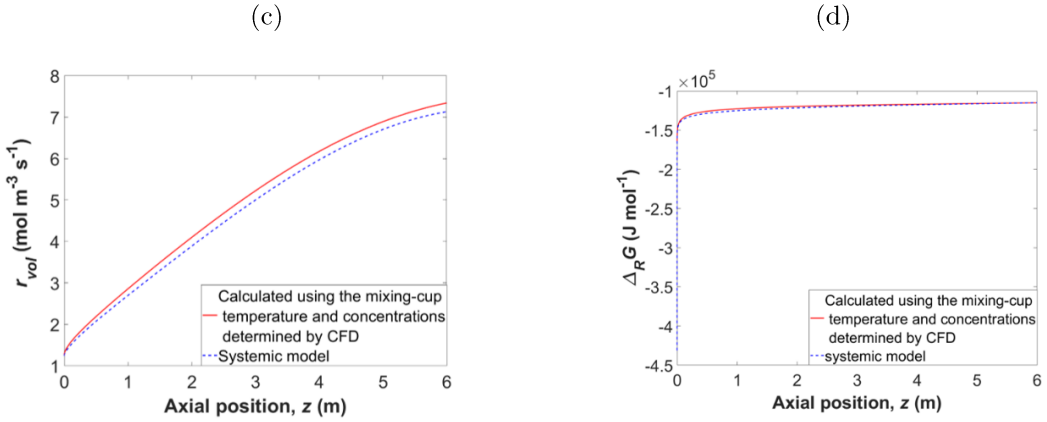

Figure 3.10: Case study 3, comparison between the systemic process model and CFD of the axial profiles of: (a) Mixing-cup temperature of the reactive mixture. (b) Mixing-cup concentration of acetic anhydride. (c) Reaction rate. (d) Local Gibbs free energy of reaction.

Figure 3.10b compares the axial variations along the HER of the mixing-cup concentration of acetic anhydride as calculated by the systemic model and CFD. CFD concentration data were 1D reduced to determine the local mixing-cup concentrations. The results are in good agreement although the systemic model slightly underestimates the rate of consumption of acetic anhydride (i.e., the reaction rate) in the first 3 meters of the HER.

Figure 3.10c compares the reaction rates along the HER. It should be emphasized that the 1D reduced CFD reaction rate is not calculated using the mixing-cup reaction rate averaging. Instead, reaction rate is calculated using the kinetic expression estimated with the local mixing-cup temperature and concentration values from CFD generated data. In other words, they correspond to the reaction rate which would be calculated using a perfectly precise systemic model, i.e., a 1D model which would lead to the same mixing-cup temperatures and concentrations as CFD. Figure 3.10 shows that the results are in good agreement although the systemic model slightly underestimates the reaction rate all over the HER length. However, it should be recalled that Figure 3.10b indicates that over the last 3 meters of the HER, the systemic approach overestimates the decrease of the concentration of acetic anhydride. These differences in the results between Figure 3.10b and Figure 3.10 are due to the averaging procedure of the CFD data. Indeed, whereas concentrations are mixing-cup averaged from the 2D CFD field, reaction rates are instead determined from these mixing-cup values of temperature and concentration, rather than being directly averaged from the 2D local profiles. Therefore, given the nonlinear dependence of the reaction kinetic parameters on temperature and concentration, any 1D modelling approach would result in differences in the prediction of reaction rates unless the temperature and concentration fields are radially uniform. This point will be further detailed later in this section since it constitutes the main reason why 1D EGMod approaches lead to much less accurate results than CFD when dealing with reactive flows.

Figure 3.10d compares the axial profile of Gibbs free energy of reaction as calculated by the systemic model and by CFD. As for the reaction rate, 1D reduced CFD profiles are not

directly averaged from the 2D CFD data but are calculated using the expression of Gibbs free energy evaluated with the mixing-cup temperatures and concentrations following the procedure detailed in Chapter 2 (Section 2.5.2). Results of the systemic model and CFD are in good agreement. Gibbs free energy is minimal at the inlet due to a very low acetic acid fraction (leading to a reaction quotient approaching zero) and increases downstream as the reaction progresses.

Figure 3.11 illustrates the CFD-calculated (2D local EGMod approach) contour plot of $\dot{s}'''_{ch}$, the local entropy generation due to the chemical reaction. As it could be expected, this contour plot is quite similar to that illustrating the reaction rate (Figure 3.9a) since chemical entropy is mainly generated in zones where reaction rates are the highest.

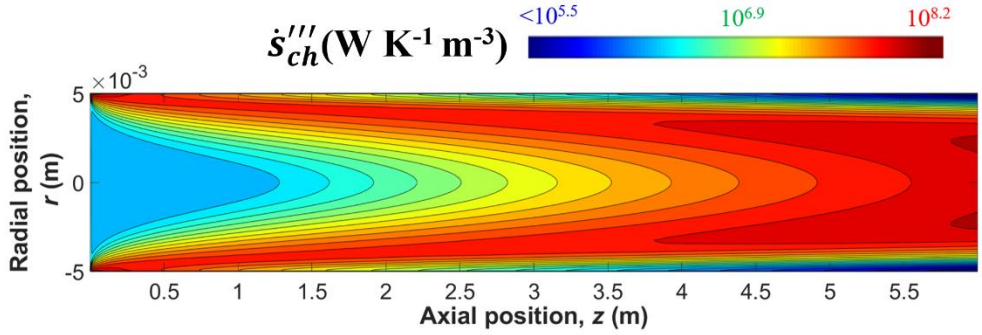

Figure 3.11: Case study 3: CFD contour plots of $\dot{s}'''_{ch}$, the local entropy generation rate by chemical reaction in the inner pipe. Note that a logarithmic scale is used for the colorbar.

To allow comparison with 1D approaches, the chemical entropy generation rate per unit length, $\dot{s}'_{ch}$ [W K^{-1} m^{-1}], is determined by integrating $\dot{s}'''_{ch}$ [W K^{-1} m^{-3}], the volumetric source term on each cross-section and the results are shown in Figure 3.12.

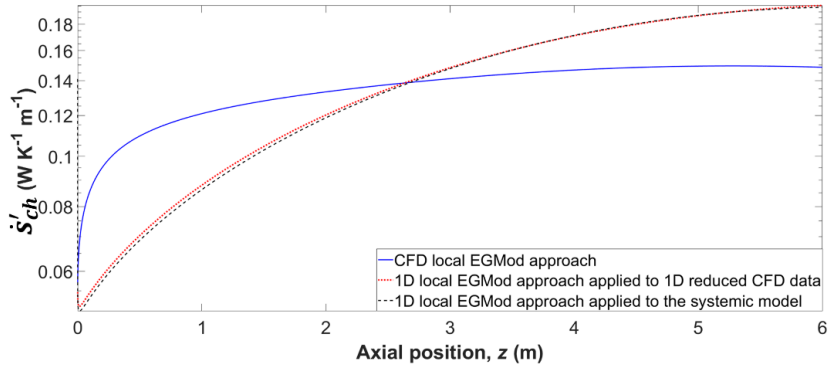

Figure 3.12: Case study 3: local rate of entropy generation by chemical reaction: comparison between the "CFD local" EGMod approach (continuous blue curve) and the "1D local" EGMod approach applied to the 1D systemic model (dashed black curve) and to the 1D reduced CFD data (dotted red curve).

Comparison between the results provided by the 1D EGMod approach when applied to the 1D reduced CFD data (dotted red curve in Figure 3.12) or the systemic process model (dashed black curve) shows an excellent agreement. Indeed, as indicated previously, the differences between their results are mainly due to the limited accuracy of the Nusselt number correlations, which proves sufficient here since the systemic model predicts mixing-cup temperatures similar to those obtained by CFD (Figure 3.12a). Therefore, the rate of reaction and Gibbs free energy (Figure 3.10c and Figure 3.10d) of the systemic model are close to those calculated based on the mixing-cup temperatures and concentrations given by CFD. Except at the inlet, both approaches predict a continuous increase in the rate of chemical entropy generation downstream as the reaction rate increases. At the inlet, entropy generation rate drops abruptly from a finite value to zero. This numerical singularity is due to the fact that the absence of acetic acid leads to a Gibbs free energy of reaction tending towards minus infinity.

In contrast, Figure 3.12 reveals that the CFD local EGMod approach (continuous blue curve) exhibits completely different results compared to 1D based approaches. This result proves that 1D approaches, where at each axial position the chemical reaction rate is calculated based on a single representative value of temperature and concentrations (i.e., the mixing-cup average), do not allow a correct estimation of the entropy generation rate when the temperature or concentration fields are not radially uniform. Indeed, the concentrations and temperature fields are strongly intercorrelated. On the one hand, as it can be noticed from the contour plots of Figure 3.5 and Figure 3.9b, low temperatures values in the mixture are generally associated with high concentrations of acetic anhydride because the reaction does not progress significantly in these zones. On the other hand, due to the limited diffusion rates in liquids, high temperatures values in the mixture are primarily associated with low concentrations of acetic anhydride which is depleted in these areas. Hence, 1D approaches, as they cannot account for such radial heterogeneities, systematically lead to errors in the calculation of chemical entropy. This result highlights the limits of systemic 1D modelling which proves imprecise in determining the entropy generation rate in real reactors where large concentration and temperature radial gradients generally occur.

Finally, focusing on the CFD local EGMod approach, Figure 3.12 shows that the rate of entropy generation at the inlet is close to zero as the reaction is slow at the beginning. Entropy generation subsequently increases rapidly as the reaction rate progresses promptly due to the heating by the utility fluid. At the end of the HER, the reaction rate and therefore, the chemical entropy generation rate, tend to stabilize because the effects of increasing temperature on reaction kinetics are counterbalanced by the decrease of the acetic anhydride concentration. Finally, if the length of the HER was greater, the local chemical entropy generation rate would have decreased and would reach zero once the acetic anhydride is entirely consumed.

d. Entropy generation due to mass transfer

As discussed earlier, entropy is also generated by mass transfer, i.e., due to concentration gradients. In the CFD local EGMod approach, this contribution to entropy generation can be calculated using Equation 1.3.14, and there is no formulation available in the literature to estimate this entropy generation term in 1D models. Therefore, whenever this contribution to entropy generation is significant, 1D approaches would lead to important errors compared to CFD EGMod approaches.

Figure 3.13 illustrates the CFD-calculated (2D local EGMod approach) contour plot of $\dot{s}_{\mu}'''$, the local entropy generation due to mass transfer. Comparison with Figure 3.9b reveals that, as expected, the mass-transfer induced entropy generation is maximum in areas where the chemical reaction induces high concentration gradients. It is minimal near the inlet since the mixture is injected in the HER with a uniform composition as well as in the area close to the axis of the HER. It should be noted that, despite the axial symmetry, the mass transfer induced entropy is not exactly nil at the HER axis due to axial concentration gradients.

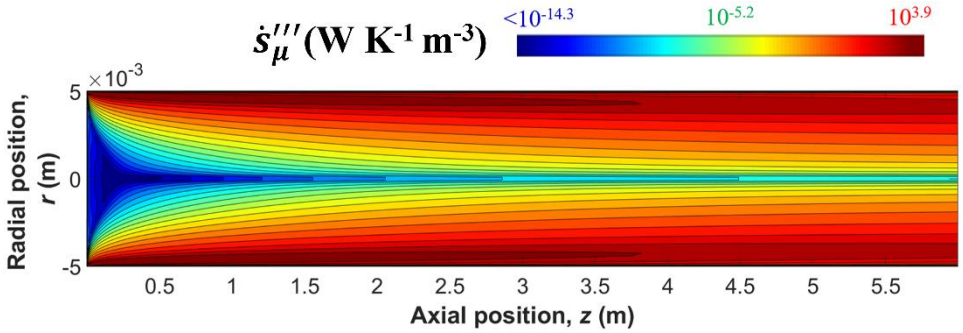

Figure 3.13: Case study 3: CFD contour plots of $\dot{s}_{\mu}'''$, the local entropy generation rate by mass transfer in the inner pipe. Note that a logarithmic scale is used for the colorbar.

To facilitate the comparison of results, the mass transfer-induced entropy generation rate per unit length, $\dot{s}_{\mu}'$ [W K^{-1} m^{-1}], is determined by integrating $\dot{s}_{\mu}'''$ [W K^{-1} m^{-3}], the volumetric source term, on each cross-section and the results are shown in Figure 3.14 along with those relating to the other source terms (and which have been discussed previously). Entropy generation rate by mass transfer (dotted blue curve) follows the same trend than the chemical entropy curve (continuous green) since concentration gradients in this case are solely due to the chemical reaction. Mass transfer-induced entropy is minimal at the reactor inlet where the mixture is assumed to be perfectly mixed and homogeneous, meaning there are no radial concentration gradients, resulting in negligible entropy generation. Subsequently, it rapidly increases as the reaction progresses promptly due to high reactant concentrations and heating by the utility fluid, which generates large local concentration gradients. Thereafter, the reaction rate, and so the entropy generation by mass transfer, tend to stabilize. Finally, if the length of the HER was much greater, the mass transfer entropy generation rate would have decreased

and would reach zero once the acetic anhydride is entirely consumed and the concentrations fields completely uniformed.

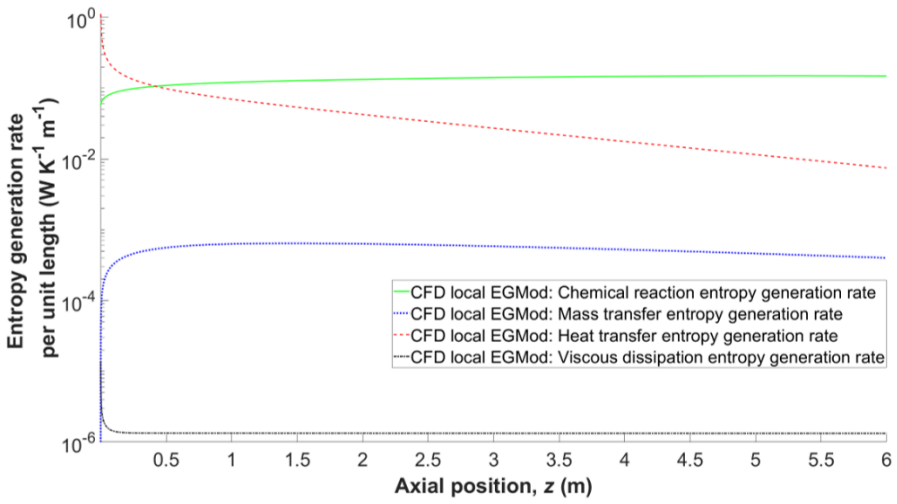

Figure 3.14: Case study 3: comparison of the entropy generation rates per unit length calculated using the CFD local EGMod approach. Note that a logarithmic scale is used for the coordinate axis.

Figure 3.14 shows that in the current case study, mass transfer contribution to entropy generation is one to two orders of magnitudes smaller than the contributions of chemical reaction or heat transfer. However, it should be noted that mass transfer effects on entropy generation would be much more significant if the reactants were not initially mixed or in a gas phase reaction where the mass diffusivity is about four orders of magnitude higher than in liquids. As noted previously, whenever this term is large, 1D EGMod approaches would lead to significant errors in determining the total entropy generation rate.

e. Total entropy generation

The total entropy generation rates calculated using the different EGMod approaches for the third case study are summarized in Table 3.5. The results of the CFD local EGMod approach reveal that, as could be noticed from Figure 3.14, chemical reaction is the primary source of entropy generation in the system, closely followed by heat transfer, while mass transfer and viscous dissipation effects are negligible.

As expected theoretically, for a given process model (systemic, 2D CFD or 1D reduced CFD data), both local and global EGMod approaches give similar results with less than 1% difference. Fortuitously, the results from different process models are also similar. In fact, despite significantly different shapes between the CFD curve and the 1D data, the chemical entropy curves illustrated in Figure 3.14, by chance, exhibit similar integral values (corresponding to the total rate of chemical entropy generation in the HER for a 6m length). Differences would have been much greater for a different HER length. Indeed, as discussed throughout this section, in the presence of chemical reaction and/or mass transfer, unless

temperature and concentration fields are radially uniform, 1D EGMod approaches lead to significant errors in the evaluation of the entropy generation rates.

Table 3.5: Case study 3: comparison of the total entropy generation rate predicted by the different EGMod approaches.

EGMod approach	**Total generated entropy, $\dot{S}_{tot}$ (W K^{-1})**	**Relative difference between global and local EGMod approaches applied to a same process model (%)**
"CFD local" approach	$\dot{S}_{tot}$ = 1.076 W K^{-1} ➢ $\dot{S}_{ch}$ = 8.124 10^{-1} W K^{-1} ➢ $\dot{S}_{\mu}$ = 3.240 10^{-3} W K^{-1} ➢ $\dot{S}_{h}$ = 2.608 10^{-1} W K^{-1} ➢ $\dot{S}_{\eta}$ = 8.047 10^{-6} W K^{-1}	0.28%
"CFD global" approach	$\dot{S}_{tot}$ = 1.073 W K^{-1}	
"1D local" approach applied to the systemic model	$\dot{S}_{tot}$ = 1.102 W K^{-1} ➢ $\dot{S}_{ch}$ = 8.367 10^{-1} W K^{-1} ➢ $\dot{S}_{h}$ = 2.651 10^{-1} W K^{-1} ➢ $\dot{S}_{\eta}$ = 8.449 10^{-6} W K^{-1}	0.27%
"1D global" approach applied to the systemic model	$\dot{S}_{tot}$ = 1.099 W K^{-1}	
"1D local" approach applied to the 1D reduced CFD data	$\dot{S}_{tot}$ = 1.103 W K^{-1} ➢ $\dot{S}_{ch}$ = 8.119 10^{-1} W K^{-1} ➢ $\dot{S}_{h}$ = 2.620 10^{-1} W K^{-1} ➢ $\dot{S}_{\eta}$= 8.115 10^{-6} W K^{-1}	0.73%
"1D global" approach applied to the 1D reduced CFD data	$\dot{S}_{tot}$ = 1.091 W K^{-1}	

3.2.4 Results comparison

The comparison highlights the modelling-induced differences in the results which are due to the inevitable inaccuracies of 1D modelling in the prediction of the temperature and/or concentration fields, but also to inherent approximations in the assessment of entropy generation based on a 1D assumption.

Specifically, the study underlines that, in simple flow configurations (purely tubular HER) for which precise correlations are available, a 1D systemic model is quite accurate in estimating the entropy generated by viscous dissipation compared to a CFD modelling, both using global and local EGMod. It is noteworthy that the global modelling approach can only estimate the entropy generated by viscous dissipation through the temperature rise originated from the viscous heating in incompressible flows. It was also shown that, for dilute system, entropy generation by heat transfer is reasonably similar for both EGMod approaches.

Additionally, this study highlighted that the chemical reaction can significantly contribute to entropy generation in reactive systems and is a main source of discrepancy between 1D systemic and CFD models. It pointed out that 1D modelling for reactive systems can be challenging due to, firstly, the lack of correlations for heat transfer involving heat generation caused by the exothermicity of the reaction inside the pipe. Secondly, it was shown that there are some differences in the local entropy generation due to chemical reaction profiles calculated between the CFD and the systemic model due to radial gradients that are not considered in 1D modelling, although the systemic model can accurately predict temperature and concentration profiles in the HER. Furthermore, the CFD modelling can take into account the entropy generated by mass transfer which is not possible by considering the 1D mathematical formulation of entropy generation (Kjelstrup approach).

Ultimately, it was demonstrated for each modelling approach that both global and local EGMod yield similar results. However, the local EGMod offers valuable insights into the distribution of entropy production for each phenomenon. This study has shown that, for a system involving only viscous dissipation and heat transfer, the systemic modelling approach would be more suitable and time-saving that CFD modelling. However, the use of simpler modelling approach is not recommended for systems involving a chemical reaction with a high thermicity and/or high concentrations, as the modelling errors for such system is expected to increase. A CFD approach would ensure more accurate results and is thus recommended for those systems.

In any case, for determining the optimal design of equipment using entropy generation minimization, 1D EGMod approaches have inherent limitations when applied to non-classical or complex shapes, since accurate friction factor and Nusselt number correlations are generally available for basic geometries only. In such situations, CFD becomes a more reliable modelling

tool. Nevertheless, 1D models remain valuable for preliminary optimisation, sensitivity analyses, and for providing physical insights at a reduced computational cost.

3.3 1D Optimisation results and discussion

As previously stated, the optimisation problem was formulated in the framework of the hydrolysis of acetic anhydride carried out in a double-pipe HER. The reactive liquid mixture flows in the inner tube, while an inert heat carrier circulates in the annular space. Two reactor configurations are considered: (i) a conventional tubular reactor with constant inner diameter, and (ii) a profiled HER with a variable internal diameter along the axial direction. In both cases, the wall thickness and annular gap are kept constant (e_w = 1 mm, e_{an} = 1 cm), and the HER is assumed to be adiabatic;

The multi-objective optimisation (Chapter 2, Section 2.6) was defined with two competing goals: (i) the minimization of the total entropy generation rate ($\dot{S}_{tot}$) and (ii) the minimization of the HER volume (V_{HER}):

$$\underset{\vec{v}}{\text{Min}}\,\vec{F} = \underset{\vec{v}}{\text{Min}}[\dot{S}_{tot}, V_{HER}]^T \qquad 3.3.1$$

where $\vec{v}$ represents the vector of decision variables. The number of decision variables depends on the configuration considered. For the purely tubular HER, two decision variables are considered, the total reactor length, L, and the inner tube diameter, d_i. For the profiled HER, a more complex design space was defined with twelve decision variables, including the total reactor length L, the inlet inner tube diameter $d_{i,inl}$, and the slopes of the ten successive sections, α_m.

This optimisation was subject to the following set of constraints:

- Process model equations: the 1D plug-flow model described in Chapter 2, Section 2.4, which couples mass and energy balances for both fluids with the chemical kinetics of acetic anhydride hydrolysis.
- Boundary conditions: the inlet conditions defined in Chapter 2, Section 2.3
- Terminal constraints: a minimum outlet conversion of 80% was imposed to ensure practical reactor designs.
- Path constraints: the internal diameter was restricted to remain within physical limits along the reactor axis (0.5 cm ≤ d_i ≤ 10 cm).
- Bounds on decision variables: reactor length between 0.1 and 10 m, and slope values restricted to $-\frac{\pi}{2} < \alpha_m < \frac{\pi}{2}$.

The optimisation was performed using the one-dimensional HER model, which is based on the ideal plug-flow assumption without axial dispersion. In this framework, all variables (temperature, composition, pressure) are considered uniform over the cross-section and vary only in the axial direction. While this model neglects radial gradients and potential hydrodynamic complexities, it provides a computationally efficient approach suitable for multi-

objective optimisation. The underlying hypotheses and limitations of this model will be discussed later in this work.

3.3.1 Reference case

a. On the need for a conversion constraint

The necessity of imposing a minimum conversion constraint in the optimisation problem becomes evident when examining entropy generation in a simple tubular reactor whose inner diameter and length are both allowed to vary. In this analysis, the full variation space defined in Chapter 2 (i.e., 0.1 m < L < 10 m and 0.5 cm < d_i <10 cm) was explored, without applying any constraints on temperature or conversion. The objective was to isolate and evaluate the sole effect of the design on entropy generation. The results are presented in Figure 3.15.

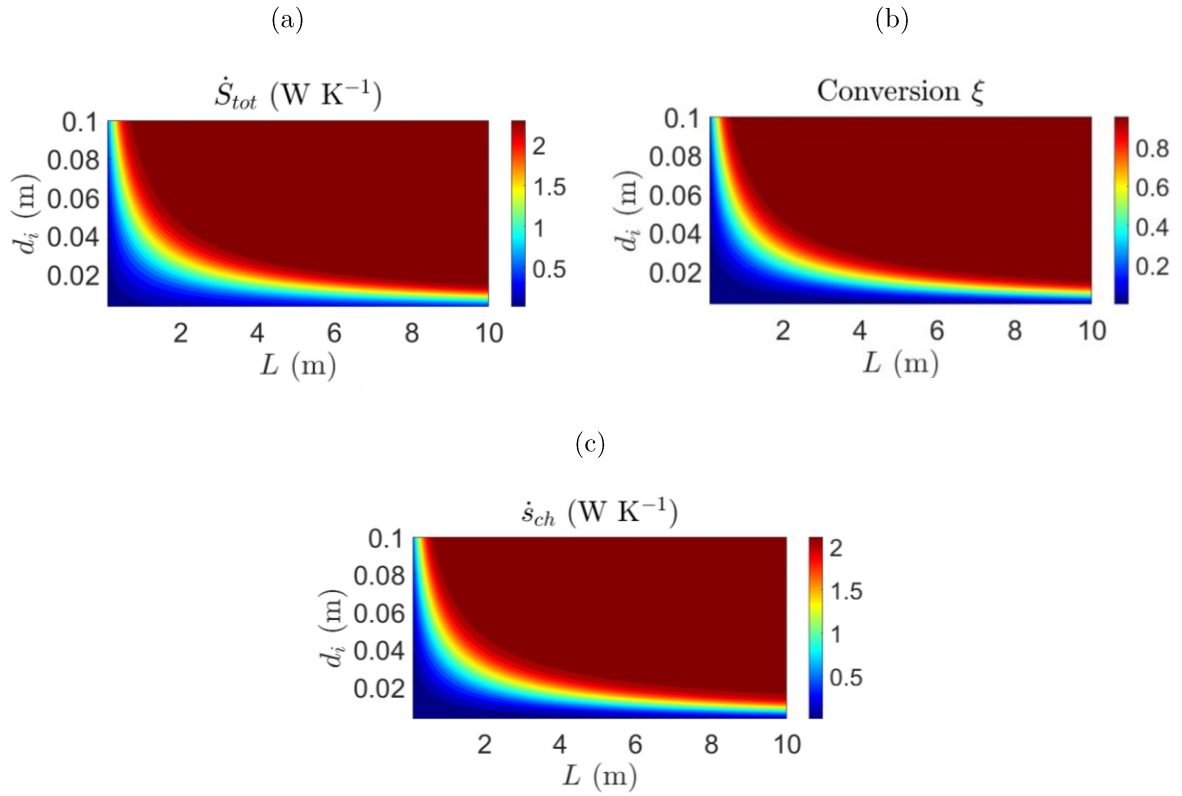

Figure 3.15: Geometric parameters impact for tubular geometries on the (a) total entropy generation (b) conversion (c) chemical reaction entropy generation.

Figure 3.15a shows that, as expected, minimum entropy generation occurs in reactors whose diameter and length both approach zero—conditions under which no reaction takes place due to vanishing residence time, and no heat transfer occurs due to the negligible surface area. The figure also reveals that the highest total entropy generation occurs for reactors with both large lengths and large diameters. As illustrated in Figure 3.15b and Figure 3.15c, this elevated entropy is primarily due to chemical reaction, whose entropy production increases significantly with conversion, as previously discussed in Section 3.2.3.

Figure 3.15c also reveals the presence of a large region where entropy generation appears to be nearly constant over a wide range of diameter–length combinations. This plateau corresponds to geometries that achieve full conversion—beyond which no additional entropy is produced by the reaction.

As discussed earlier in this paragraph, the configurations that minimize entropy generation are those with extremely small diameters or lengths, where little to no reaction occurs. In other words, the lowest-entropy solution is simply the absence of a reactor. Although thermodynamically optimal in terms of entropy generation, such a design has no practical value from an engineering perspective.

Therefore, to ensure an insightful comparison among reactor geometries, a minimum conversion constraint must be imposed. It is also worth noting that this constraint could be expressed as an equality, since no optimal geometry would realistically exceed the imposed conversion without also significantly increasing entropy generation through chemical reaction.

In practice, all Pareto optimal solutions achieve a conversion nearly equal to the target conversion. Indeed, additional conversion beyond the minimum imposed conversion results in an increase in both the HER volume and total entropy generation. Therefore, mathematically, it would have been better to express Equation 2.6.17 as an equality rather than as an inequality constraint. However, the optimisation problem is solved using a genetic algorithm as explained in Chapter 2, and equality constraints pose challenges for this type of algorithm by preventing it from identifying feasible solutions within an acceptable computational time. Thus, from a numerical perspective, Equation 2.6.17 is formulated as an inequality constraint to enable the algorithm to identify feasible solutions, which are refined from generation to generation until they converge toward a conversion practically equal to the imposed one.

b. Optimisation of the reference case

First, an optimisation of the reference case was carried out using the reference operating conditions (Chapter 2, Table 2.3), according to the procedure described in Chapter 2. This optimisation, as well as the subsequent ones presented in Section 3.3, is performed using the 1D model introduced in Chapter 2, Section 2.4, implemented in Matlab, and follows the methodology outlined in Chapter 2, Section 2.6.3. The results for both the simple tubular and the piecewise-profiled geometries are presented in Figure 3.16. The extreme points of the profiled HER Pareto front, corresponding respectively to the minimum HER volume and the minimum entropy generation rate, will be referred to as MPCVol (Minimal Profiled Configuration Volume) and MPCEnt (Minimal Profiled Configuration Entropy Generation Rate).

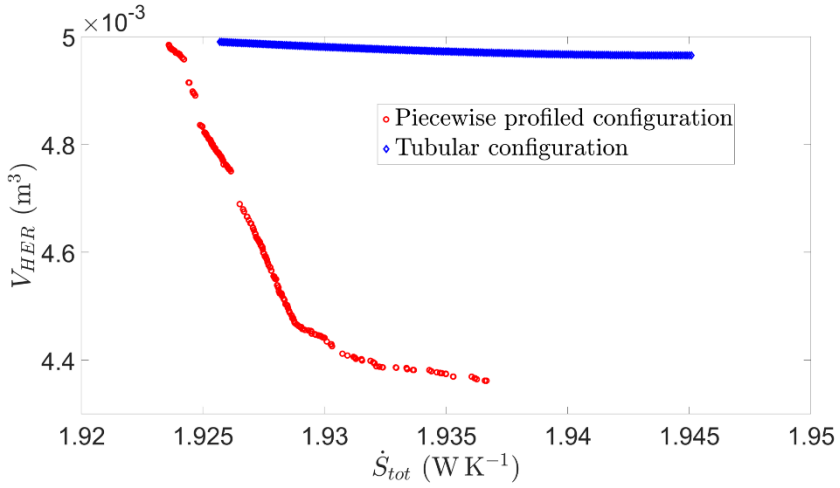

Figure 3.16: Pareto fronts for the reference case study.

It can be observed that the difference in total entropy generation between the two configurations is negligible. However, the piecewise-profiled geometry achieves a significant volume reduction, from 5 L to approximately 4.4 L (a 12.5% decrease) with only a marginal increase in entropy generation. This reduction can be attributed to the geometrical profiles shown in Figure 3.17.

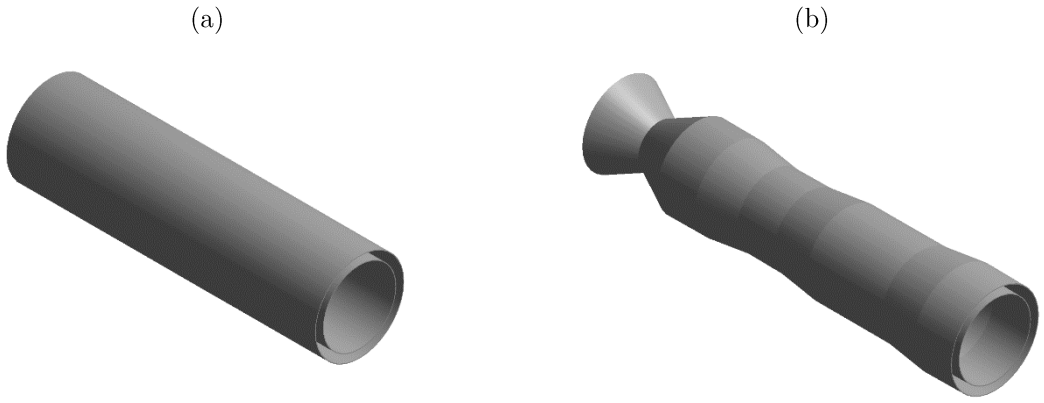

Figure 3.17: 3D representation of the MPCEnt (a) and MPCVol (b) points of the reference caste study.

As expected from the Pareto front, the MPCEnt geometry (Figure 3.17a), closely resembles a large-diameter tubular reactor. In contrast, the MPCVol geometry features a sharp narrowing at the inlet, followed by a wider section with a slightly converging profile, then a diverging section. Detailed comparison between these designs is presented in Figure 3.18.

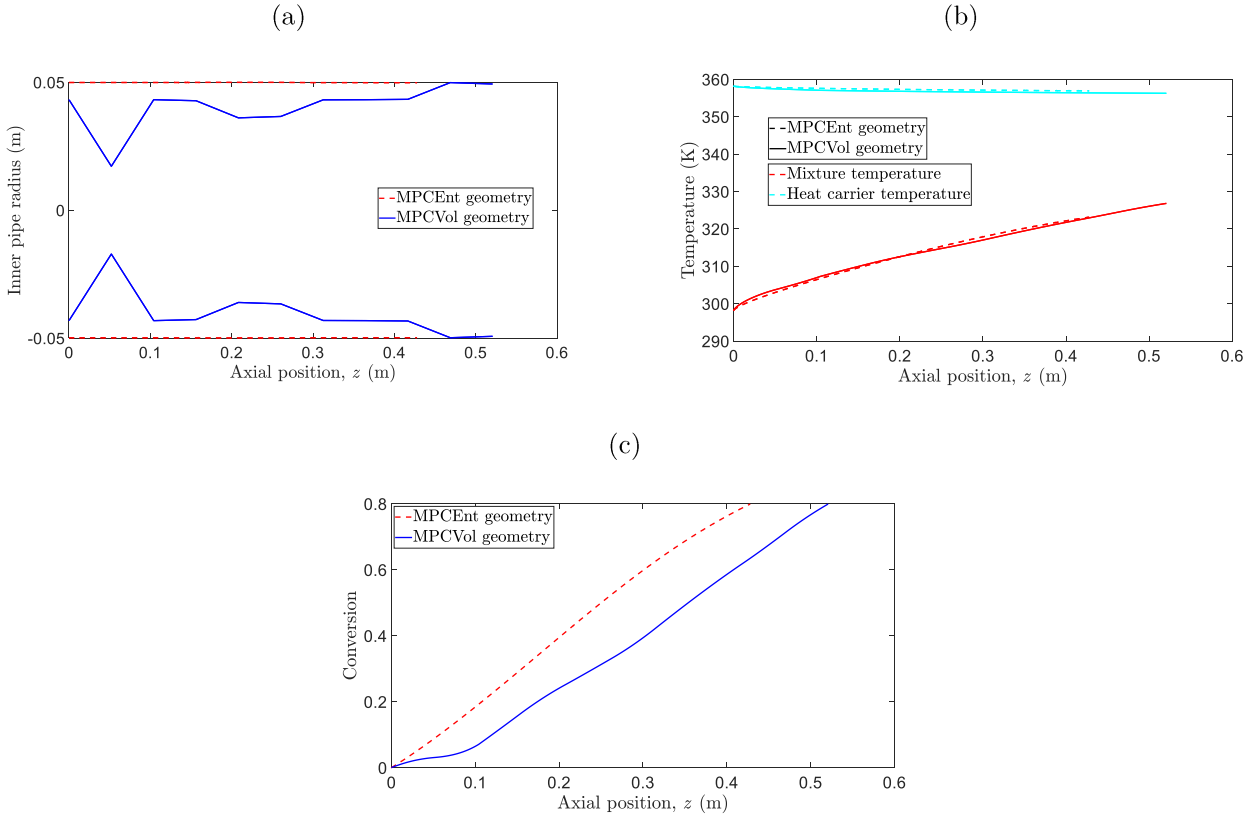

Figure 3.18: MPCVol and MPCEnt points of the reference case study: (a) Inner pipe radius profiles, (b) Temperature profiles, (c) Acetic anhydride conversion rate profiles.

Temperature profiles (Figure 3.18b) are quite similar in both geometries. A more pronounced difference arises in the conversion profiles. Figure 3.18 shows that while both profiles run parallel along most of the reactor length, the narrowed inlet in the MPCVol geometry results in a lower conversion rate in the first few centimetres. This local effect is further illustrated in the entropy generation profiles of Figure 3.19.

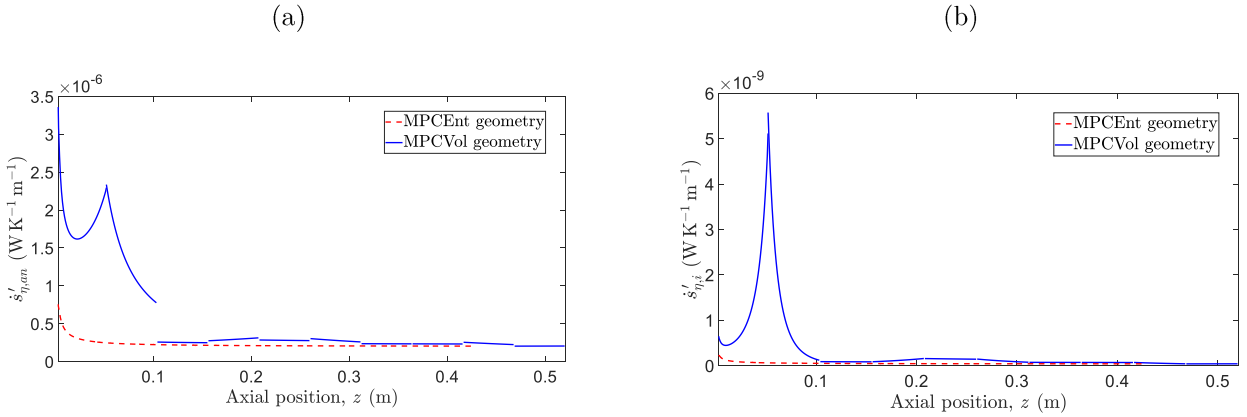

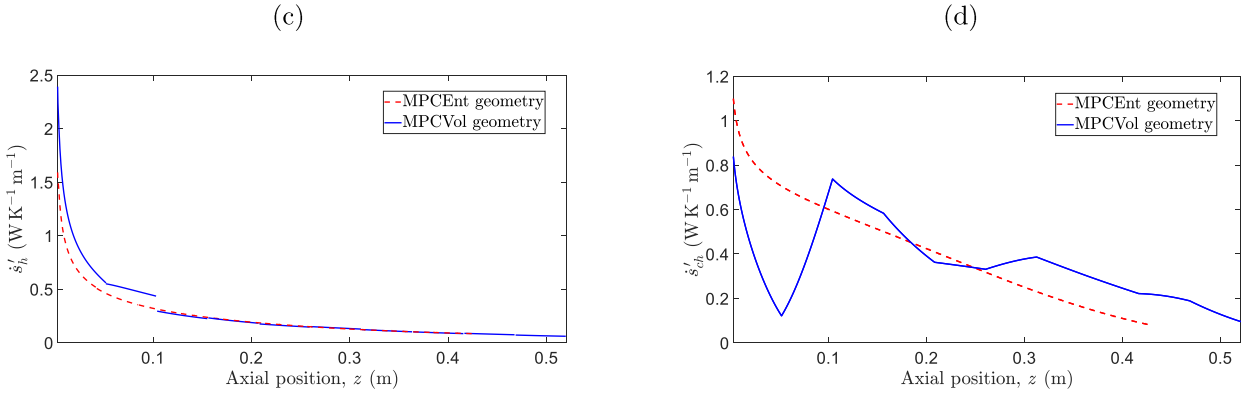

Figure 3.19: Local entropy generation rates in both the MPCEnt and MPCVol geometries: (a) Viscous dissipation in the heat carrier, (b) Viscous dissipation in the reactive mixture, (c) Heat transfer, (d) Chemical reaction.

The discontinuities in the entropy generation profiles arise from the cos(α) factor introduced in the 1D model to account for the local slope in converging and diverging sections. As expected, the narrowing causes a localized increase in entropy generation due to viscous dissipation near the inlet and on both sides of the HER (Figure 3.19a and Figure 3.19b). Beyond this reactor section, the entropy generation levels remain relatively close between the two geometries, although slightly higher in the more constricted sections.

Regarding entropy generation from heat transfer (Figure 3.19c), the MPCVol geometry shows a higher entropy generation near the reactor inlet (between 0 and 10 cm). This can be attributed to the reduced reacting volume in the narrowed section compared to the larger-diameter MPCEnt geometry. The smaller reaction volume by lowering the residence time, leads to a lower heat generation from the exothermic reaction. Thus, as the reactive mixture temperature is less heated, its temperature difference with the heat carrier is higher than in the MPCEnt geometry which explains the observed increase in local entropy generation in the MPCVol geometry.

It is worth noting that, while the Nusselt number (Equation B.4, Chapter 2) remains essentially constant in fully developed laminar flow (aside from the entrance region), the heat transfer coefficient h_i in the reactive mixture increases as the diameter decreases. However, because the heat transfer area ($A = \pi d_i L$) is directly proportional to the diameter, the overall heat flux ($Q = h_i A \Delta T$) is not significantly altered by the narrowed section. The decisive factor is therefore the heat released by the exothermic volumetric reaction: in the larger-diameter MPCEnt geometry, the greater reacting volume generates more heat, thereby reducing the thermal gradients with the hotter heat carrier fluid. These smaller gradients translate into lower local entropy generation. This effect is particularly visible near the inlet, where the two geometries differ in diameter, but becomes less pronounced downstream when the diameters are comparable or when the reaction heat release is less significant.

The largest difference is observed in entropy generation due to the chemical reaction (Figure 3.19d). As expected from the conversion profile, the MPCVol geometry shows a sharp initial decrease in entropy generation due to the sudden volume reduction, followed by a return to a trend similar to that of the MPCEnt geometry. This drop is a direct consequence of the volumetric nature of the reaction rate as less volume at the inlet leads to lower local reaction rates and, therefore, lower entropy generation.

A quantitative comparison between the two designs is provided in Table 3.6. For a slight increase of entropy generation only, the MPCVol geometry allows achieving a noticeable 12.5% reduction in the reactor volume compared to the MPCEnt design. As seen in earlier sections, viscous dissipation contributes negligibly to the total entropy in both cases. The slight increase in total entropy for the MPCVol geometry is primarily due to enhanced heat transfer, partially offset by a small reduction in entropy generation from the chemical reaction. Since the chemical contribution represents over 90% of the total entropy generation, this small shift has a limited impact on the overall entropy balance, which remain close in the two geometries.

Table 3.6: HER volume and entropy generation rate of the MPCVol and MPCEnt points in the reference case study (piecewise profiled configuration).

	MPCEnt design	**MPCVol design**
V_{HER}	4.98 L	4.36 L
$\dot{S}_{tot}$	1.92 W K^{-1}	1.94 W K^{-1}
	➢ 2.17×10^{-11} and 9.93×10^{-8} W K^{-1} (less than 0.1%) due to viscous dissipation in the mixture and heat carrier flow respectively.	➢ 1.62×10^{-10} and 2.78×10^{-7} W K^{-1} (less than 0.1%) due to viscous dissipation in the mixture and heat carrier flow respectively.
	➢ 1.12×10^{-1} W K^{-1} (5.8%) due to heat transfer.	➢ 1.38×10^{-1} W K^{-1} (7.1%) due to heat transfer.
	➢ 1.81 W K^{-1} (94.2%) due to the chemical reaction.	➢ 1.80 W K^{-1} (92.9%) due to the chemical reaction.

Finally, the optimal perfectly cylindrical shape of the MPCEnt geometry with a large constant diameter can be attributed to the absence of thermal constraints in the system. As shown in Figure 3.18b, temperatures remain well below critical values, such as the boiling point of water (~100°C), even with the exothermic nature of the reaction. Thus, there is no need to modify the geometry to manage temperature rise, and the optimisation favours a larger diameter to minimize viscous dissipation and entrance effects.

3.3.2 Equipartition of entropy generation and driving forces: comparison between MPCEnt and a suboptimal geometry for the reference case

To investigate the equipartition of driving forces in our case study, two geometries were compared: (i) the optimal MPCEnt geometry previously obtained, with a nearly constant diameter of 10 cm and a length of 43 cm, and (ii) a suboptimal tubular geometry with a constant diameter of 3 cm and a length of 2.56 m, both leading to conversion of 80 %. The results for both configurations are presented in Table 3.7.

Table 3.7: HER volume and entropy generation rate of the reference MPCEnt and suboptimal geometries.

	MPCEnt design	**Suboptimal design**
V_{HER}	4.98 L	1.81 L
	1.92 W K^{-1}	2.00 W K^{-1}
$\dot{S}_{tot}$	➢ 2.17×10^{-11} and 9.93×10^{-8} W K^{-1} (less than 0.1%) due to viscous dissipation in the mixture and heat carrier flow respectively. ➢ 1.12×10^{-1} W K^{-1} (5.8%) due to heat transfer. ➢ 1.81 W K^{-1} (94.2%) due to the chemical reaction.	➢ 1.19×10^{-8} and 1.45×10^{-6} W K^{-1} (less than 0.1%) due to viscous dissipation in the mixture and heat carrier flow respectively. ➢ 2.16×10^{-1} W K^{-1} (10.8%) due to heat transfer. ➢ 1.78 W K^{-1} (89.2%) due to the chemical reaction.

It can be observed that the suboptimal geometry requires a significantly smaller reactor volume to achieve the same conversion level (80%), but leads to higher entropy generation. Since both configurations are tubular, the comparison essentially contrasts a long and narrow reactor (suboptimal geometry) with a short and wide one (MPCEnt geometry).

The driving forces corresponding to each entropy generation mechanism (as described in Chapter 1, Section 1.4) are shown in Figure 3.20.

(a) (b)

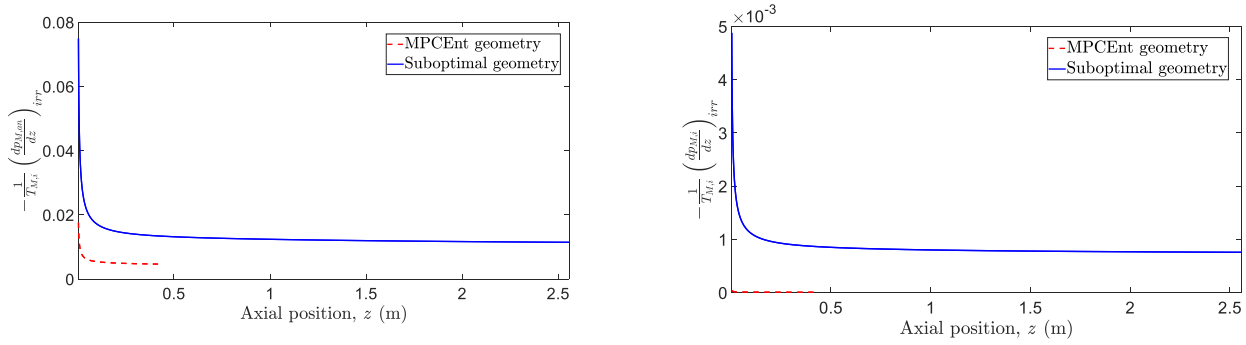

(c) (d)

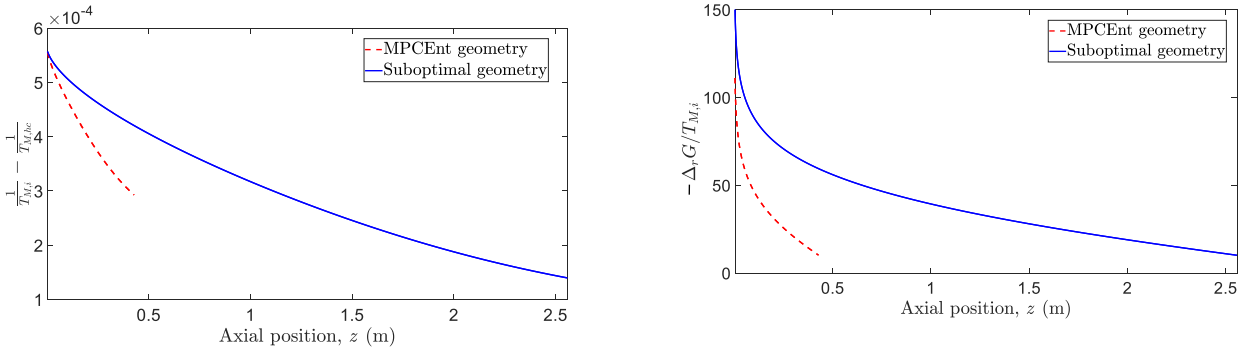

Figure 3.20: Driving forces in both the MPCEnt geometry and the suboptimal geometry: (a) Viscous dissipation in the heat carrier, (b) Viscous dissipation in the reactive mixture, (c) Heat transfer and (d) Chemical reaction.

Figure 3.20a and Figure 3.20b show the driving forces of entropy generation due to viscous dissipation in the heat carrier and in the reactive fluid, respectively. As expected, the narrower diameter results in a higher driving force, as it is linked to the pressure drop, which is significantly larger for smaller diameters. Conversely, the larger diameter produces very low pressure losses, and thus the driving force appears almost negligible in Figure 3.20b (although it remains slightly positive).

Figure 3.20c depicts the difference in the inverse of the temperature between the mixture and the heat carrier. Since the MPCEnt favours a longer residence time and consequently a higher heat exchanged, it is not surprising that the temperature gradient decreases more rapidly.

Finally, Figure 3.20d presents the driving force of entropy generation arising from the chemical reaction. As expected, the Gibbs free energy of the reaction approaches zero as the reaction progresses toward equilibrium. It is noteworthy that, although the profiles of the chemical reaction driving forces differ, this does not necessarily result in a different total entropy generation for the chemical reaction. Indeed, as discussed in Chapter 1, Section 1.4, the entropy generation is the product of a flux by its driving force. Therefore, given the differences in reaction rate profiles between the two cases, the product of the reaction rate with the corresponding driving force can lead to similar total entropy generation due to the chemical reaction, as it the case in Table 3.7.

According to the principle of equipartition of driving forces, a reactor geometry that minimizes entropy generation tends to exhibit a uniform distribution of driving forces in space and/or time. In steady-state conditions, as in this study, only the spatial uniformity was considered. To quantify this uniformity, it is necessary to trace the local entropy generation or the local driving force along the reactor length. Then, for each entropy generation source or driving forces, the area between the curve and its spatially weighted average—calculated as

the integral of the function over the domain divided by the total length—was computed using the trapezoidal method over unevenly spaced points. A schematic illustration of this criterion is presented in Figure 3.21.

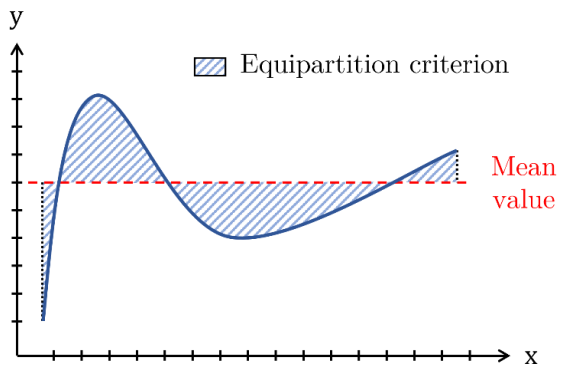

Figure 3.21: Schematic representation of the equipartition criterion.

If the area tends to zero, it means that the equipartition is reached. This criterion represents the total deviation of the profile from its average, by integrating the absolute difference along the domain. It provides a quantitative measure of how much the profile fluctuates around its mean level, regardless of whether the deviations are above or below the average, thus offering a robust indicator of equipartition of entropy generation.

For each configuration and each entropy generation mechanism, this index was calculated over the reactor length. The corresponding results are shown in Table 3.8.

Table 3.8: Equipartition criterion for the driving forces for MPCEnt and suboptimal designs.

	MPCEnt design	**Suboptimal design**
Viscous dissipation in the reactive mixture	1.10×10^{-6}	3.98×10^{-3}
Viscous dissipation in the heat carrier	4.13×10^{-4}	2.54×10^{-4}
Heat transfer	2.74×10^{-5}	2.42×10^{-4}
Chemical reaction	6.86	4.64×10^{1}

Table 3.8 indicates that the MPCEnt geometry leads to lower entropy generation and more uniform driving forces for all mechanisms except for the viscous dissipation in the heat carrier, that remain a largely minor contribution to the total entropy, which confirm the principle of equipartition of driving forces in this case study. This suggests, in agreement with the optimisation of the reference case, that tubular HER with larger diameters perform better than their narrower counterparts in term of entropy generation. A similar observation was reported by Bejan (1982), who emphasized that, for heat exchangers, achieving thermodynamically efficient designs requires constructing wider units. Additionally, the study

by Magnanelli et al. (2019) also identified that their optimal geometry favoured wider HER diameters

The second equipartition principle, related to the spatial distribution of local entropy generation rather than driving forces, was also evaluated. For each local entropy generation profile (shown in Figure 3.22), the same equipartition index was computed and reported in Table 3.9.

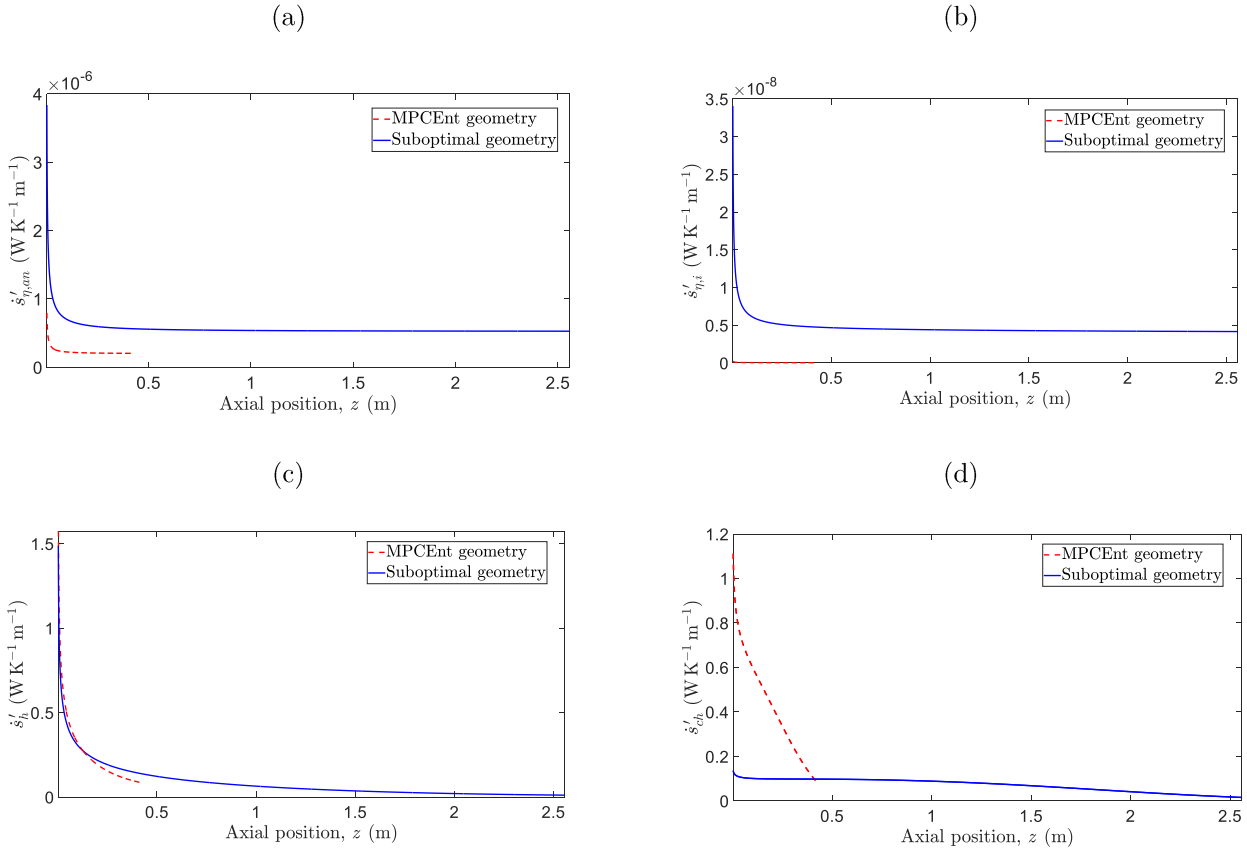

Figure 3.22: Local entropy generation rates in both the MPCEnt and the suboptimal geometries: (a) Viscous dissipation in the heat carrier, (b) Viscous dissipation in the reactive mixture, (c) Heat transfer, (d) Chemical reaction.

Table 3.9: Equipartition criterion for the local entropy generations for MPCEnt and suboptimal designs.

	MPCEnt design	**Suboptimal design**
Viscous dissipation in the reactive mixture	6.07×10^{-12}	1.40×10^{-9}
Viscous dissipation in the heat carrier	1.58×10^{-8}	1.35×10^{-7}
Heat transfer	6.73×10^{-2}	1.74×10^{-1}
Chemical reaction	8.40×10^{-2}	6.31×10^{-2}
Total generation	1.54×10^{-1}	2.48×10^{-1}

Table 3.9 shows that the principle of local equipartition of entropy generation, which states that a geometry minimizing its entropy generation exhibits an equipartition of local entropy generation is satisfied for all sources except for the chemical reaction. This highlights that the principle applies to the total entropy generation rather than to each individual source, even when one source of entropy generation is dominant.

Regarding the principle of equipartition of driving forces, it was observed that the local equipartition of entropy generation is satisfied for all contributions except for the chemical reaction. In particular, for the geometry that minimizes total entropy generation, all contributions are more evenly distributed, with the notable exception of the chemical reaction. The principle of equipartition of entropy generation thus indicates that a geometry minimizing its total entropy generation tends to exhibit a balanced distribution among the local contributions. This emphasizes that the principle primarily applies to the overall entropy generation, rather than to each individual source, even when one source is dominant.

Indeed, as shown in Table 3.9, the magnitude of the difference in entropy generation due to heat transfer is greater than that of the chemical reaction. Consequently, since the heat transfer contribution is more evenly distributed in the MPCEnt geometry, the uneven distribution of chemical entropy is compensated, resulting in a more uniform total entropy generation in the MPCEnt configuration.

In conclusion, the comparison between the optimal MPCEnt geometry and the suboptimal tubular configuration highlights the impact of reactor design on entropy generation and the spatial distribution of driving forces. The MPCEnt geometry, characterized by a short and wide tubular reactor, leads to lower total entropy generation and more uniform driving forces for all mechanisms, except for minor contributions such as viscous dissipation in the heat carrier. This confirms that, in agreement with the principle of equipartition of driving forces, minimizing entropy generation is associated with a more even spatial distribution of the thermodynamic forces. Moreover, the analysis shows that even when local driving forces of a specific source, such as the chemical reaction, are not fully uniform, the total entropy generation can remain relatively uniform due to compensating contributions from other mechanisms, particularly heat transfer. These results reinforce the conclusion that, for tubular HER, larger diameters are generally more favourable in terms of thermodynamic efficiency, corroborating previous findings by Bejan (1982) and Magnanelli et al. (2019).

3.3.3 Influence of the inlet mixture temperature

As previously discussed in the reference case, the optimal geometry, resulting in an ideal tubular profile (tube with a uniform diameter), can be partially attributed to the fact that temperature was not explicitly constrained during the optimisation process. To better understand the influence of the temperature, particularly the inlet temperature of the reactant mixture, this parameter was specifically investigated.

In this sensitivity analysis (and in all others), the same operating conditions as in the reference case were maintained, and only one parameter was varied at a time. The constraints imposed during optimisation (on diameter, length, minimal conversion, etc.) remained active throughout all studies. The impact of inlet mixture temperature on the Pareto fronts is presented in Figure 3.23, where three different inlet temperatures were tested, $T_{M,i,inl} = 278$ K, $T_{M,i,inl} = 298$ K (the reference inlet temperature) and $T_{M,i,inl} = 318$ K. All other operating conditions remained the same as the reference case and can be found in Chapter 2, Section 2.3b.

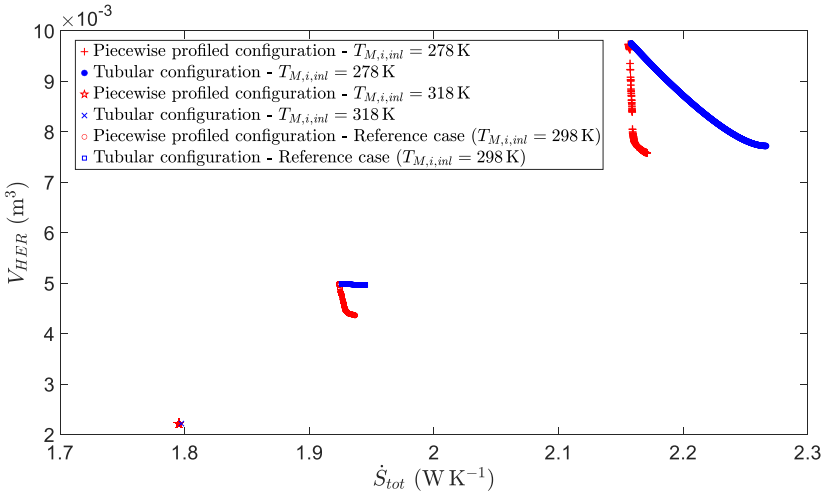

Figure 3.23: Pareto fronts for different inlet mixture temperature.

Figure 3.23 shows that increasing the inlet temperature leads to a decrease in both reactor volume and entropy generation. Additionally, the Pareto fronts appear wider at lower inlet temperatures, suggesting that multiples optimal geometries can be explored but higher temperatures represent a better compromise since both objective functions improve. However, this comes with a trade-off: heating the mixture upstream may generate entropy outside the system boundary, which is not accounted for in this study.

The optimal geometries corresponding to the two additional cases are shown in Figure 3.24. As with the reference case, the MPCEnt geometries tend to follow a tubular profile with the largest allowable diameter. The MPCVol geometry obtained for the low inlet temperature case shows a similar pattern, featuring an initial sharp narrowing followed by a milder contraction, before stabilizing into a fully tubular section. This behaviour is likely attributed

to the inlet effects: indeed, a narrow section increases the local Reynolds number, which leads to a higher Nusselt number in the case of a thermally developing flow. As a result, a reduction in reactor volume is achieved despite the additional length required.

Interestingly, the MPCVol geometry for the high inlet temperature case is nearly identical to its MPCEnt counterpart, due to the narrowness of the corresponding Pareto front.

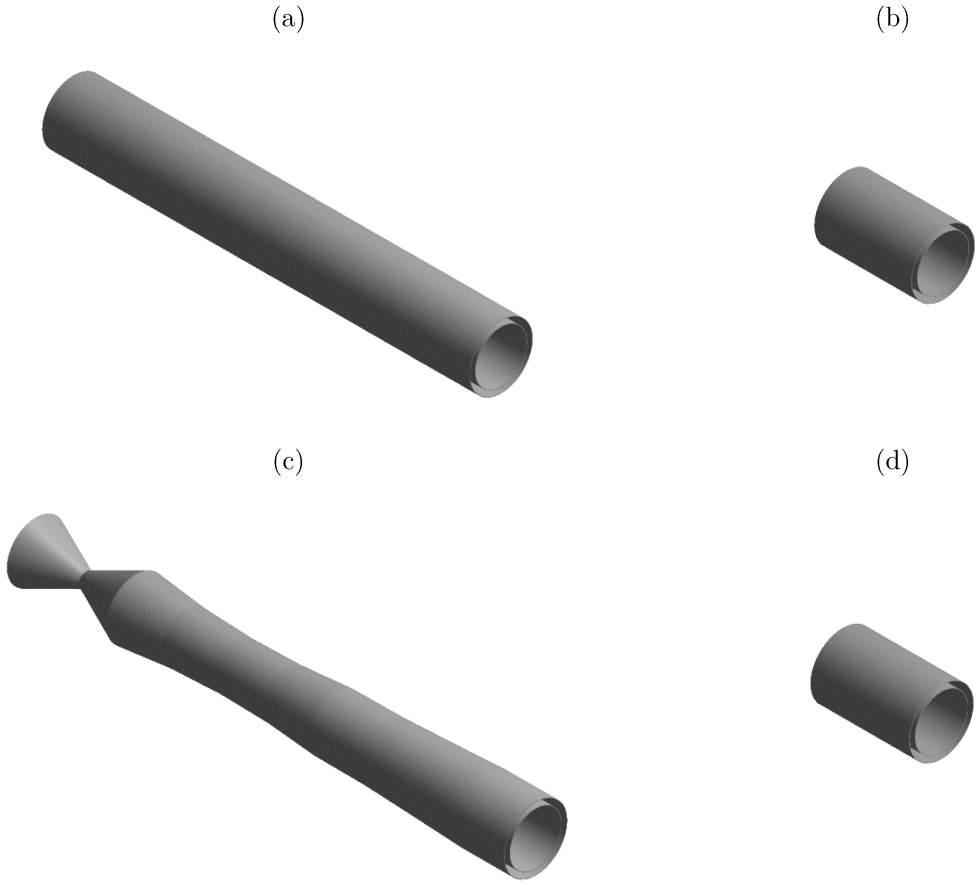

Figure 3.24: 3D representation of the MPCEnt (a) and MPCVol (c) points for $T_{M,i,inl}$ = 278 K, and the MPCEnt (b) and MPCVol (d) for $T_{M,i,inl}$ = 318 K.

The temperature and conversion profiles for both cases ($\boldsymbol{T_{M,i,inl}}$ = 278 K and $\boldsymbol{T_{M,i,inl}}$ = 318 K) are presented in Figure 3.25. It can be observed that the shorter geometry resulting from a higher inlet temperature achieves faster conversion over a shorter reactor length. In contrast, the lower inlet temperature requires a longer reactor to reach the same 80% conversion. This behaviour is primarily due to the kinetic acceleration at elevated temperatures.

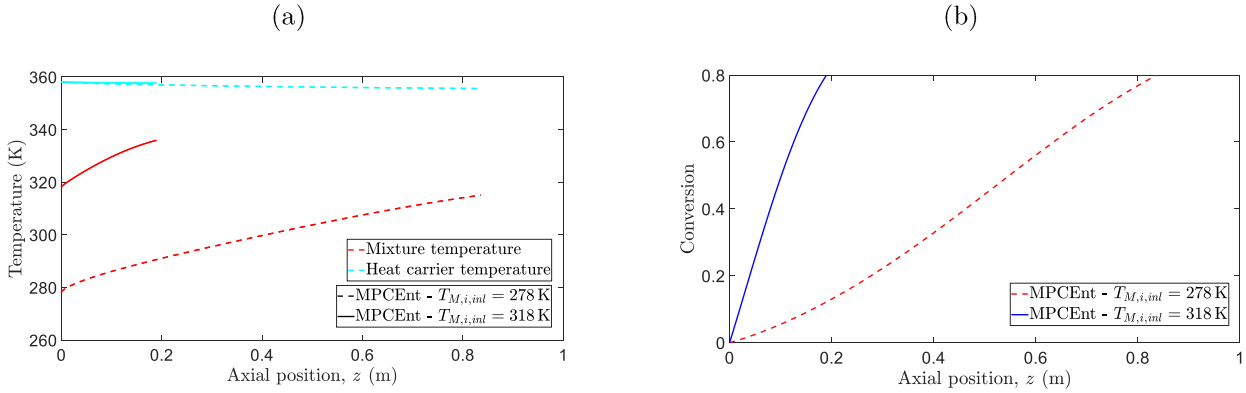

Figure 3.25: MPCEnt points for $T_{M,i,inl}$ = 278 K and $T_{M,i,inl}$ = 318 K: (a) Temperature profiles, (b) Acetic anhydride conversion profiles.

Figure 3.26 presents the local entropy generation profiles for both MPCEnt geometries for $T_{M,i,inl}$ = 278 K and $T_{M,i,inl}$ = 318 K. The impact of both designs on viscous dissipation in the mixture and the heat carrier (Figure 3.26a and Figure 3.26b) appears similar. Figure 3.26c shows that lower inlet temperatures lead to increased entropy generation from heat transfer, which is consistent with larger temperature gradients and longer reactor length. Finally, Figure 3.26d illustrates the significant influence of inlet fluid temperature on the entropy generation associated with the chemical reaction. In the low-temperature case, entropy generation due to reaction is distributed more uniformly along the reactor, with a nearly linear decline.

This behaviour can be explained by the influence of inlet temperature on the reaction kinetics. At higher inlet temperature, the higher reaction rate rises sharply near the inlet, reaches its maximum around 3 cm, and then rapidly declines. Although the reaction rate remains higher throughout the reactor in this configuration, the Gibbs free energy shows the opposite trend, being consistently lower. As the absolute value of Gibbs free energy decreases when the system approaches completion, this explains the crossing observed in the entropy generation profiles shown in Figure 3.26d.

In contrast, for the lower inlet temperature, the reaction rate (much lower at the beginning due to lower inlet mixture temperature) increases more gradually, reaching its maximum only around 50 cm, with a nearly constant profile along the reactor length compared to the steeper variations observed in the high-temperature case. This difference in the spatial distribution of the reaction rate leads to significant differences in the local entropy generation profile associated with the chemical reaction.

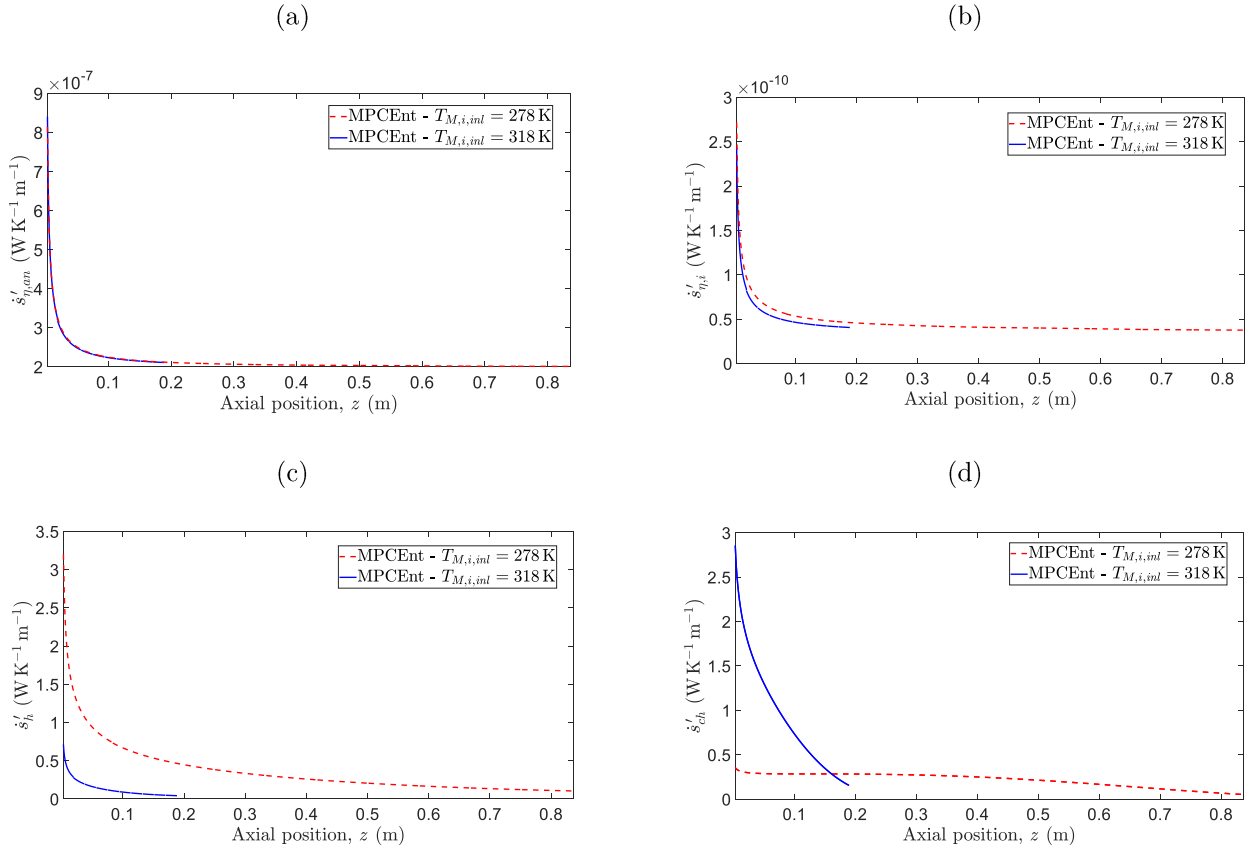

Figure 3.26: Local entropy generation rates in MPCEnt points for $T_{M,i,inl}$ = 278 K and $T_{M,i,inl}$ = 318 K: (a) Viscous dissipation in the heat carrier, (b) Viscous dissipation in the reactive mixture, (c) Heat transfer, (d) Chemical reaction.

The objective function values (reactor volume and total entropy generation) for the three inlet temperatures are presented in Table 3.10 for the corresponding MPCEnt geometries (which are all purely tubular, but with variable length). As previously observed, increasing the inlet temperature reduces both reactor volume and entropy generation. Specifically, a decrease of 20 °C in the inlet temperature results in a 96% increase in reactor volume, while an increase of 20 °C leads to a 64% decrease. Entropy generation is also affected, increasing by 13% in the low-temperature case and decreasing by 6% in the high-temperature case. These variations are not directly proportional to the imposed temperature changes, which is not surprising as both contributions are not mathematically proportional to this parameter. The reduction in entropy generation at higher temperature arises from a decrease in both the heat transfer and chemical reaction contributions—an expected result, since higher temperatures tend to reduce entropy generation according to the thermodynamic relationships (Equations 2.6.4 and 2.6.5) discussed in Chapter 2.

Table 3.10: HER volume and entropy generation rate of the MPCEnt points of the three mixture inlet temperatures.

	$T_{M,i,inl} = 278\ K$	$T_{M,i,inl} = 298\ K$	$T_{M,i,inl} = 318\ K$
V_{HER}	9.74 L	4.98 L	2.21 L
$\dot{S}_{tot}$	2.16 W K^{-1} ➢ 3.90×10^{-11} and 1.82×10^{-7} W K^{-1} (less than 0.1%) due to viscous dissipation in the mixture and heat carrier flow respectively. ➢ 3.10×10^{-1} W K^{-1} (14.4%) due to heat transfer. ➢ 1.85 W K^{-1} (95.6%) due to the chemical reaction.	1.92 W K^{-1} ➢ 2.17×10^{-11} and 9.93×10^{-8} W K^{-1} (less than 0.1%) due to viscous dissipation in the mixture and heat carrier flow respectively. ➢ 1.12×10^{-1} W K^{-1} (5.8%) due to heat transfer. ➢ 1.81 W K^{-1} (94.2%) due to the chemical reaction.	1.80 W K^{-1} ➢ 1.13×10^{-11} and 5.00×10^{-8} W K^{-1} (less than 0.1%) due to viscous dissipation in the mixture and heat carrier flow respectively. ➢ 2.70×10^{-2} W K^{-1} (1.5%) due to heat transfer. ➢ 1.77 W K^{-1} (98.5%) due to the chemical reaction.

In summary, this sensitivity analysis highlights the strong influence of inlet mixture temperature on both reactor volume and entropy generation. Higher inlet temperatures systematically reduce reactor volume and entropy generation, primarily due to the acceleration of reaction kinetics, which allows for faster conversion over shorter lengths. Conversely, lower inlet temperatures not only require longer reactors to achieve the same target conversion, but also result in higher entropy generation, particularly from heat transfer, owing to larger temperature gradients and extended reactor lengths. While lower temperatures offer a broader set of potential geometries, higher temperatures represent a more favourable compromise between reactor size and thermodynamic efficiency. However, it should be noted that preheating the mixture upstream could induce additional entropy generation outside the system boundaries, which has not been accounted for in the present study.

3.3.4 Influence of the inlet heat carrier temperature

Another investigated parameter was the inlet temperature of the heat carrier. In addition to the reference case ($T_{M,i,inl}$ = 358 K), whose operating conditions are detailed in Chapter 2, Section 2.3b, two further scenarios were considered: one with an increased inlet temperature of 368 K (+10 °C) and another with a decreased inlet temperature of 348 K (–10 °C).

The resulting Pareto fronts are presented in Figure 3.27.

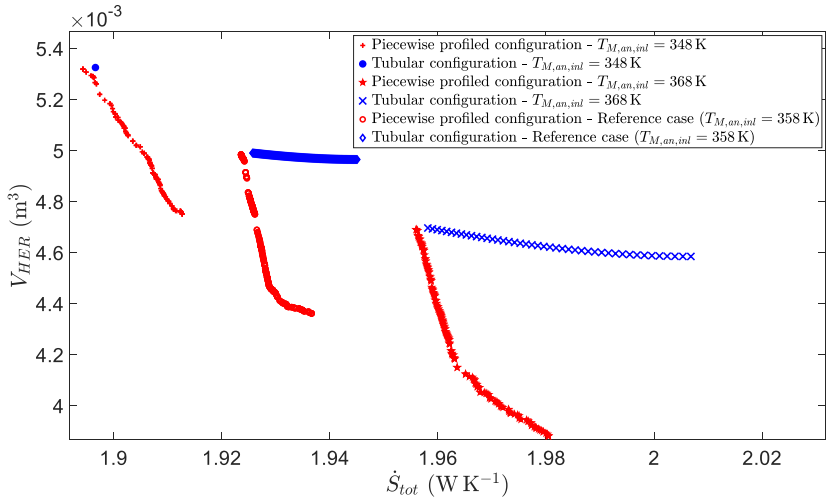

Figure 3.27: Pareto fronts for different inlet heat carrier temperature.

Figure 3.27 shows that lower inlet heat carrier temperatures lead to reduced entropy generation but at the cost of an increased reactor volume. Moreover, as observed in the two previous parameter studies, the minimal-entropy configurations converge toward the same solution meaning tubular geometries identified in the entropy minimization approach. This is confirmed in Figure 3.28, where both MPCEnt geometries exhibit a tubular profile. However, the MPCVol geometries display more complex shapes: in both cases, the profiles include two consecutive narrowings—a sharp initial contraction followed by a milder one—before diverging slightly and transitioning to a final tubular section. This trend was previously observed in other MPCVol geometries as well.

(a) (b)



(c) (d)

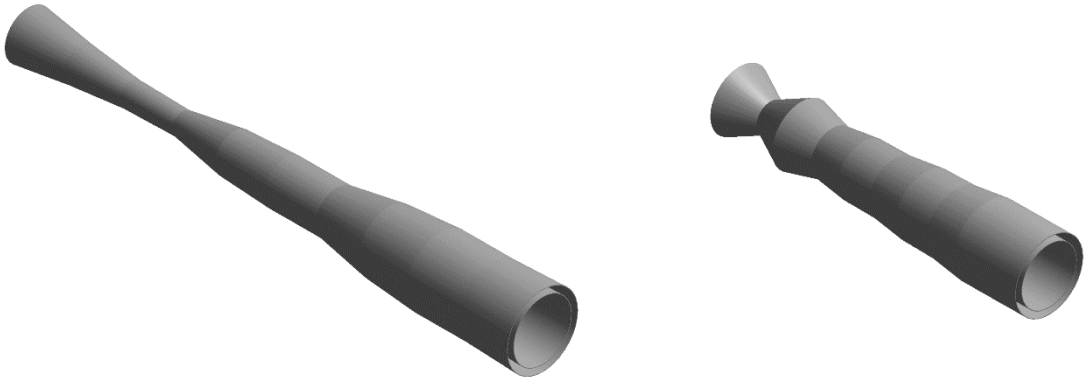

Figure 3.28: 3D representation of the MPCEnt (a) and MPCVol (c) points for $T_{M,an,inl} = 348$ K, and the MPCEnt (b) and MPCVol (d) for $T_{M,an,inl} = 368$ K.

The influence of the heat carrier's inlet temperature on temperature and conversion profiles is shown Figure 3.29. Lower inlet temperatures (Figure 3.29a) lead to smaller temperature gradients. Smaller temperature gradients result in less efficient heat transfer, which is detrimental for reactions requiring fast kinetics. Since a hotter heat carrier promotes higher reaction rates, this reduced driving force ultimately requires longer reactor lengths to achieve the desired conversion (Figure 3.29b).

This effect is further reflected in Figure 3.30, which shows the local entropy generation due to heat transfer (Figure 3.30a) and chemical reaction (Figure 3.30b). In Figure 3.30a, where entropy generation due to heat transfer is globally lower across the reactor length in the case of the reduced inlet temperature compared to the reference case. Additionally, Figure 3.30b indicates that entropy generation due to chemical reactions is only marginally affected by the variation of the inlet heat carrier temperature, leading to similar profiles across the cases.

(a) (b)

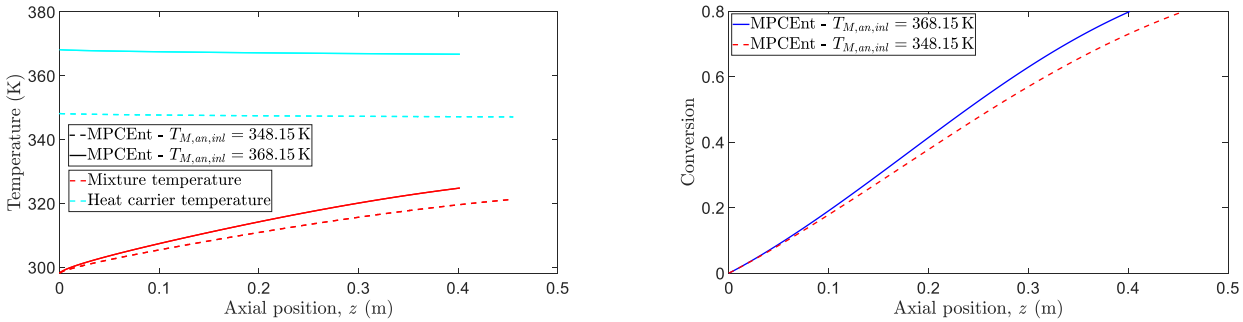

Figure 3.29: MPCEnt points for $T_{M,an,inl} = 348$ K and $T_{M,an,inl} = 368$ K: (a) Temperature profiles, (b) Acetic anhydride conversion profiles.

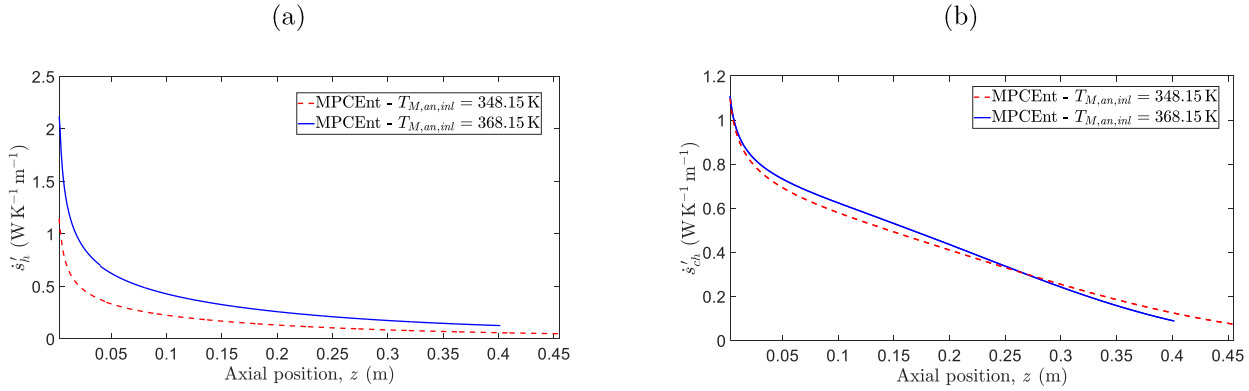

Figure 3.30: Local entropy generation rates in MPCEnt points for $T_{M,an,inl}$ = 348 K and $T_{M,an,inl}$ = 368 K: (a) Heat transfer, (b) Chemical reaction.

These trends are further confirmed by the data in Table 3.11. As anticipated from the local entropy generation profiles, lowering the inlet temperature of the heat carrier reduced entropy generation from heat transfer, owing to the reduced temperature gradients. Although the reactor length is extended to compensate for these lower gradients—thereby favouring additional entropy generation—this does not outweigh the higher entropy levels observed in the configuration with higher gradients resulting from the hotter heat carrier. Moreover, the additional entropy generation from heat transfer is not compensated by the relatively small reduction in entropy generation from chemical reactions, which appears to be only weakly, if at all, affected by the change in temperature.

Table 3.11: HER volume and entropy generation rate of the MPCEnt points of the three heat carrier inlet temperatures.

	$T_{M,an,inl}$ = 348 K	$T_{M,an,inl}$ = 358 K	$T_{M,an,inl}$ = 368 K
V_{HER}	5.32 L	4.98 L	4.70 L
$\dot{S}_{tot}$	1.89 W K^{-1} ➢ 2.27 × 10^{-11} and 1.08 × 10^{-7} W K^{-1} (less than 0.1%) due to viscous dissipation in the mixture and heat carrier flow respectively. ➢ 7.97 × 10^{-2} W K^{-1} (4.2%) due to heat transfer. ➢ 1.81 W K^{-1} (95.8%) due to the chemical reaction.	1.92 W K^{-1} ➢ 2.17 × 10^{-11} and 9.93 × 10^{-8} W K^{-1} (less than 0.1%) due to viscous dissipation in the mixture and heat carrier flow respectively. ➢ 1.12 × 10^{-1} W K^{-1} (5.8%) due to heat transfer. ➢ 1.81 W K^{-1} (94.2%) due to the chemical reaction.	1.96 W K^{-1} ➢ 2.05 × 10^{-11} and 9.13 × 10^{-8} W K^{-1} (less than 0.1%) due to viscous dissipation in the mixture and heat carrier flow respectively. ➢ 1.48 × 10^{-1} W K^{-1} (7.5%) due to heat transfer. ➢ 1.81 W K^{-1} (92.5%) due to the chemical reaction.

Overall, the inlet temperature of the heat carrier is shown to significantly impact the balance between reactor size and entropy generation. Although lower heat carrier inlet temperatures reduce local thermal entropy generation due to lower heat transfer rates, they

require longer reactors due to weaker thermal driving forces and slower kinetics, which overall, at the HER scale, results in higher heat fluxes and thermal entropy generation. Conversely, higher inlet temperatures enhance reaction rates and reduce reactor volume, but at the expense of increased entropy generation. The entropy minimization strategy consistently converges toward tubular geometries, while MPCVol solutions exhibit more complex contraction–expansion profiles. Importantly, variations in the heat carrier temperature affect entropy generation mainly through heat transfer, while the contribution from chemical reactions remains almost unchanged.

3.3.5 Influence of the mixture mass flow rate

Finally, the last parameter investigated is the mass flowrate of the reactive mixture. To assess its impact on the optimal configurations, two additional cases were studied: one in which the mixture mass flowrate was halved compared to the reference case, where $\dot{m}_{i,inl} = 5.53\ 10^{-3}$ kg s^{-1}, and another where it was doubled. The other operating conditions were kept identical and can be found in Table 2.3 in Chapter 2, Section 2.3.b. The resulting Pareto fronts are presented in Figure 3.31.

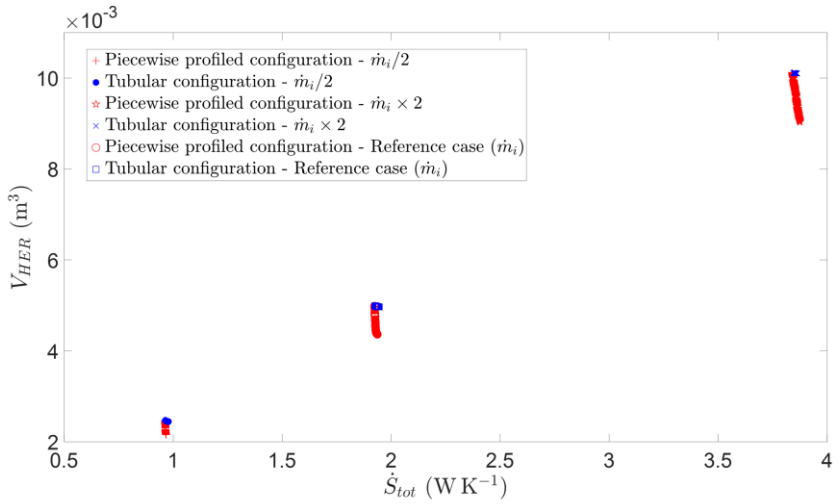

Figure 3.31: Pareto fronts for different inlet mixture mass flow rate.

Both objective functions—reactor volume and entropy generation—exhibit approximately proportional behaviours with respect to the inlet mass flowrate. As shown in Figure 3.31, increasing the mixture mass flowrate leads to both higher reactor volume and higher entropy generation. This trend can be explained by the need to maintain sufficient residence time for the reaction to proceed. For instance, in the lower mass flowrate MPCEnt configuration, the residence time is approximately 600 s for an average reaction time of 935 s, whereas in the higher mass flowrate MPCEnt configuration, the residence time is roughly 615 s for a similar reaction time profile. These results indicate that higher mass flowrates require a larger reactor volume to ensure that the reactive mixture remains within the reactor long enough to achieve the target conversion. Consequently, even though the reaction kinetics remain unchanged, the geometric adaptation, specifically a longer reactor, is necessary to compensate for the increased flowrate and to maintain the target conversion.

As shown in Figure 3.32, the optimal geometries for MPCEnt cases remain tubular in shape. Additionally, the previously discussed double narrowing pattern is again observed in the MPCVol geometries.

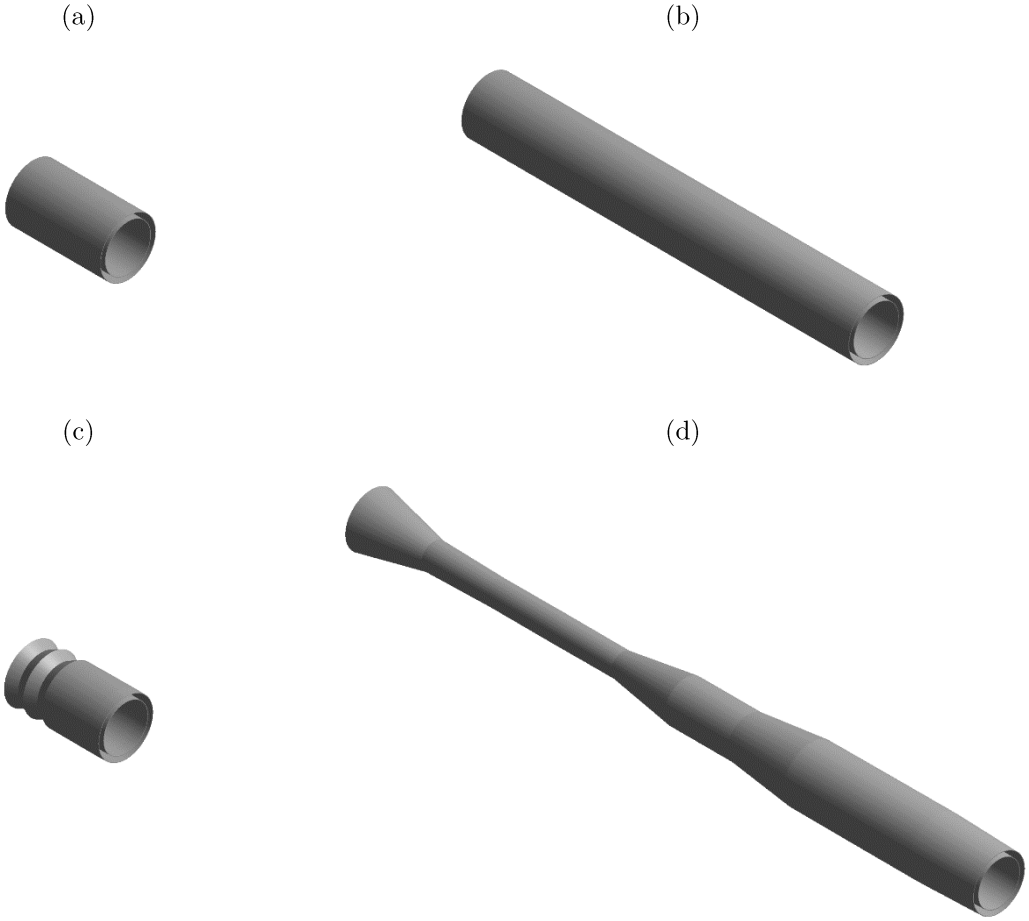

Figure 3.32: 3D representation of the MPCEnt (a) and MPCVol (c) points for $\dot{m}_i/2$, and the MPCEnt (b) and MPCVol (d) for $\dot{m}_i \times 2$.

Figure 3.33 shows that reducing the mixture mass flow rate results in a steeper temperature rise and a faster conversion progression along the reactor length. This trend is primarily due to the longer residence time, since both MPCEnt geometries have nearly the same diameter of about 10 cm. Consequently, the first 20 cm of the reactor length behave almost identically in both cases, but the lower flow rate corresponds to a lower velocity, which in turn increases the residence time and accelerates the overall conversion.

As a result, the same amount of heat transferred by the hotter heat carrier induces a more significant temperature rise in the mixture, which in turn accelerates the reaction rate due to thermal kinetic effects.

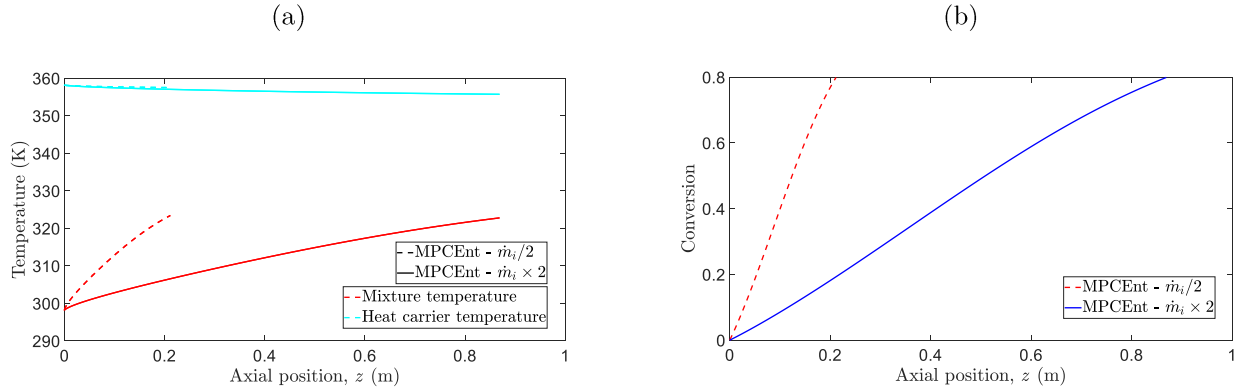

Figure 3.33: MPCEnt points for $\dot{m}_i/2$ and $\dot{m}_i \times 2$: (a)Temperature profiles, (b) Acetic anhydride conversion profiles.

These observations are consistent with the local entropy generation profiles shown in Figure 3.34. Specifically, Figure 3.34a shows that the lower flowrate case study leads to reduced entropy generation by heat transfer, most likely due to smaller thermal gradients caused by the rapid temperature rise. Moreover, Figure 3.34b indicates that the chemical reaction entropy generation is also lower in the low-flowrate case, with significantly reduced local generation along the reactor length.

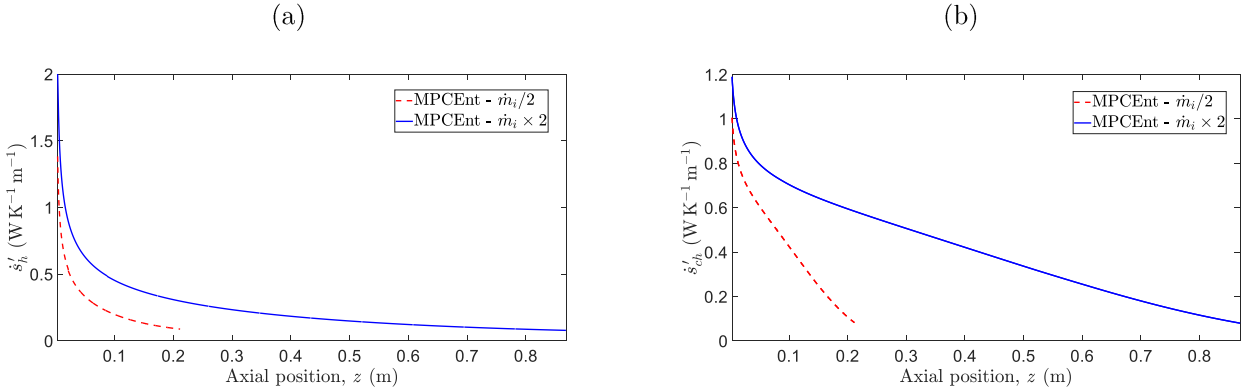

Figure 3.34: Local entropy generation rates in MPCEnt points for $\dot{m}_i/2$ and $\dot{m}_i \times 2$: (a) Heat transfer, (b) Chemical reaction.

Finally, Table 3.12 confirms the trends observed in the Pareto fronts. Doubling the inlet mass flowrate leads to a 103% increase in reactor volume, while halving it results in a 50% decrease. The same proportional trend is seen for entropy generation: the low-flowrate MPCEnt geometry results in a 50% reduction in total entropy generation, whereas the high-flowrate case causes a 100% increase. This behaviour is mainly driven by the chemical reaction contribution, as a higher mass flowrate, combined with the constraint of achieving a fixed conversion, leads to a greater number of moles reacted, and consequently to increased entropy generation from chemical reactions.

Table 3.12: HER volume and entropy generation rate of the MPCEnt piecewise profiles geometries for the three heat carrier mass flowrates.

	$\frac{\dot{m}_i}{2}$	$\dot{m}_i$	$\dot{m}_i \times 2$
V_{HER}	2.47 L	4.98 L	10.10 L
$\dot{S}_{tot}$	9.63×10^{-1} W K^{-1} ➢ 2.69×10^{-12} and 5.47×10^{-8} W K^{-1} (less than 0.1%) due to viscous dissipation in the mixture and heat carrier flow respectively. ➢ 5.76×10^{-2} W K^{-1} (6.0%) due to heat transfer. ➢ 9.05×10^{-1} W K^{-1} (94.0%) due to the chemical reaction.	1.92 W K^{-1} ➢ 2.17×10^{-11} and 9.93×10^{-8} W K^{-1} (less than 0.1%) due to viscous dissipation in the mixture and heat carrier flow respectively. ➢ 1.12×10^{-1} W K^{-1} (5.8%) due to heat transfer. ➢ 1.81 W K^{-1} (94.2%) due to the chemical reaction.	3.84 W K^{-1} ➢ 1.77×10^{-10} and 1.89×10^{-7} W K^{-1} (less than 0.1%) due to viscous dissipation in the mixture and heat carrier flow respectively. ➢ 2.16×10^{-1} W K^{-1} (5.6%) due to heat transfer. ➢ 3.62 W K^{-1} (94.4%) due to the chemical reaction.

In summary, the mass flowrate of the reactive mixture strongly influences both reactor volume and total entropy generation. Higher flowrates require longer reactors to maintain sufficient residence time for the reaction, resulting in increased reactor volume as well as a higher entropy generation, particularly from the chemical reaction, as the greater number of reacting moles amplifies the associated entropy contribution. Conversely, lower flowrates reduce residence time constraints, leading to shorter reactors, steeper temperature rises, faster conversion, and lower entropy generation. The MPCEnt geometries remain tubular across all flowrates, while MPCVol configurations exhibit the characteristic double-narrowing pattern. Overall, adjusting the mass flowrate necessitates geometric adaptations to ensure the target conversion while controlling entropy production.

3.3.6 Influence of the heat carrier mass flow rate

The influence of the heat carrier mass flow rate was investigated by halving and doubling its value relative to the reference case ($\dot{m}_{an,inl} = 4.83\ 10^{-2}$ kg s^{-1}). The other operating conditions were kept identical and can be found in Table 2.3 in Chapter 2, Section 2.3.b. The resulting Pareto fronts are compared to that of the reference configuration in Figure 3.35.

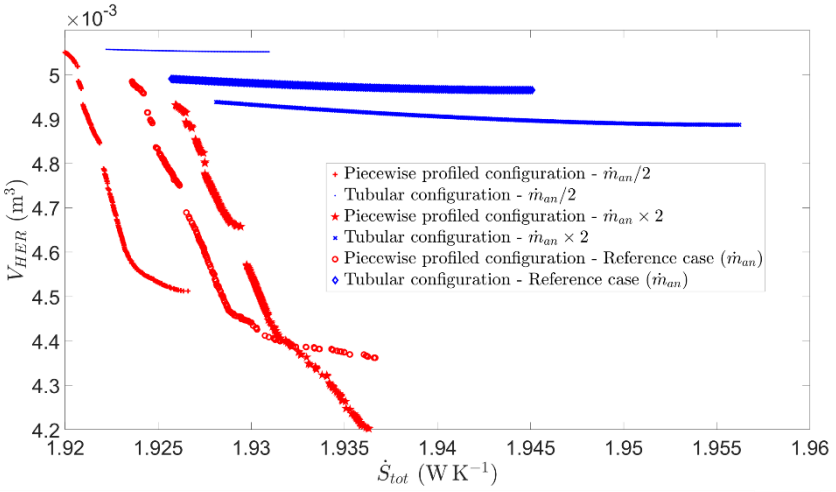

Figure 3.35: Pareto fronts for different inlet heat carrier mass flow rate.

As illustrated in Figure 3.35, increasing the heat carrier mass flow rate leads to higher entropy generation but allows for a reduction in reactor volume in the optimal configurations. Consistent with the reference case, the MPCEnt geometries remain characterized by large-diameter cylindrical reactors. Concerning the HER length, for lower mass flow rates, the reduced heat transfer efficiency necessitates longer reactors to achieve the target performance. Moreover, as Figure 3.35 indicates, lower heat carrier mass flow rates result in larger reactor volumes and longer residence times for the reactive fluid. This trend is consistent with the fact that insufficient heating of the reactive fluid reduces the reaction rate, thereby requiring additional volume to compensate.

Table 3.13 highlights that varying the heat carrier mass flow rate has only a marginal effect on the objective functions, i.e., total entropy generation and HER volume. This limited impact arises from the fact that the overall heat transfer process is not limited by by the inner reactive fluid side, where the lower heat transfer coefficient imposes the dominant resistance to heat transfer. However, increasing the heat carrier flow rate still slighly increase the relative contribution of heat transfer to the total entropy generation due to the overall greater temperature gradients. The entropy generated by the chemical reaction remains nearly unchanged. As a result, total entropy generation increases slightly with higher heat carrier flow rates.

Table 3.13: HER volume and entropy generation rate of the MPCEnt piecewise profiles geometries for the three heat carrier mass flowrates.

	$\frac{\dot{m}_{an}}{2}$	$\dot{m}_{an}$	$\dot{m}_{an} \times 2$
V_{HER}	5.05 L	4.98 L	4.93 L
	1.92 W K^{-1}	1.92 W K^{-1}	1.93 W K^{-1}
$\dot{S}_{tot}$	➢ 2.18 × 10^{-11} and 2.34 × 10^{-8} W K^{-1} (less than 0.1%) due to viscous dissipation in the mixture and heat carrier flow respectively. ➢ 1.08 × 10^{-1} W K^{-1} (5.6%) due to heat transfer. ➢ 1.81 W K^{-1} (94.4%) due to the chemical reaction.	➢ 2.17 × 10^{-11} and 9.93 × 10^{-8} W K^{-1} (less than 0.1%) due to viscous dissipation in the mixture and heat carrier flow respectively. ➢ 1.12 × 10^{-1} W K^{-1} (5.8%) due to heat transfer. ➢ 1.81 W K^{-1} (94.2%) due to the chemical reaction.	➢ 2.14 × 10^{-11} and 4.37 × 10^{-7} W K^{-1} (less than 0.1%) due to viscous dissipation in the mixture and heat carrier flow respectively. ➢ 1.15 × 10^{-1} W K^{-1} (6.0%) due to heat transfer. ➢ 1.81 W K^{-1} (94.0%) due to the chemical reaction.

In summary, variations in the heat carrier mass flow rate have a limited impact on reactor performance. While higher flow rates slightly increase total entropy generation due to enhanced temperature gradients, they allow for a minor reduction in reactor volume. Conversely, lower flow rates reduce heat transfer effectiveness, leading to longer reactors, but the effect on overall entropy generation remains small. This behaviour highlights that the dominant thermal resistance lies within the reactive mixture rather than in the heat carrier, and that the MPCEnt geometries maintain their tubular shape regardless of the heat carrier flow rate.

3.3.7 Summary of the 1D optimisation main results

To conclude the study of the 1D model where the influence of multiple parameters on the optimal geometries was investigated, the principal observations are resumed in Table 3.14.

Table 3.14: Summary of key findings from 1D model optimisation.

Parameters studied	Effect on MPCEnt $\dot{S}_{tot}$	Effect on MPCEnt V_{HER}
Increase of inlet mixture temperature	Decreases	Decreases
Increase of inlet heat carrier temperature	Increases	Decreases
Increase of inlet heat carrier mass flowrate	Increases	Decreases
Increase of inlet mixture mass flowrate	Increases	Increases

Across all studied parameters, several key observations can be made. For the hydrolysis of acetic anhydride, the optimal configurations aimed at minimizing entropy generation consistently correspond to a simple tubular reactor with the largest possible diameter. In contrast, geometries minimizing reactor volume typically display a profile characterized by two successive contractions followed by a divergent section. This trend can be attributed to the fact that inlet narrowing allows a significant volume reduction without penalizing conversion, probably due to the higher Nusselt number values in the thermally developing section of the flow.

The preference for large diameters in all MPCEnt geometries can be explained by two main factors. First, the reaction occurs under laminar flow, which implies that the local heat flux between the reactive mixture and the heat carrier is largely independent of the section diameter. A larger diameter increases the local residence volume, thereby enhancing the reaction rate, particularly because the reaction is exothermic and locally heats the mixture. Second, as previously noted, the reaction is only moderately exothermic, meaning that the mixture temperature remains below the heat carrier temperature and well below the water boiling point. Consequently, there is no need to impose a maximum temperature constraint and for the geometry to change to manage any temperature rise.

Taken together, these considerations justify the selection of a simple, large-diameter tubular reactor. Additionally, viscous dissipation is negligible in this case and does not influence the optimal designs.

It is noteworthy that chemical reaction entropy generation remains the dominant contribution in all configurations, while viscous dissipation remains negligible throughout. In the reference case, optimisation allows reducing the reactor volume by up to 12%, while the corresponding reduction in entropy generation is limited to only 1%. This suggests that prioritizing volume minimization could be more advantageous than targeting entropy reduction alone, particularly when the gain in entropy is marginal.

Another important observation is that, since the optimal geometries are consistently simple tubular shapes, there is no need for advanced or customized reactor manufacturing in the context of this specific reaction. However, this conclusion might not hold for significantly more exothermic/endothermic reactions, where heat management would become more critical. In such cases, more complex HER designs could be required to control thermal gradients effectively.

Moreover, in the specific case of liquid-phase reactions in simple double-pipe HER systems under laminar flow conditions, the only two relevant contributions to entropy generation are heat transfer and chemical reaction. Viscous dissipation, as shown in this study, plays no significant role and therefore does not influence the optimal geometry.

It is also crucial to highlight the limitations of the present work. The results obtained using the 1D model should be validated through more detailed CFD simulations or experimental data. The 1D model does not account for radial profiles, minor pressure losses associated with abrupt cross-sectional changes, nor for flow disturbances (e.g., recirculation zones or dead volumes) that such changes might induce.

Finally, it is important to emphasize that the correlations used in this work were originally developed for non-reactive fluid flow in tubes. Their application to reactive systems may introduce discrepancies that should be addressed in future studies using more representative models.

3.4 CFD optimisation

As mentioned in Chapter 2, a CFD-based optimisation was conducted using Fluent and the ANSYS Workbench optimisation module. Initially, optimisation was performed using the MOGA multi-objective genetic algorithm applied to a surrogate model constructed from the surface response of a design of experiments, and the results, with the verified points, is presented in Figure 3.36.

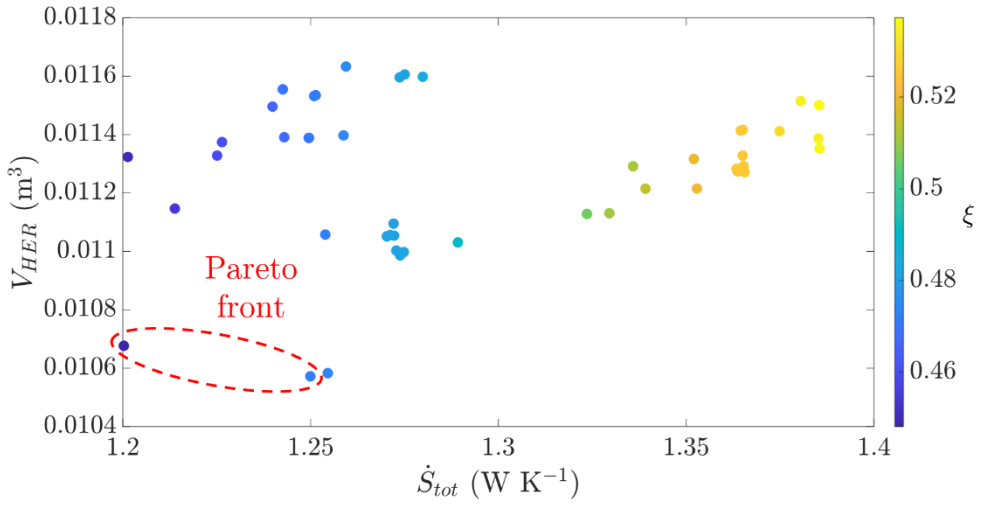

Figure 3.36: Results of the CFD surface response optimisation.

Figure 3.36 shows that the Pareto front did not satisfy the imposed conversion requirement for any of the verified points. This outcome stems from an optimisation process conducted without predefined initial data. The Pareto front presented here is based solely on the candidate points validated by CFD simulations. This underlines the limitations of the CFD-based optimisation approach: while non-validated points initially appeared to meet the conversion constraint, their verification revealed results that diverged significantly from expectations. This discrepancy reflects the inherent complexity of the system, where numerical instabilities or convergence issues can introduce biases and lead to misleading predictions. Moreover, the vast design space, characterized by highly complex shapes, increases the occurrence of suboptimal points and consequently prolongs the optimisation time. These difficulties, in turn, can propagate errors into the regression models, yielding inaccurate surrogate predictions and resulting in configurations that are far from optimal once tested.

To address these shortcomings, a second optimisation strategy was implemented. In this approach, additional initial points derived from the 1D optimisation results were incorporated into the candidate set. These reference points correspond to those of the purely tubular Pareto front discussed in Section 3.3.1, with an additional 20 cm of reactor length added to account for the inherent inaccuracies of the 1D model. The Pareto front obtained from this improved strategy, based exclusively on validated CFD points, is presented in Figure 3.37.

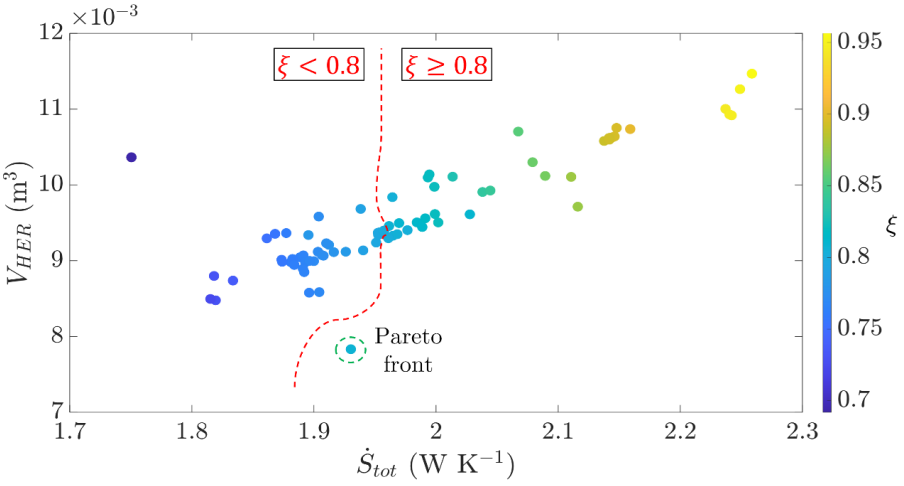

Figure 3.37: Results of the CFD surface response optimisation with additional initial points.

The results obtained using initial points from the 1D optimisation are noticeably closer to the CFD optimisation outcomes expected concerning right prediction about outlet conversion. In this Pareto front generated by the CFD optimisation, the MPCEnt and MPCVol configurations, for the valid Pareto front conversion wise, coincide and correspond to a purely tubular HER with a large diameter.

A comparison between the MPCEnt geometry derived from the 1D model (Figure 3.18) and that obtained through CFD is presented in Figure 3.38.

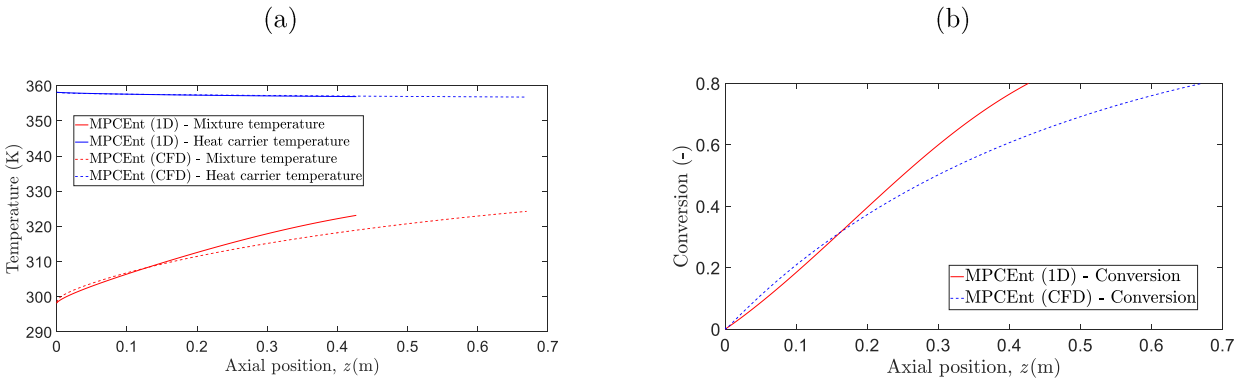

Figure 3.38: Comparison of MPCEnt geometries between 1D and CFD optimisation: (a) Temperature profiles, (b) Conversion profiles.

As anticipated from the discussion in Section 3.2, the 1D model provides a reasonable prediction of the temperature profiles. The conversion profile also agrees reasonably well in the initial section of the reactor but shows increasing deviations beyond the first 20 cm. In this region, the 1D model predicts a steeper conversion trend compared to CFD, highlighting the need for additional reactor length to achieve the target conversion of 80% in the CFD simulation. This divergence can be attributed to the inherent limitations of the 1D approach in representing nonlinear reaction kinetics under the influence of temperature and concentration gradients, as previously discussed in Section 3.2.3.Consequently, the local

performance of the HER is lower than that predicted by the idealized plug flow behaviour assumed in the 1D approach.

The 2D temperature, reaction rate and anhydride acetic contours are shown in Figure 3.39.

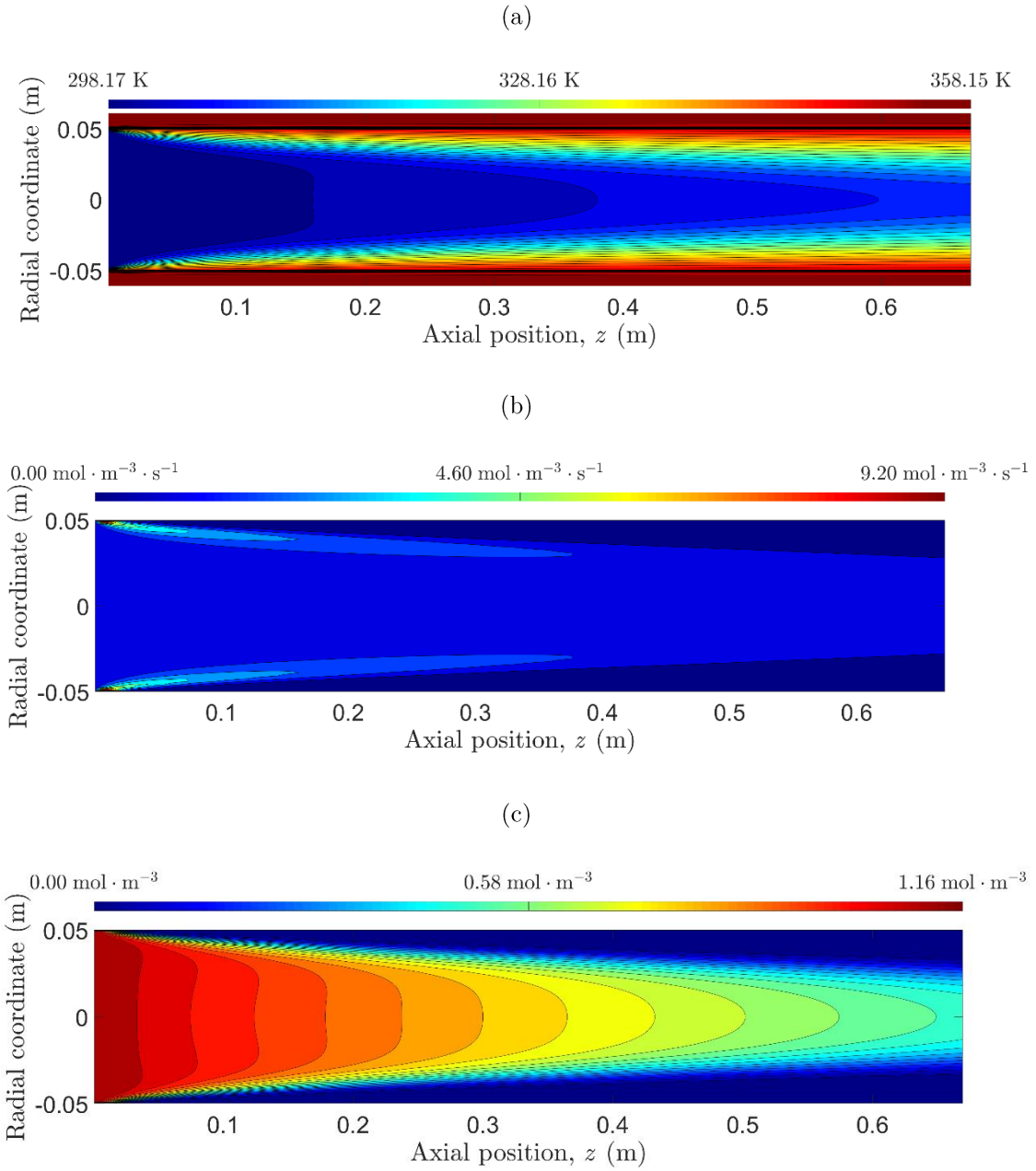

Figure 3.39: CFD MPCEnt geometry contours: (a) Temperature, (b) Reaction rate and (c) Anhydride acetic concentration.

Figure 3.39b shows that the reaction rate is initially higher near the wall at the reactor inlet, which is consistent with the observations made in Section 3.2.2. This behaviour can be attributed to the higher local temperature in this region, as the heat carrier is hotter. However, as the flow progresses, the reaction rate near the wall decreases significantly, most likely due

to the depletion of reactants consumed earlier at these locations, as illustrated in Figure 3.39c. In contrast, the reaction continues to occur in the core of the inner pipe, although at a relatively low rate, since the temperature in this region, as shown in Figure 3.39a, remains comparatively lower than that of the heat carrier. As a result, the local reaction rate is lower than that predicted by the 1D model, which assumes a uniform reaction across the entire cross-section. This discrepancy accounts for the longer reactor length required in the CFD model.

The comparison of entropy generation between the two MPCEnt geometries is presented in Table 3.15.

Table 3.15: Comparison of both MPCEnt geometries for both 1D and CFD optimisation.

	MPCEnt geometry 1D	**MPCEnt geometry CFD**
$\boldsymbol{V_{HER}}$	4.98 L	7.83 L
$\boldsymbol{L}$	0.43 m	0.67 m
$\dot{\boldsymbol{S}}_{\boldsymbol{tot}}$	1.92 W K^{-1} ➢ 2.17×10^{-11} and 9.93×10^{-8} W K^{-1} (less than 0.1%) due to viscous dissipation in the mixture and heat carrier flow respectively. ➢ 1.12×10^{-1} W K^{-1} (5.8%) due to heat transfer. ➢ 1.81 W K^{-1} (94.2%) due to the chemical reaction.	1.90 W K^{-1} ➢ 2.46×10^{-11} and 1.35×10^{-7} W K^{-1} (less than 0.1%) due to viscous dissipation in the mixture and heat carrier flow respectively. ➢ 1.00×10^{-1} W K^{-1} (5.3%) due to heat transfer. ➢ 5.76×10^{-4} W K^{-1} (less than 0.1%) due to the mass transfer. ➢ 1.80 W K^{-1} (94.7%) due to the chemical reaction.

The slight discrepancy observed between the CFD-based MPCEnt total entropy generation reported in Figure 3.37 and the values in Table 3.15 arises from the fact that the entropy generation on the Pareto front was obtained through a global entropy balance, whereas the values presented in Table 3.15 were calculated using the local entropy generation calculation approach. It should also be emphasized that the optimisation was performed with a coarser mesh compared to the detailed study presented in Section 3.2, and under a more relaxed convergence criterion (whether on residual thresholds or on the maximum number of iterations allowed). These factors inevitably introduce a minor deviation between the two approaches, which nevertheless remains within an acceptable margin (0.53% for the CFD MPCEnt geometry). Such an additional source of inaccuracy in CFD-based optimisation is unavoidable, as both the mesh density and the convergence criteria directly influence the computational time. Stricter settings would indeed improve accuracy, but at the cost of a drastic increase in computational effort, making a compromise between precision and feasibility necessary in CFD optimisation. Indeed, surrogate models provide an effective means of reducing the computational cost associated with CFD-based optimisation. However, the reliability of a

surrogate model is highly dependent on the size and representativeness of the training dataset, and insufficient sampling can compromise both its accuracy and generalisability. In the present work, the CFD optimisation results indicate that additional simulations would have been necessary to further enhance the predictive accuracy and robustness of the surrogate model.

It should be noted, however, that the use of surrogate models is not systematically more efficient than direct optimisation. In practice, generating an adequate training dataset may require a significant number of CFD simulations, and in some cases, the time invested in training the surrogate can exceed the converging time for a direct optimisation. The main advantage of this approach lies rather in its flexibility and reusability: once trained, the surrogate can be readily applied to a wide range of operating conditions, or used to perform sensitivity analyses and multi-objective optimisation at a fraction of the computational cost. This makes surrogate modelling particularly attractive when the design space to be explored is large or when several optimisation scenarios must be considered.

Overall, it can be observed that, despite the differences in reactor length, the entropy generation was accurately predicted by the 1D model. However, the additional length required in the CFD case results in a significantly larger reactor volume.

This study highlights the complementary roles of 1D modelling and CFD in the optimisation of reactor geometries. The 1D model proves to be a valuable tool for guiding the CFD-based optimisation process, particularly in highly nonlinear and complex problems such as the present case involving twelve decision variables. On its own, CFD optimisation is computationally intensive and often challenging to converge; preliminary 1D results therefore play a key role in accelerating the search for optimal geometries while reducing the associated computational cost. At the same time, CFD provides a more detailed description of radial profiles, which are inherently neglected by the 1D approach and therefore offer more accurate results. This enhanced resolution offers critical insights into local variations in concentration, temperature, and velocity, albeit at the expense of significantly higher computational effort.

3.5 Conclusion

This chapter has provided a comprehensive evaluation of entropy generation in a heat exchanger reactor performing the hydrolysis of acetic anhydride, combining systemic 1D modelling and CFD simulations. The comparison between global and local entropy generation formulations demonstrated that both yield consistent overall results, but the local approach provides unique insights into the distribution of irreversibilities across heat transfer, viscous dissipation, and chemical reaction.

The stepwise analysis revealed that, for dilute liquid-phase systems under laminar flow, viscous dissipation has a negligible impact on entropy generation, while heat transfer and especially chemical reaction remain the dominant contributions. The 1D model proved effective for capturing global tendencies, performing sensitivity analyses, and guiding preliminary optimisation, whereas CFD simulations offered a more reliable representation of radial profiles and localized phenomena. As a result, both approaches should be viewed as complementary: the 1D framework is well-suited for rapid exploration of operating conditions, while CFD ensures accuracy in systems where strong thermal gradients or complex geometries are involved.

From an optimisation perspective, the study showed that, for the hydrolysis of acetic anhydride, the optimal configurations consistently converge towards simple tubular geometries with large diameters. This result implies that entropy generation minimization does not necessarily justify the use of complex, diameter-varying profiles in this case, as the reduction in entropy was limited compared to the gain in reactor compactness. More generally, the manufacturability of optimised geometries should be considered: while advanced shapes may offer slight thermodynamic improvements, their higher fabrication cost and complexity may not be justified for moderately exothermic liquid-phase reactions. However, for reactions with stronger thermal effects, non-trivial geometries might be necessary to control heat transfer and avoid runaway conditions, making CFD-based optimisation particularly valuable.

Finally, this work has underlined the importance of coupling multi-scale approaches for reactor design. 1D models accelerate the search for promising operating windows, CFD refines the prediction of entropy sources and radial distributions, and surrogate models trained from CFD (including AI-driven regressions) represent a promising avenue to combine accuracy with computational efficiency. Together, these approaches provide a robust framework for entropy-based process intensification.

List of Figures

Figure 3.1: Case study 1: CFD contour plot of the gauge pressure (flow direction from left to right, as illustrated in Figure 2.1 of Chapter 2)..... 123

Figure 3.2: Case study 1: comparison of the axial profiles of gauge pressure between the systemic process model and CFD. Note that for the inner pipe flow, the results of the two models are practically similar and are therefore difficult to differentiate visually..... 124

Figure 3.3: Case study 1: CFD contour plots of $s\eta'''$, the local entropy generation rate by viscous dissipation. Note that a logarithmic scale is used for the colorbar. 124

Figure 3.4: Case study 1, local rate of entropy generation by viscous dissipation: comparison between the "CFD local" EGMod approach (continuous blue curve) and the "1D local" EGMod approach applied to the 1D systemic model (dashed black curve) and to the 1D reduced CFD data (dotted red curve)..... 125

Figure 3.5: Case study 2: CFD contour plot of temperature on a midplane of the heat exchanger. 128

Figure 3.6: Case study 2: comparison of the axial profiles of mixing-cup temperature between the systemic process model and CFD. Note that for the inner pipe flow, the results of the two models are practically similar and are therefore difficult to differentiate visually... 129

Figure 3.7: Case study 2: CFD contour plots of sh''', the local entropy generation rate through heat transfer. Note that a logarithmic scale is used for the colorbar..... 129

Figure 3.8: Case study 2, local rate of entropy generation by heat transfer: comparison between the "CFD local" EGMod approach (continuous blue curve) and the "1D local" EGMod approach applied to the 1D systemic model (dashed black curve) and to the 1D reduced CFD (dotted red curve)..... 130

Figure 3.9: Case study 3, CFD contour plots on a midplane of the inner pipe of the: (a) global reaction rate of hydrolysis (b) acetic anhydride molar concentration..... 136

Figure 3.10: Case study 3, comparison between the systemic process model and CFD of the axial profiles of: (a) Mixing-cup temperature of the reactive mixture. (b) Mixing-cup concentration of acetic anhydride. (c) Reaction rate. (d) Local Gibbs free energy of reaction. 137

Figure 3.11: Case study 3: CFD contour plots of sch''', the local entropy generation rate by chemical reaction in the inner pipe. Note that a logarithmic scale is used for the colorbar. 138

Figure 3.12: Case study 3: local rate of entropy generation by chemical reaction: comparison between the "CFD local" EGMod approach (continuous blue curve) and the "1D local" EGMod approach applied to the 1D systemic model (dashed black curve) and to the 1D reduced CFD data (dotted red curve)..... 138

Figure 3.13: Case study 3: CFD contour plots of $s\mu'''$, the local entropy generation rate by mass transfer in the inner pipe. Note that a logarithmic scale is used for the colorbar... 140

Figure 3.14: Case study 3: comparison of the entropy generation rates per unit length calculated using the CFD local EGMod approach. Note that a logarithmic scale is used for the coordinate axis..... 141

Figure 3.15: Geometric parameters impact for tubular geometries on the (a) total entropy generation (b) conversion (c) chemical reaction entropy generation..... 147

Figure 3.16: Pareto fronts for the reference case study. 149

Figure 3.17: 3D representation of the MPCEnt (a) and MPCVol (b) points of the reference caste study..... 149

Figure 3.18: MPCVol and MPCEnt points of the reference case study: (a) Inner pipe radius profiles, (b) Temperature profiles, (c) Acetic anhydride conversion rate profiles..... 150

Figure 3.19: Local entropy generation rates in both the MPCEnt and MPCVol geometries: (a) Viscous dissipation in the heat carrier, (b) Viscous dissipation in the reactive mixture, (c) Heat transfer, (d) Chemical reaction..... 151

Figure 3.20: Driving forces in both the MPCEnt geometry and the suboptimal geometry: (a) Viscous dissipation in the heat carrier, (b) Viscous dissipation in the reactive mixture, (c) Heat transfer and (d) Chemical reaction..... 154

Figure 3.21: Schematic representation of the equipartition criterion..... 155

Figure 3.22: Local entropy generation rates in both the MPCEnt and the suboptimal geometries: (a) Viscous dissipation in the heat carrier, (b) Viscous dissipation in the reactive mixture, (c) Heat transfer, (d) Chemical reaction..... 156

Figure 3.23: Pareto fronts for different inlet mixture temperature..... 158

Figure 3.24: 3D representation of the MPCEnt (a) and MPCVol (c) points for $T_{M,i,inl}$ = 278 K, and the MPCEnt (b) and MPCVol (d) for $T_{M,i,inl}$ = 318 K. 159

Figure 3.25: MPCEnt points for $T_{M,i,inl}$ = 278 K and $T_{M,i,inl}$ = 318 K: (a) Temperature profiles, (b) Acetic anhydride conversion profiles..... 160

Figure 3.26: Local entropy generation rates in MPCEnt points for $T_{M,i,inl}$ = 278 K and $T_{M,i,inl}$ = 318 K: (a) Viscous dissipation in the heat carrier, (b) Viscous dissipation in the reactive mixture, (c) Heat transfer, (d) Chemical reaction..... 161

Figure 3.27: Pareto fronts for different inlet heat carrier temperature..... 163

Figure 3.28: 3D representation of the MPCEnt (a) and MPCVol (c) points for $T_{M,an,inl}$ = 348 K, and the MPCEnt (b) and MPCVol (d) for $T_{M,an,inl}$ = 368 K..... 164

Figure 3.29: MPCEnt points for $T_{M,an,inl}$ = 348 K and $T_{M,an,inl}$ = 368 K: (a) Temperature profiles, (b) Acetic anhydride conversion profiles..... 164

Figure 3.30: Local entropy generation rates in MPCEnt points for $T_{M,an,inl}$ = 348 K and $T_{M,an,inl}$ = 368 K: (a) Heat transfer, (b) Chemical reaction..... 165

Figure 3.31: Pareto fronts for different inlet mixture mass flow rate. 167

Figure 3.32: 3D representation of the MPCEnt (a) and MPCVol (c) points for $mi2$, and the MPCEnt (b) and MPCVol (d) for $mi \times 2$..... 168

Figure 3.33: MPCEnt points for $mi2$ and $mi \times 2$: (a)Temperature profiles, (b) Acetic anhydride conversion profiles..... 169

Figure 3.34: Local entropy generation rates in MPCEnt points for $mi2$ and $mi \times 2$: (a) Heat transfer, (b) Chemical reaction..... 169
Figure 3.35: Pareto fronts for different inlet heat carrier mass flow rate..... 171
Figure 3.36: Results of the CFD surface response optimisation..... 175
Figure 3.37: Results of the CFD surface response optimisation with additional initial points. 176
Figure 3.38: Comparison of MPCEnt geometries between 1D and CFD optimisation: (a) Temperature profiles, (b) Conversion profiles. 176
Figure 3.39: CFD MPCEnt geometry contours: (a) Temperature, (b) Reaction rate and (c) Anhydride acetic concentration. 177

List of Tables

Table 3.1: Presentation of the six EGMod approaches. 120
Table 3.2: Summary of the operating conditions considered for each case study..... 122
Table 3.3: Case study 1: comparison of the total entropy generation rate predicted by the different EGMod approaches. 127
Table 3.4: Case study 2: comparison of the total entropy generation rate predicted by the different EGMod approaches. 133
Table 3.5: Case study 3: comparison of the total entropy generation rate predicted by the different EGMod approaches. 142
Table 3.6: HER volume and entropy generation rate of the MPCVol and MPCEnt points in the reference case study (piecewise profiled configuration)..... 152
Table 3.7: HER volume and entropy generation rate of the reference MPCEnt and suboptimal geometries. 153
Table 3.8: Equipartition criterion for the driving forces for MPCEnt and suboptimal designs..... 155
Table 3.9: Equipartition criterion for the local entropy generations for MPCEnt and suboptimal designs..... 156
Table 3.10: HER volume and entropy generation rate of the MPCEnt points of the three mixture inlet temperatures. 162
Table 3.11: HER volume and entropy generation rate of the MPCEnt points of the three heat carrier inlet temperatures..... 165
Table 3.12: HER volume and entropy generation rate of the MPCEnt piecewise profiles geometries for the three heat carrier mass flowrates. 170
Table 3.13: HER volume and entropy generation rate of the MPCEnt piecewise profiles geometries for the three heat carrier mass flowrates. 172
Table 3.14: Summary of key findings from 1D model optimisation..... 173

Table 3.15: Comparison of both MPCEnt geometries for both 1D and CFD optimisation. 178

Bibliography

Bejan, Adrian. Entropy generation through heat and fluid flow. Wiley, 1982.

Magnanelli, E., Solberg, S. B. B., & Kjelstrup, S. (2019). Nature-inspired geometrical design of a chemical reactor. Chemical Engineering Research and Design, 152, 20-29.

Chapter 4

Modelling of a heat-exchanger reactor for a heterogeneous reaction: SO_2 oxidation case study

Table of Contents

Chapter 4 185

Abstract 190

4.1 Introduction 191

4.2 SO_2 oxidation reaction 192

4.3 Heat-exchanger reactor configuration 195

4.3.1 HER geometries: uniform and piecewise profiled configurations 195

4.3.2 Operating and geometric parameters 197

4.4 Systemic process model 200

4.4.1 Mass and momentum balances 200

4.4.2 Heat balances 203

4.4.3 Species mass balances 206

4.4.4 Systemic modelling limitations 207

4.5 CFD model 208

4.6 Multi-objective optimisation problem formulation 212

4.6.1 Objective functions 212

4.6.2 Multi-objective optimisation problem 214

4.6.3 Numerical procedure 216

4.7 Conclusion 217

Appendix A. Calculation of the friction coefficient in the annular space flow 221

Appendix B. Heat transfer in the packed bed: simplifying assumptions 222

B.1 Equivalent radial thermal conductivity of the packed bed 222

B.2 Equivalent axial thermal conductivity of the packed bed and axial thermal Péclet number 224

B.3 Prater criterion and pseudo-homogenous model assumption 225

Appendix C. Calculation of Nusselt number in the annular space flow 227

Appendix D. Mass transfer in the packed bed: simplifying assumptions 228

D.1 External mass transfer resistance 228

D.2 Calculation of the effective diffusivity in the catalyst pellets 229

D.3 Internal mass transfer resistance and Weisz criterion 231

Appendix E. Detailed characterization of the MPCEnt and MPCVol designs of the reference case study 232

E.1 Mass transfer limitation 232

E.1 Heat transfer limitation 234

Nomenclature

a	Activity (-)
A_h	Heat transfer surface area (m^2)
c	Concentration (mol m^{-3})
$\bar{c}_p$	Specific heat capacity at constant pressure (J kg^{-1} K^{-1})
C_f	Friction coefficient following Darcy-Weisbach formulation (-)
$C_{inertial}$	Inertial loss coefficient (m^{-1})
$\mathfrak{D}$ (without subscript)	Molecular diffusivity (m^2 s^{-1})
$\mathfrak{D}_{eff}$	Effective mass diffusivity coefficient in the catalyst (m^2 s^{-1})
$\mathfrak{D}_K$	Knudsen diffusivity in the catalyst pores (m^2 s^{-1})
D_H	Hydraulic diameter (m)
d_i	Inner diameter of the inner tube (m)
d_p	Diameter of the catalyst pellets (m)
d_{pore}	Pores diameter in the V_2O_5 catalyst (m))
e	Thickness or width (m)
$\vec{\boldsymbol{F}}$	Vector of objective functions (-)
F	Molar flow rate (mol s^{-1})
F_a	Aspect ratio (-)
f_{ext}	External mass transfer resistance fraction (-)
h	Local heat transfer coefficient (W m^{-2} K^{-1})
k	Turbulence kinetic energy (m^2 s^{-2})
k_p	Convective mass transfer coefficient (m s^{-1})
k_r	SO_2 oxidation reaction rate coefficient (mol kg_c^{-1} Pa^{-1} s^{-1})
K	Porous medium permeability (m^2)
K_p	Equilibrium constant the reaction (-)
L	HER total length (m)
M	Molecular weight (kg mol^{-1})
Nu	Nusselt number (-)
p	Pressure (Pa)
$\vec{\boldsymbol{p}}$	Outlet pressure vector (Pa)
p_{atm}	Atmospheric pressure (Pa)
Pe_t	Thermal Péclet number (-)
Pr	Prandtl number (-)
R_{gas}	Universal Gas Constant (J mol^{-1} K^{-1})
Re	Reynolds number (-)
Re_p	Particle Reynolds number (-)
$\bar{r}$	Apparent rate of reaction (mol kg_c^{-1} s^{-1})
$\bar{r}_{vol,j}$	Volumetric formation rate of species j (kg m^{-3} s^{-1})
$r_{vol,j}$	Formation rate of species j (mol m^{-3} s^{-1})

r^*	Shape factor of the annulus space (-)
$\dot{S}$	Entropy generation rate (W K^{-1})
$\dot{s}'$	Rate of entropy generation per unit length (W K^{-1} m^{-1})
$\dot{s}'''$	Volumetric entropy generation rate (W K^{-1} m^{-3})
s°	Standard state entropy (J mol^{-1} K^{-1})
Sc	Schmidt number (-)
Sh	Sherwood number (-)
T	Absolute temperature (K)
$\vec{u}$	Reynolds-averaged velocity vector (m s^{-1})
u_D	Average Darcean (superficial) velocity (m s^{-1})
u	Velocity of the fluid (m s^{-1})
$\dot{V}$	Volumetric flow rate under actual conditions (m^3 s^{-1})
V	Volume (m^3)
V_{HER}	Total volume of the heat exchanger reactor (m^3)
$\vec{v}$	Vector of decision variables (-)
$\vec{X}$	Vector of process variables (-)
x	Molar fraction (-)
Y	Mass fraction (-)
z	Axial position along the system (m)

Greek letters

α	Local slope of the diameter profile (-)
α_m	Slope of the mth HER section (-)
$\Delta_R G$	Gibbs free energy of reaction (J mol^{-1})
$\Delta_R G^\circ$	Standard Gibbs free energy of reaction (J mol^{-1})
$\Delta_f h^\circ$	Standard enthalpy of formation (J mol^{-1})
$\Delta_R h$	Heat of reaction (J mol^{-1})
$\Delta_R h^\circ$	Standard enthalpy of reaction (J mol^{-1})
ε (without subscript)	Bed porosity (-)
ε_{AB}	Energy of molecular interaction (erg)
ε_j	Lennard–Jones parameter for species j
ε_p	Internal porosity of the catalyst particles (-)
ε_{rad}	Thermal emissivity of the catalyst and the central wall (-)
η	Dynamic viscosity (Pa s)
κ	Boltzmann constant (erg K^{-1})
λ	Thermal conductivity (W m^{-1} K^{-1})
$\bar{\bar{\lambda}}$	Thermal conductivity tensor (W m^{-1} K^{-1})
μ	Chemical potential (J mol^{-1})
ν_j	Stoichiometric coefficient of species j (-)
ξ	Conversion (-)
ρ	Density (kg m^{-3})
σ	Collision diameter (Å)

σ_{AB}	Average collision diameter (Å)
τ_p	Tortuosity factor of the catalyst particles (-)
$\bar{\bar{\tau}}$	Viscous shear stress tensor (Pa)
$\varphi_s^{'}$	Weisz criterion (-)
ψ	Sensible heat flux per unit length (W m^{-1})
Ω_D	Collision integral for molecular diffusion (-)

Subscripts

an	Refers to the fluid circulating in the annulus
ax	Refers to the axial direction
c	Refers to the catalyst
ch	Refers to the chemical reaction
cond	Refers to the conduction
eff	Refers to the effective properties of the packed bed
f	Refers to the fluid phase
flow	Refers to the flow
h	Refers to the heat transfer
i	Refers to the fluid circulating in the inner pipe
inl	Refers to the inlet of the HER
irr	Refers to an irreversible transformation
j	Refers to the species j
l	Refers to laminar
gas	Refers to gas phase
M	Refers to the mixing-cup
max	Refers to the maximum
min	Refers to the minimum
p	Refers to the catalyst particles
r	Refers to the radial direction
rad	Refers to thermal radiation
s	Refers to the solid phase in the packed bed
surf	Refers to the surface of catalyst particles
tot	Refers to the total
turb	Refers to turbulent flow
w	Refers to the wall
η	Refers to the viscous dissipation
μ	Refers to the mass transfer

Abbreviations

CFD	Computational Fluid Dynamics
DOE	Design of Experiments
HER	Heat Exchanger Reactor
MOGA	Multi-Objective Genetic Algorithm

Abstract

This chapter develops the modelling framework for a heat-exchanger reactor (HER) dedicated to the catalytic oxidation of sulphur dioxide into sulphur trioxide. Two complementary approaches are considered: a one-dimensional (1D) systemic model and a two-dimensional (2D) Computational Fluid Dynamics (CFD) model. The systemic model is formulated through mass, momentum, and energy balances to be integrated along the reactor length, with explicit treatment of pressure drop, temperature evolution, and species conversion. Assumptions underlying the pseudo-homogeneous formulation are discussed in detail, together with their limitations in the case of a strongly exothermic and nonlinear reaction such as SO_2 oxidation.

In parallel, the CFD model is constructed using ANSYS Fluent, where the packed bed is described as a porous medium. This approach enables a more detailed resolution of local transport phenomena while accounting for the complex coupling of flow, heat transfer, and chemical kinetics. Beyond these systemic and CFD formulations, the chapter also establishes the optimisation framework applied to HER geometries. Reactor compactness (minimal volume) and thermodynamic performance (minimal entropy generation) are defined as simultaneous objectives to be optimised. The optimisation is carried out under explicit operational constraints, including a minimum SO_2 conversion, upper temperature bound to limit the catalyst deactivation, and admissible pressure drop to ensure feasible operation. The numerical procedure, constraints, and optimisation variables are defined to guarantee the consistent application of both models in subsequent analyses.

Overall, this chapter establishes the methodological foundation for the parametric studies and for the comparison between systemic and CFD modelling approaches developed in the following chapter.

4.1 Introduction

The objective of this chapter is to present the modelling approaches used for the study of the heat-exchanger reactor (HER) applied to the oxidation of sulphur dioxide (SO_2). As in the case of the hydrolysis of acetic anhydride, two models are considered: a one-dimensional (1D) model and a Computational Fluid Dynamics (CFD) model. Both aim to simulate the chemical reaction in a double-pipe HER, either with a uniform diameter (classical tubular configuration) or with profiled geometries. Each model has its own limitations, reflecting the trade-off between computational cost and accuracy: the 1D model provides rapid results but with limited precision, whereas the CFD model is more complex but, if properly constructed, can offer detailed local insights.

Section 4.2 introduces the SO_2 oxidation reaction, detailing its thermodynamic properties and kinetic parameters, which are fundamental to both systemic and CFD models.

Section 4.3 describes the geometrical configuration and operational principles of the HER, including the reference design used throughout the study. This section also outlines the physical structure of the reactor, which integrates heat exchange within the catalytic zone to manage the strong exothermicity of the SO_2 oxidation reaction.

Section 4.4 presents the one-dimensional (1D) systemic process model, which includes a set of algebraic-differential equations representing mass, momentum, and energy balances along the reactor axis. Subsections provide detailed formulations for the pressure profile and momentum balance (Section 4.4.1), the temperature distribution and heat balance (Section 4.4.2), and the species concentration profiles and mass balances (Section 4.4.3). Section 4.4.4 discusses the limitations of the 1D approach, particularly in capturing radial gradients and validating the model assumptions for a highly exothermic and nonlinear reaction such as SO_2 oxidation. It also highlights uncertainties related to the kinetic parameters used.

Section 4.5 introduces the computational fluid dynamics (CFD) model, which serves as a complementary approach to the 1D model. 2D axisymmetric simulations are implemented using ANSYS Fluent, employing a porous media approximation to represent the packed catalytic bed. This section discusses the implementation of momentum, heat, and species transport equations in the finite volume framework.

Section 4.6 formulates the multi-objective optimisation problem, aimed at identifying optimal HER geometries that balance reactor compactness (minimal volume) and thermodynamic efficiency (minimal entropy generation).

4.2 SO_2 oxidation reaction

In parallel with the study of acetic anhydride hydrolysis, the oxidation of sulphur dioxide (SO_2) into sulphur trioxide (SO_3) was also investigated. This gas-phase reaction was selected due to its high industrial relevance, particularly in the context of sulfuric acid production. The oxidation of SO_2 to SO_3 constitutes a key step that follows the combustion of sulphur. The resulting SO_2 is typically processed in catalytic reactors, which are often configured as multiple adiabatic stages with intermediate cooling, or as single units equipped with internal heat exchangers (Fogler, 1992).

The reaction proceeds over a vanadium pentoxide (V_2O_5) catalyst and can be represented as:

$$SO_2 + \frac{1}{2}O_2 = SO_3$$

This exothermic and reversible reaction is governed by chemical equilibrium. Its equilibrium conversion is highly sensitive to both temperature and pressure. As illustrated in Figure 4.1, increasing the temperature results in a lower conversion to SO_3 at thermodynamic equilibrium, in accordance with Le Chatelier's principle. Conversely, increasing the system pressure enhances the conversion, since the reaction leads to a net reduction in the number of gas-phase moles.

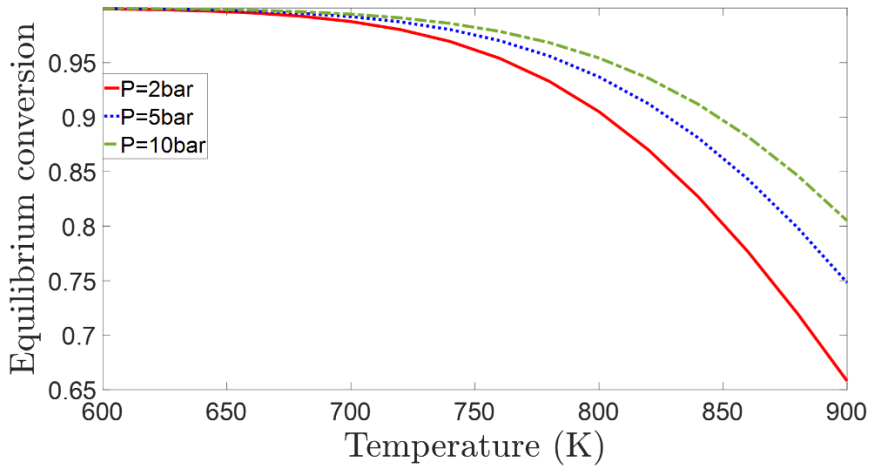

Figure 4.1: Effect of temperature on equilibrium conversion at different pressures for the composition described in Section 4.3 (11 mol% SO_2, 10 mol% O_2, 1 mol% SO_3, 78 mol% N_2).

It is important to note that thermodynamic analysis alone is insufficient, as it would suggest that lower temperatures are always more favourable for the reaction. In reality, the reaction kinetics must also be considered, since higher temperatures are generally required to achieve a sufficiently high reaction rate. Therefore, the optimisation must identify a compromise temperature path that ensures a high reaction rate while maintaining an adequate equilibrium conversion. The reaction modelling adopted in this thesis is based on the results

reported by Fogler (1992). This author provides an apparent reaction rate (including intrinsic kinetics and mass transfer limitations) which is expressed as follows for the oxidation reaction:

$$\bar{r} = k_r \sqrt{\frac{p_{SO_2}}{p_{SO_3}}} \left[p_{O_2} - \left(\frac{p_{SO_3}}{p_{SO_2} K_p p_{atm}^{-0.5}} \right)^2 \right] \quad 4.2.1$$

where $\bar{r}$ [mol kg_c^{-1} s^{-1}] is the apparent reaction rate, p_j [Pa] the partial pressure of species j and p_{atm} [Pa] the atmospheric pressure. K_p [-] and k_r [mol kg_c^{-1} Pa^{-1} s^{-1}] are respectively the equilibrium constant and the reaction rate constant respectively, and are calculated as follows:

$$K_p = \exp\left(-\frac{\Delta_R G^\circ(T)}{R_{gas} T} \right) \quad 4.2.2$$

$$k_r = 9.8692 \cdot 10^{-3} \exp\left(-\frac{176008}{1.8\,T} - 110.1 \ln(1.8T) + 912.8 \right) \quad 4.2.3$$

where R_{gas} [J mol^{-1} K^{-1}] is the universal gas constant, T [K] the absolute temperature and $\Delta_R G^\circ$ [J mol^{-1}] is the standard Gibbs energy of reaction which calculation is detailed in Chapter 2. The thermodynamical data used for this calculation for the SO_2 oxidation reaction components are detailed in Table 4.1.

Table 4.1: Thermophysical properties of the species (Linstrom and Mallard, 2001).

	Symbol	SO_2	SO_3	O_2	N_2
Standard state entropy (298.15K) (J mol^{-1} K^{-1})	$s^\circ_{j,gas}$	2.49 10^2	2.56 10^2	2.05 10^2	1.91 10^2
Standard state enthalpy of formation (298.15K) (J mol^{-1})	$\Delta_f h^\circ_j$	-2.97 10^5	-3.95 10^5	0	0

The experiments conducted by Fogler (1992), from which Equation 4.2.1 was derived, were performed under operating conditions that exhibited internal diffusional limitations due to relatively large catalyst particles, over the temperature range of 709–830 K for conversions above 5%. Therefore, this kinetic expression corresponds to an apparent reaction rate.

The oxidation reaction is exothermic with a standard enthalpy of reaction at 298.15 K of approximately –98.9 kJ · mol^{-1}. It is useful to estimate the adiabatic temperature rise, i.e., the temperature increase that would occur if all the heat released by the reaction remained in the gas phase (no heat exchange with the environment). The adiabatic temperature rise is computed from the energy balance:

$$\Delta T_{adiab} = -\frac{\Delta_R h^\circ C_{so_2,inl}}{\rho_i \bar{c}_{p_i}} \quad 4.2.4$$

where ΔT_{adiab} [K] is the adiabatic temperature rise, $\Delta_R h^{\circ}$ [J mol^{-1}] the standard enthalpy of reaction, $C_{so_2,inl}$ [mol m^{-3}] is the inlet SO_2 concentration, ρ_i [kg m^{-3}] is the gas density and $\bar{c}_{p_i}$ [J kg^{-1} K^{-1}] is the gas specific heat capacity.

For the reference inlet temperature of 778 K, the adiabatic temperature rise is estimated at approximately 316 K. This substantial increase highlights the necessity of an efficient thermal management strategy. In particular, the use of a HER appears especially well-suited in this study, as it enables effective control of the heat released during the reaction.

4.3 Heat-exchanger reactor configuration

4.3.1 HER geometries: uniform and piecewise profiled configurations

The catalytic oxidation of sulphur dioxide is investigated in a double-pipe HER. In this configuration, the reacting gas mixture flows through the inner tube containing a fixed catalytic bed, while the cooling fluid, a molten HITEC salt, circulates in the annular space to remove the heat released by the highly exothermic reaction.

Two HER configurations are considered. The first corresponds to a simple tubular design with a uniform inner diameter (Figure 4.2). This configuration is optimised with respect to the tube diameter and total reactor length, serving as a reference case and providing a baseline for assessing the benefits of more advanced reactor geometries.

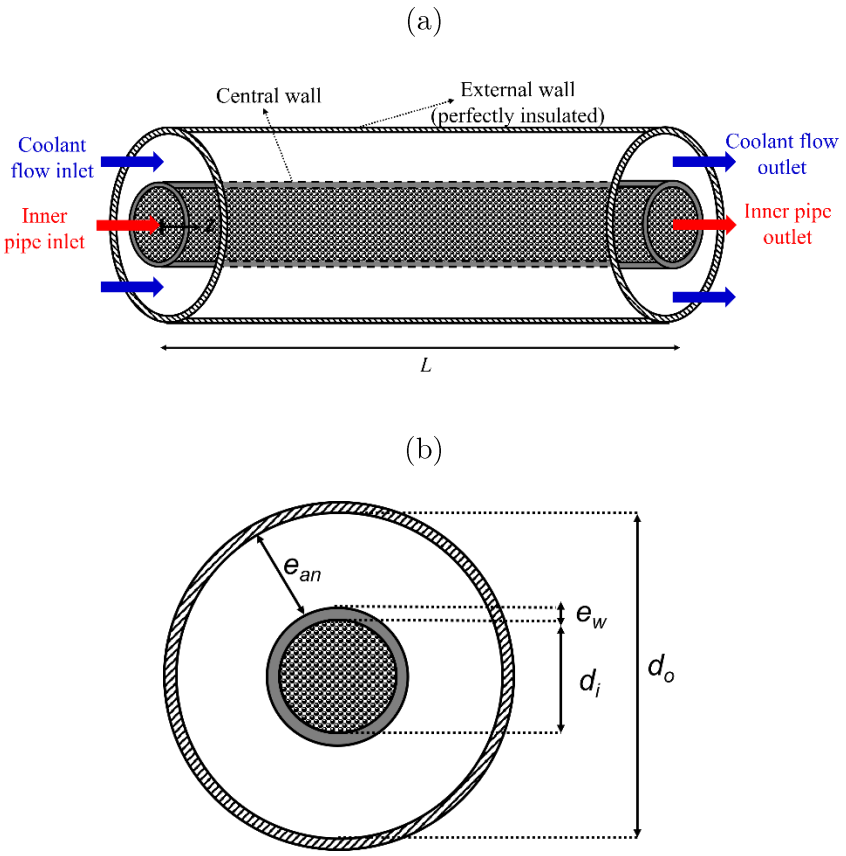

Figure 4.2: Schematic representation of the double pipe HER for the SO_2 oxidation: (a) Side view. (b) Front view.

The second configuration (Figure 2.2) introduces a piecewise variable-diameter design, in which the reactor is divided into ten equal-length segments, each defined by a linearly varying diameter with slope α (a schematic representation of slope α is provided in Chapter 2, Section 2.3). This setup is optimised not only with respect to the inlet diameter and the overall length, but also by adjusting the slope of each segment in order to identify the most favourable

geometry. Compared with the tubular configuration, this approach highlights the performance gains achievable with variable-diameter designs.

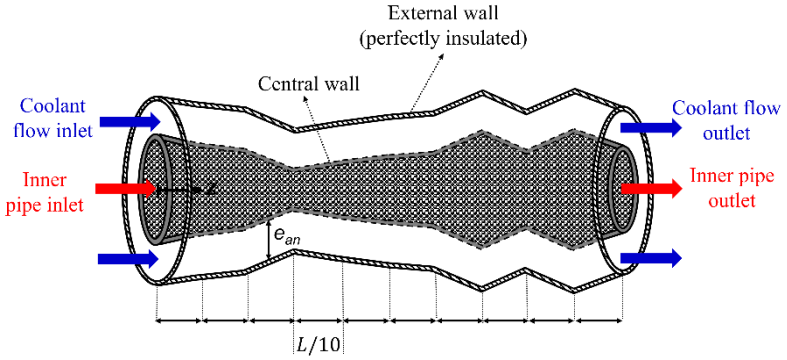

Figure 4.3: Schematic representation of the double pipe HER piecewise profiled configuration.

As in the previous case (Chapter 2 and Chapter 3 dealing with the homogeneous reaction), while the internal diameter of each segment may vary, the thicknesses of both the inner wall and the annular space remain constant. Both configurations were optimised to generate Pareto fronts, thereby illustrating the trade-off between entropy generation and reactor volume. The operating and geometrical parameters of this study are presented below.

4.3.2 Operating and geometric parameters

The investigated configuration and reference operating conditions for this chemical reaction are directly inspired by the work of Magnanelli et al. (2019). The present study extends their model in several important ways. First, instead of assuming an isothermal wall, the cooling utility is explicitly included in the process model, allowing the corresponding entropy generation to be accounted for. Second, the uniform heat transfer coefficient assumed in the earlier study is replaced by locally calculated coefficients that account for variations in the reactor geometry, fluid properties and flow rate. Third, radiative heat transfer effects, neglected by Magnanelli et al. (2019), are incorporated. Radiation becomes significant at high operating temperatures, as those encountered in SO_2 oxidation reactors. Fourth, the restrictive outlet constraints (fixed temperature and pressure) imposed by Magnanelli et al. (2019) are relaxed, thereby enabling a more realistic exploration of design alternatives. Finally, to ensure industrial relevance and operational safety, a path constraint is imposed on the maximum local temperature.

For both setups, the inner pipe, of a varying internal diameter d_i, is supposed to be filled with V_2O_5 spherical catalyst pellets of diameter $d_p = 4.57$ mm, forming a packed bed having a porosity $\varepsilon = 0.45$. Apart from d_i and L, which are used as decision variables in the multi-objective optimisation problem, all the geometric parameters of the HER are fixed, and their values are summarized in Table 4.2.

Table 4.2: Fixed geometric parameters of the HER.

Variable	Symbol	Value
Annular space width (m)	e_{an}	$1.0\ 10^{-2}$
Central wall thickness (m)	e_w	$1.0\ 10^{-3}$
Catalyst bed porosity (-)	ε	0.45
Catalyst particle diameter (m)	d_p	$4.57\ 10^{-3}$

The reactive gaseous mixture, with a molar flow rate $F_{i,inl} = 2.15 \times 10^{-1}$ mol s^{-1} (where the subscript 'inl' refers to 'inlet', at $z = 0$) is introduced into the packed bed at a pressure of $p_{M,i,inl} = 5$ bar and a temperature of $T_{M,i,inl} = 778$ K. Its inlet composition consists of 11 mol% of SO_2, 10 mol% O_2, 1 mol% of SO_3 and 78 mol% N_2. The mixture density is supposed to obey the ideal gas law and varies along the reactor due to changes in temperature (heat transfer with the coolant) and pressure (pressure drop). The heat capacities of each component have been considered temperature-dependent, using the correlations from Linstrom and Mallard (2001). The remaining thermophysical properties of the mixture, which is considered homogenous, i.e., independent from temperature and pressure, are reported in Table 4.3 and have been taken from Magnanelli et al. (2019).

Table 4.3: Gas mixture properties and operating conditions of the HER (maintained constant during optimisation, unless specified otherwise).

Properties	Symbol	Value
Catalyst density (kg m^{-3})	ρ_c	984.4
Thermal conductivity of the central wall (W m^{-1} K^{-1})	λ_w	15
Reactive mixture molar flowrate at the inlet (mol s^{-1})	$F_{i,inl}$	2.15 10^{-1}
Reactive mixture temperature at the inlet (K)	$T_{M,i,inl}$	778
Reactive mixture – absolute – pressure at the inlet (Pa)	$p_{M,i,inl}$	5×10^5
SO_2 mole fraction of the reactive mixture at the inlet (-)	$x_{SO_2,inl}$	0.11
O_2 mole fraction of the reactive mixture at the inlet (-)	$x_{O_2,inl}$	0.1
SO_3 mole fraction of the reactive mixture at the inlet (-)	$x_{SO_3,inl}$	0.01
N_2 mole fraction of the reactive mixture at the inlet (-)	$x_{N_2,inl}$	0.78
Dynamic viscosity of the reactive mixture at 298 K (Pa s)	η_i	3.72 10^{-5}
Thermal conductivity of the reactive mixture at 298 K (W m^{-1} K^{-1})	λ_i	0.03

Table 4.4: Coolant properties and operating conditions of the HER (maintained constant during optimisation, unless specified otherwise).

Properties	Symbol	Value
Molten salt flow rate (m^3 s^{-1})	$\dot{V}_{an}$	1.58 10^{-3}
Molten salt temperature at the inlet (K)	$T_{M,an,inl}$	703
Molten salt – absolute – pressure at the inlet (Pa)	$p_{M,an,inl}$	2 10^5
Molten salt specific heat capacity at 298 K (J kg^{-1} K^{-1})	$\bar{c}_{p,an}$	1.507 10^3
Molten salt density at 298 K (kg m^{-3})	ρ_{an}	1.785 10^3
Molten salt dynamic viscosity (Pa s)	η_{an}	1.7 10^{-3}
Molten salt thermal conductivity, (W m^{-1} K^{-1})	λ_{an}	0.61

The flow regime in the packed bed depends on the particle Reynolds number, calculated as follows:

$$Re_p = \frac{\rho_i \, u_{D,i} \, d_p}{\eta_i} = \frac{F_i M_i \, d_p}{\eta_i \, \frac{\pi \, d_i^2}{4}} \qquad 4.3.1$$

where ρ_i [kg m^{-3}] is the density of the mixture, η_i [Pa s] its dynamic viscosity, $u_{D,i}$ [m s^{-1}] the flow Darcean (or superficial) velocity and M_i [kg mol^{-1}] the reactive mixture molar mass. The Reynolds number varies with the axial position due to changes in density (resulting from pressure and temperature variations) and flow rate (caused by chemical and physical contraction or expansion), yet it remains greater than 100 throughout the entire reactor. For instance, at the inlet conditions, the particle Reynolds number ranges approximately from 140 for the largest reactor diameter d_i investigated (9 cm) to 4 900 for the smallest one (1.5 cm), always exceeding the threshold of 100 above which the flow becomes turbulent.

For temperature control, since the reaction is exothermic, a cooling fluid is circulated in the annulus space of the HER in co-current mode. A central wall, of thickness e_w= 1 mm, assumed to be made of stainless steel having a thermal conductivity λ_w = 15 W m^{-1} K^{-1}, separates the packed bed and the coolant. The width of the annular space, e_{an}, (where the subscript 'an' refers to 'annulus section') is fixed to 1 cm, leading to a hydraulic diameter of $D_{H,an}$ = 2 cm. The outer wall of the annular region is perfectly insulated. Given the high temperatures at which the sulphur dioxide oxidation reaction is carried out, the Hitec molten salt (53 wt% KNO_3, 40 wt% $NaNO_2$ and 7 wt% $NaNO_3$) is considered as coolant and is introduced at a temperature $T_{M,an,inl}$ = 703 K and a pressure $p_{M,an,inl}$ = 2 bar. This choice of the utility fluid was based solely on its stability at high temperatures (Marvillet, 2003), without considering other factors that would typically influence such decision, as cost, safety, and availability. For simplicity, the thermophysical properties of the molten salt were assumed independent of temperature and pressure, and their values, taken from Cavaseno (1979), are reported in Table 4.4. For efficient heat transfer, consistent with industrial practice, a coolant flow rate of $\dot{V}_{an}$ = 1.58×10^{-3} m^3 s^{-1} is used to achieve a sufficiently high Reynolds number, thus ensuring a turbulent flow regime over the whole HER length:

$$Re_{an} = \frac{\rho_{an}\, u_{an}\, D_{H,an}}{\eta_{an}} > 10\,000 \qquad 4.3.2$$

where u_{an} [m s^{-1}] is the average velocity of the molten salt flow. The operating conditions of the HER, summarized in Table 4.3, will serve as a reference throughout this study. As explained later, several multi-objective optimisations are conducted, with each optimisation involving the modification of a single operating parameter to investigate its effect on the Pareto front and optimal designs.

4.4 Systemic process model

In this study, a 1D pseudo-homogeneous model is used to simulate a continuous plug flow HER operating in steady state. The 1D approach implies calculating a single representative value for temperature, pressure and concentration at each axial position. The pseudo-homogeneous approach assumes that the gaseous mixture and the catalyst particles share the same temperature field. This simplifies mathematical modelling by addressing the complex interactions between the solid and fluid phases using lumped heat transfer parameters. It yields good results when the reaction rate and heat are not sufficient to create important local temperature differences between the two phases, and when there are no heat/mass transfer limitations of the reaction. Additional data about the 1D model hypothesis are presented in Appendix E. Specifically, the axial profiles of the external mass transfer resistance fraction, as well as the Prater and Weisz criteria, are presented. Their values support the validity of the simplifying modelling assumptions used to represent the transport phenomena in the HER. The full set of system equations used for the one-dimensional modelling is presented below.

4.4.1 Mass and momentum balances

a. Reactive fluid

Concerning pressure, its variations along the HER are due to two several effects. The first one is viscous dissipation, which converts mechanical energy into heat and tends to reduce the pressure in the downstream direction. This phenomenon constitutes the mechanical contribution to entropy generation. The second effect occurs only in the profiled configuration, where the flow cross-section area varies. It involves the reversible conversion of the static pressure into kinetic energy and vice versa, in accordance with the Bernoulli principle. Although this effect leads to pressure variation, it does not result in mechanical entropy generation, as the transformation is reversible. For the reactive mixture flow in the packed bed, pression variations along the HER express as follows:

$$\frac{dp_{M,i}}{dz} = -\frac{1}{\varepsilon^2}\rho_i u_{M,D,i}\frac{du_{M,D,i}}{dz} + \left(\frac{dp_{M,i}}{dz}\right)_{irr} \quad 4.4.1$$

$$p_{M,i}(z=0) = p_{M,i,inl} \quad 4.4.2$$

where $p_{M,i}$ [Pa] the mean pressure of the inner fluid and $p_{M,i,inl}$ [Pa] its value at the inlet, set to 5 bar here unless another value is specified.

The epsilon squared in the denominator of the first term on the right-hand side arises from the kinetic energy's dependence on the square of the interstitial velocity, rather than the Darcy velocity. The viscous dissipation contribution term in Equation 4.4.1 is calculated using the Ergun Equation:

$$\left(\frac{dp_{M,i}}{dz}\right)_{irr} = -\frac{1}{\cos(\alpha/2)}\left(\frac{150}{d_p^2}\eta\frac{(1-\varepsilon)^2}{\varepsilon^3}u_{M,D,i} + \frac{1.75\rho_i}{d_p}\frac{(1-\varepsilon)}{\varepsilon^3}u_{M,D,i}^2\right) \quad 4.4.3$$

As discussed in Section 2.4.1 of Chapter 2, an angle of $\alpha/2$ is expected to provide a better estimation of the average mixture flow direction within a profiled packed bed compared to an angle of α. It is noteworthy that due to the small size of the catalyst particles, the hydraulic permeability of the packed bed is low enough to prevent any significant flow recirculation at the transitions between sections with different inclinations. As a result, the Ergun equation is expected to accurately estimate the pressure drop in both tubular and profiled HER configurations, although it neglects flow development effects.

The average local Darcean velocity of the gaseous mixture, $u_{M,D,i}$, is calculated as follows:

$$u_{M,D,i} = \frac{F_i\, R_{gas}\, T_{M,i}}{p_{M,i}\,\frac{\pi\, d_i^2}{4}\cos\left(\frac{\alpha}{2}\right)} \quad 4.4.4$$

where R_{gas} [J mol^{-1} K^{-1}] is the universal gas constant, F_i [mol s^{-1}] the total molar flowrate of the gas mixture and $T_{M,i}$ [K] its mean temperature. The gaseous mixture, assumed to follow the ideal gas law, shows velocity variations due to thermal (heat transfer with the coolant and the heat of reaction) and chemical (changes in composition) expansion or contraction. In the 'profiled configuration', the modification of the flow cross-sectional area along the HER leads to additional variations in the velocities of both streams.

b. Heat carrier fluid

Pressure variation along the coolant flow, expresses as:

$$\frac{dp_{M,an}}{dz} = -\rho_{M,an}u_{M,an}\,\frac{du_{M,an}}{dz} + \left(\frac{dp_{M,an}}{dz}\right)_{irr} \quad 4.4.5$$

$$p_{M,an}(z=0) = p_{M,an,inl} \quad 4.4.6$$

where the first right hand side term corresponds to the reversible pressure variation and the second one represents viscous dissipation and is calculated as follows:

$$\left(\frac{dp_{M,an}}{dz}\right)_{irr} = -\frac{1}{\cos\alpha}4\,C_{f,an}\frac{\rho_{an}}{2}\frac{u_{M,an}^2}{D_{H,an}} \quad 4.4.7$$

where $C_{f,an}$ is the friction coefficient (following the Darcy-Weisbach formulation) in the annular space flow, $p_{M,an}$ [Pa] the mean pressure of the coolant fluid and $p_{M,an,inl}$ [Pa] its value at the inlet, set to 5 bar unless another value is specified. The cosine term in Equation 4.4.7 accounts for the fact that the flow direction is inclined at an angle α relative to the z-axis, i.e., to move

a distance dz along the HER, the fluid must traverse a pipe length equal to $dz/\cos\alpha$. The friction coefficient, $C_{f,an}$, was determined using the correlation reported by Rohsenow et al. (1998), detailed in Appendix A, which is valid for fully developed turbulent flows in annular sections. Thus, even in the profiled HER configuration, at each axial position, the friction coefficient is approximated as being that of a locally fully developed flow. Using this correlation implies neglecting entrance head losses and the effects of flow development. However, this is considered a convenient approximation due to the sufficient high length of the HER and the sufficiently thin width of the annulus, which should prevent any significant recirculation. In any case, there is no general correlation in the literature dedicated to precise calculation of pressure drop in a series of annular ducts with arbitrary relative inclinations.

The HITEC salt chosen as coolant for the SO_2 oxidation reactor is treated as incompressible, which means that its average velocity, $u_{M,an}$, follows Equation 4.4.8.

$$u_{M,an} = \frac{\dot{V}_{an}}{\frac{\pi}{4}\left[(d_i + 2e_w + 2e_{an})^2 - (d_i + 2e_w)^2\right]\cos\alpha} \qquad 4.4.8$$

4.4.2 Heat balances

a. Reactive fluid

When dealing with packed bed through the pseudo-homogenous approach, an effective thermal conductivity is required for describing heat transfer phenomena. This effective conductivity lumps the effects of several complex phenomena including conduction in the solid particles, conduction between the particles through their contact area, radiative heat transfer between the particles, conductive heat transfer in the fluid phase, convective heat transfer between the fluid and the solid, etc. Therefore, the effective thermal conductivity is anisotropic, reflecting the directional dependence of heat transfer due to the flow effects. As detailed in Appendix B, the axial thermal Péclet number, calculated using the axial equivalent thermal conductivity, is sufficiently large. Therefore, in the axial direction, heat transfer is mainly due to advective transport.

To clarify the thermal interactions considered in the following balance, Figure 4.4 schematically illustrates the temperature distribution across the central wall, separating the annular coolant from the packed bed. This representation highlights the different temperature levels involved in the heat exchange, namely the bulk coolant temperature, the wall temperature, and the mean packed-bed temperature, which are explicitly used in the subsequent equations.

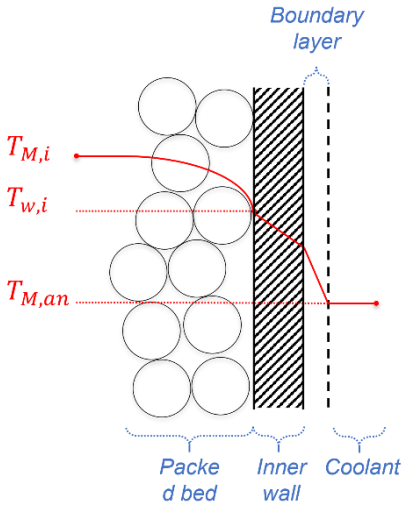

Figure 4.4: Radial temperature profile.

The heat balance in the packed bed expresses as follows:

$$\rho_i \dot{V}_i \frac{d\left(\bar{c}_{p,i} T_{M,i}\right)}{dz} = \psi + \frac{\pi d_i^2}{4}(1-\varepsilon)\rho_c \bar{r}(-\Delta_R h^\circ) \tag{4.4.9}$$

$$T_{M,i}(z=0) = T_{M,i,inl} \tag{4.4.10}$$

where $\bar{r}$ [mol kg_c^{-1} s^{-1}] is the apparent reaction rate, $\Delta_R h^\circ$ [J mol^{-1}] the standard heat of reaction and $T_{M,i,inl}$ [K] the inlet gas mixture temperature set to 778 K unless otherwise specified.

The heat flux per unit length exchanged through the inner wall between the heat carrier and the packed bed, ψ, is calculated using the electrical/thermal resistance analogy. Applying this analogy between the bulk of the coolant fluid to the inner surface of the central wall (i.e., the surface in contact with the packed bed) gives:

$$\psi = \frac{\left(T_{M,an} - T_{w,i}\right)}{\cos(\alpha)\left[\frac{1}{h_{an}\pi(d_i + 2e_w)} + \frac{ln\left(\frac{d_i + 2e_w}{d_i}\right)}{2\pi\lambda_w}\right]} \qquad 4.4.11$$

where $T_{w,i}$ [K] is the local temperature of the inner surface of the central wall, and h_{an} [W m^{-2} K^{-1}] is the convective heat transfer coefficient between the coolant flow and the central wall. The cosine term accounts for the fact that as the fluid traverses a distance dz along the HER, it exchanges heat with a section of the central wall that has a length equal to $dz/\cos\alpha$. As detailed in Appendix C, h_{an} is calculated using the correlation proposed by Vikhansky and Eskin (2024), which is established for turbulent flows in annular spaces with smooth walls.

Between the inner face of the central wall and the packed bed, heat is transferred by convection with the flowing mixture, and thermal radiation with the catalyst pellets, assuming the gas is completely transparent to infrared radiation. Therefore, the heat flux per unit length exchanged between the coolant and the packed bed, ψ, is calculated using the following equation:

$$\psi = \frac{\sigma}{\frac{2}{\varepsilon_{rad}} - 1}\frac{\pi d_i}{\cos\alpha}\left(T_{w,i}^4 - T_{M,i}^4\right) + h_i\frac{\pi d_i}{\cos\alpha}\left(T_{w,i} - T_{M,i}\right) \qquad 4.4.12$$

The first term at the right-hand side of Equation 4.4.12 represents radiative heat transfer contribution, following the model of Whitaker (1980), where σ is the Stefan-Boltzmann constant (approximately to 5.67 10^{-8} W m^{-2} K^{-4}) and ε_{rad} is the thermal emissivity in the infrared domain of the catalyst and the central wall (ε_{rad}=0.35). Given the high operating temperatures, radiative contribution to heat transfer is not negligible, particularly in hot spot zones. The second term at the right-hand side of Equation 4.4.12 represents convective heat transfer contribution. In addition to the coolant and bed temperatures $T_{M,an}$ and $T_{M,i}$, which are determined by integration of ordinary differential Equations 4.4.14, 4.4.9, Equations 4.4.11 and 4.4.12 involve two additional unknowns, ψ and $T_{w,i}$. At each integration step, these unknowns are determined by iteratively solving the non-linear algebraic Equations 4.4.11 and 4.4.12 using the Levenberg-Marquardt method.

In Equation 4.4.12, the local wall to bed convective heat transfer coefficient, $h_{w,i}$, is evaluated using the correlation of Li and Finlayson (1977) (reported in Rode (2019)):

$$Nu_i = \frac{h_i d_i}{\lambda_i} = 2.26\, Pr_i^{0,33} Re_p^{0.8} \exp\left(-\frac{6d_p}{d_i}\right) \qquad 4.4.13$$

where Nu_i is the Nusselt number of convective heat transfer between the packed bed and the wall and Pr_i the mixture Prandtl number. This correlation is applicable for randomly packed spherical pellets of uniform diameter, specifically for a particle Reynolds number range of 20 $\leq Re_p \leq$ 7 600 and a particle-to-bed diameter ratio range of 0.05 $\leq d_p/d_i \leq$ 0.3.

To calculate the local Prandtl number value in Equation 4.4.13, the mixture's dynamic viscosity and thermal conductivity are assumed to be constant, with values of 3.72 10^{-5} Pa s and 0.03 W m^{-1} K^{-1}, respectively, as reported in Table 4.3. In contrast, the mixture's heat capacity varies with composition and temperature. It is calculated as a mole fraction-weighted sum of the heat capacities of each species, with their values at a given temperature determined using the correlations provided in the NIST Chemistry Webbook (Linstrom and Mallard, 2001).

b. Heat carrier fluid

The axial temperature profiles of both the heat carrier and the reactive mixture streams are determined using an energy balance. Viscous heating is insignificant compared to the heat flux exchanged between the two streams (low Brinkman number) and is therefore neglected in the heat balance. Additionally, the velocity of the coolant fluid is sufficient for axial conduction to be disregarded in comparison to advection (high turbulent thermal Péclet number). Thus, the heat equation of the coolant expresses as follows:

$$\rho_{an} \dot{V}_{an} \bar{c}_{p,an} \frac{dT_{M,an}}{dz} + \psi = 0 \qquad 4.4.14$$

$$T_{M,an}(z = 0) = T_{M,an,inl} \qquad 4.4.15$$

where ψ [W m^{-1}] is the heat flux exchanged per unit length between the coolant and the packed bed and $T_{M,an,inl}$ [K] the inlet coolant temperature set to 703 K unless otherwise specified. The calculation of this term is detailed later in this section. The temperature $T_{M,an}$ in Equation 4.4.14 represents the mass-weighted average temperature (i.e., mixing-cup temperature) of the coolant flow. In any case, in turbulent flows, the temperature field is generally uniform across the flow sections, except within a thin boundary layer.

4.4.3 Species mass balances

a. Reactive fluid

The species mole flow rate varies along the packed bed due to the chemical reaction, and the mixture flow rate and density vary due to changes in composition and temperature. The mass conservation equation of each species in the mixture expresses as follows:

$$\frac{dF_j}{dz} = \nu_j \frac{\pi d_i^2}{4}(1-\varepsilon)\rho_c\,\bar{r} \qquad 4.4.16$$

$$F_j(z=0) = F_{j,inl} \qquad 4.4.17$$

where F_j [mol s^{-1}] is the molar flow rate of a species j of the gaseous mixture, $F_{j,inl}$ [mol s^{-1}] the inlet molar flux of species j, ν_j its stoichiometry coefficient and $\bar{r}$ [mol kg$_c^{-1}$ s^{-1}] the apparent reaction rate. Integration of Equation 4.4.16 allows determining the local molar flow rate of each species. The local species concentrations, mole fractions and the mixture flow rate can be consequently calculated using the ideal gas law. Unless otherwise specified, $F_{SO_2,inl} = 2.37\ 10^{-2}$ mol s^{-1}, $F_{O_2,inl} = 2.15\ 10^{-2}$ mol s^{-1}, $F_{SO_3,inl} = 2.15\ 10^{-3}$ mol s^{-1} and $F_{N_2,inl} = 1.68\ 10^{-6}$ mol.

b. Heat carrier fluid

The coolant fluid consists solely of HITEC salt; therefore, no transformation occurs. The species mass balance can thus be written as:

$$\frac{dF_{an}}{dz} = 0 \qquad 4.4.18$$

$$F_{an}(z=0) = F_{an,inl} \qquad 4.4.19$$

where F_{an} [mol s^{-1}] is the molar flux of the heat carrier fluid and $F_{an,inl}$ [mol s^{-1}] its inlet molar flux. Unless otherwise specified, $F_{an,inl} = 32.4$ mol s^{-1}.

4.4.4 Systemic modelling limitations

In the SO_2 oxidation case, for each geometry investigated, mass transfer limitations were assessed using two criteria. The first criterion, denoted as f_{ext}, represents the external resistance fraction (Villermaux, 1982), i.e., the ratio of the gaseous boundary layer resistance to the total mass transfer resistance. The second one, the Weisz criterion, φ'_s, which assesses the significance of concentration gradients inside the catalyst pellet. The calculation of these two criteria is detailed in Appendix D. Since their values are highly dependent on the HER design and can vary along the axial position, they were assessed and discussed for the optimal configuration of the reference cases in Appendix E.

The analysis of the different criteria confirms the validity of the simplifying assumptions adopted in this work. The evaluation of the external mass transfer resistance fraction shows that f_{ext} remains below the 0.05 threshold for all studied conditions, with only a marginal exceedance at high pressure (10 bar), which does not affect the overall conclusions. This demonstrates that external mass transfer limitations are negligible and that bulk and surface concentrations can be considered equivalent.

Conversely, the Weisz criterion largely exceeds the threshold value of 0.1, indicating the presence of significant internal diffusion limitations within the catalyst pellets. In this context, the experimentally determined kinetic law (Fogler, 1992) must be regarded as an apparent kinetic rate already incorporating these effects. Its direct use in a pseudo-homogeneous model is therefore consistent.

Finally, the Prater-type criteria reveal negligible temperature gradients across both the catalyst particles and the fluid veins, with maximum differences below 0.5 K. This confirms that thermal equilibrium between phases is rapidly established, thereby justifying the use of a homogeneous thermal description.

Overall, these results demonstrate that a pseudo-homogeneous model is appropriate for describing the reference case study. The negligible external mass transfer and heat transfer resistances simplify the formulation, while the intrinsic incorporation of internal diffusion effects into the apparent kinetic law ensures the physical consistency of the approach.

4.5 CFD model

The system was also modelled using CFD in order to perform multi-objective optimisation and to compare the results with those obtained from the 1D model. The heat carrier flow in the annular region being turbulent, direct numerical simulation of its hydrodynamics require prohibitive computational time. Therefore, turbulence effects were modelled using the realizable k-ε turbulence model. Near-wall treatment is handled through the Menter–Lechner wall function approach, which ensures proper resolution of the boundary layer behaviour without requiring extremely fine near-wall mesh. Thus, the governing equations in the annular region, where HITEC salt is assumed to flow with constant density, are as follows:

$$div(\vec{\boldsymbol{u}}) = 0 \tag{4.5.1}$$

$$\overrightarrow{\boldsymbol{div}}\left(\rho_{an}\vec{\boldsymbol{u}} \otimes \vec{\boldsymbol{u}}\right) = -\vec{\nabla}p - \overrightarrow{\boldsymbol{div}}(\bar{\bar{\boldsymbol{\tau}}}) \tag{4.5.2}$$

$$div\left(\rho_{an}\left(\bar{h} + \frac{u^2}{2}\right)\vec{\boldsymbol{u}}\right) = div\left[\left(\lambda_{an} + \lambda_{turb,an}\right)\vec{\nabla}T\right] \tag{4.5.3}$$

with

$$\bar{\bar{\boldsymbol{\tau}}} = -\left(\eta_{an} + \eta_{turb,an}\right)\left[\bar{\bar{\nabla}}\vec{\boldsymbol{u}} + \bar{\bar{\nabla}}^{T}\vec{\boldsymbol{u}} - \frac{2}{3}div(\vec{\boldsymbol{u}})\bar{\bar{\mathbf{1}}}\right] + \frac{2}{3}\rho_{an}k\bar{\bar{\mathbf{1}}} \tag{4.5.4}$$

where $\vec{\boldsymbol{u}}$ [m s^{-1}] is the Reynolds-averaged velocity vector, $\bar{\bar{\boldsymbol{\tau}}}$ [Pa] the effective viscous shear stress tensor, $\boldsymbol{k}$ [m^2 s^{-2}] the turbulence kinetic energy and $\eta_{turb,an}$ [Pa s] the turbulent viscosity in the annular flow, calculated through the realizable k-ε model. $\lambda_{turb,an}$ [W m^{-1} K^{-1}] is the turbulent conductivity in the annular flow which is calculated as follows:

$$\lambda_{turb,an} = \frac{\bar{c}_{p,an}\eta_{turb,an}}{Pr_{turb,an}} \tag{4.5.5}$$

where $Pr_{turb,an}$ denotes the turbulent Prandtl number in the annular flow, and is assigned the classical value of 0.85.

The central region of the reactor is filled with a porous catalytic medium (design to reflect a pipe filled with particle), where the flow is assumed laminar. The hydrodynamics in this domain are governed by the following Navier–Stokes–Brinkman type equations:

$$div(\rho_i\vec{\boldsymbol{u}}) = 0 \tag{4.5.6}$$

$$\varepsilon \overrightarrow{\boldsymbol{div}}(\rho_i \vec{\boldsymbol{u}} \otimes \vec{\boldsymbol{u}}) = -\varepsilon \vec{\boldsymbol{\nabla}} p - \varepsilon \, \boldsymbol{div}(\bar{\bar{\boldsymbol{\tau}}}) - \varepsilon^2 \frac{\eta_i}{K} \vec{\boldsymbol{u}} - \varepsilon^2 C_{inertial} \rho_i \mid \vec{\boldsymbol{u}} \mid \vec{\boldsymbol{u}} \tag{4.5.7}$$

$$\begin{aligned} \varepsilon div\left(\rho_i \left(\bar{h} + \frac{u^2}{2}\right)\vec{\boldsymbol{u}}\right) \\ = div\left(\bar{\bar{\boldsymbol{\lambda}}}_{\boldsymbol{i,eff}} . \vec{\boldsymbol{\nabla}} T\right) - div(\bar{\bar{\boldsymbol{\tau}}} . \vec{\boldsymbol{u}}) - div\left[(\mathfrak{D} + \mathfrak{D}_{turb})\rho_i \sum \vec{\boldsymbol{\nabla}}(Y_j)\bar{h}_j\right] \\ - \rho^{app} \bar{r} \sum \frac{\Delta_f h^\circ}{M_j} \end{aligned} \tag{4.5.8}$$

$$\varepsilon div(\rho_i Y_j \vec{\boldsymbol{u}}) = div\left[(\mathfrak{D} + \mathfrak{D}_{turb})\rho_i \vec{\boldsymbol{\nabla}}(Y_j)\right] + \bar{r}_{vol,j} \tag{4.5.9}$$

where $\vec{\boldsymbol{u}}$ represents the Reynolds-averaged physical (and not the Darcean) velocity vector. Turbulence effects within the porous medium were modelled using the Realizable k–ε model, and the effective shear stress was computed in the same manner as in the heat carrier flow, as defined in Equation 4.5.4. It is noteworthy that turbulence treatment in the porous medium is approximative as Ansys Fluent does not account for the pellets effects on turbulence generation or dissipation. In Equation 4.5.7, K [m^2] represents the porous medium permeability and $C_{inertial}$ [m] its inertial loss coefficient. By identification to the Ergun equation (Equation 4.4.3), the values of these parameters were calculated as follows:

$$K = \frac{d_p^2}{150} \frac{\varepsilon^3}{(1-\varepsilon)^2} \tag{4.5.10}$$

$$C_{inertial} = \frac{3.5}{d_p} \frac{(1-\varepsilon)}{\varepsilon^3} \tag{4.5.11}$$

In Equation 4.4.8, $\bar{\bar{\boldsymbol{\lambda}}}_{\boldsymbol{i,eff}}$ denotes the effective thermal conductivity tensor. As discussed in Section 4.4.2, the presence of flow induces orthotropic behaviour of the effective thermal conductivity within the porous medium. The tensor $\bar{\bar{\boldsymbol{\lambda}}}_{\boldsymbol{i,eff}}$ was determined following the same approach as in the 1D model, namely through Equations B.1 and B.6.

In Equations 4.5.8 and 4.5.9, $\mathfrak{D}$ [$m^2\ s^{-1}$] the mass diffusivity of the species in the mixture (assumed constant and equal to 1 10^{-5} $m^2\ s^{-1}$) and ρ_i [kg m^{-3}] the mixture local density. Y_j is the mass fraction of species j, $\bar{h}_j$ [J kg^{-1}] its specific enthalpy, $\Delta_f h^\circ$ [J mol^{-1}] its molar enthalpy of formation at local temperature and $\bar{r}_{vol,j}$ [kg m^{-3} s^{-1}] its volumetric rate of creation. $\mathfrak{D}_{turb}$ [$m^2\ s^{-1}$] is the turbulence diffusivity which was calculated assuming a uniform turbulent Schmidt number, Sc_{turb}, of 0.7:

$$Sc_{turb} = 0.8 = \frac{\eta_{turb,i}}{\rho_i \mathfrak{D}_{turb}} \tag{4.5.12}$$

In the porous domain, the mixture thermophysical properties (specific heat, thermal conductivity, viscosity) are calculated using mass-weighted mixing laws, and its density is

computed from the incompressible ideal gas law. A thermal equilibrium model is assumed between the gas and solid phases, as justified by the criteria provided in Appendix B.

As noted in Section 4.4.2 on the 1D modelling of the HER, packed beds often exhibit a temperature "jump" at the wall due to the reduced effective thermal conductivity in the near-wall region compared to the bulk. Within the equivalent porous media framework, two modelling strategies are commonly employed to represent this sharp gradient. The first adjusts the effective near-wall thermal conductivity to reflect reduced particle contacts at the wall. The second, adopted throughout this thesis, represents the near-wall temperature offset by introducing a convective transfer coefficient, h_w, at the wall–bed interface.

Since ANSYS Fluent does not natively model this phenomenon, it must be implemented using a user-defined function combined with a modelling workaround. The approach is to induce the temperature jump across the inner wall of the HER (separating the packed bed from the heat carrier) rather than localizing it strictly at the interface. Consequently, at each axial position along the HER, the local thermal conductivity of the inner wall is adjusted to produce the desired temperature drop

$$\frac{e_w}{\lambda_{w,eff}} = \frac{1}{h_w} \qquad 4.5.13$$

Thus, at each axial position, based on local fluid properties and flow conditions, h_w, is calculated from the empirical correlations presented below, and the wall's effective thermal conductivity, $\lambda_{w,eff}$, is adjusted accordingly

The local wall Nusselt number and convective coefficient are evaluated using a correlation adapted from Li and Finlayson (1977) and reported in Rode (2019), which is commonly applied for flow in packed beds:

$$\mathrm{Nu_w} = \frac{h_w d_p}{\lambda_i} = 1.19 Pr_i^{0,33} Re_p^{0,79} \qquad 4.5.14$$

where Pr_i denotes the average (over the section) Prandtl number of the reactive mixture, and Re_p the average particle Reynolds number at the given axial position. User-defined functions are employed to compute these quantities based on the local flow and fluid properties in each flow section.

The numerical procedure described above ensures that, at each axial position, the wall thermal resistance matches that of the wall boundary layer. In essence, regions with higher fluid velocity or higher Reynolds number result in a larger local $\lambda_{w,eff}$, effectively reproducing the spatially varying heat transfer from the fluid to the wall. Thus, in regions of low fluid

velocity and Reynolds number, smaller values of $\lambda_{w,eff}$ are applied, reflecting the reduced heat transfer at the wall caused by low turbulence levels.

At the annular space and inner pipe inlets, uniform profiles of velocity, temperature, and species concentrations are imposed. The porous domain inlet is modelled as a pressure inlet, where uniform pressure and temperature are set. The annular region inlet is defined as a mass flow inlet, allowing control of the desired flow rate, and its outlet is set at a fixed pressure to ensure proper outlet conditions (and optimisation constraints presented in Section 4.6.2). The porous outlet is defined as a mass flow outlet to maintain the imposed flow rate. A symmetry boundary condition is applied along the HER axis. At all solid walls, a no-slip condition is enforced, and zero-gradient conditions are applied for species mass fractions in the wall-normal direction. The outer wall and both ends of the central pipe are treated as adiabatic. Conjugate heat transfer is enforced at the internal surfaces of the central pipe, where the heat flux is continuous and fluid and solid temperatures are matched at the interface.

4.6 Multi-objective optimisation problem formulation

This section addresses the multi-objective optimisation of HERs. The detailed formulation of the optimisation problem is presented below. As previously discussed in Section 4.3, two reactor configurations are optimised under identical constraints and objective functions: a purely tubular HER and a piecewise profiled HER. The purpose is to construct a Pareto front for each configuration in order to assess the potential improvements in terms of entropy generation and reactor volume, and to evaluate the added value of employing a variable-diameter geometry in achieving these objectives.

4.6.1 Objective functions

a. Local entropy generation approach: 1D model

For each reactive case, the Pareto front illustrating the trade-off between two objective functions is determined, using the systemic modelling as a preliminary study before confirming the results through a CFD simulation. The first objective function to minimize is the volume of the HER, V_{HER}, which is proportional to the space occupied and to the mass of catalyst in the SO_2 oxidation case. This volume is estimated using the same methodology described in Chapter 2, Section 2.6.1.

The second objective function to be minimized is the total entropy generation rate in the HER, denoted as $\dot{S}_{tot}$ [W K^{-1}]. Using the local method, the total entropy generation rate per unit length of the HER, denoted as $\dot{s}_{tot}$ [W K^{-1} m^{-1}], is the sum of different contributions (Johannessen and Kjelstrup, 2004, and Michaud et al., 2024) as presented in Chapter 1:

$$\dot{s}_{tot}^{'} = \dot{s}_{\eta,i}^{'} + \dot{s}_{\eta,an}^{'} + \dot{s}_{h}^{'} + \dot{s}_{ch}^{'} \tag{4.6.1}$$

The only difference in the formulation, compared to the entropy generation equation presented in Chapter 2, Section 2.6.1, lies in the expression of the chemical reaction contribution, which is slightly modified to account for the fixed bed. Specifically, the last term on the right hand-side of Equation 4.6.1, $\dot{s}_c$ [W K^{-1} m^{-1}], represents the chemical reaction contribution to entropy generation and is calculated as follows for the SO_2 oxidation:

$$\dot{s}_{ch}^{'} = -\frac{\pi d_i^2}{4}(1-\varepsilon)\rho_c \bar{r}\frac{\Delta_R G}{T_{M,i}} \tag{4.6.2}$$

where $\Delta_R G$ [J mol^{-1}] is the reaction Gibbs energy, which is evaluated at the local bed temperature $T_{M,i}$, as follows:

$$\Delta_R G\left(T_{M,i}\right) = \Delta_R G^{\circ}\left(T_{M,i}\right) + R_{gaz} T_{M,i} \ln\left(\prod\left(a_j\right)^{\nu_j}\right) \tag{4.6.3}$$

where $\Delta_R G^\circ$ [J mol^{-1}] is the standard Gibbs energy of reaction and a_j [-] is the activity of species j.

Given that the operating conditions considered in the SO_2 oxidation involve relatively low pressures and high temperatures, the gas mixture is assumed to follow the ideal gas law. Therefore, the activities of the species correspond to the ratio of the partial pressure of species j to the reference pressure which is of one atmosphere.

Finally, the total entropy generation rate, $\dot{S}_{tot}$, is computed by integrating the local entropy source terms along the length of the HER:

$$\dot{S}_{tot} = \int_0^L \dot{s}'_{tot}\, \mathrm{d}z \qquad 4.6.4$$

b. Local entropy generation approach: CFD model

For the CFD modelling, as for the acetic anhydride hydrolysis case study, the entropy generation term is the sum of the following contributions:

$$\dot{s}'''_{tot} = \dot{s}'''_{\eta} + \dot{s}'''_{h} + \dot{s}'''_{\mu} + \dot{s}'''_{ch} \qquad 4.6.5$$

where $\dot{s}'''_{\eta}$, $\dot{s}'''_{h}$, $\dot{s}'''_{\mu}$ and $\dot{s}'''_{ch}$ represent the volumetric entropy generation rates which are respectively due to viscous dissipation, heat transfer, mass transfer and chemical reaction. Their formulations are the same as those introduced in Chapter 2, Section 2.6.1.

The total entropy generation rate of the system, $\dot{S}_{tot}$ [W K^{-1}], can be deduced by volume integration over the numerical domain (the total volume of the HER):

$$\dot{S}_{tot} = \iiint \dot{s}'''_{tot}\, dV \qquad 4.6.6$$

where dV represents an infinitesimal volume (usually approximated as the volume of the CFD mesh cells).

4.6.2 Multi-objective optimisation problem

The multi-objective optimisation problem is stated as follows:

$$\underset{\vec{v}}{\text{Min}}\,\vec{F} = \underset{\vec{v}}{\text{Min}}[\dot{S}_{tot}, V_{HER}]^T \quad 4.6.7$$

where $\vec{F}$ is the vector of objective functions and $\vec{v}$ represents the vector of decision variables. For the tubular HER, the decision variables include two variables, the total length of the HER, L, and the internal diameter of the inner tube, d_i. In the case of the profiled HER, there are 12 decision variables: the total length, L, the internal diameter of the packed bed at the inlet, $d_{i,inl}$ and the slopes of the 10 sections, denoted as α_m (where $1 \leq m \leq 10$). A positive slope indicates a divergent section of the HER, while a negative one to a convergent section.

This minimization multi-objective problem is subject to:

a- The process model equations, described in Section 4.4, which constitutes an algebraic-differential system of equations (the algebraic equation arises from radiative heat transfer between the wall and the bed, while the differential equations stem from momentum, energy, and species balances):

$$\vec{f}\left(z, \vec{X}, \frac{d\vec{X}}{dz}, \vec{v}\right) = \vec{0} \quad 4.6.8$$

where $\vec{X}$ represents the set of process variables, including the temperature and pressure of the reactive mixture and the heat carrier, and the composition of the reactive mixture. Solving this system of equations for a given vector of decision variables allows for the computation of the objective functions.

b- The boundary conditions listed in Section 4.3, which remain unchanged across the various case studies conducted except if other conditions are specified:

$$\vec{X}(z = 0) = \vec{X}_{inl} \quad 4.6.9$$

c- End point or terminal inequality constraints. They correspond to constraints which must be satisfied at the end of the integration domain, i.e., at $z = L$:

$$\vec{p}(z = L) = [p_i(z = L), p_{an}(z = L)]^T \geq [1\ \text{atm}, 1\ \text{atm}]^T \quad 4.6.10$$

$$\xi(z = L) \geq \xi_{min} \quad 4.6.11$$

Outlet pressure constraints (Equation 4.6.10) are imposed for practical reasons, for the SO_2 oxidation case, specifically to allow flows discharge under atmospheric pressure conditions.

The variable ξ [-] represents the chemical reaction conversion. The minimal conversion to achieve, denoted as ξ_{min}, is set to 0.8 across the various case studies conducted, unless otherwise specified.

d- Path constraints. They correspond to constraints which must be satisfied at each point of the integration domain, i.e., $\forall\, z \in [0, L]$. For the SO_2 oxidation case, the constrains are:

$$1.5\ \text{cm} \leq d_i \leq 9\ \text{cm} \tag{4.6.12}$$

$$T_i \leq T_{max} \tag{4.6.13}$$

The constraints expressed in Equation 4.6.12 ensure compliance with the applicability domain of the correlation of Li and Finlayson (1977) presented in Equation 4.4.13, which is valid for a catalyst particle to bed diameter ratio in the range of $0.05 \leq d_p/d_i \leq 0.3$. The constraint expressed in Equation 4.6.13 establishes the maximum allowable temperature in the packed bed to prevent hot spots that can lead to catalyst degradation and sintering. This maximum allowable bed temperature, for the SO_2 oxidation case, denoted as T_{max}, is set at 880 K (Fogler, 1992) for all case studies conducted, unless otherwise specified.

e- Decision variables bounds. These inequality constraints establish the permissible values for the decision variables, thereby defining the feasible region in which the optimal solutions can be identified:

$$0.1\ \text{m} \leq L \leq 10\ \text{m} \tag{4.6.14}$$

$$-\frac{\pi}{2} < \alpha_m < \frac{\pi}{2} \ \text{for}\ 1 \leq m \leq 10 \tag{4.6.15}$$

The constraints outlined in Equation 4.6.14 define the permissible length for the HER, while those in Equation 4.6.15 apply exclusively to the profiled configuration. All slopes of diameter profiles, except for vertical sections, are permitted. In practice, the bounds established for the decision variables remained unreached throughout the optimisation process, meaning they did not influence any of the optimal designs.

4.6.3 Numerical procedure

The process model described in Section 4.4, formulated as a system of algebraic-differential equations, was implemented and solved using MATLAB. The differential equations were integrated using a variable-step solver based on backward differentiation formulas. At each integration step, the accompanying algebraic equations were solved using the Levenberg-Marquardt algorithm.

The multi-objective optimisation problem (Section 4.6.2) was addressed using the NSGA-II (Non-dominated Sorting Genetic Algorithm II), also implemented in MATLAB. As a global optimisation algorithm, NSGA-II is particularly well-suited to handling complex and nonlinear optimisation problems. In contrast to gradient-based methods, it avoids entrapment in local minima, thereby enabling the identification of a diverse set of Pareto-optimal solutions. For each case study, the algorithm generates a Pareto front, illustrating the trade-off between minimizing the HER volume and reducing the entropy generation rate.

Due to time constraints, no CFD-based optimisation was conducted within the present work. A logical next step would be to develop a more detailed and comprehensive CFD model and use it as a foundation for multi-objective optimisation. Such an approach would allow a more accurate assessment of the spatial distributions of temperature, velocity, and concentration, capturing phenomena that are not fully represented in the 1D model. Additionally, integrating CFD-based optimisation could provide deeper insights into the potential benefits of variable-diameter geometries and the interplay between entropy generation and reactor performance, ultimately guiding the design of more efficient HERs.

4.7 Conclusion

This chapter has presented the modelling framework developed for the study of SO_2 oxidation in a HER. Building on the previous case study of acetic anhydride hydrolysis, this second application addressed a more complex system, characterised by a heterogeneous catalytic reaction and a strong exothermicity. The choice of this reaction required careful consideration of both mass and heat transfer limitations, which were evaluated through classical criteria such as Prater and Weisz numbers. These analyses justified the use of a pseudo-homogeneous description with apparent kinetics, while also underlining the need for caution in interpreting results under conditions where transport limitations may become significant.

Two complementary modelling strategies were implemented. The one-dimensional systemic model was formulated through mass, momentum, and energy balances integrated along the reactor length, enabling a rapid yet approximate representation of the process. Its limitations were explicitly discussed, particularly regarding the treatment of radial transport phenomena and the reliability of simplified assumptions when applied to a highly nonlinear and heat-sensitive reaction. In parallel, a CFD model was developed using a porous medium approach within ANSYS Fluent, solving the coupled hydrodynamic, thermal, and species transport equations in a two-dimensional axisymmetric geometry. This second modelling strategy provides detailed spatial resolution and offers a valuable benchmark against which to assess the predictive capability of the 1D model.

Finally, the chapter introduced the formulation of a multi-objective optimisation problem, combining reactor compactness (via total volume minimisation) with thermodynamic efficiency (via entropy generation minimisation). The definition of objective functions, decision variables, and the numerical strategy establishes a consistent framework for systematically exploring HER geometries adapted to SO_2 oxidation.

Overall, this chapter provides the theoretical and methodological basis for the parametric study and model comparison presented in the next chapter. The systemic and CFD models will be confronted to assess their respective predictive capabilities, and the optimisation framework will be applied to identify the design trade-offs governing the development of compact and efficient HERs for heterogeneous reactions such as SO_2 oxidation for various operating conditions.

List of Figures

Figure 4.1: Effect of temperature on equilibrium conversion at different pressures for the composition described in Section 4.3 (11 mol% SO_2, 10 mol% O_2, 1 mol% SO_3, 78 mol% N_2). 192

Figure 4.2: Schematic representation of the double pipe HER for the SO_2 oxidation: (a) Side view. (b) Front view. 195

Figure 4.3: Schematic representation of the double pipe HER piecewise profiled configuration..... 196

Figure 4.4: Radial temperature profile..... 203

Figure 4.5: Schematic representation of the two maximum temperature differences criteria..... 225

Figure 4.6: MPCEnt and MPCVol geometries of the reference case: (a) 3D representation of the MPCVol geometry, (b) 3D representation of the MPCEnt geometry and (c) Packed bed radius profiles..... 232

Figure 4.7: Axial profiles of f_{ext} along the MPCVol and MPCEnt designs of the reference case study..... 233

Figure 4.8: Axial profiles of the Weisz criterion along the MPCVol and MPCEnt designs of the reference case study..... 233

Figure 4.9: Axial profiles of the temperature difference between the centre and the surface of the catalyst particles along the MPCVol and MPCEnt designs of the reference case study. 234

Figure 4.10: Axial profiles of the temperature difference across the fluid vein along the MPCVol and MPCEnt designs of the reference case study..... 234

List of Tables

Table 4.1: Thermophysical properties of the species (Linstrom and Mallard, 2001)... 193

Table 4.2: Fixed geometric parameters of the HER..... 197

Table 4.3: Gas mixture properties and operating conditions of the HER (maintained constant during optimisation, unless specified otherwise). 198

Table 4.4: Coolant properties and operating conditions of the HER (maintained constant during optimisation, unless specified otherwise)..... 198

Bibliography

Cavaseno, V. (Ed.). (1979). Process heat exchange. McGraw-Hill.

Díaz-Heras, M., Belmonte, J. F., & Almendros-Ibáñez, J. A. (2020). Effective thermal conductivities in packed beds: Review of correlations and its influence on system performance. Applied Thermal Engineering, 171, 115048.

Fogler, H. S. (1992). Elements of chemical reaction engineering (2nd ed.). Prentice Hall P T R.

Johannessen, E., & Kjelstrup, S. (2004). Minimum entropy production rate in plug flow reactors: An optimal control problem solved for SO_2 oxidation. Energy, 29(12–15), 2403–2423.

Krupiczka, R. (1967). Analysis of thermal conductivity in granular materials. International Chemical Engineering, 7(1), 122.

Li, C.-H., & Finlayson, B. A. (1977). Heat transfer in packed beds—A reevaluation. Chemical Engineering Science, 32(9), 1055–1066.

Linstrom, P. J., & Mallard, W. G. (2001). The NIST chemistry webbook: A chemical data resource on the internet. Journal of Chemical & Engineering Data, 46(5), 1059–1063. https://doi.org/10.1021/je000236i

Magnanelli, E., Solberg, S. B. B., & Kjelstrup, S. (2019). Nature-inspired geometrical design of a chemical reactor. Chemical Engineering Research and Design, 152, 20–29. https://doi.org/10.1016/j.cherd.2019.09.022

Marvillet, C. (2003). Fluides caloporteurs et frigoporteurs—Définitions. Critères de choix. Thermique pour l'industrie. https://doi.org/10.51257/a-v1-be9570

Mazidi, M., Behbahani, R. M., & Fazeli, A. (2017). Ce promoted V_2O_5 catalyst in oxidation of SO_2 reaction. Applied Catalysis B: Environmental, 209, 190–202.

Michaud, A., Hreiz, R., & Portha, J. F. (2024). Entropy generation analysis for designing efficient and sustainable heat exchangers and chemical reactors: From 1D modelling to detailed CFD simulations. Chemical Engineering Science, 300, 120615.

Ranz, W. E. (1952). Friction and transfer coefficients for single particles and packed beds. Chemical Engineering Progress, 48, 247–253.

Rode, S. (2019). Opérations polyphasiques en génie des procédés: Hydrodynamique, transferts, réactions, séparations mécaniques.

Rohsenow, W. M., Hartnett, J. P., & Cho, Y. I. (1998). Handbook of heat transfer. McGraw-Hill.

Schotte, W. (1960). Thermal conductivity of packed beds. AIChE Journal, 6(1), 63-67.

Sciacovelli, A., & al. « Entropy Generation Analysis as a Design Tool—A Review ». Renewable and Sustainable Energy Reviews, vol. 43, 2015, p. 1167 81. DOI.org (Crossref), https://doi.org/10.1016/j.rser.2014.11.104

Techo, R., Tickner, R. R., & James, R. E. (1965). An accurate equation for the computation of the friction factor for smooth pipes from the Reynolds number. Journal of Applied Mechanics, 32(2), 443–443. https://doi.org/10.1115/1.3625826

Vikhansky, A., & Eskin, D. (2024). Modeling of turbulent flows through annuli with smooth and rough walls; drag reduction and heat transfer. Applied Thermal Engineering, 124671.

Villermaux, J. (1982). Génie de la réaction chimique: Conception et fonctionnement des réacteurs. Technique et documentation.

Wang, Q., Liang, X., Liu, B., Song, Y., Gao, G., & Xu, X. (2020). Thermal conductivity of V_2O_5 nanowires and their contact thermal conductance. Nanoscale, 12(2), 1138–1143. https://doi.org/10.1039/C9NR08803B

Welty, J., Rorrer, G. L., & Foster, D. G. (2014). Fundamentals of momentum, heat, and mass transfer. John Wiley & Sons.

Whitaker, S. (1980). Radiant energy transport in porous media. Industrial & Engineering Chemistry Fundamentals, 19(2), 210–218.

Appendix A. Calculation of the friction coefficient in the annular space flow

In the SO_2 oxidation case, the coolant flow in the annular space is turbulent. To determine the friction coefficient (Darcy-Weisbach formulation) for fully developed turbulent flow in annular ducts, Rohsenow et al. (1998) recommend calculating an equivalent laminar diameter, $d_{an,l}$, as follows:

$$d_{an,l} = D_{H,an} \frac{1 + r^{*2} + \frac{1 - r^{*2}}{ln(r^*)}}{(1 - r^*)^2} \quad \text{A.1}$$

where r^* is the outer diameter to the inner diameter ratio of the annulus:

$$r^* = \frac{d_i + 2e_w + 2e_{an}}{d_i + 2e_w} \quad \text{A.2}$$

The Reynolds number based on this equivalent laminar diameter, $Re_{D_{an,l}}$, is then determined as follows:

$$Re_{d_{an,l}} = \frac{\rho_{an} u_{M,an} d_{an,l}}{\eta_{an}} \quad \text{A.3}$$

Using this modified Reynolds number in the correlation developed by Techo et al. (1965) for turbulent flow in round pipes allows for the estimation of the friction coefficient in the annular zone:

$$\frac{1}{\sqrt{C_{f,an}}} = 1.7372\, ln\left(\frac{Re_{d_{an,l}}}{1.964\, ln\left(Re_{d_{an,l}}\right) - 3.8215}\right) \quad \text{A.4}$$

Appendix B. Heat transfer in the packed bed: simplifying assumptions

Packed beds are typically modelled as continuous porous media, where the macroscopic properties depend on the characteristics of both the solid and fluid phases, as well as the effects of flow. This appendix presents the equations used to calculate the equivalent properties of the porous medium, along with the simplifying assumptions employed in modelling heat transfer phenomena within the packed bed.

B.1 Equivalent radial thermal conductivity of the packed bed

Due to the flow effects, the equivalent properties of the bed, particularly its thermal conductivity, are anisotropic. This section deals with the estimation of the packed bed effective conductivity in the radial (and orthoradial) direction, $\lambda_{eff,r}$, i.e., in the direction normal to the mean flow.

The radial conductivity of the packed bed consists of three contributions, as detailed in the following equation:

$$\lambda_{eff,r} = \lambda_{cond} + \lambda_{flow,r} + \lambda_{rad} \tag{B.1}$$

The first term on the right-hand side, λ_{cond}, represents the contribution of heat conduction through the bed in the absence of flow (whether forced or natural convection) and is therefore sometimes referred to as "stagnant thermal conductivity." This term accounts for heat conduction occurring within the stagnant fluid, within each solid particle, and between adjacent solid particles at their contact points. In the case of randomly packed spherical particles, this contribution is isotropic (i.e., the same in both radial and axial directions) and is calculated in this thesis using the correlation established by Krupiczka (1967) (and reported in Díaz-Heras et al. (2020)):

$$\lambda_{cond} = \lambda_f \left(\frac{\lambda_s}{\lambda_f}\right)^{0.280 - 0.757 \log_{10}(\varepsilon) - 0.057 \log_{10}\left(\frac{\lambda_s}{\lambda_f}\right)} \tag{B.2}$$

where λ_f and λ_s are the thermal conductivity of the fluid and solid phases respectively. In this study, the thermal conductivity of the gaseous mixture is taken to be 0.03 W m^{-1} K^{-1}, while the thermal conductivity of the catalyst is assumed to be equal to that of V_2O_5, which was extrapolated from data reported in the work of Wang et al. (2020) and considered to be equal to 1.5 W m^{-1} K^{-1}.

The second term on the right-hand side of Equation B.1, $\lambda_{flow,r}$, represents the heat transfer enhancement in the radial direction due to flow effects. It is modelled here using the usual correlation reported in Díaz-Heras et al. (2020) based on several studies, established for forced convection in beds consisting of randomly packed spherical particles of uniform size:

$$\lambda_{flow,r} = 0.1\lambda_f Re_p Pr \tag{B.3}$$

The third term on the right-hand side of Equation B.1, λ_{rad}, represents the equivalent thermal conductivity due to radiative heat transfer, and becomes significant at sufficiently high temperatures. This contribution is independent of the flow, and in the case of beds of randomly packed spherical particles, it is isotropic. In this work, it is evaluated using the model of Schotte (1960), which assumes a that the fluid is transparent to heat radiation:

$$\lambda_{rad} = \frac{1-\varepsilon}{\frac{1}{\lambda'} + \frac{1}{\lambda_s}} + \varepsilon\lambda' \tag{B.4}$$

For randomly packed spherical particles, the variable λ' is calculated as follows (Schotte, 1960):

$$\lambda' = 0.229\varepsilon d_p \varepsilon_{rad} \frac{T^3}{10^6} \tag{B.5}$$

where ε_{rad} is the thermal emissivity of the solid particles.

B.2 Equivalent axial thermal conductivity of the packed bed and axial thermal Péclet number

Like the radial direction, the axial conductivity (i.e., in the mean flow direction) of the packed bed, $\lambda_{eff,ax}$, also consists of three contributions:

$$\lambda_{eff,ax} = \lambda_{cond} + \lambda_{flow,ax} + \lambda_{rad} \quad \text{B.6}$$

The calculation of the conductive and radiative contributions, which are isotropic, has been detailed in Section B.1. The flow contribution is modelled as follows (Díaz-Heras et al., 2020):

$$\lambda_{flow,ax} = 0.7\lambda_f Re_p Pr \quad \text{B.7}$$

The coefficient of 0.7 represents the average of the values reported in the literature for flows in randomly packed beds of spherical particles, which range from 0.5 to 1.

The axial thermal Péclet number, $Pe_{t,ax}$, representing the ratio of advective transport of enthalpy over the effective conduction rate in the axial direction, expresses as follows:

$$Pe_{t,ax} = \frac{\rho\, \bar{c}_p\, u_{D,i}\, L}{\lambda_{eff,ax}} \quad \text{B.8}$$

where ρ and $\bar{c}_p$ are the mixture density and heat capacity respectively. For the investigated cases, the axial thermal Péclet number ranges between 100 and 230. Such high values of $Pe_{t,ax}$ indicate that heat in the packed bed is primarily transported axially through the advective transport of enthalpy by the mean flow while other transport phenomena in the axial direction can be neglected.

B.3 Prater criterion and pseudo-homogenous model assumption

Two criteria were evaluated to assess the maximum temperature difference within a catalyst pellet ($\Delta T_{c,max}$) and the maximum temperature in the gas boundary layer near the pellet surface ($\Delta T_{f,max}$). These two criteria are illustrated in Figure 4.5.

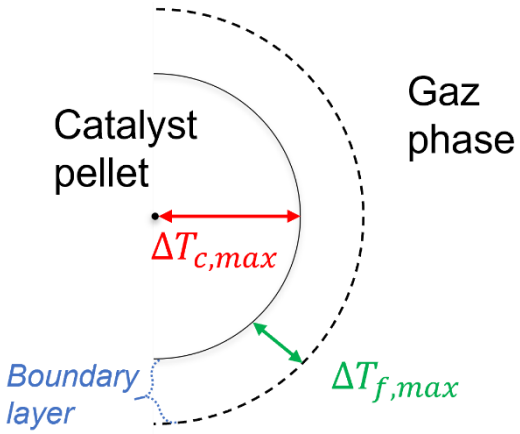

Figure 4.5: Schematic representation of the two maximum temperature differences criteria.

The Prater criterion (Villermaux, 1982) allows for the estimation of the maximum temperature difference between the centre and the surface of the catalyst particles. It assumes that the SO_2 concentration within the catalyst particles is negligible. The Prater criterion is expressed in terms of $\lambda_{eff,r}$, the effective radial conductivity (Section B.1), as it is lower than the axial conductivity (Section B.2):

$$\Delta T_{c,max} = \frac{\mathfrak{D}_{eff,SO_2,c}(-\Delta_r h^\circ)c_{SO_2,surf}}{\lambda_{eff,r}} \qquad \text{B.9}$$

where $\Delta T_{c,max}$ [K] is the expected maximum temperature difference between the centre and the surface of catalyst particles, $\mathfrak{D}_{eff,SO_2,c}$ [m^2 s^{-1}] the effective diffusivity of SO_2 in the catalyst particles (its calculation is detailed in Appendix D), and $c_{SO_2,surf}$ [mol m^{-3}] the SO_2 concentration at the surface of the catalyst particles. As for the other criteria, this criterion calculation was performed based on SO_2, the limiting reactant.

The maximum temperature difference in the fluid phase at the pellet scale, i.e., the temperature between the bulk and the particles surface, is estimated as follows (Villermaux, 1982):

$$\Delta T_{f,max} = \frac{k_p\,(-\Delta_r h^\circ)c_{SO_2}}{h_p}\, f_{ext} \qquad \text{B.10}$$

where $\Delta T_{f,max}$ [K] is the maximum temperature difference in the fluid phase in the boundary layer close to a catalyst pellet, k_p [m s^{-1}] is the convective mass transfer coefficient between the

fluid and the catalyst particles (which calculation is detailed in Appendix D), h_p [W m^{-2} K^{-1}] is the convective heat transfer coefficient between the fluid and the catalyst particles, c_{SO_2} [mol m^{-3}] the bulk (or mixing-cup) SO_2 concentration in the fluid phase and f_{ext} the external resistance fraction, the estimation of which is detailed in Appendix D. The convective heat transfer coefficient, h_p, is calculated using the correlation of Ranz (1952) (reported in Rode (2019)) which was developed for transitional and turbulent flows in spherical packed beds:

$$Nu_p = \frac{h_p d_i}{\lambda_f} = 2 + 1.8 {Re_p}^{1/2} Pr^{1/3} \qquad \text{B.11}$$

In the simulations presented in this work, both $\Delta T_{f,max}$ and $\Delta T_{c,max}$ were found to be highest at the HER's inlet, but they remained below 0.5 K.

Appendix C. Calculation of Nusselt number in the annular space flow

The local heat transfer coefficient between the coolant flow (circulating in the annular space of the HER) and the central wall, was calculated using the correlation of Vikhansky and Eskin (2024) developed for turbulent flows in annular ducts with smooth walls:

$$Nu_{an} = \frac{h_{an} D_{H,an}}{\lambda_{an}} = \frac{\left(\frac{C_{f,an}}{8}\right)(Re_{an} - 1000)\, Pr_{an}}{1 + 12.7\sqrt{\frac{C_{f,an}}{8}}\left(Pr_{an}^{2/3} - 1\right)}\left[1 + \left(\frac{D_{H,an}}{z}\right)^{\frac{2}{3}}\right] F_a \qquad \text{C.1}$$

where $C_{f,an}$ is the friction coefficient (Darcy-Weisbach formulation) in the coolant flow (which calculation is detailed in Appendix A), z (m) the axial position and Pr_{an} the Prandtl number of the molten salt (calculated using the thermophysical properties reported in Table 4.3). F_a is an empirical factor accounting for the aspect ratio of the annulus and the wall boundary conditions. In the case of an insulated outer wall and heat transfer with the inner wall of the annulus, as in the HER configuration considered in this study, Pr_{an} is calculated as follows:

$$F_a = 0.75\left(\frac{d_i + 2e_w}{d_i + 2e_w + 2e_{an}}\right)^{-0.17} \qquad \text{C.2}$$

Appendix D. Mass transfer in the packed bed: simplifying assumptions

This appendix addresses the modelling of mass transfer phenomena in packed bed catalyst reactors, specifically focusing on the criteria used to evaluate the occurrence of internal or external mass transfer limitations of the chemical reaction.

D.1 External mass transfer resistance

External mass transfer resistance refers to the mass transfer resistance present in the gaseous boundary layer. A reaction is considered limited by mass transfer when its rate is determined by the diffusion of reactants in the boundary layer between the fluid bulk and the catalyst, rather than by the intrinsic kinetics. In this case, the diffusion of gaseous molecules acts as the bottleneck for the overall reaction rate.

The importance of the external mass transfer resistance is evaluated through the calculation of the external resistance fraction, f_{ext}, which represents the proportion of the total resistance to mass transfer that is attributed to reactants diffusion around the catalyst pellet. It is defined as follows (Villermaux, 1982):

$$f_{ext} = \frac{c_j - c_{j,surf}}{c_j} = \frac{\rho_c \bar{r} d_p}{6 k_p c_j} \qquad \text{D.1}$$

where c_j and $c_{j,surf}$ [mol m^{-3}] are the concentration of species j in the fluid bulk and at the catalyst pellet surface respectively. For the calculation of f_{ext}, species j is chosen to be the limiting reactant, SO_2 in the present case. Given the heat/mass transfer analogy, the convective mass transfer coefficient, k_p [m s^{-1}], is calculated using the correlation of Ranz (1952) (Equation B.11) initially developed for heat transfer around packed spherical pellets:

$$Sh_p = \frac{k_p d_i}{\mathfrak{D}_j} = 2 + 1.8 {Re_p}^{1/2} {Sc_j}^{1/3} \qquad \text{D.2}$$

where $\mathfrak{D}$ [m^2 s^{-1}] represents the molecular diffusivity in the gas phase, taken equal to 10^{-4} m^2 s^{-1}, a typical value for gas diffusivity at the range of temperatures considered in this thesis. Sh [-] and Sc [-] are respectively the Sherwood and Schmidt numbers.

When f_{ext} values are below 0.05, concentration gradients within the gaseous boundary layer are negligible, and the surface concentration can then be approximated as equal to the bulk gas concentration.

D.2 Calculation of the effective diffusivity in the catalyst pellets

This section focuses on the calculation of $\mathfrak{D}_{eff}$ [m^2 s^{-1}], the effective species diffusivity in the pores of the catalyst particles, which is needed for determining the Prater (Section B.3) and Weisz (Section D.3) criteria. It is calculated as follows (Villermaux, 1982):

$$\mathfrak{D}_{eff,j} = \frac{\varepsilon_p}{\tau_p}\left(\frac{1}{\frac{1}{\mathfrak{D}_{K,j}} + \frac{1}{\mathfrak{D}_j}}\right) \tag{D.3}$$

where ε_p [-] is the internal porosity of the catalyst particles, $\mathfrak{D}_j$ and $\mathfrak{D}_{K,j}$ [m^2 s^{-1}] the molecular diffusivity and Knudsen diffusivity of species j, and τ_p is the tortuosity factor of the catalyst particles. Fogler (1992) did not provide values for ε_p and τ_p for the catalyst used in the experiments. Therefore, typical values of 0.4 and 4 were assumed for these parameters, respectively.

Since SO_2 is the limiting reactant, its effective diffusivity has been considered to determine the Prater and Weisz criteria. For simplicity, the molecular diffusivity of SO_2, $\mathfrak{D}_{SO_2}$, has been calculated assuming a binary mixture consisting only of SO_2 and N_2. This assumption is realistic because N_2 comprises around 80 mol% of the mixture. The binary mixture assumption allows determining $\mathfrak{D}_{SO_2}$ using the kinetic theory of gases as follows:

$$\mathfrak{D}_{SO_2} = \frac{0.001858T^{\frac{3}{2}}}{p\sigma_{AB}^2\Omega_D}\left[\frac{1}{M_{SO_2}} + \frac{1}{M_{N_2}}\right]^{1/2} \tag{D.4}$$

where T [K] is the temperature, p the pressure expressed in atmospheres, M_j the molar mass of species j expressed in grams per mol and Ω_D [-] is the collision integral for molecular diffusion. σ_{AB} [Å] is the average collision diameter between the two species, calculated as:

$$\sigma_{AB} = \frac{\sigma_{SO_2} + \sigma_{N_2}}{2} \tag{D.5}$$

where σ_j [Å] is the collision diameter for species j. The values of σ_{SO_2} and σ_{N_2} are taken as 4.29 and 3.68 Å respectvely (Welty et al., 2014). The collision integral coefficient was regressed from tabulated values reported in Welty et al. (2014) as follows:

$$\Omega_D = 1.4765\left(\frac{\kappa T}{\varepsilon_{AB}}\right)^{-0.383} \tag{D.6}$$

where κ is the Boltzmann constant equal to about 1.38×10^{-16} erg K^{-1}. ε_{AB} [erg] is the energy of molecular interaction for the binary system SO_2 and N_2 and can be calculated as follows:

$$\frac{\varepsilon_{AB}}{\kappa} = \sqrt{\frac{\varepsilon_{SO_2}}{\kappa}\frac{\varepsilon_{N_2}}{\kappa}} \qquad \text{D.7}$$

The values of $\frac{\varepsilon_{SO_2}}{\kappa}$ and $\frac{\varepsilon_{N_2}}{\kappa}$ are taken from Welty et al. (2014) and are respectively equals to 252 K and 91.5 K.

For the calculation of the Knudsen diffusivity of SO_2 in Equation D.3, the following equation (Rode, 2019) is used:

$$\mathfrak{D}_{K,SO_2} = \frac{2d_{pore}}{3}\sqrt{\frac{2R_{gas}T}{\pi M_{SO_2}}} \qquad \text{D.8}$$

where d_{pore} [m] is the pores diameter in the V_2O_5 catalyst. Since it was not documented in Fogler (1992), the value of d_{pore} was taken as 61×10^{-9} m, as reported in Mazidi et al. (2017).

D.3 Internal mass transfer resistance and Weisz criterion

Heterogeneous catalytic reactions may be limited by internal diffusion when the rate at which reactants diffuse within the catalyst's porous structure is lower than the rate of the chemical reaction, leading to a decrease of the overall catalyst efficiency as portions of the catalyst remain underused. The occurrence of internal mass transfer limitations can be predicted using the Weisz criterion, φ_s', which represents the ratio of the catalytic reaction rate to the rate of diffusion of reactants into the catalyst:

$$\varphi'_{s,j} = \frac{\rho_c \bar{r} d_p^2}{36 D_{eff,j} c_{j,surf}} \qquad \text{D.9}$$

For Weisz criterion values less than 0.1, concentration gradients in the pellet, and thus internal limitations, can be neglected. The Weisz criterion is evaluated here for SO_2, as it is the limiting reactant. The effective diffusivity of SO_2 in the catalyst pellets is calculated following the procedure detailed in Section D.2.

Appendix E. Detailed characterization of the MPCEnt and MPCVol designs of the reference case study

Various criteria were assessed for each geometry investigated to support the simplifying modelling assumptions adopted (pseudo-homogenous model). This appendix presents the local profiles of some of these criteria for the MPCEnt and MPCVol designs of the reference case study. The 3D designs and diameter profiles are presented in Figure 4.6 and will be discussed in detail in Chapter 5.

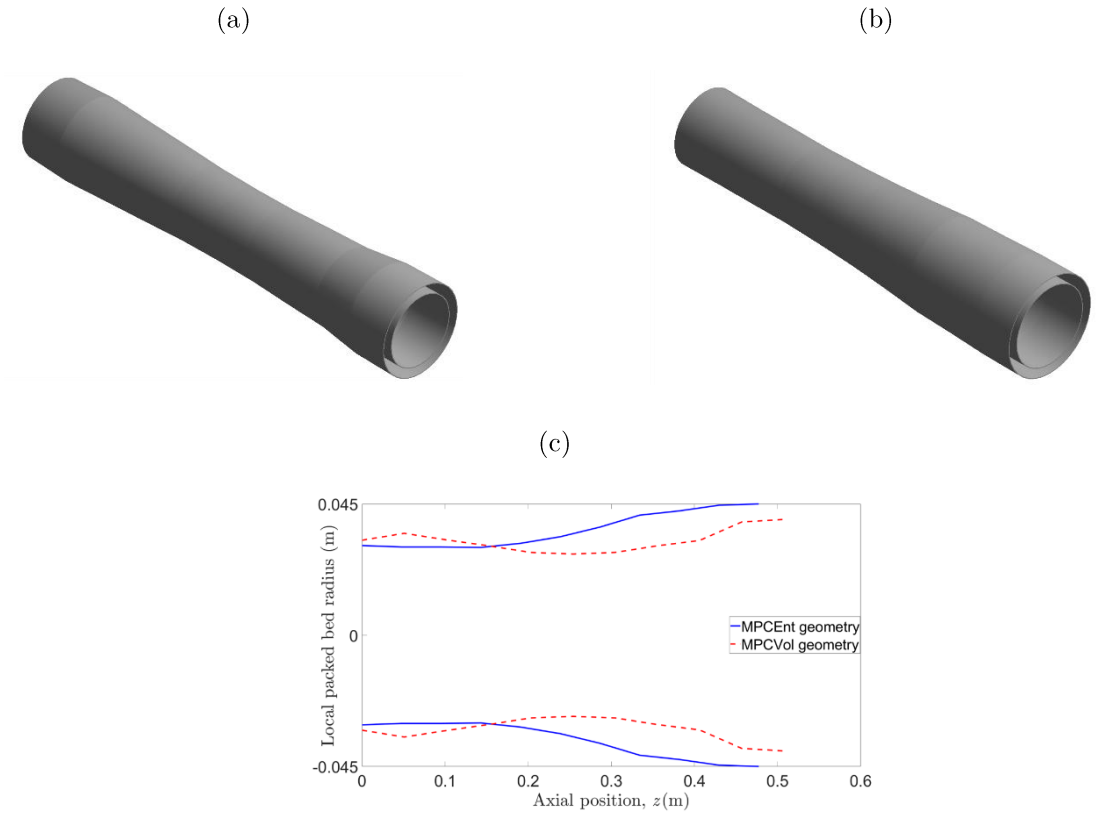

Figure 4.6: MPCEnt and MPCVol geometries of the reference case: (a) 3D representation of the MPCVol geometry, (b) 3D representation of the MPCEnt geometry and (c) Packed bed radius profiles.

E.1 Mass transfer limitation

The external mass transfer resistance fraction, f_{ext}, represents the proportion of the total resistance to mass transfer that is attributed to reactants diffusion around the catalyst pellet. Figure 4.7 illustrates its variation along the MPCEnt and MPCVol geometries of the reference case study. It reveals that f_{ext} remains below the 0.05 threshold, indicating that concentration gradients between the fluid bulk and the catalyst surface are negligible. Thus, the SO_2 concentration in the bulk of the gas flow can be assumed to be equal to that at the surface of the catalyst pellet. For the majority of the evaluated geometries, the fraction stays below the 0.05 limit throughout the entire packed bed length. A slight exceedance was observed at a

mixture inlet pressure of 10 bar, where f_{ext} reached a maximum of 0.06. However, with such small deviation, this criterion can be still considered valid in this case as well.

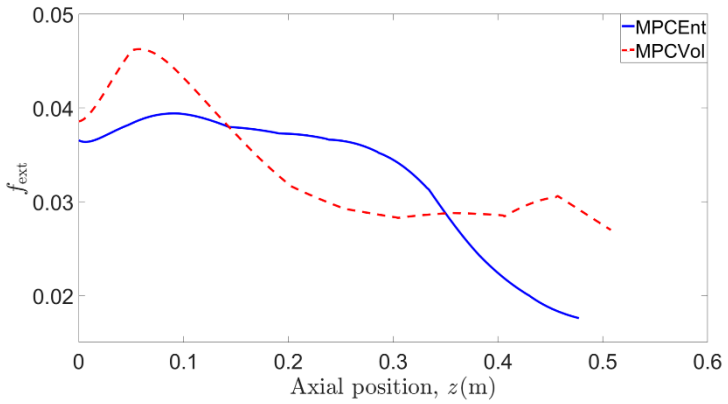

Figure 4.7: Axial profiles of f_{ext} along the MPCVol and MPCEnt designs of the reference case study.

The occurrence of internal mass transfer can be assessed using the Weisz criterion, as discussed in Chapter 4. Figure 4.8 illustrates its variation along the MPCEnt and MPCVol geometries of the reference case study. The results show that the Weisz criterion exceeds the 0.1 threshold across the entire packed bed length, indicating that the reaction rate is externally diffusion-limited. Therefore, as noted by Fogler (1992), the reaction rate provided in Equation 4.2.1 represents an apparent reaction rate, i.e., it incorporates the effects of mass transfer limitations under the operating conditions at which it was determined. Figure 4.8 shows that the Weisz criterion generally decreases in the downstream direction along the reactor, which is expected, as it is proportional to the apparent reaction rate (Equation D.9), which decreases with conversion. Depending on the configuration and axial position, the Weisz criterion typically ranges from 1 to 6 in the case studies investigated.

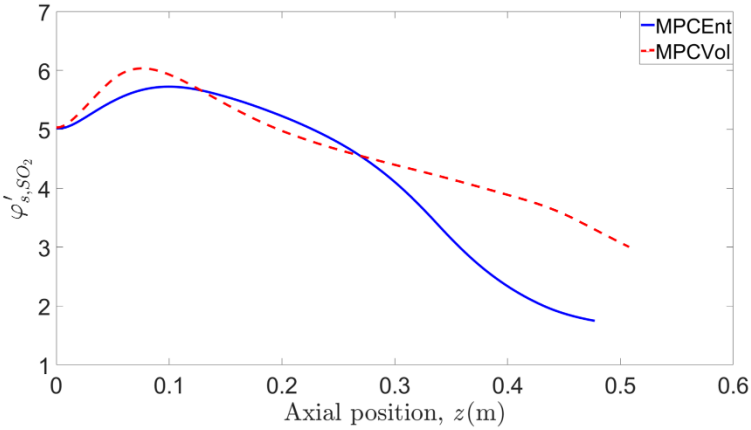

Figure 4.8: Axial profiles of the Weisz criterion along the MPCVol and MPCEnt designs of the reference case study.

E.1 Heat transfer limitation

The magnitude of temperature differences at the scale of the pellet or the pores of the packed bed is evaluated using the Prater criteria, as discussed in Chapter 4. These criteria allow for the determination of $\Delta T_{c,max}$, the temperature difference across the catalyst pellet, and $\Delta T_{f,max}$, the temperature difference across the fluid vein. The axial profiles of $\Delta T_{c,max}$ and $\Delta T_{f,max}$ (Equation B.9 and Equation B.10) along the MPCEnt and MPCVol geometries for the reference case study are shown in Figure 4.9 and Figure 4.10, respectively. It is evident that for both geometries, the temperature differences remain below 0.5 K throughout the entire packed bed length. Furthermore, for all Pareto-optimal designs reported, these criteria consistently remain below 0.5 K, indicating negligible temperature differences between the solid and fluid phases. This supports the validity of the homogeneous model, where the temperature is assumed to be uniform across both phases.

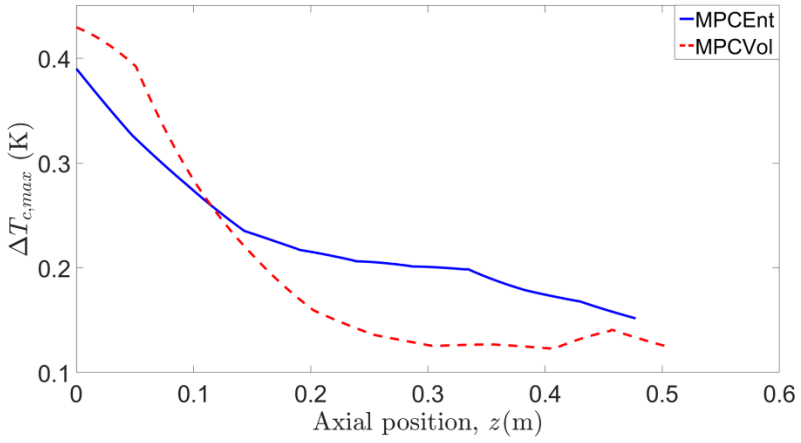

Figure 4.9: Axial profiles of the temperature difference between the centre and the surface of the catalyst particles along the MPCVol and MPCEnt designs of the reference case study.

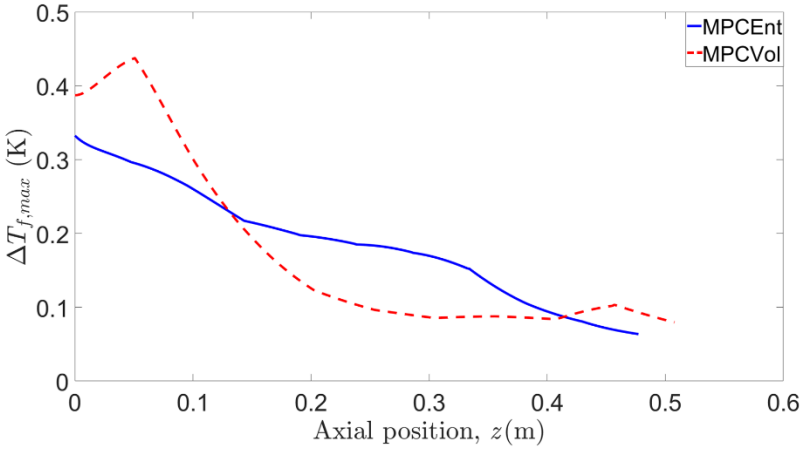

Figure 4.10: Axial profiles of the temperature difference across the fluid vein along the MPCVol and MPCEnt designs of the reference case study.

Those criteria values enable the use of a homogeneous model, rather than a heterogeneous modelling approach, which would require calculating a local convective mass transfer coefficient

and solving an algebraic equation at each position along the bed to determine the species concentrations at the catalyst surface. From a theoretical standpoint, a pseudo-homogeneous model combined with an intrinsic kinetic law would not be valid, as internal mass transfer limitations would necessitate a heterogeneous description. However, since the available reaction rate (as provided by Fogler, 1992) corresponds to an apparent rate that already accounts for internal transport effects, it can be consistently implemented within a pseudo-homogeneous modelling framework.

Chapter 5

Entropy Generation Minimization Results for the heterogeneous case study: Gas-Phase SO_2 oxidation

Table of Contents

Chapter 5 236

Abstract 238

5.1 Introduction 239

5.2 1D model optimisation results 240

5.2.1 Reference case study 241

5.2.2 Effects of the inlet pressure of the reactive mixture 248

5.2.3 Influence of the maximum allowable temperature constraint 253

5.2.4 Influence of the inlet heat carrier temperature 255

5.2.5 Influence of the inlet gas molar flowrate 259

5.2.6 Influence of the inlet gas temperature 264

5.2.7 Influence of the inlet gas O_2/SO_2 molar ratio 268

5.2.8 Influence of the required conversion 273

5.2.9 Summary of the 1D optimisation key results 277

5.3 2D model comparison 280

5.4 Conclusion 284

Nomenclature

F	Molar flow rate (mol s^{-1})
p	Pressure (Pa)
$\dot{S}_{tot}$	Total entropy generation rate (W K^{-1})
$\dot{s}'$	Rate of entropy generation per unit length (W K^{-1} m^{-1})
T	Absolute temperature (K)
V_{HER}	Total volume of the heat exchanger reactor (m^3)
x_j	Molar fraction of species j (-)
z	Axial position along the system (m)

Greek letters

ξ	Conversion (-)
ϕ	Heat flux exchanged per HER unit length between the coolant and the packed bed (W m^{-1})

Subscripts

an	Refers to the fluid circulating in the annulus
ch	Refers to the chemical reaction
h	Refers to heat transfer
i	Refers to the fluid circulating in the inner pipe
inl	Refers to the inlet of the HER
M	Refers to the mixing-cup (i.e., mass-flow weighted averaging)
max	Refers to the maximum
min	Refers to the minimum
tot	Refers to the total
η	Refers to viscous dissipation

Abbreviations

CFD	Computational Fluid Dynamics
EGMod	Entropy Generation Modelling
HER	Heat Exchanger Reactor
MPCEnt	Minimal Profiled Configuration Entropy generation rate
MPCVol	Minimal Profiled Configuration Volume

Abstract

This chapter investigates the catalytic oxidation of sulphur dioxide (SO_2) into sulphur trioxide (SO_3), a heterogeneous, exothermic gas-phase reaction of significant industrial relevance. Building on 1D and CFD modelling frameworks introduced in Chapter 4, the study performs parametric and shape optimisation of heat-exchanger reactors (HERs) under realistic operational constraints, including target conversion, maximum allowable temperature, and pressure drop limits. Multi-objective optimisation highlights trade-offs between reactor compactness and thermodynamic performance, revealing that profiled reactor geometries outperform conventional tubular designs in terms of entropy generation and reactor volume. Key operating parameters—such as inlet pressure, temperature, molar flow rate, O_2/SO_2 ratio, maximum allowable temperature, and conversion target—strongly influence the optimal design and dominant sources of entropy. 1D models provide rapid insights into geometry-performance relationships, while CFD simulations capture critical local phenomena, including radial temperature gradients and hot spots, essential for safe and reliable operation. The results demonstrate the significant potential of shape optimisation to develop compact, thermodynamically efficient HERs, especially under stringent operational, with heat transfer identified as the main driver for entropy reduction.

5.1 Introduction

The catalytic oxidation of sulphur dioxide (SO_2) into sulphur trioxide (SO_3) is a key step in sulphuric acid production and constitutes a heterogeneous, gas-phase reaction with strong industrial relevance. Compared with the hydrolysis of acetic anhydride studied in Chapter 3, this case introduces two major differences: the reaction is heterogeneous, occurring on a catalytic surface, and it takes place in the gas phase, where mass and heat transfer strongly influence reactor performance. These characteristics, combined with the highly exothermic and nonlinear nature of SO_2 oxidation, make the optimisation of heat-exchanger reactors particularly challenging.

Building on the systemic and CFD models formulated in Chapter 4, as well as the associated optimisation framework and operational constraints (conversion targets, maximum admissible temperature to prevent catalyst deactivation, and pressure drop limits for feasible operation), Chapter 5 analyses the design of the SO_2 oxidation converter. Section 5.2 applies the one-dimensional (1D) model to a multi-objective optimisation study, leading to the construction of Pareto fronts that capture the trade-offs between reactor compactness and thermodynamic performance. The influence of several operating parameters is examined, including inlet pressure, inlet mixture and heat-carrier temperatures, inlet gas molar flow rate, O_2/SO_2 molar ratio, and required conversion. Section 5.3 then compares these optimisation results with those obtained from CFD simulations, providing insights into the limitations of each modelling approach and their implications for the design of efficient SO_2 converters.

5.2 1D model optimisation results

The multi-objective optimisation problem for the catalytic oxidation of sulphur dioxide in a double-pipe heat-exchanger reactor (HER) is formulated as follows:

$$\underset{\vec{v}}{\text{Min}}\,\vec{F} = \underset{\vec{v}}{\text{Min}}[\dot{S}_{tot}, V_{HER}]^T \qquad 5.2.1$$

where $\vec{v}$ represents the vector of decision variables. The choice of the decision variables depended on the configuration considered. For the purely tubular HER, two variables were considered, he total reactor length, L, and the inner tube diameter, d_i. For the profiled HER, a more complex design space was defined with twelve decision variables, including the total reactor length L, the inlet inner tube diameter $d_{i,inl}$, and the slopes of the ten successive sections, α_m. A positive slope corresponds to a divergent section, whereas a negative slope indicates a convergent one.

This optimisation problem is constrained by several conditions:

- Process model equations: The governing equations, described in Chapter 4, Section 4.4, form a system of 1D plug-flow model with coupled algebraic-differential equations due to the inclusion of radiative heat transfer. These equations account for the temperature, pressure, and composition of both the reacting gas mixture and the heat transfer fluid.
- Boundary conditions: the inlet conditions defined in Chapter 4, Section 4.3.2
- Terminal constraints: a minimum outlet conversion of 80% and a minimal outlet pressure of 1 atm were imposed to ensure practical reactor designs.
- Path constraints: at any axial position, the inner pipe diameter d_i remains between 1.5 cm and 9 cm and the temperature of the gas mixture must be under 880 K.
- Bounds on decision variables: total reactor length between 0.1 and 10 m, and slope values restricted to $-\frac{\pi}{2} < \alpha_m < \frac{\pi}{2}$.

The investigated system consists of a fixed bed of V_2O_5 catalyst pellets, housed in the inner pipe of the HER, where the exothermic SO_2 oxidation occurs. The cooling fluid, molten HITEC salt, circulates through the annular space to evacuate the released heat. Both the tubular and profiled HER configurations are optimised to generate Pareto fronts, illustrating the trade-off between entropy generation and reactor volume. Compared to previous studies, the present work extends the modelling by including explicit heat transfer with the cooling fluid, spatially varying heat transfer coefficients, and radiative contributions. Moreover, restrictive outlet constraints are relaxed, and a safety path constraint on the maximum bed temperature is enforced. A one-dimensional pseudo-homogeneous plug flow model is used, assuming uniform temperature between the catalyst particles and the gas phase.

5.2.1 Reference case study

a. Pareto front

The reference case study involves solving the optimisation problem within the constraints outlined in Chapter 4, Section 4.6, based on the operating conditions specified in Chapter 4, Section 4.3.2, Table 4.3. Figure 5.1 illustrates the Pareto fronts for both the tubular and profiled HER configurations. All Pareto optimal solutions achieve a SO_2 conversion that is practically equal to the minimum imposed one of 80%. Indeed, as already noted, designs leading to a higher conversion are suboptimal as they require additional HER volume and higher entropy generation.

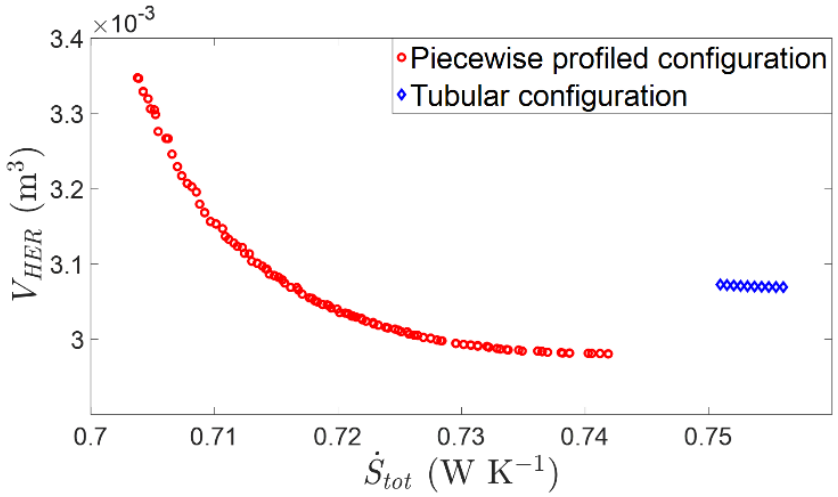

Figure 5.1: Pareto fronts illustrating the trade-off between the volume V_{HER} and the generated entropy $\dot{S}_{tot}$ for the tubular (blue diamonds) and profiled (red circles) HER configurations.

Figure 5.1 illustrates that profiled configuration designs outperform the tubular geometries. Indeed, the profiled configurations achieve the target conversion rate of SO_2 while exhibiting a lower entropy generation rate. The Pareto fronts underscore the conflicting nature of the two objectives: minimizing entropy generation and minimizing volume. Most importantly, Figure 5.1 confirms that shape optimisation can effectively reduce the irreversibility rates associated with a given operation, supporting the conclusions of the pioneering paper by Magnanelli et al. (2019), or reduce the required catalyst volume. Thus, while the tubular configuration permits a minimal HER volume of about 3.07 L, the profiled design allows improving this metric by over 3%, resulting in a minimal HER volume of about 2.98 L. On the other hand, while the minimal entropy generation rate permitted by the tubular configuration is about 7.51×10^{-1} W K^{-1}, the profiled configuration allows for a further significant reduction of approximately 6.7%, achieving the desired conversion rate with a total entropy generation rate of about 7.04×10^{-1} W K^{-1} only.

Indeed, the capabilities of tubular geometries are limited by the optimisation problem constraints. For relatively small diameters, a long HER length is required to achieve the target conversion rate, resulting in excessive pressure drops, particularly in the reactive mixture flow, which hinders compliance with the discharge pressure constraints (Equation 4.6.10).

Conversely, for relatively large diameters, the mixture velocity decreases, causing a significant temperature rise due to the exothermic reaction (despite an increase in the heat flux exchanged with the coolant as explained below) and creating a severe hot spot in the entrance zone, which violates the maximum temperature constraint (Equation 4.6.13). Therefore, the tubular configurations presented in Figure 5.1 correspond to intermediate packed bed diameters that meet the problem constraints. On the other hand, the profiled configuration, as it makes use of sections of varying diameters, manages to handle the optimisation problem constraints more effectively.

b. Field variables profiles

The 3D geometries corresponding to the extreme points of the profiled HER Pareto front - namely, the configuration with the minimum HER volume (referred to as MPCVol, for Minimal Profiled Configuration Volume) and the one with the minimum entropy generation rate (referred to as MPCEnt, for Minimal Profiled Configuration Entropy generation) are illustrated in Figure 3.17. The MPCVol design features a convergent section in the first half and a divergent section in the second half, whereas the MPCEnt point adopts a fully divergent geometry.

(a) (b)

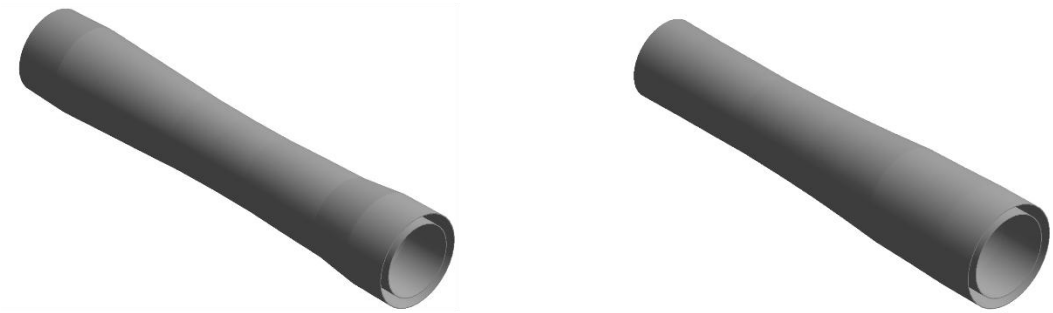

Figure 5.2: 3D representation of the MPCVol (a) and MPCEnt (b) points of the reference caste study.

These design variations have a significant effect on the temperature, pressure, and composition profiles, as shown in Figure 5.3.

(a) (b)

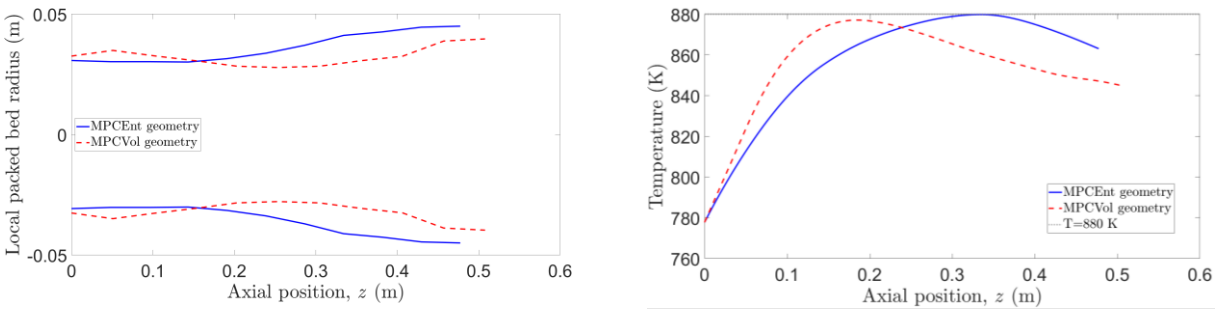

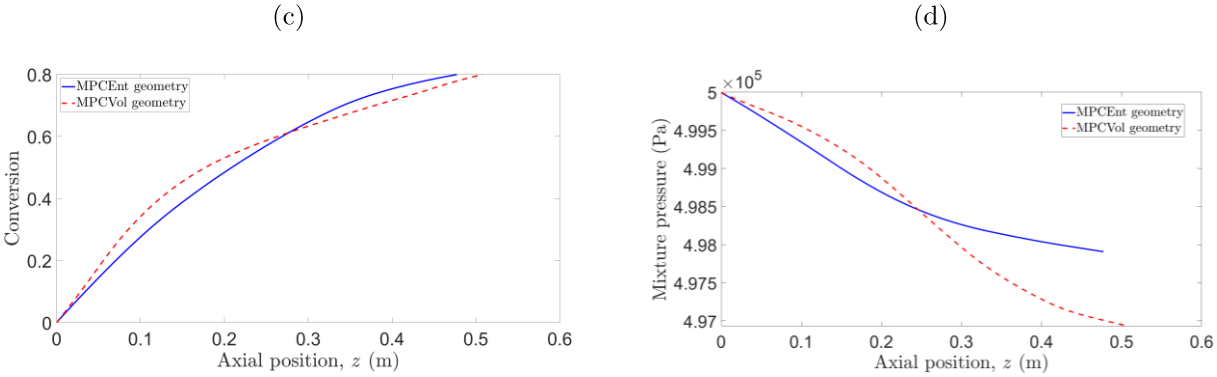

Figure 5.3: MPCVol and MPCEnt points of the reference case study: (a) Packed bed radius profiles, (b) Packed bed temperature profiles, (c) SO_2 conversion rate profiles, (d) Mixture pressure profiles.

Figure 5.3a illustrates the variations in packed bed radius along the axial position. The total lengths of the MPCVol and MPCEnt designs are approximately 0.51 m and 0.48 m, respectively. Figure 5.3b shows the temperature profiles of the reactive mixture in both geometries. To reduce clutter, the coolant temperature profiles are not shown in the figures. This omission is justified by the negligible temperature increase of the coolant between the inlet and the outlet, which is less than 1 K, due to its high mass flow rate.

It is insightful to examine how heat transfer varies with changes in the tube diameter. In the present system, the limiting thermal resistance is located at the reactive mixture side, so the analysis focuses on this coefficient. As shown in Chapter 4 (Equation *4.4.13*), the Nusselt number can be expressed as:

$$\mathrm{Nu} \propto Re_p^{0.8} \exp(-\frac{1}{d_i})$$

where Re_p is the particle Reynolds number. Since the gas velocity is the only parameter dependent on the inner tube diameter, $Re_p \propto d_i^{-2}$, which leads to

$$\mathrm{Nu} \propto d_i^{-1.6} \exp(-\frac{1}{d_i})$$

and therefore

$$\mathrm{h} \propto d_i^{-2.6} \exp(-\frac{1}{d_i})$$

Considering the heat transfer area $A = \pi d_i L$, the resulting heat flux is proportional to

$$Q = h_i A \Delta T \propto d_i^{-1.6} \exp(-\frac{1}{d_i})$$

Consequently, the heat flux through the tube is influenced by two competing effects. The first term, $d_i^{-1.6}$, indicates that the heat flux tends to decrease as the tube diameter increases due to lower turbulence. In contrast, the exponential term, $\exp(-\frac{1}{d_i})$, which accounts for wall

effects in the packed bed, increases with diameter, particularly at small diameters, as it approaches unity for large diameters (where wall effects become negligible compared to an infinitely large packed bed). Because these two contributions act in opposition, there exists a threshold diameter at which their effects balance. Below this threshold, the exponential term dominates, so increasing the diameter leads to higher heat flux. Above the threshold, the $d_i^{-1.6}$ term prevails, causing the heat flux to decrease with increasing diameter. By differentiating the expression, this threshold diameter can be calculated as 0.625 m. For reference, the inner diameter in the present study is constrained between 1.5 cm and 9 cm. Therefore, within this range, the exponential term dominates, and increasing the tube diameter enhances the cooling of the mixture.

However, the heat released by the exothermic reaction must also be considered. At the reactor inlet, the reaction-generated heat exceeds the heat removed by the coolant. In this region, a reduced diameter, although limiting the heat transfer to the coolant, slows the temperature rise by reducing the residence time (and thus reactor volume for the volumetric reaction). This effect locally decreases the reaction rate and the heat generated, mitigating excessive temperature peaks. Conversely, in the downstream portion of the reactor, where the reaction heat diminishes, the heat flux to the coolant becomes the dominant factor in temperature control. As a result, increasing the diameter in this zone enhances the mixture cooling, since the uncontrolled temperature rise from the reaction is no longer significant.

Thus, in both designs, the local diameter of the packed bed remains sufficiently small to ensure a sufficient gas velocity, thereby keeping the mixture temperature below the imposed limit of 880 K. In the MPCEnt design, the diverging geometry leads to an increase in the heat flux exchanged along the axial position. In addition, moving downstream and sufficiently far from the inlet, the heat generated by the exothermic reaction begins to decrease, as the reaction slows down due to the lower reactant concentrations. Consequently, the MPCEnt design effectively manages the temperature constraint by ensuring that the maximum temperature limit of 880 K is reached only at the point where convective heat transfer surpasses the heat generated by the reaction, and after which the mixture temperature starts to decline. This allows a gradual temperature rise that does not generate as much entropy over the HER length due to lower temperature gradients in the first part of the HER. It is noteworthy that reaching the maximum temperature indicates that this constraint limits further improvements to the objective functions by restricting the feasible region.

In the MPCVol geometry, the reactor is wider at the inlet, where the exothermic reaction causes a significant temperature rise despite the large heat flux exchanged. The HER then narrows along the middle section to reduce the reactor volume, which lowers the local heat flux and helps maintain a relatively higher temperature as the reaction rate decreases. Finally, a diverging section is required to achieve the target conversion, resulting in an additional reactor length compared to the MPCEnt configuration. This geometry likely reflects an optimal trade-off between the volume savings obtained by narrowing the central section and the additional cost in length and divergence needed to reach the desired conversion.

Figure 5.3d illustrates the pressure variations of the mixture and coolant in both the MPCEnt and MPCVol geometries. As explained in Chapter 4, Section 4.4.1, pressure is irreversibly reduced and transformed into heat by viscous heating, particularly in narrow flow sections. In convergent sections, pressure diminishes through reversible transformation into kinetic energy, while it increases in divergent sections through the opposite transformation, however, this change is negligeable face to the viscous dissipation, presenting a globally decreasing pressure. Additionally, variations in temperature and composition affect the pressure profile of the gaseous mixture by modifying its density and, consequently, its velocity.

c. Local entropy generation

Figure 3.19 illustrates the profiles of local entropy source terms along the HER in both the MPCEnt and MPCVol geometries. Figure 3.19a and Figure 3.19b depict local entropy generation rates due to viscous dissipation in the coolant flow and the packed bed, respectively. The discontinuous variation in the diameter slopes across the 10 HER sections of the profiled HER configuration results in discontinuities in the viscous (Figure 3.19a and Figure 3.19b) and heat transfer (Figure 3.19c) contributions to entropy generation at the same locations. These discontinuities are particularity noticeable in Figure 3.19a due its scale, i.e., the very low magnitudes of entropy generation rates by viscous dissipation in the coolant flow. The molten salt being treated as incompressible; its volume flow rate remains constant along the HER. Additionally, its temperature varies only slightly. Consequently, on the one hand, the profile of entropy generation in the coolant fluid due to viscous dissipation (Figure 3.19a) primarily depends on the HER design, increasing in narrow flow sections and decreasing in wider ones. On the other hand, the volume flow rate of the gaseous mixture varies with changes in temperature, composition and pressure. Additionally, the mixture temperature, which appears in Equation *2.6.2* describing the local entropy generation rate due to viscous dissipation in the gas phase, exhibits significant variations. As a result, although mechanical entropy generation in the packed bed (Figure 3.19b) tends to increase in narrow section, its profile does not necessarily align with the HER design given that the flow rate and mixture properties vary in the axial direction.

(a) (b)

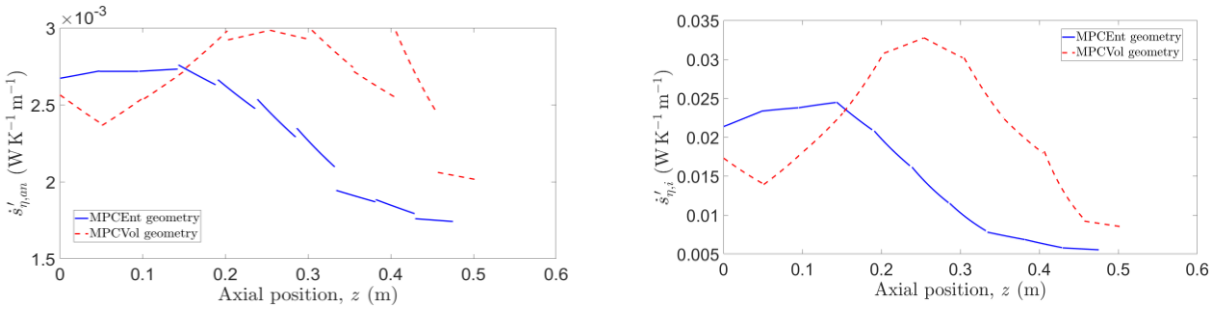

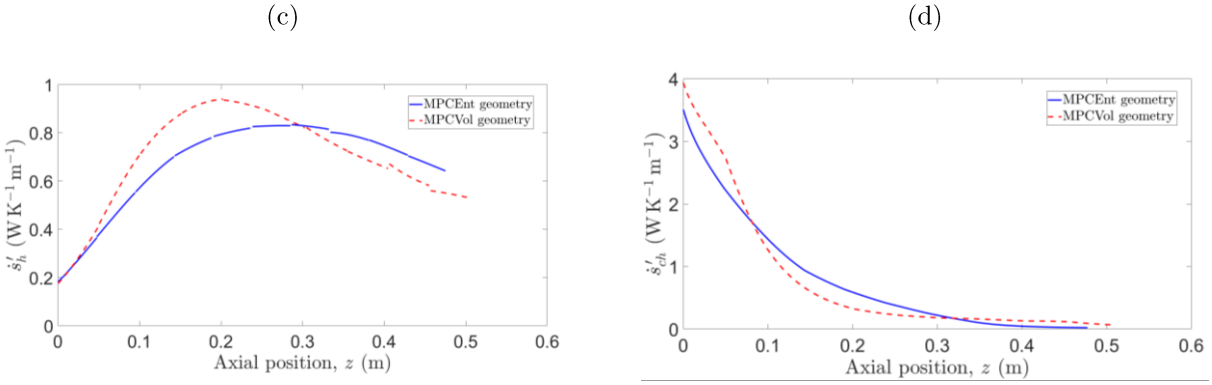

Figure 5.4: Local entropy generation rates in both the MPCEnt and MPCVol geometries: (a) Viscous dissipation in the coolant, (b) Viscous dissipation in the reactive mixture, (c) Heat transfer, (d) Chemical reaction.

Figure 3.19c illustrates the axial profile of $\dot{s}_h$, the local entropy generation rate due to heat transfer. According to Equation *2.6.4*, $\dot{s}'_h$ is influenced by the temperatures of both the mixture and the coolant fluids, as well as ψ, the heat flux between the two flows. ψ, in turn, is affected by the temperature difference between the flows, the heat transfer surface area, and to a lesser extent, the velocities of the flows through the heat transfer coefficients. Consequently, the $\dot{s}'_h$ profiles are complex to analyse in detail. However, they exhibit maximum values in sections with significant temperature differences between both fluid flows and sufficiently high heat transfer surface area.

Figure 3.19d illustrates the axial profile of $\dot{s}'_{ch}$, the local entropy generation rate due to the chemical reaction. According to Equation *2.6.5*, $\dot{s}'_{ch}$ is influenced by the section of the packed bed, the reaction rate, the mixture temperature and the Gibbs free energy which indicates the thermodynamic feasibility of the reaction, and which value depends on composition and temperature. The data in Figure 3.19d show that chemical entropy generation is maximal at the entrance of the HER, where the reaction rate is the highest due to elevated concentrations of reactants and sufficient temperature.

Finally, Table 3.6 summarizes the performance of both the MPCEnt and MPCVol geometries regarding the achieved objective functions, presenting the percentage contribution of each phenomenon to the total entropy generation. The table reveals that the contributions of viscous generation are negligible. Overall, due to the relatively short length of the optimal HER designs and moderate diameter variations, pressure losses are small and contribute only marginally to overall entropy generation. Chemical reaction effects contribute significantly to entropy generation; however, their values, primarily dependent on the conversion rate of SO_2, vary only slightly between the two designs. Specifically, compared to the MPCVol geometry, the MPCEnt design reduces the chemical entropy generation from 3.77×10^{-1} to 3.74×10^{-1} W K^{-1} only, corresponding to a modest reduction of approximately 0.8%. Conversely, the contribution from heat transfer, which is nearly as significant as that of the chemical reaction, is notably lower in the MPCEnt design. Specifically, compared to the MPCVol geometry, the MPCEnt design reduces the thermal entropy generation from 3.53 ×

10^{-1} to 3.23×10^{-1} W K^{-1}, representing a substantial reduction of approximately 9%. This suggests that heat transfer is the primary parameter on which dynamic optimisation acts to reduce total entropy generation in the present case study.

Table 5.1: HER volume and entropy generation rate of the MPCVol and MPCEnt designs in the reference case study.

	MPCEnt design	**MPCVol design**
V_{HER}	3.35 L	2.98 L
$\dot{S}_{tot}$	7.04×10^{-1} W K^{-1}: ➢ 7.33×10^{-3} and 1.12×10^{-3} W K^{-1} (1.0% and 0.2%) due to viscous dissipation in the mixture and coolant flow respectively. ➢ 3.23×10^{-1} W K^{-1} (45.7%) due to heat transfer. ➢ 3.74×10^{-1} W K^{-1} (53.1%) due to the chemical reaction.	7.42×10^{-1} W K^{-1}: ➢ 1.04×10^{-2} and 1.48×10^{-3} W K^{-1} (1.4% and 0.2%) due to viscous dissipation in the mixture and coolant flow respectively. ➢ 3.53×10^{-1} W K^{-1} (47.6%) due to heat transfer. ➢ 3.77×10^{-1} W K^{-1} (50.8%) due to the chemical reaction.

In summary, the comparison between tubular and profiled HER geometries demonstrates the clear advantage of shape optimisation. Profiled configurations not only achieve the target SO_2 conversion but also reduce total entropy generation compared to tubular designs, highlighting the conflicting nature of minimizing volume and irreversibility. The MPCVol and MPCEnt geometries illustrate the extremes of the Pareto front: MPCVol prioritizes minimal reactor volume with a convergent-divergent profile, whereas MPCEnt focuses on minimizing entropy generation through a fully divergent design. Analysis of temperature, pressure, and local entropy generation profiles reveals that heat transfer, particularly in regions with large temperature differences, is the dominant factor controlling entropy reduction. In contrast, viscous dissipation contributes negligibly, and the impact of chemical reaction entropy generation varies only slightly between designs. Overall, the profiled configurations effectively manage flow, temperature, and reaction constraints along the reactor length, allowing both improved thermal management and reduced reactor volume, with heat transfer optimisation being the main driver of total entropy reduction.

5.2.2 Effects of the inlet pressure of the reactive mixture

In this section, the effects of the inlet pressure of the reactive mixture in the optimal HER design is studied. The same optimisation problem as in the reference case study is solved; however, instead of using an inlet pressure of 5 bar, inlet pressure values of 2 bar and 10 bar are considered for the reactive mixture. All other operating and boundary conditions remain unchanged, and their values are reported in Chapter 4, Section 4.3.2, Table 4.3 and Table 4.4.

Before focusing on the Pareto fronts and the optimal designs, it is important to first analyse the effects of operating pressure on the equilibrium of the reaction. The oxidation of SO_2 is an exothermic reversible reaction in gaseous phase, which implies the existence of a maximum achievable conversion rate that depends on pressure, temperature, and the mixture inlet (or initial) composition. Based on Equation *4.2.2*, the equilibrium conversion rate of SO_2 can be calculated and the results are plotted in Figure 5.5 for the 3 operating pressures considered in this study: 2, 5 and 10 bar. The equilibrium conversion defines the upper limit of conversion attainable for specific temperature and pressure conditions, due to the constraints imposed by the thermodynamics.

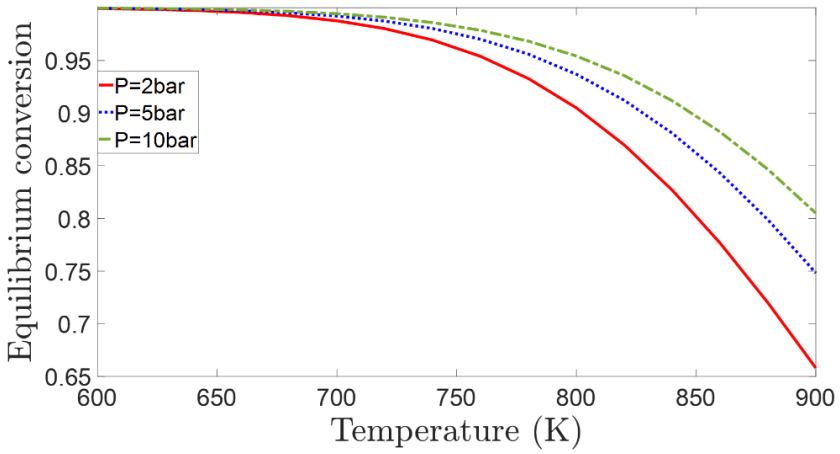

Figure 5.5: Effects of temperature and pressure on the equilibrium conversion rate of SO_2 for the inlet mixture composition reported in Chapter 4, Table 4.3.

Figure 5.5 illustrates that the equilibrium conversion rate of SO_2 decreases with increasing temperature, in accordance with the Le Chatelier's principle for an exothermic forward reaction. Conversely, the equilibrium conversion rate increases with higher operating pressures. This effect arises from the stoichiometry of the reaction. Specifically, an increase in pressure favours the forward reaction in this case because it reduces the total number of moles involved: it involves 0.5 moles of O_2 and 1 mole of SO_2 reacting to produce a single mole of SO_3. Figure 5.5 indicates that achieving a conversion of 0.8 at an inlet pressure of 2 bar, implies that the pressure drop must be kept to a minimum, and the mixture must be cooled to at least 850 K before the outlet of the HER.

Figure 5.6 illustrates the Pareto fronts for both the tubular and profiled HER configurations under the three investigated inlet gas pressures. All Pareto optimal solutions

achieve a SO_2 conversion rate that closely meets the minimum imposed abatement efficiency of 80%. It is noteworthy that since the gas molar flow rate is maintained at 2.15 $\times 10^{-1}$ mol s^{-1} (as specified in Chapter 4, Table 4.3) across all the three case studies, the actual volumetric flow rate, and consequently the gas velocity, increases as the pressure decreases.

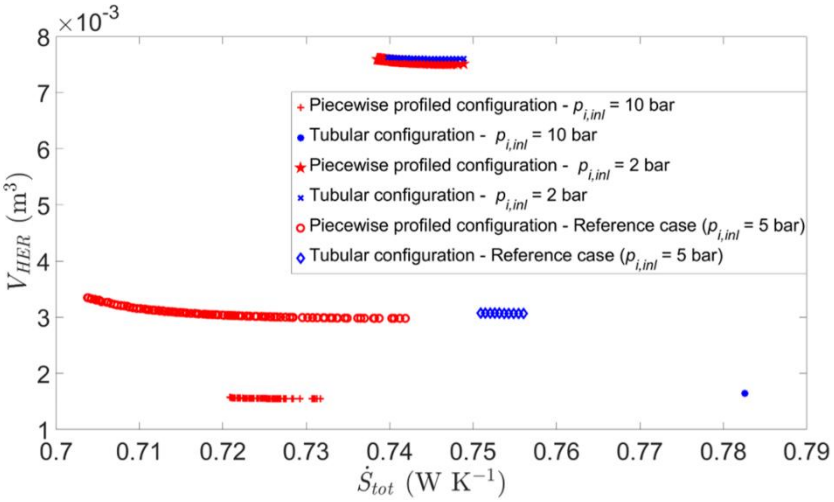

Figure 5.6: Pareto fronts for different inlet gas pressures.

Figure 5.6 demonstrates that as pressure increases, the required HER volume decreases due to the enhanced reaction rate, as indicated in Equation *4.2.1*. In addition, entropy generation depicted in the Pareto front does not follow a clear trend with varying pressure. The absence of a systematic trend is primarily due to the optimisation constraints limiting the feasible design space. Indeed, at an inlet gas pressure of 2 bar, the maximum diameter limit strongly restricts the feasible configurations. On the other hand, at 10 bar, the maximum temperature limitation (880 K) becomes the dominant constraint, limiting the range of feasible designs.

Focusing on the case study with $p_{M,i,inl} = 2$ bar, Figure 5.6 reveals that, compared to the tubular design, the profiled configuration allows only moderate reduction of the HER volume and/or the generated entropy. Indeed, under these operating conditions, the reaction rate is low while the gas velocity is high. As a result, to meet the target SO_2 conversion and limit pressure drop, the optimiser tends to increase the packed bed diameter until it reaches the upper diameter bound as the heat generated by the slower reaction is not an issue. Consequently, as illustrated in Figure 5.7a and Figure 5.7c, the MPCVol and MPCEnt points at $p_{M,i,inl} = 2$ bar closely resemble a tubular HER (with a imperceptible divergence of less than 1 mm between the maximum and minimum diameter over the total length) with a packed bed diameter of nearly 9 cm, which is the maximum allowable diameter. These designs still incorporate some slight profiling, however, its effects on the required volume or generated entropy are minor.

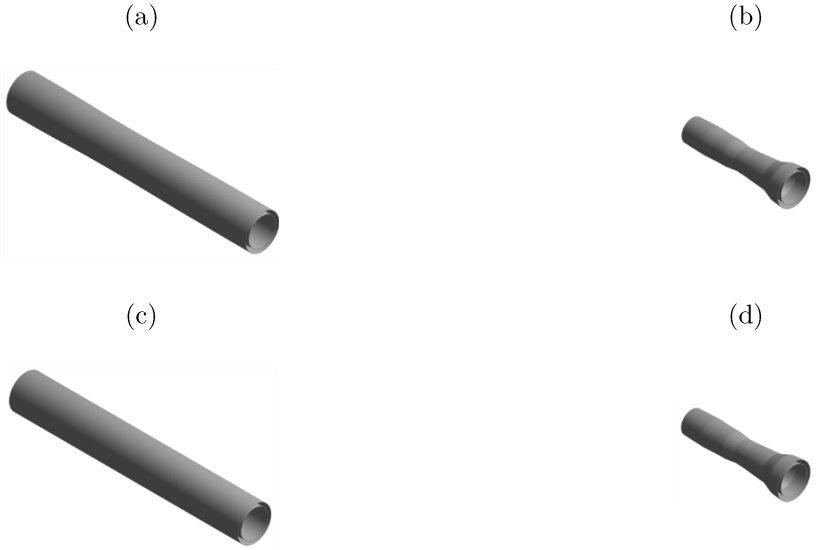

Figure 5.7: 3D representation of the MPCVol (a) and MPCEnt (c) points at $p_{M,i,inl}$= 2 bar, and the MPCVol (b) and MPCEnt (d) at with $p_{M,i,inl}$= 10 bar.

At an inlet pressure of 10 bar, Figure 5.7 shows that, compared to the tubular geometry, the profiled configuration allows achieving a reduction in the HER volume of about 5.7%, and enables significantly reducing the entropy generation rate by approximately 7.9%. Indeed, at such high pressures, the gas velocity is low, while the reaction rate is significantly increased, leading to a substantial temperature rise in the packed bed and therefore the need for a smaller reacting volume. In this context, geometric profiling offers significant advantages: by controlling heat transfer and gas velocity, it manages the gas temperature profile, keeping it below the authorized limit while minimizing heat transfer and associated entropy generation. In fact, by decreasing the local packed bed diameter in zones of high reaction rates, and thus increasing the local mixture velocity, the local temperature rise can be maintained below the imposed threshold. The packed bed diameter is increased in the remaining regions to limit pressure drop and ensure convenient heat transfer rates. As a result, the profiled configuration authorizes significant reduction of the process irreversibility.

Figure 5.8 illustrates the variations in packed bed radius and temperature profiles along the axial position for the MPCEnt designs at inlet gas pressures of 2 bar and 10 bar. At 2 bar, due to the low reaction rate, the optimal packed bed radius stays close to the upper bound of 4.5 cm, and the gas temperature remains below the authorized limit. After the mixture reaches its maximal temperature, the HER extends over a sufficient length to allow adequate cooling as a sufficiently low temperature is necessary to achieve the target conversion of SO_2 at such a low pressure (Figure 5.5). Conversely, at an inlet gas pressure of 10 bar, the target conversion of SO_2 can be attained even at relatively high temperatures. As a result, in the MPCEnt design, the target conversion is achieved within the maximum temperature zone, limiting further heat transfer and thereby reducing additional entropy generation.

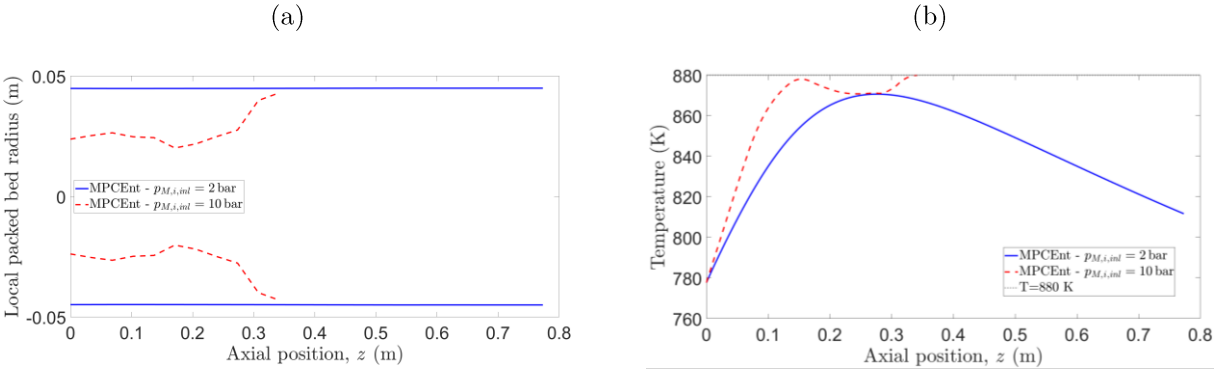

Figure 5.8: MPCEnt points at inlet gas pressures of 2 and 10 bar: (a) Packed bed radius profiles, (b) Packed bed temperature profiles.

The performance of the MPCEnt geometries in relation to the achieved objective functions and the contribution of each entropy source is summarized in Table 5.2 for the three gas inlet pressures examined. The contribution of viscous dissipation in the gas phase increases as pressure decreases, driven by higher gas velocities and longer HER designs; however, it remains a minor component of the total entropy generation in the present situations. Heat transfer contribution also decreases with increasing pressure due to lower cooling requirements and shorter geometries. In contrast, chemical entropy generation rises with increasing pressure, attributed to higher reaction rates, as stated in Equation *4.2.1*, and contributes to more than half of the total entropy generation at an inlet gas pressure of 10 bar.

Table 5.2: HER volume and entropy generation rate of the MPCEnt points of the three gas inlet pressures.

	$p_{M,i,inl}$ = 2 bar	$p_{M,i,inl}$ = 5 bar	$p_{M,i,inl}$ = 10 bar
V_{HER}	7.60 L	3.35 L	1.58 L
$\dot{S}_{tot}$	7.40×10^{-1} W K^{-1} ➢ 2.74×10^{-2} and 1.48×10^{-3} W K^{-1} (3.7% and 0.2%) due to viscous dissipation in the mixture and coolant flow respectively. ➢ 3.91×10^{-1} W K^{-1} (52.9%) due to heat transfer. ➢ 3.20×10^{-1} W K^{-1} (43.3%) due to the chemical reaction.	7.04×10^{-1} W K^{-1} ➢ 7.33×10^{-3} and 1.12×10^{-3} W K^{-1} (1.0% and 0.2%) due to viscous dissipation in the mixture and coolant flow respectively. ➢ 3.23×10^{-1} W K^{-1} (45.7%) due to heat transfer. ➢ 3.74×10^{-1} W K^{-1} (53.1%) due to the chemical reaction.	7.21×10^{-1} W K^{-1} ➢ 4.33×10^{-3} and 1.44×10^{-3} W K^{-1} (0.6% and 0.2%) due to viscous dissipation in the mixture and coolant flow respectively. ➢ 2.93×10^{-1} W K^{-1} (40.7%) due to heat transfer. ➢ 4.22×10^{-1} W K^{-1} (58.2%) due to the chemical reaction.

In summary, the effect of the reactive mixture inlet pressure on HER performance highlights the interplay between reaction kinetics, gas velocity, and geometric constraints. At low pressures (2 bar), the reaction rate is limited and gas velocity is high, leading the optimiser

to favour nearly tubular designs with maximum allowable diameter, resulting in only minor reductions in volume and entropy generation compared to tubular geometries. Conversely, at high pressures (10 bar), the reaction rate is significantly enhanced while the gas velocity is lower, producing a substantial temperature rise in the packed bed. Profiled geometries in this scenario effectively manage heat transfer and local velocities, reducing both HER volume and total entropy generation by controlling the temperature within the allowed limit. Overall, chemical reaction dominates entropy generation at high pressure, while viscous dissipation and heat transfer play secondary roles. This analysis confirms that geometric profiling is particularly advantageous under conditions of high reaction rates, where temperature control and irreversibility reduction are critical.

5.2.3 Influence of the maximum allowable temperature constraint

The results presented in the previous sections indicate that, unless the reaction rate is sufficiently low to stay below the temperature constraint, the maximum allowable temperature constraint significantly restricts the feasible solution space and directly influences the optimal designs. To further investigate the impact of this temperature constraint, the optimisation problem is solved again but with the maximum allowable temperature set to 840 K instead of 880 K (Equation 4.6.13). All other parameters and boundary conditions remain unchanged, and their values are reported in Chapter 4, Section 4.3.2, Table 4.3 and Table 4.4. The resulting Pareto fronts are illustrated in Figure 5.9 and are compared to those from the reference case.

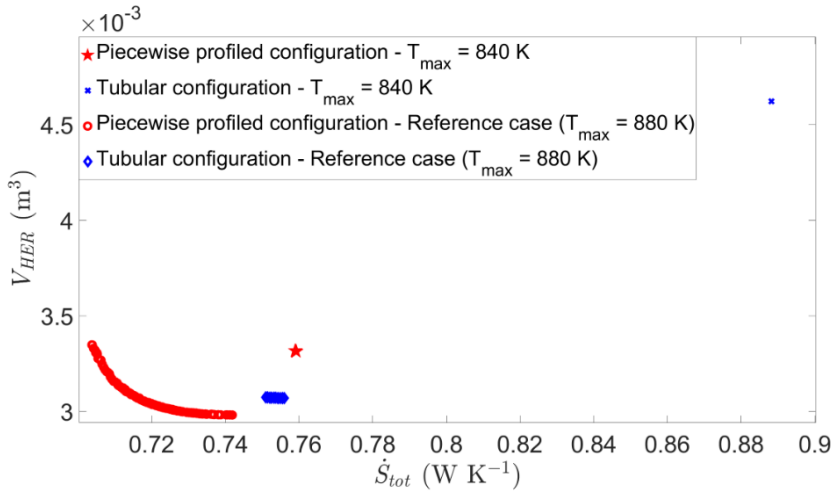

Figure 5.9: Effects of the allowable temperature constraint on the Pareto fronts.

Figure 5.9 shows that, as expected, the designs achieved setting a maximum temperature of 880 K enable lower entropy generation and lower HER volume compared to those obtained under a temperature constraint of 840 K. Indeed, the stricter temperature constraint further limits the feasible solution space, leading to less performant designs in terms of achievable objection functions values.

Under the strict constraint of a maximum temperature of 840 K, the Pareto fronts get much narrower, each one corresponding practically to a unique design, featuring only slight variations. Consequently, the optimal tubular designs have a packed diameter of approximately 5.75 cm and a length of 0.62 m. Smaller diameters result in non-optimal geometries exhibiting an increased entropy generation along with a higher volume (due to significantly higher length for reaching the desired conversion), while larger diameters lead to a hot spot where the temperature exceeds 840 K in the first part of the HER due to the exothermic reaction as explained in Section 5.2.1. For larger diameters, the reaction heat is more significant than the heat exchange through the wall, leading to an excess of heat generated compared to the cooling capacity. This results in insufficient dissipation in the HER, causing the formation of a hot spot where the temperature exceeds the imposed limit. The optimal profiled configuration designs also exhibit strong similarities, largely due to the limited range of feasible solutions. As a result, only the MPCEnt design is presented in Figure 5.10 for illustration. While the physical

reasoning behind the resulting complex shape is not immediately apparent, the mathematical optimisation reveals its purpose: this design effectively maintains the packed bed temperature below 840 K (Figure 5.11) while minimizing entropy generation throughout the process. Compared to tubular geometries, the profiled configuration offers significant enhancements, enabling a potential reduction in HER volume by up to 28.3% and a decrease in entropy generation rate by as much as 14.5%. This case study highlights the potential of shape optimisation in designing highly efficient reactors that meet stringent operational constraints, achieving levels of efficiency and compactness far beyond those possible with conventional geometries due to local heat transfer control.

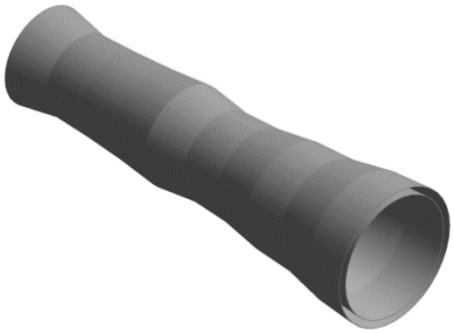

Figure 5.10: MPCEnt design for a maximal allowable temperature of 840 K.

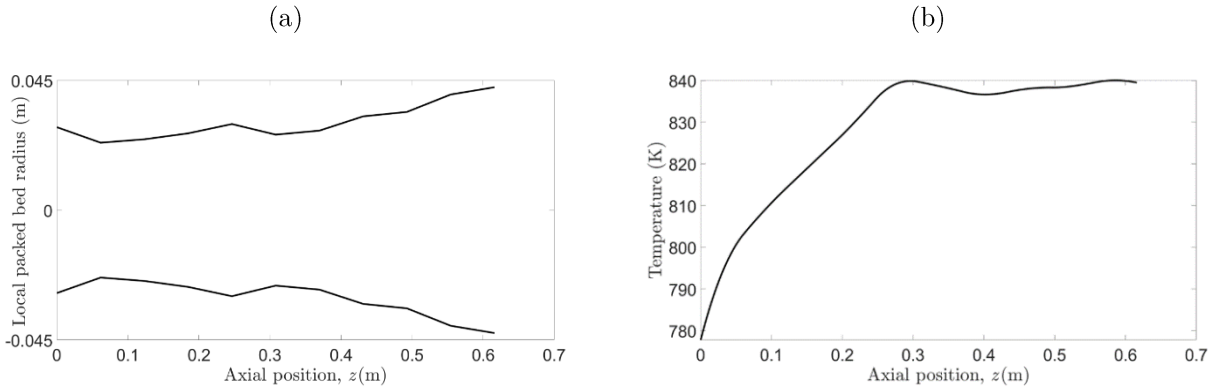

Figure 5.11: MPCEnt point for a maximum allowable temperature of 840 K: (a) Packed bed radius profile, (b) Packed bed temperature profile.

In summary, tightening the maximum allowable temperature constraint from 880 K to 840 K strongly limits the feasible design space, resulting in narrower Pareto fronts and nearly unique optimal geometries. Under this stricter limit, tubular designs must balance diameter and length to avoid hot spots while still achieving the target conversion, whereas profiled configurations can more effectively control local temperatures, leading to substantial reductions in both HER volume (up to 28.3%) and total entropy generation (up to 14.5%). This analysis demonstrates that geometric profiling is particularly valuable under stringent thermal constraints, enabling higher efficiency and more compact reactor designs by locally managing heat transfer and reaction rates.

5.2.4 Influence of the inlet heat carrier temperature

The impact of the inlet heat carrier temperature was also investigated. In the reference case, the inlet gas temperature is $T_{M,i,inl}$ = 778 K and the inlet temperature of the coolant is set to $T_{M,an,inl}$ = 703 K. To assess the influence of the inlet heat coolant temperature, two additional optimisations were conducted: one with the inlet temperature reduced by 50 K ($T_{M,an,inl}$= 653 K) compared to the reference case, and another with it increased by 50 K ($T_{M,an,inl}$ = 753 K). All other parameters and boundary conditions remain unchanged, and their values are reported in Chapter 4, Section 4.3.2, Table 4.3 and Table 4.4. The resulting Pareto fronts for these cases are compared to the reference situation in Figure 5.12.

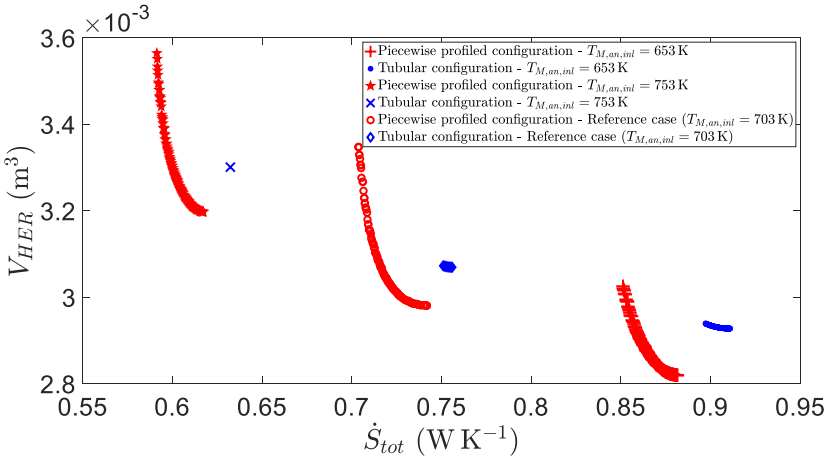

Figure 5.12: Pareto fronts for different inlet coolant temperature.

Several observations can be made from Figure 5.12, particularly regarding the tubular geometries. It is evident that the Pareto front corresponding to the lower inlet temperature is wider than the other two. As the coolant inlet temperature increases, the Pareto front becomes narrower. This trend can be explained by the fact that a higher inlet temperature leads to less effective cooling, making it more difficult to control the temperature profile of the reactive mixture. As a result, the range of viable designs for simple tubular reactors becomes more limited as the maximum temperature constraint is rapidly reached.

Notably, a higher inlet temperature results in longer optimal reactor lengths and lower entropy generation within the reactor. However, this reduction in entropy generation must be interpreted with caution, as it overlooks the entropy produced when heating the coolant before entering the reactor. In other words, part of the entropy generation is shifted outside the system boundary and is therefore not accounted for in the present analysis.

Figure 5.13 shows the geometries obtained for the MPCEnt and MPCVol obtained under both increased and decreased coolant inlet temperatures. As expected, the optimal geometries corresponding to the higher coolant inlet temperature are longer, in order to compensate for the reduced heat transfer rate. Indeed, when the coolant is hotter, its heat removal capacity

decreases (lower temperature gradients), requiring smaller reactor diameters at the inlet to reduce reaction heat. However, reducing the diameter negatively affects the volumetric reaction rate, which lowers conversion at a given axial position. As a result, a longer reactor length is necessary to reach the 80% conversion target.

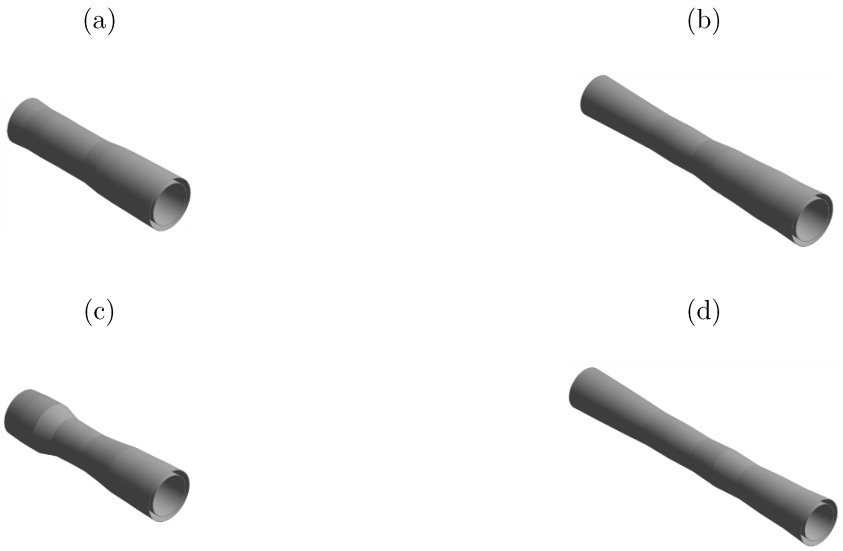

Figure 5.13: 3D representation of the MPCEnt (a) and MPCVol (c) points for $T_{M,an,inl} = 653$ K, and the MPCEnt (b) and MPCVol (d) at $T_{M,an,inl} = 753$ K.

Interestingly, Figure 5.13a, Figure 5.13b, and Figure 5.14a reveal that the MPCEnt geometries exhibit a consistent shape: a slightly converging section followed by a more pronounced diverging section. This similarity is also apparent in the temperature profiles shown in Figure 5.14b, where all cases display a similar pattern, an initial temperature increase followed by a plateau region in which the temperature is maintained as high as possible to maximize the reaction rate.

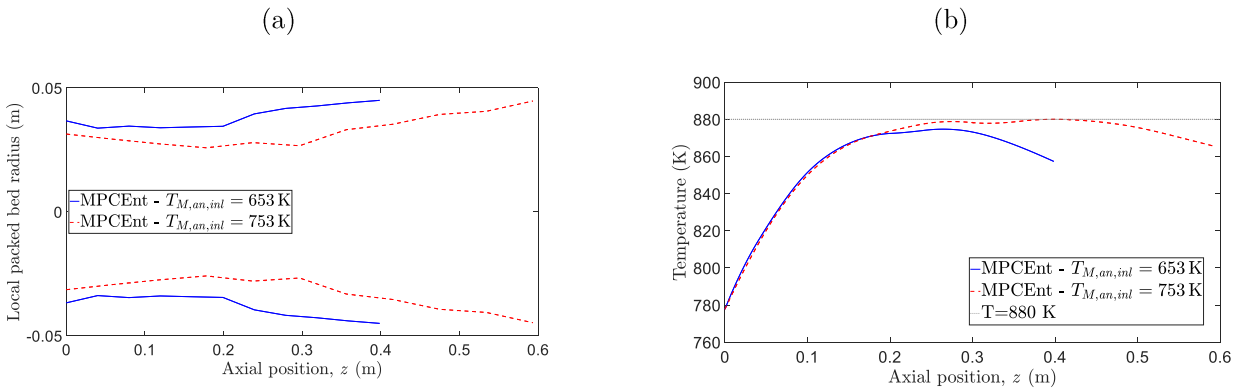

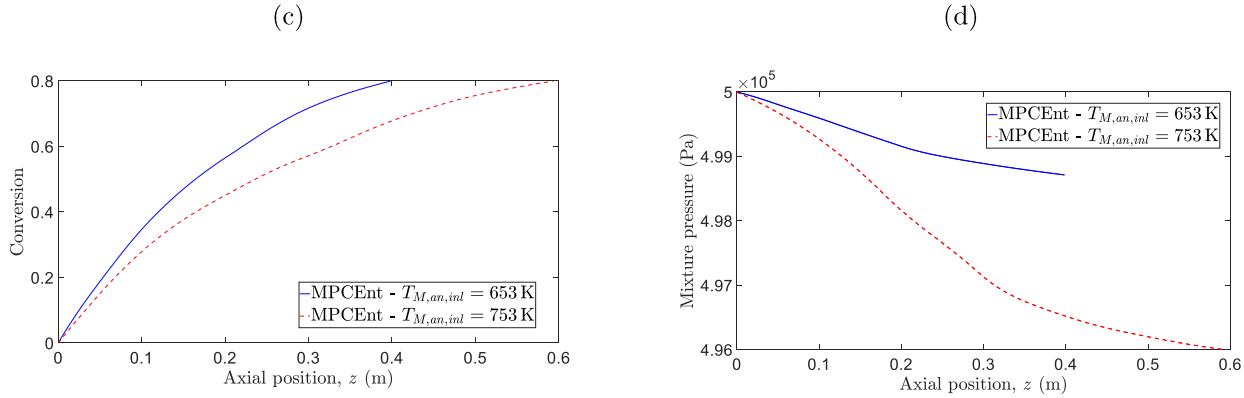

Figure 5.14: MPCEnt points for $T_{M,an,inl}$ = 653 K and $T_{M,an,inl}$ = 753 K: (a) Packed bed radius profiles, (b) Packed bed temperature profiles, (c) SO_2 conversion rate profiles, (d) Mixture pressure profiles.

This temperature rise is more significant in the case with the higher coolant temperature, where the system more easily reaches the maximal temperature limit. Conversely, the lower coolant temperature case hardly attains this upper temperature limit — a limit that, as previously discussed, is typically reached in most optimised MPCEnt geometries. This limitation is likely due to the maximum diameter constraint imposed during optimisation, which prevents a wider outlet section and thereby restricts the achievable temperature increase.

Table 5.3 summarizes the influence of coolant temperature on the entropy generation rate. No clear trend is observed in the MPCEnt reactor volume: increasing the inlet temperature by 50 K results in a 6% increase in volume, whereas decreasing it by 50 K leads to a 10% volume reduction. The main variation arises from the entropy generation due to heat transfer, which increases with decreasing coolant temperature — consistent with the larger temperature gradients. In contrast, the entropy generation associated with the chemical reaction remains nearly constant, though it tends to slightly decrease as the coolant temperature increases. This trend can be attributed to the fact that, at higher coolant temperatures, the reaction proceeds at elevated temperatures over a larger portion of the reactor length, thereby reducing local irreversibilities.

Table 5.3: HER volume and entropy generation rate of the MPCEnt corresponding to the three inlet heat carrier temperatures.

	$T_{M,an,inl} = 653\ K$	$T_{M,an,inl} = 703\ K$	$T_{M,an,inl} = 753\ K$
V_{HER}	3.03 L	3.35 L	3.56 L
$\dot{S}_{tot}$	8.52×10^{-1} W K^{-1} ➢ 4.49×10^{-3} and 9.44×10^{-4} W K^{-1} (0.5% and 0.1%) due to viscous dissipation in the mixture and coolant flow respectively. ➢ 4.69×10^{-1} W K^{-1} (55.0%) due to heat transfer. ➢ 3.78×10^{-1} W K^{-1} (44.4%) due to the chemical reaction.	7.04×10^{-1} W K^{-1} ➢ 7.33×10^{-3} and 1.12×10^{-3} W K^{-1} (1.0% and 0.2%) due to viscous dissipation in the mixture and coolant flow respectively. ➢ 3.23×10^{-1} W K^{-1} (45.7%) due to heat transfer. ➢ 3.74×10^{-1} W K^{-1} (53.1%) due to the chemical reaction.	5.92×10^{-1} W K^{-1} ➢ 1.40×10^{-2} and 1.49×10^{-3} W K^{-1} (2.4% and 0.3%) due to viscous dissipation in the mixture and coolant flow respectively. ➢ 2.16×10^{-1} W K^{-1} (36.6%) due to heat transfer. ➢ 3.60×10^{-1} W K^{-1} (60.8%) due to the chemical reaction.

In conclusion, raising the coolant inlet temperature leads to a moderate decrease in internal entropy generation (around 16% reduction compared to the reference case) but at the expense of a larger reactor volume. However, the increase in volume remains relatively modest (approximately 7%) compared to the entropy reduction benefit. It should be noted, as mentioned earlier, that increasing the utility fluid temperature may shift part of the entropy generation upstream of the HER, which must be considered in the overall system assessment.

5.2.5 Influence of the inlet gas molar flowrate

In this section, the influence of the inlet gas molar flowrate (circulating in the fixed bed and reacting via the chemical reaction) on the optimal design of the HER is investigated. The same optimisation framework used as in the reference case study is applied; however, two additional scenarios are considered: one with a 50% decrease in the inlet molar flowrate compared to the reference case ($F_{i,inl}$= = 2.15 10^{-1} mol s^{-1}), and another with a 50% increase and the resulting Pareto fronts are presented in Figure 5.15. All other operating and boundary conditions remain unchanged, with their values reported in Chapter 4, Section 4.3.2, Table 4.3 and Table 4.4.

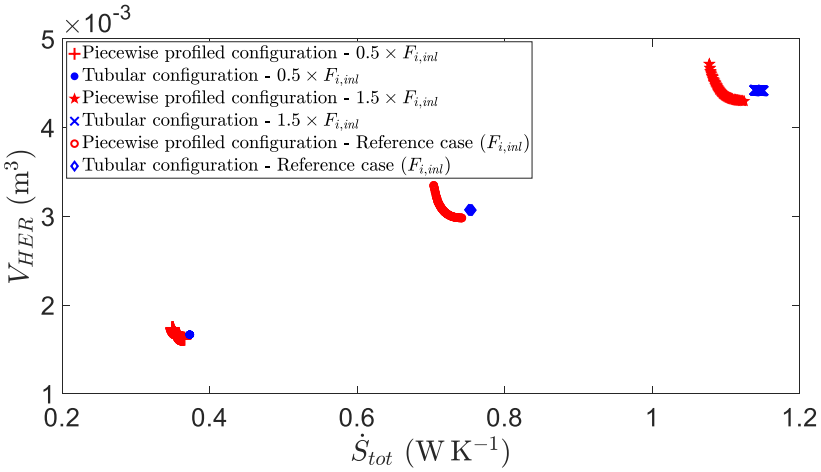

Figure 5.15: Pareto fronts for different inlet gas molar flowrate.

As illustrated in Figure 5.15, the inlet molar flowrate has a significant effect on both the reactor volume and the total entropy generated. The use of a profiled geometry enables reductions in both entropy generation and reactor volume in all cases. Both Figure 5.15 and Table 5.4 demonstrate consistent trends across the three scenarios. Specifically, when the inlet molar flowrate is reduced by 50%, the MPCEnt and MPCVol configurations yield reductions of 50% and 48% in total entropy generation and reactor volume, respectively. These reductions align closely with the imposed change in flowrate. Conversely, for the case with a 50% increase in inlet molar flowrate, the entropy generation and reactor volume increase by 53% and 41%, respectively. These results confirm that entropy generation scales almost linearly with the molar flowrate, while the reactor volume is similarly affected, though not perfectly proportionally. This discrepancy may be attributed to geometric constraints in the optimisation process, particularly the diameter limitation imposed at the reactor outlet.

A more detailed analysis of the individual entropy contributions provides additional insights. For viscous dissipation, the trend deviates significantly: entropy generation decreases by 73% for the reduced flowrate case, while it increases by 182% under the increased flowrate condition. Despite this strong variation, viscous dissipation remains a relatively minor contributor overall, although its contribution becomes more significant at higher flowrates. In

contrast, entropy generation due to chemical reaction increases with flowrate because a larger number of moles must be converted, explaining the observed rise in entropy. Entropy generation due to heat transfer also follows the overall trend: when the flowrate increases, higher heat fluxes are necessary to maintain the mixture temperature within the convenient range. Moreover, the reactor length required to achieve the target conversion becomes longer, which leads to larger temperature gradients along the reactor.

Table 5.4: HER volume and entropy generation rate of the MPCEnt points of the three gas inlet molar flowrates.

	$F_{i,inl} \times 0.5$	$F_{i,inl}$	$F_{i,inl} \times 1.5$
V_{HER}	1.74 L	3.35 L	4.72 L
$\dot{S}_{tot}$	3.50×10^{-1} W K^{-1} ➢ 1.30×10^{-3} and 9.44×10^{-4} W K^{-1} (0.4% and 0.3%) due to viscous dissipation in the mixture and coolant flow respectively. ➢ 1.59×10^{-1} W K^{-1} (45.5%) due to heat transfer. ➢ 1.88×10^{-1} W K^{-1} (53.9%) due to the chemical reaction.	7.04×10^{-1} W K^{-1} ➢ 7.33×10^{-3} and 1.12×10^{-3} W K^{-1} (1.0% and 0.2%) due to viscous dissipation in the mixture and coolant flow respectively. ➢ 3.23×10^{-1} W K^{-1} (45.7%) due to heat transfer. ➢ 3.74×10^{-1} W K^{-1} (53.1%) due to the chemical reaction.	1.08 W K^{-1} ➢ 2.25×10^{-2} and 1.33×10^{-3} W K^{-1} (2.1% and 0.1%) due to viscous dissipation in the mixture and coolant flow respectively. ➢ 4.91×10^{-1} W K^{-1} (45.6%) due to heat transfer. ➢ 5.63×10^{-1} W K^{-1} (52.2%) due to the chemical reaction.

Given the strong correlation between flowrate and both entropy generation and reactor volume, it is relevant to examine the corresponding optimal geometries shown in Figure 5.16. As expected, the geometries corresponding to the lower flowrate (Figure 5.16a and Figure 5.16c) are more compact, reflecting the lower reactants flow rate to convert. Notably, the MPCVol configurations (Figure 5.16c and Figure 5.16d) display a narrowing of the cross-sectional area, whereas the MPCEnt geometries (Figure 5.16a and Figure 5.16b) exhibit a more divergent profile.

(a) (b)



(c) (d)



Figure 5.16: 3D representation of the MPCEnt (a) and MPCVol (c) points at $F_{i,inl}$=0.5$F_{i,inl,ref}$, and the MPCEnt (b) and MPCVol (d) at $F_{i,inl}$=1.5$F_{i,inl,ref}$.

A comparative analysis of the MPCEnt geometries is provided in Figure 5.17. As in the reference case, the temperature of the gas mixture (Figure 5.17b) approaches the maximum allowable value in both cases.

For the lower molar flowrate, the temperature rise along the reactor is sharper. This can be attributed to the reduced number of moles being converted, which results in a smaller total heat generation. Consequently, the system can accommodate proportionally larger diameters compared to the higher flowrate case, as the balance between heat generated by the reaction and heat removed by the coolant is more easily maintained. The optimal geometry for higher flowrates features a narrower initial section to mitigate the heat generated by the reaction, followed by a longer reactor length with a proportionally smaller diameter to ensure temperature control and achieve the target conversion.

Furthermore, viscous dissipation (Figure 5.17d) is more pronounced in the high flowrate case, due to the increased gas velocity. This is exacerbated by the additional reactor length required to achieve 80% conversion under higher flow rate conditions (Figure 5.17c), as the increased velocity is not fully offset by the larger cross-sectional area.

(a) (b)

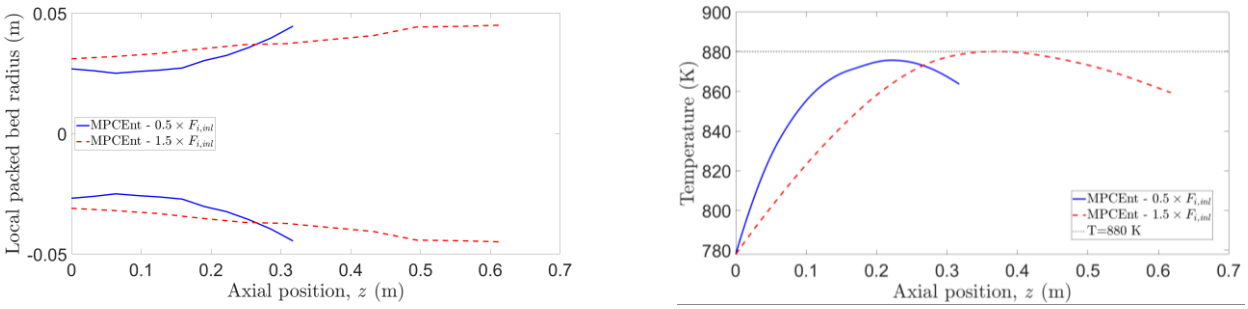

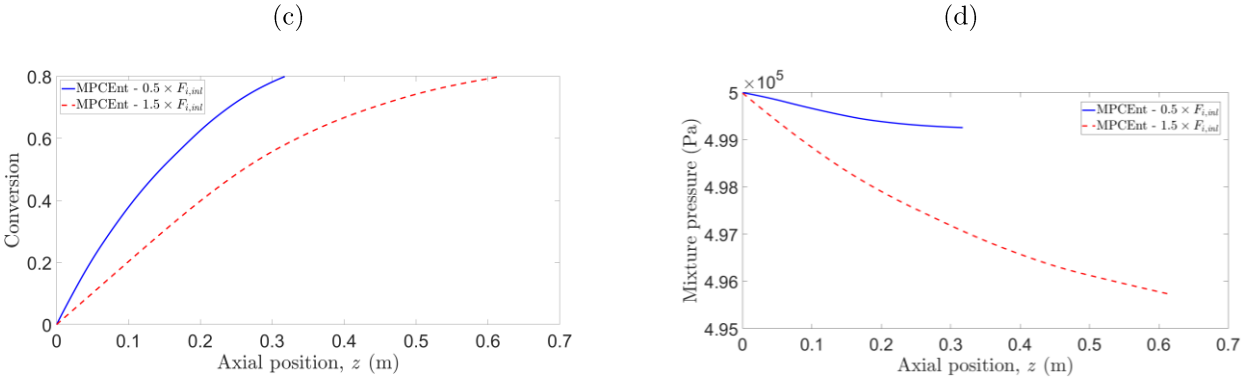

Figure 5.17: MPCEnt points for 50% reduced and 50% increased $F_{i,inl}$: (a) Packed bed radius profiles, (b) Packed bed temperature profiles, (c) SO_2 conversion rate profiles, (d) Mixture pressure profiles.

The proportional trends observed in the various contributions are further elucidated through the local entropy generation profiles shown in Figure 5.18. As previously noted, viscous dissipation does not vary proportionally to the inlet molar flow rate, owing to the nonlinear dependence of pressure drop on the gas velocity, as described by Equation 4.4.5*4.4.6*. In contrast, the entropy generated by heat transfer is consistently lower for the reduced flowrate case due to lower cooling requirement.

Figure 5.18b further indicates that entropy generation from the chemical reaction remains substantially lower for the reduced flowrate case throughout the entire reactor length. This difference is not driven by the reactor length, as is partially the case for heat transfer, but rather by a lower number of reactant moles to be converted. Although the initial reaction rate is similar in both cases, the reduced reactor volume leads to a lower overall entropy generation.

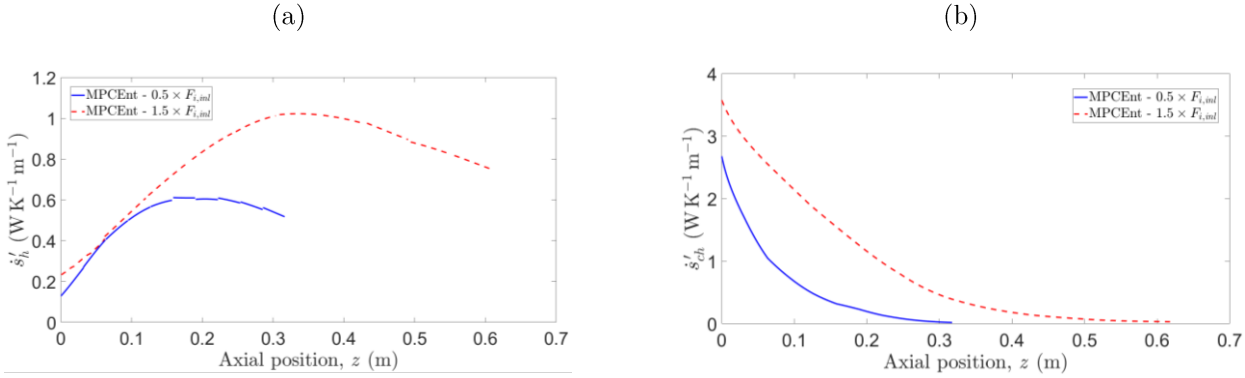

Figure 5.18: Local entropy generation rates in both MPCEnt geometries: (a) Heat transfer, (b) Chemical reaction.

In summary, the inlet molar flowrate has a strong influence on both reactor volume and total entropy generation. Lower flowrates lead to more compact reactors, sharper temperature rises, and reduced entropy generation due to both smaller heat release and lower viscous dissipation. Conversely, higher flowrates require longer reactors with narrower initial sections to manage the increased heat from the reaction, resulting in higher entropy generation and

more pronounced viscous contributions. Overall, the results highlight that optimal profiled geometries effectively adapt to variations in flowrate, maintaining temperature control while minimizing irreversibilities, with entropy generation scaling approximately proportionally to the number of moles to be converted.

5.2.6 Influence of the inlet gas temperature

The effect of the inlet gas temperature on reactor performance was investigated for three cases: the reference temperature of 778 K, a lower temperature of 728 K (50 K below the reference), and a higher temperature of 828 K (50 K above the reference). Figure 5.19 presents the corresponding Pareto fronts for these three scenarios. With the coolant inlet temperature maintained at 703 K, all configurations remained cooled (and not heated). All other parameters and boundary conditions remain unchanged, and their values are reported in Chapter 4, Section 4.3.2, Table 4.3 and Table 4.4.

For tubular configurations, it is observed that higher inlet temperatures lead to narrower Pareto fronts compared to the case with a lower inlet temperature. This suggests a reduced design flexibility when the gas is hotter at the inlet, likely due to the limited capacity of the tubular geometry to manage the thermal gradients and maintain optimal temperature profiles, i.e., maximal temperature below the allowed limit.

In contrast, the piecewise profiled configurations demonstrate significantly improved performance in terms of both reduced entropy generation and reactor volume, particularly at higher inlet temperatures. However, while the difference between high and low inlet temperatures is quite marked for the tubular configurations, the variation in performance among the piecewise profiled configurations is less pronounced. It is also noteworthy that, for higher inlet temperatures, the Pareto front is shifted upward in entropy generation. This indicates that increasing the gas temperature leads to additional entropy being produced within the system but allows for a smaller reactor volume due to the increases reaction rate.

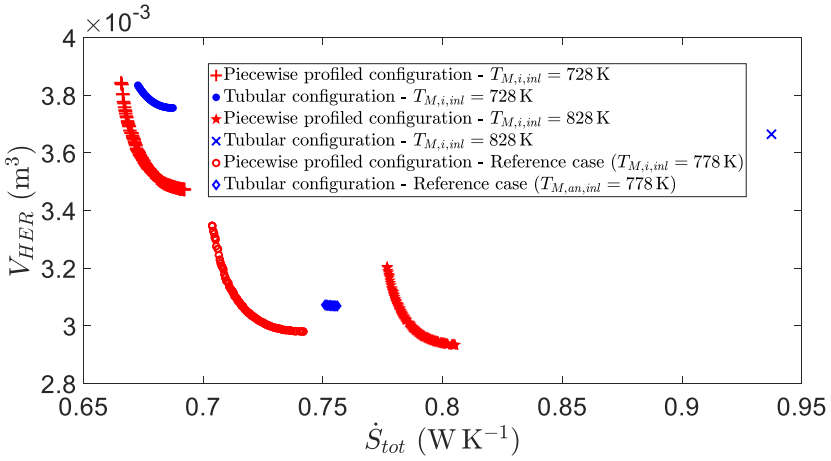

Figure 5.19: Pareto fronts for different inlet gas temperature.

Figure 5.20 illustrates the optimal geometries corresponding to each configuration. Lower inlet temperatures generally lead to longer reactor lengths. Figure 5.20c, for instance, shows a narrowing of the cross-section, which is less pronounced in the high-temperature case. Figure 5.20a reveal that the optimal MPCEnt geometry at low inlet temperature approaches a straight

cylindrical shape. This is further confirmed by Figure 5.21a, where the local packed bed diameter is close to the imposed maximum diameter constraint.

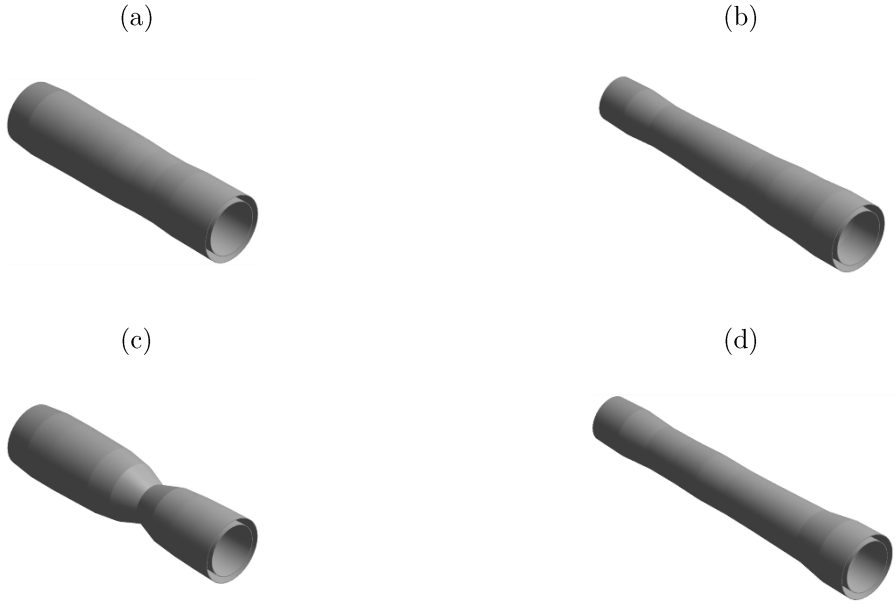

Figure 5.20: 3D representation of the MPCEnt (a) and MPCVol (c) points for $T_{M,i,inl} = 728$ K, and the MPCEnt (b) and MPCVol (d) at $T_{M,i,inl} = 828$ K.

The temperature profiles presented in Figure 5.21b illustrate the impact of inlet temperature on the optimal reactor geometry. At lower inlet temperatures, the gas temperature rises more gradually as the reaction rate is slower, allowing for wider diameters that maximize the reacting volume. In contrast, at higher inlet temperatures, the mixture rapidly approaches the maximum allowable temperature despite the low diameter, prompting a transition to a diverging geometry. This design ensures that the temperature is maintained close to the upper limit throughout the remainder of the reactor. As the reaction slows down due to reactant depletion, the HER diameter is increased through the divergent section as a large diameter becomes sufficient for removing the heat released by the reaction.

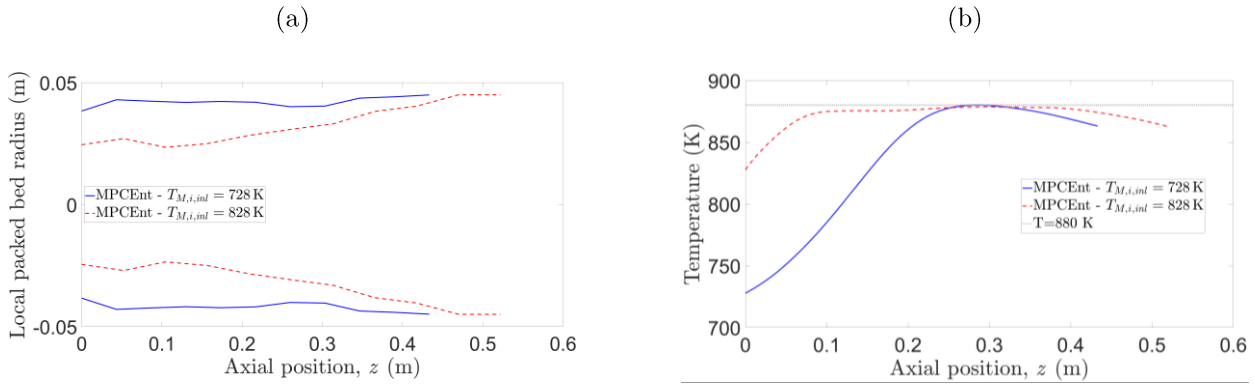

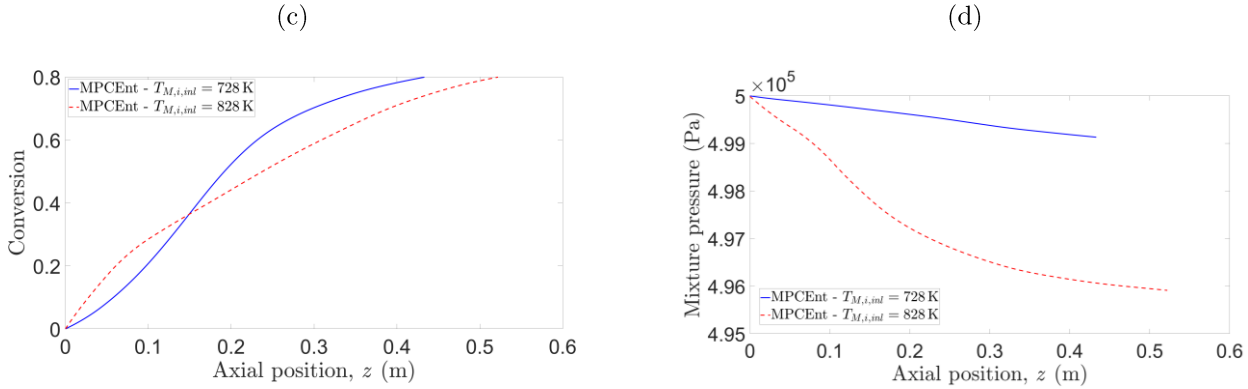

Figure 5.21: MPCEnt points for $T_{M,an,inl}$ = 728 K and $T_{M,an,inl}$ = 828 K: (a) Packed bed radius profiles, (b) Packed bed temperature profiles, (c) SO_2 conversion rate profiles, (d) Mixture pressure profiles.

As expected, entropy generation due to heat transfer (Figure 5.22c) is lower in the low-temperature cases. This results from the reduced temperature gradient between the reacting mixture and the coolant. Regarding chemical reaction-related entropy generation, an atypical behaviour is observed: instead of a monotonic decrease, a peak in entropy generation appears before diminishing again. This may be attributed to the slower temperature increase at the inlet in low-temperature cases, requiring a longer reactor length before optimal reaction conditions are achieved.

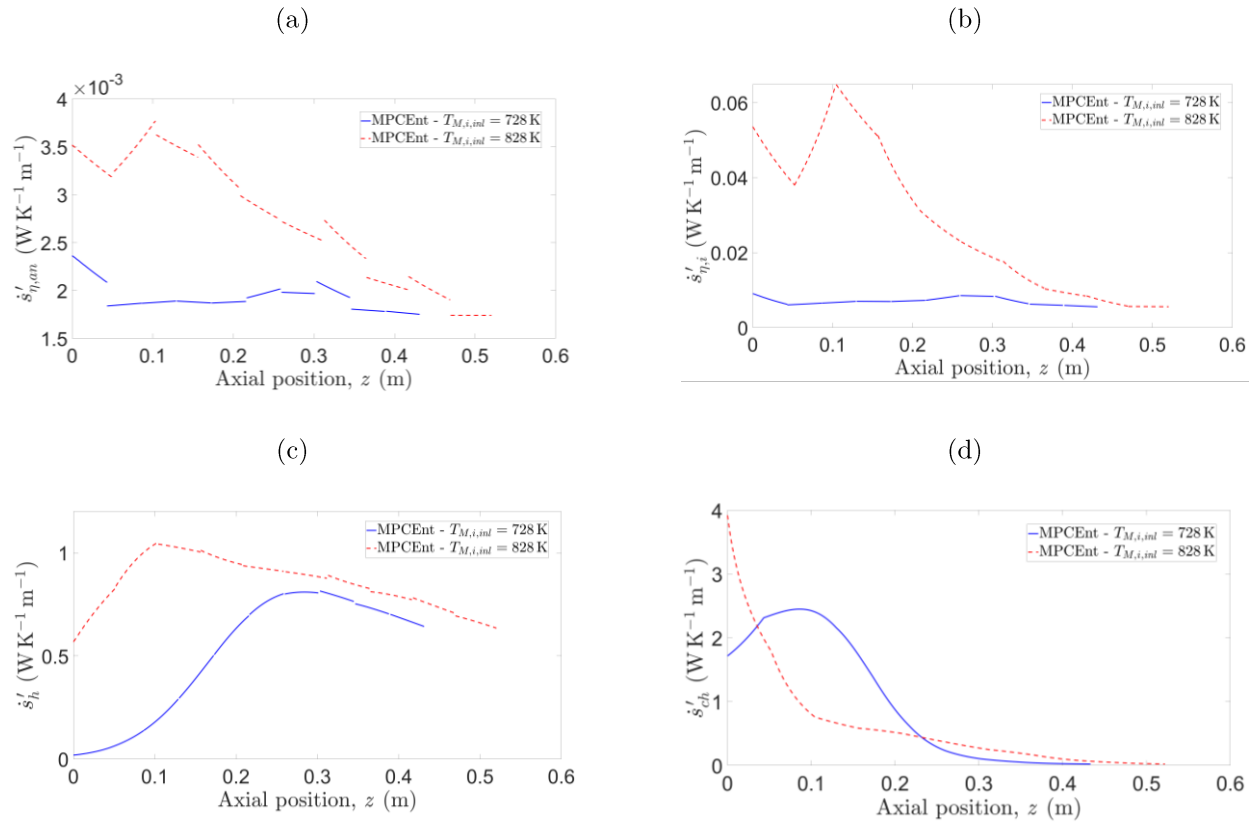

Figure 5.22: Local entropy generation rates in both MPCEnt geometries: (a) Viscous dissipation in the coolant, (b) Viscous dissipation in the reactive mixture, (c) Heat transfer, (d) Chemical reaction.

Finally, considering the different optimised MPCEnt geometries (Table 5.5), it is observed that reactor volume increases as the inlet gas temperature decreases. Interestingly, however, total entropy generation decreases with lower gas temperatures. This is primarily due to the significant reduction in entropy generated by heat transfer, which outweighs the slightly higher entropy contribution from the chemical reaction. The latter is explained by the slower reaction initiation and longer reactor residence time in colder inlet conditions, as well as the larger reactor volume.

Table 5.5: HER volume and entropy generation rate of the MPCEnt points of the three gas inlet temperatures.

	$T_{M,i,inl} = 728\ K$	$T_{M,i,inl} = 778\ K$	$T_{M,i,inl} = 828\ K$
V_{HER}	3.84 L	3.35 L	3.20 L
$\dot{S}_{tot}$	6.66×10^{-1} W K^{-1} ➢ 3.03×10^{-3} and 8.32×10^{-4} W K^{-1} (0.5% and 0.1%) due to viscous dissipation in the mixture and coolant flow respectively. ➢ 2.20×10^{-1} W K^{-1} (33.0%) due to heat transfer. ➢ 4.42×10^{-1} W K^{-1} (66.4%) due to the chemical reaction.	7.04×10^{-1} W K^{-1} ➢ 7.33×10^{-3} and 1.12×10^{-3} W K^{-1} (1.0% and 0.2%) due to viscous dissipation in the mixture and coolant flow respectively. ➢ 3.23×10^{-1} W K^{-1} (45.7%) due to heat transfer. ➢ 3.74×10^{-1} W K^{-1} (53.1%) due to the chemical reaction.	7.77×10^{-1} W K^{-1} ➢ 1.44×10^{-2} and 1.43×10^{-3} W K^{-1} (1.8% and 0.2%) due to viscous dissipation in the mixture and coolant flow respectively. ➢ 4.43×10^{-1} W K^{-1} (57.0%) due to heat transfer. ➢ 3.18×10^{-1} W K^{-1} (40.9%) due to the chemical reaction.

In summary, the inlet gas temperature strongly influences reactor performance and optimal design. Lower inlet temperatures result in longer reactors with wider diameters, allowing a more gradual temperature rise and reducing entropy generation from heat transfer, despite slightly higher contributions from chemical reactions. Higher inlet temperatures, in contrast, require diverging geometries to prevent exceeding the maximum allowable temperature, leading to increased entropy generation but enabling smaller reactor volumes due to faster reaction rates. Overall, piecewise profiled configurations outperform tubular geometries across all temperature scenarios, demonstrating enhanced flexibility in balancing temperature control, reactor volume, and entropy minimization.

5.2.7 Influence of the inlet gas O_2/SO_2 molar ratio

Another criterion studied is the inlet flow composition. The reference inlet flow composition has a molar O_2/SO_2 ratio of approximately 0.9. To assess the impact of this parameter, two additional cases were tested: one with a ratio of 0.7 and another with a ratio of 1.1 (in both situations, the inlet molar fractions of SO_2 and SO_3 are kept the same as in the reference case). It is noteworthy that for all three ratios investigated, O_2 remains the reactant in excess. All other parameters and boundary conditions remain unchanged, and their values are reported in Chapter 4, Section 4.3.2, Table 4.3 and Table 4.4. The Pareto fronts obtained for these new operating conditions are compared to the reference case in Figure 5.23.

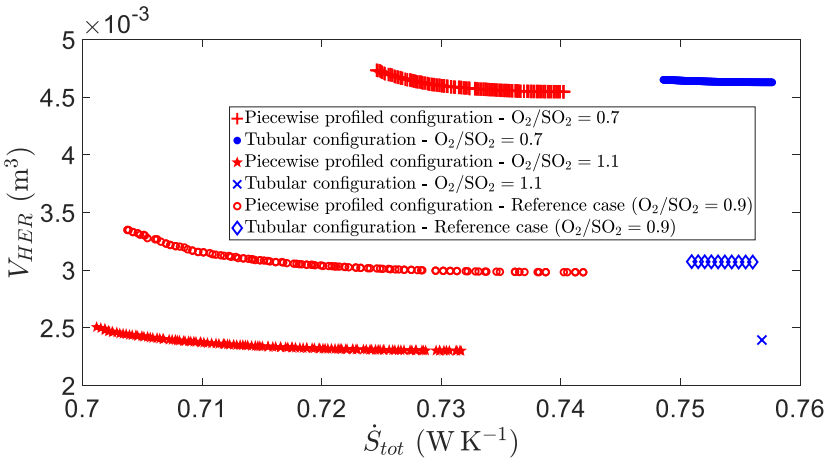

Figure 5.23: Pareto fronts for different inlet O_2/SO_2 molar ratio.

Figure 5.23 shows that increasing the inlet O_2 to SO_2 molar ratio leads to a significant reduction in reactor volume. The excess oxygen promotes faster reaction rates, thereby lowering the required reactor size to achieve the same target conversion. In parallel, the entropy generation also decreases with higher O_2 availability, although the reduction is much more pronounced when increasing the ratio from 0.7 to the reference case than from the reference to 1.1. A similar trend is observed for the reactor volume: the volume decreases between 0.7 and the reference case is larger than the additional reduction obtained when increasing the ratio from the reference to 1.1.

Figure 5.24 presents the MPCEnt and MPCVol geometries of the Pareto fronts. For both cases, the extreme configurations follow the same overall trends as those observed for the MPCEnt and MPCVol geometries of previous case studies. Indeed, in the minimal volume geometries, a narrowing of the middle section is observed, while the geometries minimizing entropy generation follow a globally divergent pattern, despite a narrowing at the inlet for both geometries with the 0.7 ratio.

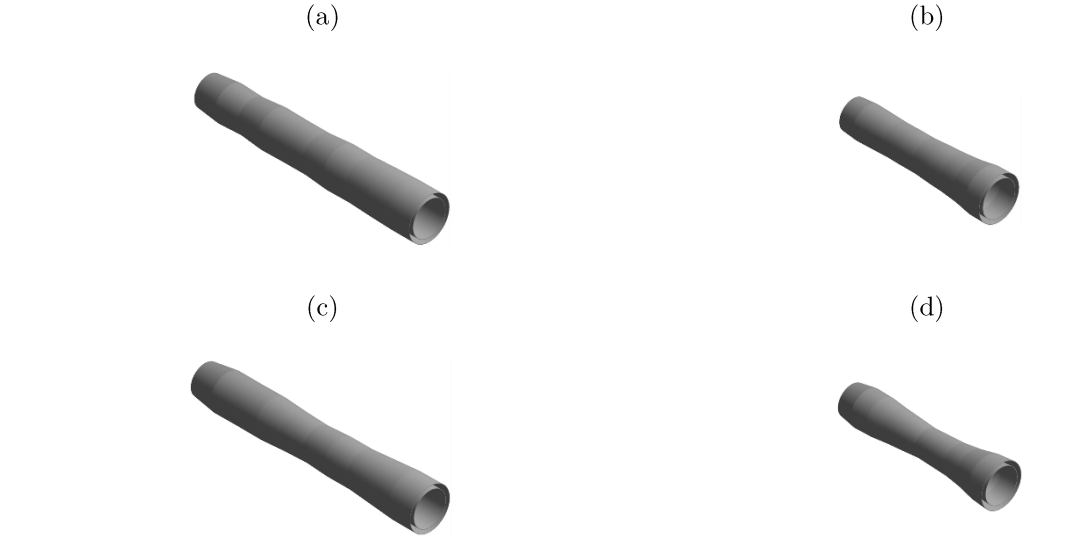

Figure 5.24: 3D representation of the MPCEnt (a) and MPCVol (c) points for $\frac{x_{inl,O_2}}{x_{inl,SO_2}} = 0.7$*, and the MPCEnt (b) and MPCVol (d) for* $\frac{x_{inl,O_2}}{x_{inl,SO_2}} = 1.1$*.*

Figure 5.24 shows that higher inlet O_2/SO_2 ratios restrict the design space toward smaller diameters while excluding larger ones. This effect arises because a more oxygen-rich mixture accelerates the reaction kinetics, resulting in a faster and more pronounced temperature rise. In a constant-diameter configuration, this temperature increase can only be effectively controlled when the diameter is small, since a lower diameter provides smaller residence time and therefore a smaller reacting volume and local heat generation. At the same time, the higher O_2 concentration reduces the required reactor length (thanks to the faster kinetics). This shorter length makes it possible to operate with a smaller diameter without facing the penalty of a long reactor—which, in the case of a less concentrated mixture, would otherwise increase entropy generation to reach the same target conversion.

The comparison of temperature, pressure, and composition profiles for both minimal-entropy generation geometries are shown in Figure 5.25:

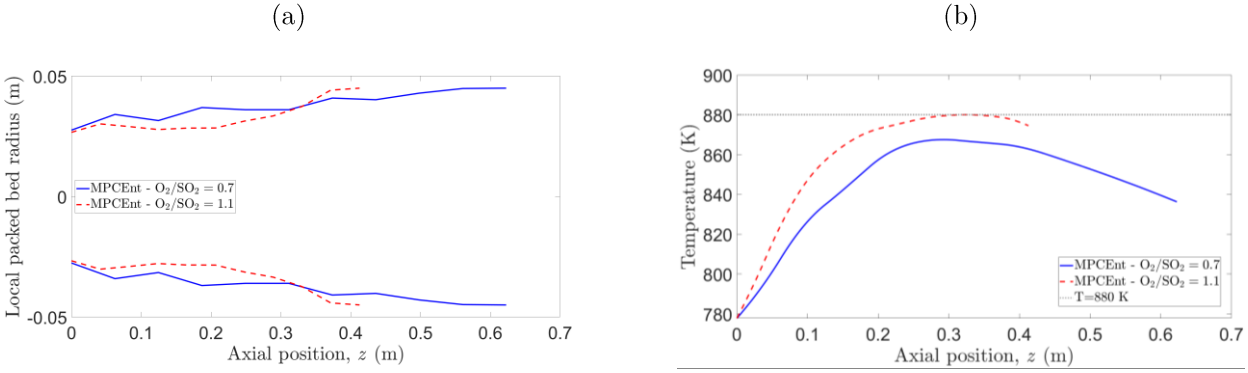

(c) (d)

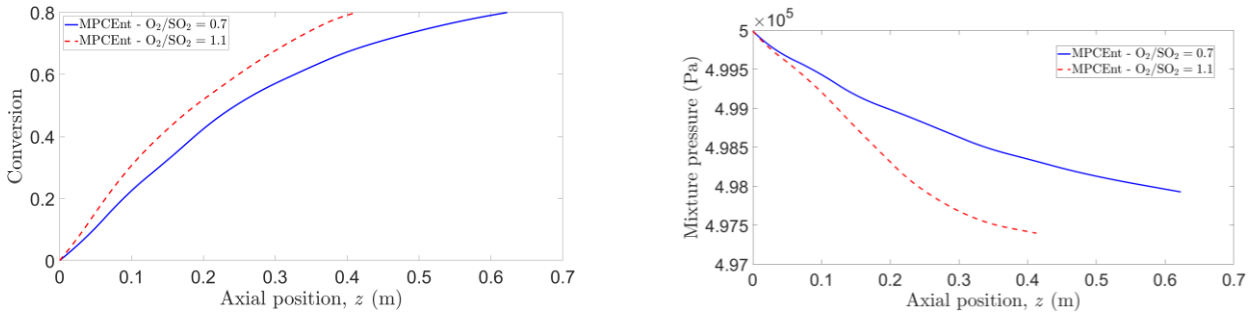

Figure 5.25: MPCEnt points for $\frac{x_{inl,O_2}}{x_{inl,SO_2}} = 0.7$ and $\frac{x_{inl,O_2}}{x_{inl,SO_2}} = 1.1$: (a) Packed bed radius profiles, (b) Packed bed temperature profiles, (c) SO_2 conversion rate profiles, (d) Mixture pressure profiles.

Figure 5.25b shows that the optimal geometry corresponding to the lower O_2/SO_2 ratio does not reach the maximum allowable temperature, in contrast to the geometry with a 1.1 ratio. In general, the temperature increase is greater in the 1.1 ratio configuration, where the inlet concentrations are 9.36 mol m^{-3} for O_2 and 8.51 mol m^{-3} for SO_2, compared to the 0.7 ratio configuration, with inlet concentrations of 5.95 mol m^{-3} for O_2 and 8.51 mol m^{-3} for SO_2.

This behaviour can be attributed to the slower exothermic reaction at lower O_2/SO_2 molar ratios, combined with a shift in the reaction equilibrium, which releases heat more gradually along an extended reactor length. As a result, the coolant has increased opportunity to remove the generated heat, while the reactor design favours larger diameters to enhance the reacting volume. This leads to a lower maximum temperature compared to the higher-ratio case, where high temperature gradients at large diameters cannot be efficiently balanced without risking insufficient cooling of the mixture.

Figure 5.26 illustrates the contribution of each source of local entropy generation within the reactor. As anticipated from the temperature profiles shown in Figure 5.25b, the local entropy generation due to heat transfer is higher in the MPCEnt geometry with the higher O_2/SO_2 molar ratio, because the larger temperature gradients associated with the higher temperature peak enhance the local thermal irreversibilities.

(a) (b)

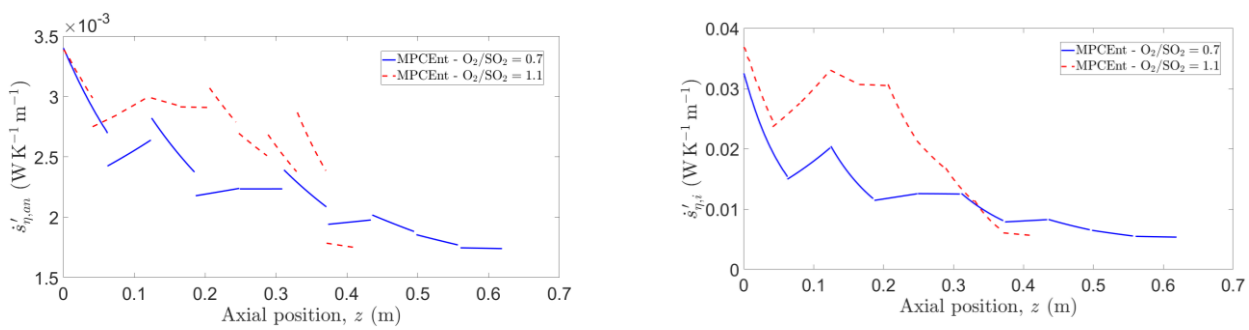

(c) (d)

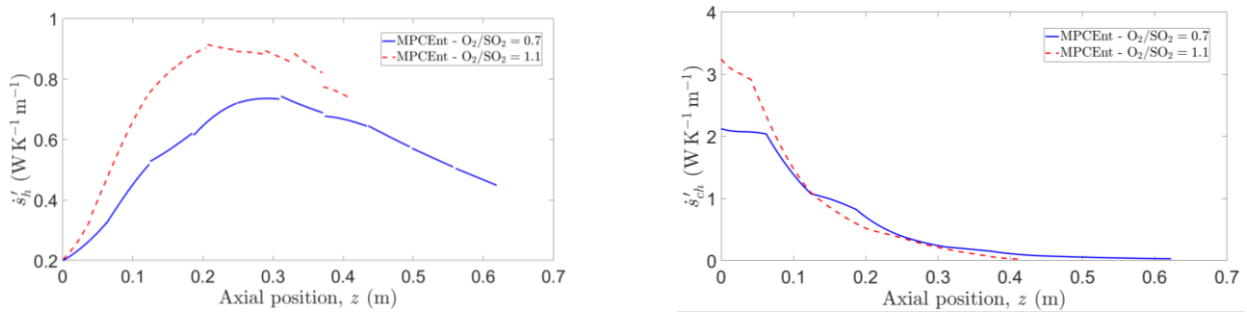

Figure 5.26: Local entropy generation rates in both MPCEnt geometries: (a) Viscous dissipation in the coolant, (b) Viscous dissipation in the reactive mixture, (c) Heat transfer, (d) Chemical reaction.

Figure 5.26d shows that the chemical reaction rate is higher in the 1.1 ratio case, which can be attributed to the higher inlet concentration of O_2 ($9.36\,\text{mol}\cdot\text{m}^{-3}$) compared to $5.95\,\text{mol}\cdot\text{m}^{-3}$ in the 0.7 ratio case, while the inlet SO_2 concentration is identical in both cases ($8.51\,\text{mol}\cdot\text{m}^{-3}$). According to the apparent reaction rate law (Equation 4.2.1), the reaction rate depends on the O_2 partial pressure to the first order. Therefore, the higher O_2 concentration in the 1.1 ratio case has a strong effect on accelerating the reaction. This difference in O_2 partial pressure leads to a faster conversion at the reactor inlet.

Despite the higher local chemical entropy generation in the 1.1 ratio case due to the higher reaction rate, the total entropy generation along most of the reactor remains similar between the two cases. This can be explained by two factors: first, the difference in reaction rates between the two cases decreases along the reactor length; second, the increasing temperature in the 1.1 ratio configuration reduces the contribution of this reaction rate difference to entropy generation, due to the inverse relationship between chemical entropy generation and temperature.

The results of the comparison between the different cases are presented in Table 5.6. Table 5.6 shows that a lower O_2/SO_2 ratio leads to lower entropy generation due to viscous dissipation in the gas phase but higher entropy generation in the coolant. This can be explained by the larger diameter favoured at lower ratios, which significantly reduces pressure losses. However, for the coolant, since the annular thickness is kept constant, the slight increase in cross-sectional area due to the larger diameter does not compensate for the additional reactor length. This results in a global increase in entropy despite the larger diameter.

Furthermore, Table 5.6 indicates that a lower O_2/SO_2 ratio leads to higher entropy generation due to heat transfer and chemical reactions. This can be attributed to the difficulty of reaching high temperatures in the presence of a coolant, requiring a longer reactor length to complete the same conversion. This additional length generates more entropy than a shorter reactor would, even though local entropy generation is generally lower for lower ratios. As a result, global entropy generation is higher for lower ratios.

Table 5.6: HER volume and entropy generation rate of the MPCEnt corresponding to the three inlet molar ratios.

	$\frac{x_{inl,O_2}}{x_{inl,SO_2}} = 0.7$	$\frac{x_{inl,O_2}}{x_{inl,SO_2}} = 0.9$	$\frac{x_{inl,O_2}}{x_{inl,SO_2}} = 1.1$
V_{HER}	4.73 L	3.35 L	2.51 L
$\dot{S}_{tot}$	7.25×10^{-1} W K^{-1} ➢ 7.25×10^{-3} and 1.39×10^{-3} W K^{-1} (1.0% and 0.2%) due to viscous dissipation in the mixture and coolant flow respectively. ➢ 3.51×10^{-1} W K^{-1} (48.5%) due to heat transfer. ➢ 3.65×10^{-1} W K^{-1} (50.4%) due to the chemical reaction.	7.04×10^{-1} W K^{-1} ➢ 7.33×10^{-3} and 1.12×10^{-3} W K^{-1} (1.0% and 0.2%) due to viscous dissipation in the mixture and coolant flow respectively. ➢ 3.23×10^{-1} W K^{-1} (45.7%) due to heat transfer. ➢ 3.74×10^{-1} W K^{-1} (53.1%) due to the chemical reaction.	7.02×10^{-1} W K^{-1} ➢ 9.11×10^{-3} and 1.12×10^{-3} W K^{-1} (1.3% and 0.2%) due to viscous dissipation in the mixture and coolant flow respectively. ➢ 3.03×10^{-1} W K^{-1} (43.1%) due to heat transfer. ➢ 3.89×10^{-1} W K^{-1} (55.4%) due to the chemical reaction.

In summary, the inlet O_2/SO_2 molar ratio significantly affects both reactor volume and entropy generation. Lower ratios lead to slower reaction rates, extended residence times, and consequently larger reactor diameters, which increase entropy generation from heat transfer and chemical reactions. Conversely, higher O_2 concentrations accelerate the reaction, allowing smaller reactors while slightly reducing overall entropy generation. The analysis indicates that increasing the O_2/SO_2 ratio is beneficial for process efficiency, although the improvement between the reference ratio (0.9) and the higher ratio (1.1) is moderate, suggesting that an optimal ratio can be identified to balance entropy minimization and reactant consumption.

5.2.8 Influence of the required conversion

A final study was conducted to examine the influence of another critical constraint in the system, the required minimal conversion, on the optimal reactor geometries. Specifically, the goal is to understand how varying the minimal conversion threshold affects the Pareto-optimal configurations. Figure 5.27 shows the Pareto fronts corresponding to different imposed conversion targets: 65%, 80% (reference), and 95%. As expected, higher conversion targets require larger reactor volumes. All other parameters and boundary conditions remain unchanged, and their values are reported in in Chapter 4, Section 4.3.2, Table 4.3 and Table 4.4. Furthermore, the Pareto fronts reveal that the relative gain in entropy generation, when compared to a simple tubular reactor configuration, is more significant at higher conversion levels.

The Pareto analysis also highlights that, although the relative entropy reduction becomes more modest at higher conversions, the potential savings in reactor volume are substantially greater. For instance, the reference case allows for a 6.9% reduction in entropy generation and a 3% decrease in volume, while a case targeting 95% conversion achieves gains of 5.1% in entropy and 26.5% in volume.

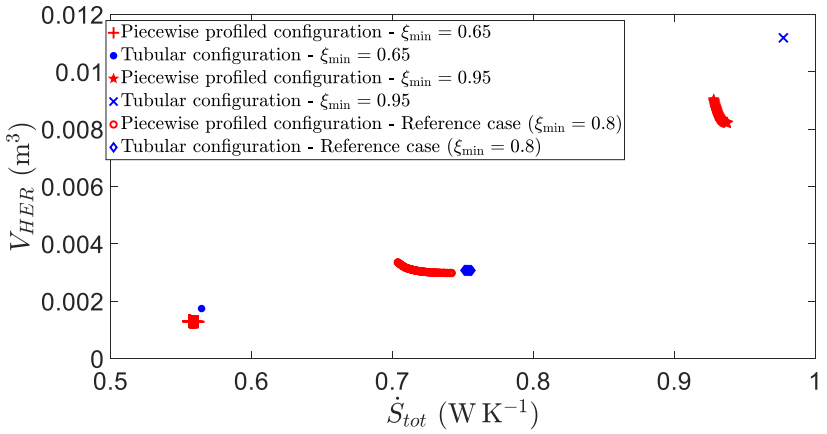

Figure 5.27: Pareto fronts for different minimal conversion.

Figure 5.28 illustrates the impact of the conversion constraint on the optimised geometries using the MPCEnt and MPCVol designs. The low-conversion geometries exhibit pronounced narrowing of the cross-section, consistent with trends previously observed. In contrast, the geometries associated with higher conversion constraints tend to be predominantly divergent for both MPCEnt and MPCVol configurations.

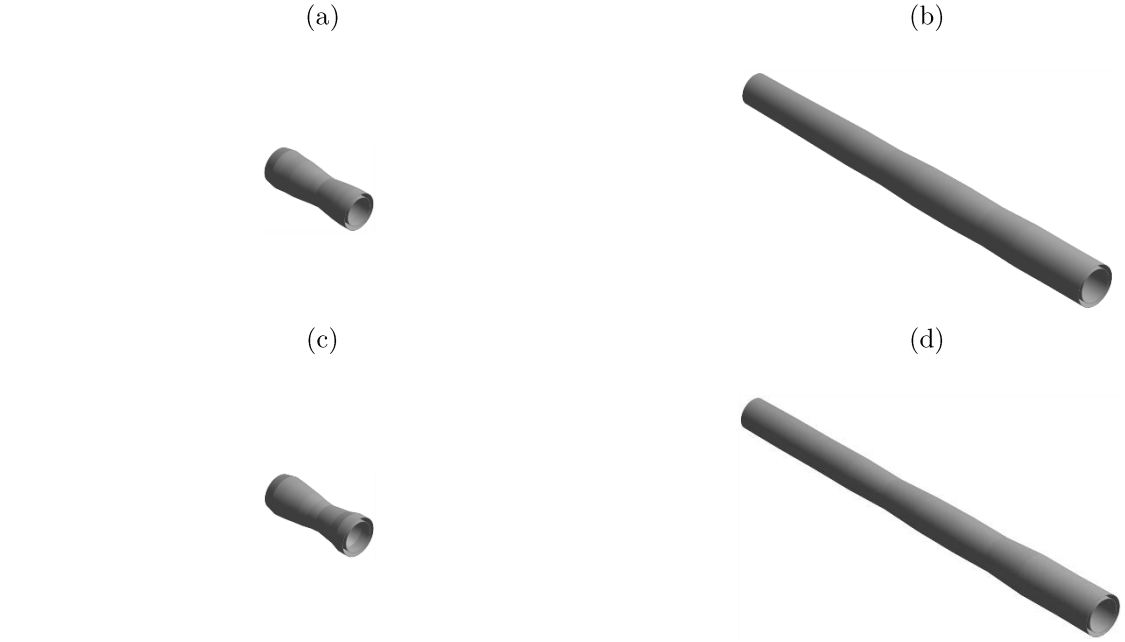

Figure 5.28: 3D representation of the MPCEnt (a) and MPCVol (c) points for ξ_{min} = 0.65, and the MPCEnt (b) and MPCVol (d) for ξ_{min} = 0.95.

A comparison between the two MPCEnt geometries is presented in Figure 5.29. It is noteworthy that the diameter profile along the reactor length differs substantially between the two cases. In particular, the optimal geometry for ξ_{min} = 0.65 does not match the geometry obtained for ξ_{min} = 0.95. This finding indicates that the optimal reactor profile depends on the conversion constraint. In particular, a geometry optimised for a higher conversion cannot be simply truncated or scaled down to meet a lower conversion requirement. While this suggests that the Pareto-optimal shapes are not directly related by a simple homothetic transformation, it should be noted that the existence of other non-dominated solutions cannot be completely ruled out.

This point is further emphasized in Figure 5.29a.

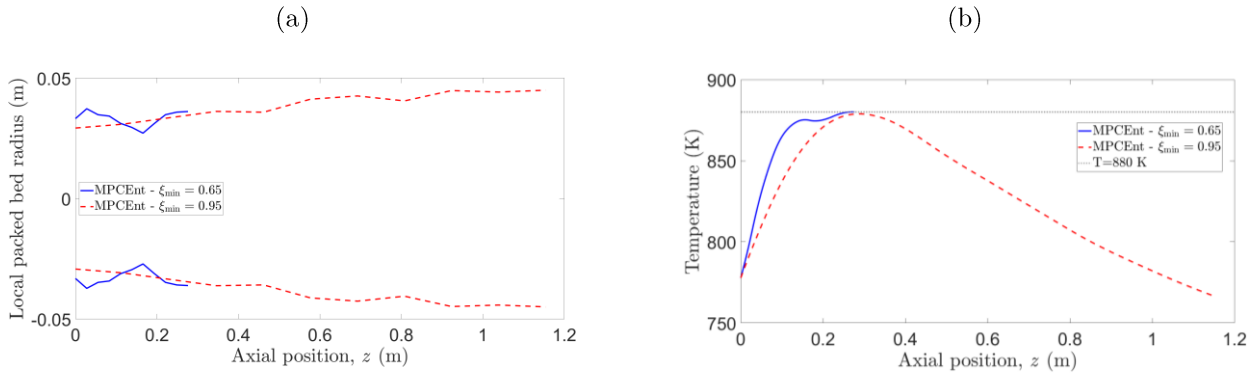

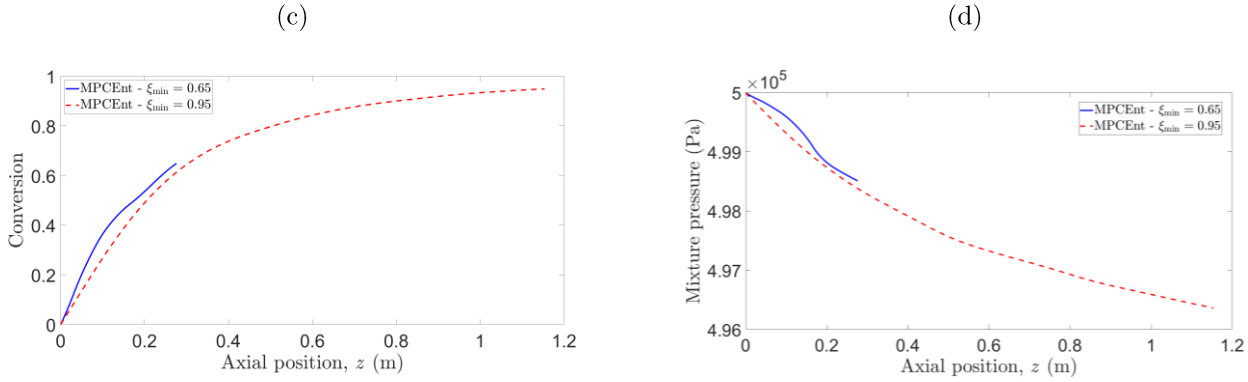

Figure 5.29: MPCEnt points for $\xi_{min} = 0.65$ and $\xi_{min} = 0.95$: (a) Packed bed radius profiles, (b) Packed bed temperature profiles, (c) SO_2 conversion rate profiles, (d) Mixture pressure profiles.

Figure 5.29b shows that the lower-conversion geometry leads to a more rapid temperature rise and achieves an outlet temperature close to 880 K. Conversely, the larger reactor optimised for $\xi_{min} = 0.95$ exhibits a slower temperature increase, reaching the 880 K limit before cooling down, with an outlet temperature well below 800 K. It is worth noting that the diameter in the second half of the reactor is limited by constraints imposed in the optimisation framework. A relaxation of these constraints could allow for greater divergence of the tube at the outlet and potentially higher outlet temperatures.

Table 5.7 compares the entropy generation across the three case studies. As expected, the reactor volume increases substantially with the conversion requirement. However, the variation in the required conversion does not translate proportionally into changes in entropy generation. When analysing the individual entropy contributions, further insights emerge. For viscous dissipation, the increase in entropy is consistent with the longer reactor length. However, for entropy due to heat transfer and chemical reaction, the situation is more nuanced.

Both entropy sources increase with higher conversion requirements, but their relative contributions shift significantly. For instance, in the low-conversion case, chemical reaction account for approximately 63% of the total entropy generated, while heat transfer contributes to 36.1%. In contrast, at 95% conversion, chemical reactions represent only 41.5% of the total entropy, whereas heat transfer contributes 56.9%. This inversion stems from the fact that, as the reaction progresses, the reactants are depleted, and the lower gas temperatures further slowdown the kinetics. Consequently, the extended reactor length promotes more heat exchange, which becomes the dominant source of entropy generation.

Table 5.7: HER volume and entropy generation rate of the MPCEnt points of the three minimal conversions.

	$\xi_{min} = 0.65$	$\xi_{min} = 0.8$	$\xi_{min} = 0.95$
V_{HER}	1.30 L	3.35 L	9.04 L
$\dot{S}_{tot}$	5.56×10^{-1} W K^{-1} ➢ 5.20×10^{-3} and 7.64×10^{-4} W K^{-1} (0.9% and 0.1%) due to viscous dissipation in the mixture and coolant flow respectively. ➢ 2.01×10^{-1} W K^{-1} (36.1%) due to heat transfer. ➢ 3.50×10^{-1} W K^{-1} (62.8%) due to the chemical reaction.	7.04×10^{-1} W K^{-1} ➢ 7.33×10^{-3} and 1.12×10^{-3} W K^{-1} (1.0% and 0.2%) due to viscous dissipation in the mixture and coolant flow respectively. ➢ 3.23×10^{-1} W K^{-1} (45.7%) due to heat transfer. ➢ 3.74×10^{-1} W K^{-1} (53.1%) due to the chemical reaction.	9.29×10^{-1} W K^{-1} ➢ 1.26×10^{-2} and 2.44×10^{-3} W K^{-1} (1.4% and 0.3%) due to viscous dissipation in the mixture and coolant flow respectively. ➢ 5.28×10^{-1} W K^{-1} (56.9%) due to heat transfer. ➢ 3.85×10^{-1} W K^{-1} (41.5%) due to the chemical reaction.

In summary, the minimal conversion requirement significantly influences the optimal reactor geometry and associated performance. Higher conversion targets necessitate larger reactor volumes and lead to more divergent profiled designs, while lower conversion targets result in more compact geometries. Although the relative reduction in total entropy generation compared to a tubular reference decrease at higher conversion levels, the potential savings in reactor volume are substantially larger. Additionally, as conversion increases, the dominant source of entropy shifts from chemical reaction to heat transfer, reflecting longer reactor lengths and slower reaction rates at lower temperatures. These results highlight those optimal geometries are not directly scalable with conversion and must be specifically tailored to the desired conversion target.

5.2.9 Summary of the 1D optimisation key results

This study advances the work of Magnanelli et al. (2019) by addressing several of its limitations and proposing a more comprehensive reactor design strategy. While the previous study focused solely on minimizing entropy generation, the present work introduces a second, often competing objective: reducing reactor size. By adopting a multi-objective optimisation framework, this study highlights the inherent trade-offs between energy efficiency and reactor compactness. Moreover, unlike the earlier model, the present work incorporates the thermal behaviour of the cooling fluid, providing a more accurate estimate of the total entropy generation. The heat transfer model is also refined, using local, geometry-dependent values rather than assuming uniform convection coefficients. In addition, radiative heat transfer is accounted for, a phenomenon whose effects become significant at high temperatures. The main findings regarding the influence of various operating parameters and optimisation constraints are summarized in Table 5.8.

The results confirm the superiority of profiled configurations over conventional tubular geometries, specially under stringent operational constraints. These designs achieve lower entropy generation and smaller reactor volumes while maintaining the desired conversion levels. The Pareto fronts illustrate the balance between minimizing irreversibilities and achieving compact designs. Thanks to their variable diameter, profiled geometries manage more effectively pressure drops and thermal hot spots, enhancing both performance and feasibility under realistic constraints. This study based of the 1D model underscores the considerable potential of shape optimisation in developing compact and thermodynamically efficient reactors that meet stringent industrial requirements, especially when the heat transfer is a main concern.

Table 5.8: Summary of key findings from 1D model optimisation.

Parameters studied	Effect on MPCEnt $\dot{S}_{tot}$	Effect on MPCEnt V_{HER}	Findings
Increase of inlet gas pressure	Increases	Decreases	Low-pressure designs are strongly constrained by the higher diameter limit. Higher pressures shift the reaction equilibrium, requiring additional cooling at low pressure (and therefore additional reactor length).
Increase of inlet gas molar flowrate	Increases	Increases	Reactor volume also increases, though not strictly proportionally.
Increase of inlet gas temperature	Increases	Decreases	Low inlet temperatures promote a nearly cylindrical shape and increase chemical reaction entropy generation. High inlet temperatures reduce volume and total entropy.

Increase of inlet gas O_2/SO_2 molar ratio	Decreases	Decreases	The reduction in entropy generation between O_2/SO_2 ratios of 0.9 and 1.1 remains limited, suggesting that an optimal ratio exists to minimize entropy generation while avoiding excessive oxygen injection.
Increase of inlet coolant temperature	Decreases	Increases	MPCEnt geometries maintain a consistent profile. At higher coolant temperatures, part of the entropy is shifted outside system boundaries and not accounted for.
Increase of maximal allowable temperature	Decreases	Decreases	A highly constrained system (low T_{max}) results in a single optimal geometry. Increasing the limit allows more design flexibility and lower entropy.
Increase of minimal conversion required	Increases	Increases	The optimal profile depends on the conversion target. A geometry optimised for high conversion cannot simply be truncated to meet lower conversion needs.

Although this study provides preliminary insights, several aspects merit further investigation. First, while the 1D model helps to outline the potential benefits of shape optimisation, more detailed 2D/3D CFD simulations, along with experimental validation, are necessary to more accurately quantify the achievable performance gains. As discussed in this work, radial temperature heterogeneities are present within the reactor, meaning that the mixing-cup temperature alone is insufficient for reliably predicting the occurrence of hot spots, which are often concentrated near the centreline of the packed bed. Furthermore, when significant radial temperature gradients exist, using an average temperature may lead to inaccurate modelling of chemical reactions, especially under non-linear kinetic regimes. CFD simulations allow overcoming these limitations, and moreover, enable calculating the entropy generation by mass transfer, for which no formulation exist in a 1D modelling framework (Michaud et al., 2024). However, in the case of packed beds, it is not feasible to simulate flow and transport phenomena at the particle scale due to the large number of particles involved. As a result, the packed bed is typically modelled using the equivalent porous medium approach. This approximation slightly reduces the predictive capability of the simulation, and experimental validation, or calibration of some parameters (convective coefficients, etc.), may be necessary to ensure its reliability.

A second major concern is the impact of mass transfer limitations on the reaction rate, which has not been addressed in this study nor in the work of Magnanelli et al. (2019). Incorporating the intrinsic reaction kinetics together with internal mass transfer limitations (instead of the apparent reaction kinetics) into the model is expected to substantially influence the optimal design of the HER. For example, the presence of external or internal mass transfer limitations may lead to larger HER volumes, as additional space and catalyst pellets are

required to compensate for reduced reaction rates. Conversely, the optimisation process may seek to mitigate these limitations by narrowing the HER cross-section in the affected regions, thereby increasing flow velocity in order to enhance the convective mass transfer. However, this increase in velocity is also likely to result in greater entropy generation, particularly through its viscous dissipation contribution, leading to modification of the compromise between minimal entropy generation and HER volume.

5.3 2D model comparison

The CFD results were compared to those of the one-dimensional model. The comparison was performed using a tubular reactor of 0. 54 m in length and 6.34 cm packed bed diameter which corresponds to the tubular design of the reference case study that involved the lowest entropy generation. As a preliminary step, a non-reactive situation was simulated to evaluate the accuracy of the 1D model in the absence of chemical reactions. The results are shown in Figure 5.30.

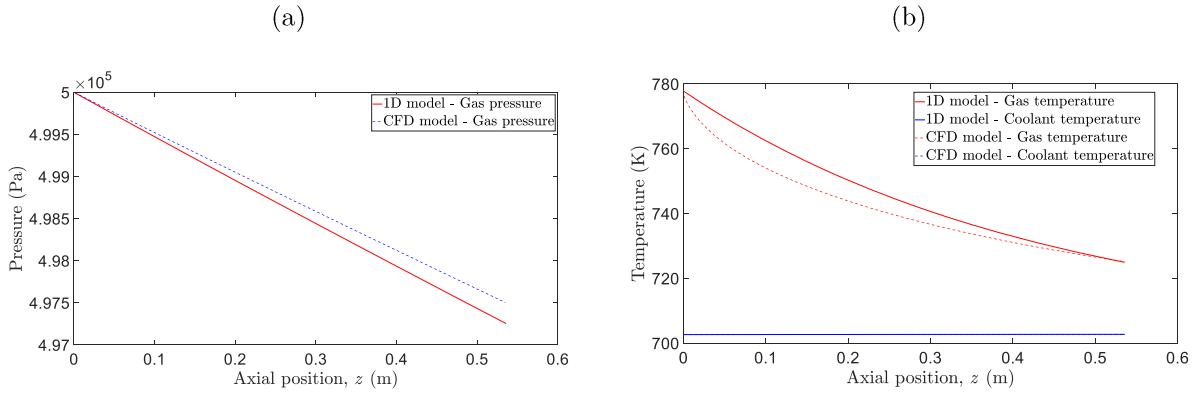

Figure 5.30: Comparison between the systemic and the CFD modelling: (a) pressure profiles, (b) temperature profiles.

As shown in Figure 5.30, a deviation of approximately 250 Pa is observed at the outlet in terms of pressure drop. This discrepancy remains relatively small and indicates a good overall agreement between the two models regarding hydrodynamics, although correlation used in the 1D model seems to slightly overestimate pressure losses. Similarly, some differences appear in the temperature predictions. A maximum deviation of around 10 K is observed, which can be attributed to two main factors. First, the 1D model does not include thermal development effects which are inherently captured in the CFD model. Second, modelling of heat transfer through the packed bed accounts for two thermal resistances in series. The first one is taken into consideration via an effective thermal conductivity representing the heat transfer within the bed, and the second, accounting for the wall effects, is modelled through an effective convective transfer rate at the wall. These two contributions rely on different correlations than those employed in the 1D model, which leads to inevitable discrepancies between the approaches.

This overestimation of the heat fluxes exchanged between the two fluids in the 1D model is particularly important in this case, as the catalyst material must not exceed a maximum temperature of 880 K. Furthermore, the CFD model incorporates both radial and axial variations of thermal conductivity, whereas the 1D model assumes infinite radial conductivity, resulting in an oversimplified temperature distribution.

When the chemical reaction is taken into account, the comparison between the CFD and the 1D model results is shown in Figure 5.31.

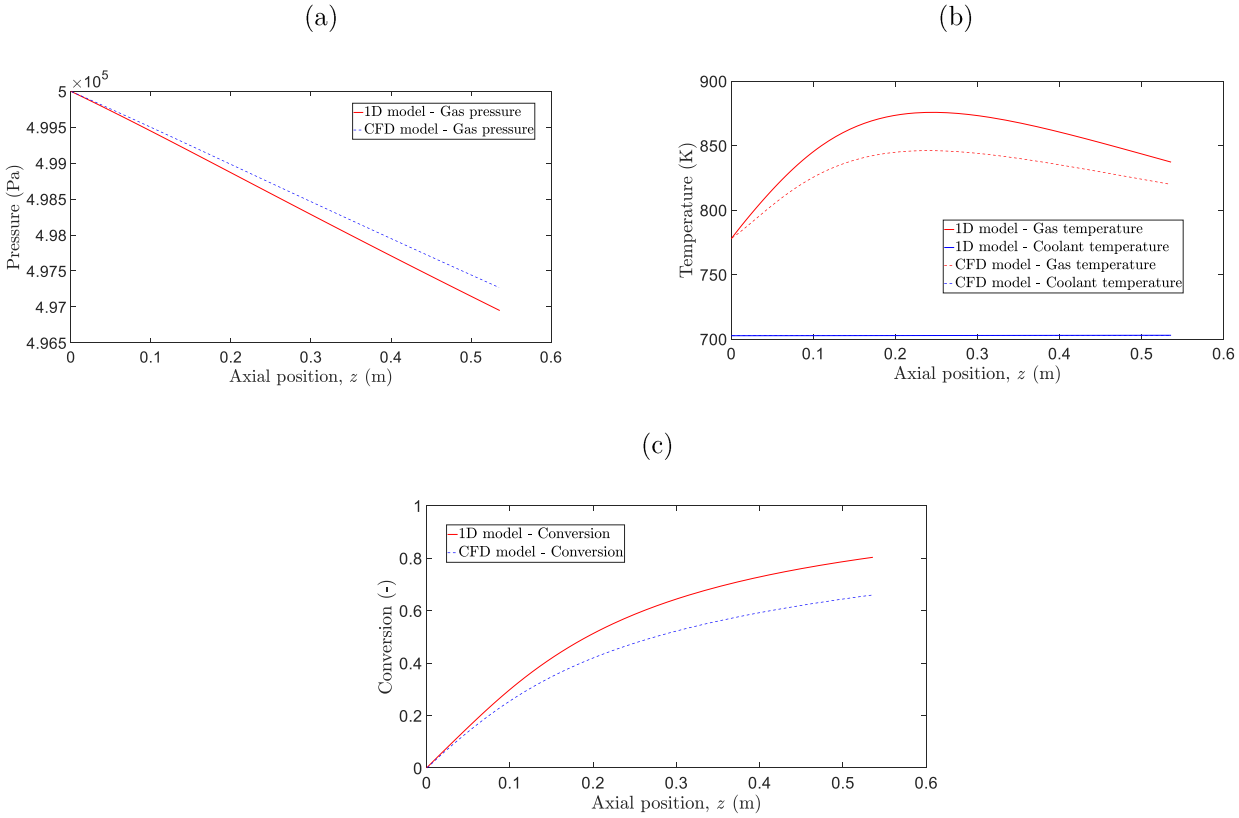

Figure 5.31: Comparison between the systemic and the CFD modelling: (a) pressure profiles, (b) temperature profiles, (c) conversion profiles.

Overall, the axial conversion profiles predicted by the 1D and CFD models are in good agreement at low conversion levels; however, discrepancies become more pronounced along the reactor length. As shown in Figure 5.31b, the bulk temperature in the CFD simulation remains well below 880 K. Figure 5.32 presents the CFD contours of temperature and reaction rate within the HER, highlighting the presence of a local hot spot near the centre of the flow at approximately 25 cm from the inlet. Such radial thermal heterogeneities are not captured by the 1D model, which only represents the averaged axial temperature profile and thus cannot accurately predict localized maxima.

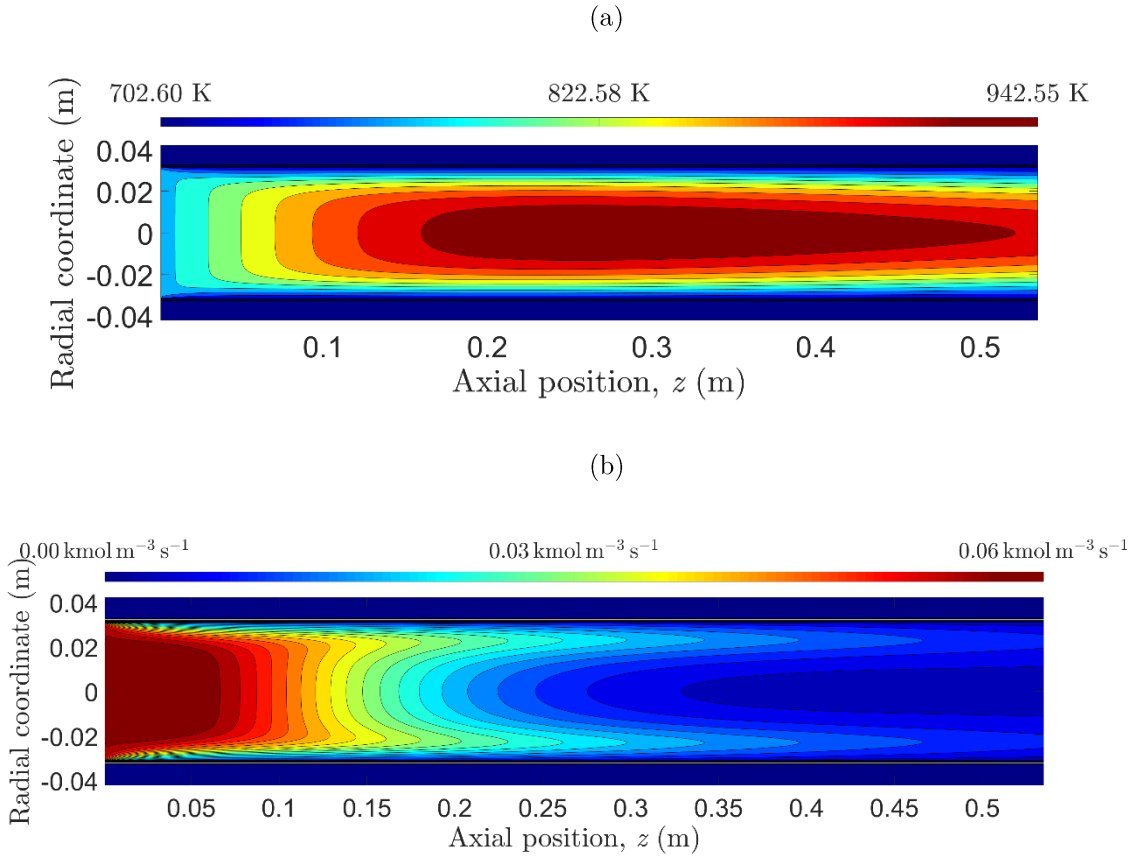

Figure 5.32: CFD modelling: (a)temperature profile, (b) reaction rate profile.

Furthermore, as observed in the analysis of Section 5.2, Figure 5.32b shows that the reaction rate is significantly higher at the inlet of the HER and decreases sharply along the reactor length. This trend results from the combined effects of reactant depletion and increasing local temperature, which inhibits the exothermic reaction due to thermodynamic equilibrium limitations. This pronounced axial variation in reaction rate explains the formation of the hot spot detected in the central region of the flow.

Although this hot spot does not appear in the mixing-cup temperature profile (Figure 5.32b), it remains significant from a process safety perspective, as local overheating can lead to catalyst deactivation or degradation. This observation highlights a critical limitation of relying solely on average or mixing-cup temperatures, which tend to smooth out local extremes and may therefore underestimate the risks associated with thermal runaway or catalyst damage. It also reinforces the relevance of high-resolution CFD simulations for the evaluation and design of thermally sensitive catalytic systems.

In conclusion, the comparison between CFD and 1D modelling for the purely tubular HER demonstrates that, while the 1D model captures the overall hydrodynamics and axial temperature profiles with reasonable accuracy, it fails to predict critical local phenomena such as radial hot spots. The non-reactive case highlighted only minor deviations in pressure drop and temperature (≈250 Pa and 10 K, respectively), indicating good agreement for simple flow

conditions. However, when chemical reactions are included, the CFD results reveal strong axial and radial variations in reaction rate and temperature that are not captured by the 1D model. In particular, the limited effective radial conductivity of the bed and the high reaction rate near the inlet, followed by rapid depletion of reactants along the reactor length, lead to the formation of a localized hot spot in the central region of the flow. While this hot spot is not reflected in bulk or mixing-cup temperatures, it represents a significant process safety concern, as local overheating could cause catalyst deactivation or degradation. These findings emphasize the importance of CFD simulations for thermally sensitive reactive systems, highlighting their ability to resolve radial heterogeneities and capture local maxima that may be overlooked by simplified 1D models. Overall, the study underscores the complementary roles of 1D and CFD approaches: 1D models provide quick and reasonably accurate predictions for preliminary design and parameter sensitivity studies, while CFD is essential for detailed thermal and reaction-rate analyses to ensure safe and reliable reactor operation.

5.4 Conclusion

The parametric and shape optimisation studies conducted on the heterogeneous exothermic reactor (HER) for the oxidation of SO_2 provide comprehensive insights into the interplay between reactor geometry, operating conditions, and process irreversibilities. Across all cases, profiled reactor configurations consistently outperform conventional tubular geometries, achieving the target SO_2 conversion while reducing both entropy generation and reactor volume.

The analysis highlights the critical role of key operating parameters:

- Inlet pressure: Higher pressures accelerate reaction rates, reducing required reactor volumes and shifting the dominant entropy source towards chemical reactions. Lower pressures, conversely, necessitate larger diameters to minimize pressure drop, resulting in designs that closely resemble tubular reactors.
- Maximum allowable temperature: This constraint strongly limits the feasible design space. Stricter temperature limits lead to narrower Pareto fronts, favouring smaller diameters in the reaction zones to prevent local overheating, while profiled geometries enable efficient temperature control and significant reductions in entropy generation.
- Inlet molar flowrate: Entropy generation and reactor volume scale approximately with the flowrate. Lower flowrates allow sharper temperature rises and larger diameters, whereas higher flowrates require narrower initial sections to mitigate the heat generated by the reaction and maintain temperature control.
- Inlet gas temperature: Lower temperatures produce longer reactors but lower entropy generation due to reduced thermal gradients, while higher temperatures increase the reaction rate, reduce the required volume, and slightly increase total entropy generation.
- Inlet O_2/SO_2 ratio: Higher oxygen availability enhances reaction rates, reduces reactor volume, and decreases entropy generation. Lower ratios result in larger diameters and longer reactor lengths, leading to higher total entropy despite locally lower thermal irreversibilities.
- Minimal conversion requirement: Higher conversion targets necessitate larger reactor volumes and divergent geometries, while lower conversion targets yield more compact designs. The dominant source of entropy shifts from chemical reactions to heat transfer as conversion increases.

This study demonstrates that optimal HER design is highly sensitive to both geometry and operating conditions. Profiled configurations enable local control of heat transfer and residence time, allowing the system to efficiently balance heat generation from the exothermic reaction with removal by the coolant. This dynamic control minimizes irreversibilities and enables more compact and efficient reactor designs compared to conventional tubular configurations. This means that heat transfer is the primary parameter on which dynamic optimisation acts to reduce total entropy generation.

CFD simulations, although not used for optimisation in this case, provided crucial insights into local phenomena neglected by the 1D model. In particular, radial temperature heterogeneities and localized hot spots near the reactor inlet were observed, caused by a limited radial conductivity of the bed, a high reaction rate and reactant depletion, which cannot be captured by averaged temperature profiles. These results emphasize the importance of CFD for assessing process safety and accurately predicting thermal and reaction-rate distributions in highly exothermic, gas-phase reactions. Overall, the study highlights the complementary roles of 1D and CFD approaches: 1D models allow efficient preliminary optimisation and sensitivity analysis, while CFD provides high-resolution validation and safety assessment.

List of Figures

Figure 5.1: Pareto fronts illustrating the trade-off between the volume $VHER$ and the generated entropy $Stot$ for the tubular (blue diamonds) and profiled (red circles) HER configurations. 241

Figure 5.2: 3D representation of the MPCVol (a) and MPCEnt (b) points of the reference caste study. 242

Figure 5.3: MPCVol and MPCEnt points of the reference case study: (a) Packed bed radius profiles, (b) Packed bed temperature profiles, (c) SO_2 conversion rate profiles, (d) Mixture pressure profiles. 243

Figure 5.4: Local entropy generation rates in both the MPCEnt and MPCVol geometries: (a) Viscous dissipation in the coolant, (b) Viscous dissipation in the reactive mixture, (c) Heat transfer, (d) Chemical reaction. 246

Figure 5.5: Effects of temperature and pressure on the equilibrium conversion rate of SO_2 for the inlet mixture composition reported in Chapter 4, Table 4.3. 248

Figure 5.6: Pareto fronts for different inlet gas pressures 249

Figure 5.7: 3D representation of the MPCVol (a) and MPCEnt (c) points at pM,i,inl= 2 bar, and the MPCVol (b) and MPCEnt (d) at with pM,i,inl= 10 bar. 250

Figure 5.8: MPCEnt points at inlet gas pressures of 2 and 10 bar: (a) Packed bed radius profiles, (b) Packed bed temperature profiles 251

Figure 5.9: Effects of the allowable temperature constraint on the Pareto fronts 253

Figure 5.10: MPCEnt design for a maximal allowable temperature of 840 K 254

Figure 5.11: MPCEnt point for a maximum allowable temperature of 840 K: (a) Packed bed radius profile, (b) Packed bed temperature profile. 254

Figure 5.12: Pareto fronts for different inlet coolant temperature 255

Figure 5.13: 3D representation of the MPCEnt (a) and MPCVol (c) points for $T_{M,an,inl}$ = 653 K, and the MPCEnt (b) and MPCVol (d) at $T_{M,an,inl}$ = 753 K 256

Figure 5.14: MPCEnt points for $T_{M,an,inl}$ = 653 K and $T_{M,an,inl}$ = 753 K: (a) Packed bed radius profiles, (b) Packed bed temperature profiles, (c) SO_2 conversion rate profiles, (d) Mixture pressure profiles. 257

Figure 5.15: Pareto fronts for different inlet gas molar flowrate. 259

Figure 5.16: 3D representation of the MPCEnt (a) and MPCVol (c) points at $F_{i,inl}$=0.5$F_{i,inl,ref}$, and the MPCEnt (b) and MPCVol (d) at $F_{i,inl}$=1.5$F_{i,inl,ref}$. 261

Figure 5.17: MPCEnt points for 50% reduced and 50% increased $F_{i,inl}$: (a) Packed bed radius profiles, (b) Packed bed temperature profiles, (c) SO_2 conversion rate profiles, (d) Mixture pressure profiles. 262

Figure 5.18: Local entropy generation rates in both MPCEnt geometries: (a) Heat transfer, (b) Chemical reaction. 262

Figure 5.19: Pareto fronts for different inlet gas temperature. 264

Figure 5.20: 3D representation of the MPCEnt (a) and MPCVol (c) points for $T_{M,i,inl}$ = 728 K, and the MPCEnt (b) and MPCVol (d) at $T_{M,i,inl}$ = 828 K. 265

Figure 5.21: MPCEnt points for $T_{M,an,inl}$ = 728 K and $T_{M,an,inl}$ = 828 K: (a) Packed bed radius profiles, (b) Packed bed temperature profiles, (c) SO_2 conversion rate profiles, (d) Mixture pressure profiles. 266

Figure 5.22: Local entropy generation rates in both MPCEnt geometries: (a) Viscous dissipation in the coolant, (b) Viscous dissipation in the reactive mixture, (c) Heat transfer, (d) Chemical reaction. 266

Figure 5.23: Pareto fronts for different inlet O_2/SO_2 molar ratio. 268

Figure 5.24: 3D representation of the MPCEnt (a) and MPCVol (c) points for $xinl, O2xinl, SO2$ = 0.7, and the MPCEnt (b) and MPCVol (d) for $xinl, O2xinl, SO2$ = 1.1. 269

Figure 5.25: MPCEnt points for $xinl, O2xinl, SO2$ = 0.7 and $xinl, O2xinl, SO2$ = 1.1: (a) Packed bed radius profiles, (b) Packed bed temperature profiles, (c) SO_2 conversion rate profiles, (d) Mixture pressure profiles. 270

Figure 5.26: Local entropy generation rates in both MPCEnt geometries: (a) Viscous dissipation in the coolant, (b) Viscous dissipation in the reactive mixture, (c) Heat transfer, (d) Chemical reaction. 271

Figure 5.27: Pareto fronts for different minimal conversion. 273

Figure 5.28: 3D representation of the MPCEnt (a) and MPCVol (c) points for ξ_{min} = 0.65, and the MPCEnt (b) and MPCVol (d) for ξ_{min} = 0.95. 274

Figure 5.29: MPCEnt points for ξ_{min} = 0.65 and ξ_{min} = 0.95: (a) Packed bed radius profiles, (b) Packed bed temperature profiles, (c) SO_2 conversion rate profiles, (d) Mixture pressure profiles. 275

Figure 5.30: Comparison between the systemic and the CFD modelling: (a) pressure profiles, (b) temperature profiles 280

Figure 5.31: Comparison between the systemic and the CFD modelling: (a) pressure profiles, (b) temperature profiles, (c) conversion profiles 281

Figure 5.32: CFD modelling: (a)temperature profile, (b) reaction rate profile 282

List of Tables

Table 5.1: HER volume and entropy generation rate of the MPCVol and MPCEnt designs in the reference case study. 247

Table 5.2: HER volume and entropy generation rate of the MPCEnt points of the three gas inlet pressures 251

Table 5.3: HER volume and entropy generation rate of the MPCEnt corresponding to the three inlet heat carrier temperatures. 258

Table 5.4: HER volume and entropy generation rate of the MPCEnt points of the three gas inlet molar flowrates. 260

Table 5.5: HER volume and entropy generation rate of the MPCEnt points of the three gas inlet temperatures 267

Table 5.6: HER volume and entropy generation rate of the MPCEnt corresponding to the three inlet molar ratios. 272
Table 5.7: HER volume and entropy generation rate of the MPCEnt points of the three minimal conversions..... 276
Table 5.8: Summary of key findings from 1D model optimisation..... 277

Bibliography

Fogler, H. S.,1992. Elements of Chemical Reaction Engineering (2nd ed.). Prentice Hall P T R.

Magnanelli, E., Solberg, S. B. B., & Kjelstrup, S. (2019). Nature-inspired geometrical design of a chemical reactor. Chemical Engineering Research and Design, 152, 20-29.

Michaud, A., Hreiz, R., & Portha, J. F., 2024. Entropy generation analysis for designing efficient and sustainable heat exchangers and chemical reactors: From 1D modelling to detailed CFD simulations. Chemical Engineering Science, 300, 120615.

General conclusion and perspectives

General conclusion

This thesis has explored the application of entropy generation minimization (EGM) as a robust design strategy for heat exchanger reactors (HERs), integrating systemic one-dimensional (1D) modelling, detailed two-dimensional (2D) axisymmetric computational fluid dynamics (CFD) simulations, and multi-objective shape optimisation. The primary goal was to develop more compact and energy-efficient reactor geometries that reduce irreversibilities while maintaining the required conversion rates for industrial applications. To achieve this, this work established the thermodynamic foundations of entropy generation analysis, encompassing both local and global formulations, and discussed the principle of entropy equipartition. A thorough literature review underscored the increasing importance of EGM among contemporary ecological and energy efficiency imperatives, while identifying shortcomings in existing modelling frameworks—particularly the necessity for more holistic approaches in chemical reactors that account for coupled phenomena like heat transfer, mass transfer, and chemical reactions (Chapter 1).

Two case studies were selected to evaluate EGM's effectiveness in realistic HER setups: the homogeneous liquid-phase acetic anhydride hydrolysis (Chapter 2 and Chapter 3) and the heterogeneous catalytic oxidation of SO_2 in a packed-bed reactor (Chapter 4 and Chapter 5). These cases introduced varying levels of complexity, from mild exothermicity in liquid systems to strong exothermicity with radiative heat transfer and porous media in gas-solid systems. Simplified 1D models facilitated initial geometry optimisation with quick but moderately reliable results, whereas CFD models provided benchmarks for accuracy, revealing radial gradients that influence irreversibility distributions, but at the cost of a longer calculation time.

A key focus of this thesis was the systematic comparison of different entropy generation modelling (EGMod) approaches across the two case studies, including 1D systemic models, 1D CFD-reduced models derived from CFD data, and full 2D/3D CFD simulations, each evaluated using both local and global entropy generation formulations. This comparative analysis precisely identified sources of discrepancies and highlighted the strengths and limitations of each method. Firstly, the equivalence between local and global entropy calculations was confirmed when applied to the same underlying system model, yielding identical total entropy generation rates. This validation is crucial for practical optimisation, as global balances are often simpler to implement than detailed local integrations, especially in preliminary design phases.

Secondly, contrasting 1D systemic models with detailed 2D/3D CFD models quantified the impact of radial profiles in temperature, pressure, and concentration on entropy generation. The 1D systemic approach, relying on cross-section-averaged values, overlooks these radial variations, which can substantially alter the estimation of entropy generation. Thirdly, the

comparison between 1D reduced models (which incorporate radial effects into axial profiles) and full CFD models isolated differences stemming from the mathematical formulation of 1D entropy generation modelling approaches. Since both CFD and 1D reduced data share similar axial profiles, the differences in the results they provide are due to the mathematical formulation of the 1D modelling of entropy generation (e.g., Kjelstrup approach). Finally, juxtaposing 1D systemic models with 1D reduced models evaluated inaccuracies from empirical correlations (e.g., Nusselt number for heat transfer and friction factor for pressure drop), which are particularly unreliable in reactive systems due to coupling between mass transfer, heat transfer and generation, and flow dynamics (in both developing or fully developed flow regimes) that most available correlations do not consider.

From the optimisation studies presented in Chapter 3 and Chapter 5, several observations can be drawn regarding the different contributions to entropy generation.

Entropy generation due to viscous dissipation was generally negligible, though it became notable in heterogeneous configurations. In purely tubular HERs, where accurate correlations are available, 1D systemic models provided reliable estimates of viscous contributions when compared to CFD, under both global and local EGMod formulations. The global approach accounts for viscous dissipation indirectly, through the temperature increase due to viscous heating, and its results are in good agreement with those calculated through local integration (i.e. pressure drop calculation). For the liquid-phase hydrolysis, viscous dissipation effects remained minor and were largely negligible relative to the thermal and chemical contributions to entropy generation. Conversely, in the gas-phase SO_2 oxidation, the presence of porous media amplified frictional effects, while profiled designs mitigated overall dissipation by employing larger diameters. Overall, the analysis indicated that 1D models are effective for predicting viscous entropy generation in simple, tubular geometries. However, CFD remains essential for complex flow conditions, where significant radial shear gradients arise and reliable correlations for frictional effects are not available.

Furthermore, thermal management emerged as the dominant lever for minimizing entropy generation through adapted designs in both case studies. In the SO_2 oxidation optimisation study (Chapter 5), profiled reactors—allowing axial variations of the packed bed diameter—proved superior to uniform tubular designs by enhancing heat transfer, reducing entropy generation from thermal gradients, and enabling smaller volumes under conversion constraints. For instance, optimised profiled geometries mitigated hot spots by dynamically adjusting heat exchange surfaces, leading to lower overall irreversibilities. In contrast, for the mildly exothermic acetic anhydride hydrolysis (Chapter 3), thermal management had less to no impact, and optimal designs reverted to simple tubular geometries. Here, entropy generation from heat transfer was modest, with limited gains from geometric modifications. Across both, the study showed that 1D models often underestimate radial thermal effects, but in simple tubular configurations with reliable correlations, they approximate CFD results reasonably well

for dilute systems. However, discrepancies could be amplified in reactive flows where exothermicity is coupled with wall heat transfer, as evidenced in Chapter 3 (Section 3.2.4) and Chapter 5 comparisons. Indeed, for a strongly exothermic gas-solid reaction, CFD simulations revealed localized hot spots near the inlet due to rapid reaction rates, which were understated in 1D models. These hot spots, underestimated in bulk temperature profiles, heighten risks of thermal runaway and catalyst deactivation via sintering.

Additionally, chemical reaction constituted a major source of entropy generation, an inevitable contribution, since the reaction must occur to achieve the desired conversion, and was the primary factor for the discrepancies observed between modelling approaches. In reactive systems, the exothermicity directly influences the temperature field, exacerbating entropy generation discrepancies. CFD captures radial reaction rate variations that 1D models miss, causing the latter misprediction entropy generation from reactions. In the hydrolysis case, even though 1D models correctly predicted the axial profiles of species concentrations, compared to CFD, they could not correctly estimate chemical entropy generation since they do not consider concentration and temperature radial gradients. The study emphasized challenges in 1D modelling for reactive systems: lack of correlations for heat transfer in the presence of internal heat generation and inherent limitations in 1D formulations (e.g., Kjelstrup approach) that overlook multidimensional effects. For high-thermicity or concentrated systems, modelling errors increase, making CFD indispensable for accuracy.

Finally, mass transfer entropy was particularly evident in CFD models, which explicitly capture diffusion-driven irreversibilities, in contrast to 1D formulations that cannot represent them. In the homogeneous hydrolysis case, mass transfer contributed only marginally (third source of entropy generation) to entropy generation due to well-mixed inlet conditions; however, CFD still revealed subtle radial effects developing along the reactor length due to the chemical reaction. Overall, CFD offered critical insights into mass transfer-related entropy contributions that 1D approaches are unable to estimate accurately.

In summary, this thesis establishes that EGM is highly interesting for exothermic heterogeneous reactions such as SO_2 oxidation, where profiled geometries yield substantial reductions in total entropy generation rates. For mildly exothermic homogeneous systems like acetic anhydride hydrolysis in liquid phase with low thermal constrains, benefits are limited, favouring purely tubular designs. The comparative EGMod analysis underscores that 1D systemic models are efficient for preliminary screening, but CFD is vital for capturing reaction and mass transfer nuances in complex systems. Local EGMod offers detailed distributions of irreversibilities, aiding targeted optimisations, while global methods, entropy balances (input-output), provides access to the overall irreversibility generated in the system without knowing the precise spatial distribution of entropy creation. Ultimately, coupling 1D and CFD—as shown in Chapter 3 (Section 3.4), in which 1D preliminary results were used as initialization for CFD optimisations—increase speed and accuracy, leading to more efficient HER designs.

Perspectives

For the future, several perspectives emerge to extend and refine the EGM framework developed in this thesis, addressing current limitations and leveraging emerging technologies for broader industrial impact.

A priority is experimental validation, particularly for the acetic anhydride hydrolysis case, where a pilot reactor was constructed but not exploited due to time constrains. Future work should focus on conducting these experiments under controlled flow conditions. Such validation would indirectly confirm entropy generation predictions by verifying axial and radial profiles of concentration, pressure, and temperature. For instance, measuring these profiles in the pilot HER could quantify actual irreversibilities from thermal transfer, viscous dissipation, and chemical reactions, bridging the gap between simulations and practice. This could also help in refining heat transfer correlations, especially in reactive flows conditions.

Modelling advancements represent another key perspective. To overcome high computational times in CFD-based optimisations, artificial intelligence (AI)-driven surrogate models, trained on CFD datasets, could accelerate multi-objective searches while preserving accuracy with a more representative dataset. Developing improved correlations for Nusselt numbers and friction factors in non-conventional geometries and reacting flows is essential. This would enhance 1D model reliability, reducing discrepancies highlighted in the thesis. Furthermore, the incorporation of two-temperature models in heterogeneous systems (distinguishing gas and solid phases), although requiring experimental calibration of specific coefficients, would enhance the accuracy of entropy generation calculations (Torabi et al., 2017).

Moreover, manufacturability challenges for profiled reactors persist currently, but additive manufacturing advancements promise to fabricate complex shapes cost-effectively, enabling practical implementation.

Finally, extending EGM to more complex systems offer exciting potential. For instance, investigating reactors with punctual cooling or heating—such as segmented HERs with localized heat exchangers—could further minimize entropy in highly exothermic processes, preventing hot spots more dynamically. Counter-current configurations, not studied here, could boost heat transfer efficiency and reduce irreversibilities. Beyond the optimisation of a single reactor, adopting a broader process-level perspective—including additional units such as heat exchangers, compressors, and pumps—could be particularly valuable. Indeed, minimizing entropy generation within one equipment may inadvertently shift irreversibilities to other units of the process, thus creating the illusion of reduced irreversibilities. As highlighted earlier in Chapter 3 and Chapter 5, optimisation results involving different inlet temperatures or pressures leading to lower entropy generation may in fact imply that entropy has been generated upstream of the HER, ultimately masking the actual extent of entropy generation

within the reactor itself. Extending the scope of EGM to the process level would therefore enable the detection of such "hidden" entropy creation, ensuring that the global performance of the process is optimised.

Overall, these perspectives, combined with experimental validation and AI-driven approaches, will foster a broader application of EGM to a wide range of complex chemical reactors, thereby addressing industrial demands and improving energy efficiency across chemical processes. In the longer term, such developments hold significant potential for reducing the environmental footprint of the chemical industry, contributing both to sustainable production practices and to global efforts in mitigating climate change.

Bibliography

Torabi, M., Karimi, N., Peterson, G. P., & Yee, S. (2017). Challenges and progress on the modelling of entropy generation in porous media: a review. International Journal of Heat and Mass Transfer, 114, 31-46.

Résumé en français

Contexte général

L'industrie chimique représente aujourd'hui l'un des principaux contributeurs aux émissions mondiales de gaz à effet de serre, ce qui en fait un domaine clé pour la mise en œuvre de procédés plus économes en énergie et durables. La réduction de l'empreinte énergétique et environnementale des procédés chimiques nécessite une attention particulière aux irréversibilités thermodynamiques qui se produisent lors des transferts de chaleur, de masse et des réactions chimiques. Dans ce contexte, cette thèse se concentre sur l'intensification des procédés par l'optimisation des réacteurs-échangeurs de chaleur (HER), en adoptant la minimisation de la génération d'entropie (Entropy Generation Minimization, EGM) comme principe directeur. L'EGM constitue un outil à la fois théorique et pratique, permettant de quantifier les pertes thermodynamiques et de proposer des stratégies pour améliorer l'efficacité globale des systèmes réactifs.

L'objectif principal de cette thèse est de démontrer l'efficacité de l'EGM pour optimiser les HERs, en combinant des modèles systémiques unidimensionnels (1D) pour des analyses rapides et des simulations de dynamique des fluides computationnelle (CFD) bidimensionnelles (2D) axisymétriques pour des analyses précises mais plus longues. Deux cas d'étude sont examinés pour évaluer l'approche dans des contextes variés : l'hydrolyse homogène de l'anhydride acétique en phase liquide, une réaction modérément exothermique, et l'oxydation catalytique hétérogène du dioxyde de soufre (SO_2) en trioxyde de soufre (SO_3) dans un réacteur à lit fixe, une réaction fortement exothermique d'importance industrielle. Ces cas permettent d'explorer les contributions des irréversibilités liées au transfert de chaleur, à la dissipation visqueuse, aux réactions chimiques et au transfert de matière, tout en optimisant la géométrie des réacteurs pour minimiser l'entropie générée et le volume du réacteur.

La thèse adopte une approche multi-échelle, intégrant des modèles 1D pour un criblage préliminaire rapide et des modèles CFD pour une analyse détaillée des phénomènes locaux. Une optimisation multi-objectifs est réalisée pour équilibrer la compacité du réacteur (volume minimal) et l'efficacité thermodynamique (entropie créée minimale), en tenant compte de contraintes opératoires réalistes telles qu'une conversion minimale et une contrainte de température maximale.

Revue de la littérature

L'EGM repose sur l'analyse thermodynamique des irréversibilités dans les systèmes réactifs, en quantifiant la génération d'entropie due à divers phénomènes physiques : transfert de chaleur, dissipation visqueuse, réactions chimiques et transfert de matière. Une revue de littérature approfondie met en évidence l'importance croissante de l'EGM dans l'optimisation des procédés, avec des applications réussies dans des domaines comme la synthèse du méthanol, la gazéification de la biomasse et les échangeurs de chaleur. Le principe d'équipartition de la

génération d'entropie, qui préconise une répartition uniforme de la création des irréversibilités à l'intérieur du réacteur, est un concept clé qui se vérifie dans de nombreuses applications.

Modélisation des HERs

Les modèles systémiques 1D, implémentés dans MATLAB, sont issus des bilans de masse, de quantité de mouvement, d'énergie et d'espèces. Ils supposent un écoulement piston idéal et négligent les gradients radiaux, ce qui les rend numériquement efficaces pour des études paramétriques rapides et l'identification de tendance globales. Ces modèles utilisent des corrélations empiriques (par exemple, pour le nombre de Nusselt ou le coefficient de friction) pour estimer les transferts de chaleur et de matière ainsi que les pertes de charge. Cependant, leurs hypothèses simplificatrices limitent leur précision dans des systèmes complexes, notamment pour les réactions fortement exothermiques où les gradients radiaux jouent un rôle significatif.

Pour surmonter les limitations des modèles 1D, des simulations CFD axisymétriques 2D sont réalisées avec ANSYS Fluent. Ces modèles résolvent les équations couplées d'hydrodynamique, de transfert de chaleur et de matière, fournissant des profils 2D détaillés de vitesse, de température et de concentration. Dans le cas de l'oxydation du SO_2, le lit fixe est modélisé comme un milieu poreux, permettant de capturer les interactions complexes entre l'écoulement, la réaction chimique et les transferts thermiques. Les simulations CFD offrent une résolution spatiale fine, essentielle pour identifier les phénomènes locaux comme les points chauds ou les gradients radiaux, qui sont critiques pour l'efficacité des procédés exothermiques.

Comparaison des approches de modélisation

La comparaison systématique des modèles 1D, 1D réduit (modèle moyenné issue des profils CFD) et CFD met en lumière leurs forces et faiblesses respectives. La comparaison entre les différentes approches de modélisation met en évidence les écarts induits par les approximations inhérentes aux modèles unidimensionnels (1D) dans la prédiction des champs de température et de concentration, ainsi que par les hypothèses utilisées pour évaluer la génération d'entropie en supposant un système 1D. L'étude montre que, pour des configurations d'écoulement simples, telles que les HER tubulaires pour lesquelles des corrélations précises sont disponibles, un modèle systémique 1D fournit une estimation fiable de l'entropie générée par dissipation visqueuse par rapport à un modèle CFD, que l'on considère l'approche globale ou locale de génération d'entropie. Il convient de noter que l'approche globale ne permet d'estimer l'entropie visqueuse que par la hausse de température induite par les frottements dans les écoulements incompressibles.

Pour des systèmes faiblement exothermique, l'entropie générée par transfert de chaleur est également assez similaire entre les deux approches. En revanche, la réaction chimique constitue une contribution significative à la génération d'entropie et représente la principale

source de divergence entre les modèles 1D et CFD. Les différences observées s'expliquent notamment par l'absence de prise en compte des gradients radiaux dans le modèle 1D, bien que celui-ci prévoie correctement les profils axiaux de température et de concentration. Par ailleurs, la modélisation CFD permet d'intégrer l'entropie générée par le transfert de matière, ce qui n'est pas possible dans la formulation 1D classique. L'étude confirme que, pour chaque méthode, les approches globale et locale fournissent des résultats globaux comparables, la formulation locale offrant toutefois une vision plus détaillée de la distribution des irréversibilités. Pour les systèmes où seules la dissipation visqueuse et le transfert thermique sont significatifs, la modélisation systémique 1D apparaît plus efficace et moins coûteuse en temps de calcul que le CFD. En revanche, pour des systèmes réactifs fortement exothermiques et/ou concentrés, les erreurs associées aux modèles 1D augmentent, rendant la modélisation CFD préférable pour garantir la précision. Enfin, dans le cadre de l'optimisation des équipements basée sur la minimisation de la génération d'entropie, les modèles 1D présentent des limites pour les géométries complexes ou non classiques, car les corrélations fiables de facteur de friction et de nombre de Nusselt sont généralement disponibles uniquement pour des géométries simples. Dans ces situations, le CFD constitue un outil plus fiable, tout en conservant une valeur importante des modèles 1D pour le criblage préliminaire, l'analyse de sensibilité et la compréhension physique à moindre coût computationnel.

Cas de l'hydrolyse de l'anhydride acétique

Dans le cadre de l'étude de l'hydrolyse de l'anhydride acétique, deux configurations de réacteur ont été considérées : un HER tubulaire classique à double tube et une géométrie à diamètre variable par segments. L'analyse de la génération d'entropie a montré que la réaction chimique constitue la contribution dominante suivi par le transfert de chaleur, tandis que les effets visqueux et le transfert de matière restent négligeables dans le régime laminaire étudié. L'optimisation multi-objectifs, combinant la minimisation du volume du réacteur et celle de l'entropie créée totale, a révélé que les géométries tubulaires simples sont suffisantes pour ce type de réaction où la température n'est pas vectrice de modification géométrique pour contrôler le transfert thermique. Les simulations CFD ont permis de confirmer ces observations et de mettre en évidence de subtiles variations radiales dans la distribution de l'entropie, liées aux gradients locaux de température et de concentration que le modèle 1D ne capture pas.

Un pilote à échelle réduite a été conçu pour valider les résultats CFD, bien que des contraintes de temps aient empêché la réalisation des expériences. La méthodologie de dimensionnement, fournit une base pour de futurs travaux expérimentaux.

Cas de l'oxydation catalytique du SO_2

L'oxydation catalytique du dioxyde de soufre constitue un système hétérogène fortement exothermique, avec des limitations locales significatives. Deux approches de modélisation ont été mises en œuvre : un modèle systémique 1D fournissant une représentation globale rapide

et une simulation CFD 2D axisymétrique utilisant un lit fixe modélisé comme milieu poreux, capable de résoudre les gradients radiaux et les effets locaux de transfert. Les optimisations ont été menées en considérant des contraintes opérationnelles réalistes, telles que la conversion minimale de SO_2, la température maximale admissible pour éviter la désactivation catalytique, et la limitation de la perte de charge. L'analyse a montré que les réacteurs à géométrie profilée permettent une meilleure gestion de la chaleur, une réduction significative de l'entropie et un volume de réacteur plus compact, tandis que les configurations tubulaires classiques sont moins performantes pour les réactions fortement exothermiques. Le transfert de chaleur constitue le paramètre dominant pour la minimisation de l'entropie, alors que la réaction chimique représente également une contribution majeure, souvent à l'origine des différences entre les modèles 1D et CFD. Les simulations CFD ont révélé des points chauds localisés et des gradients radiaux prononcés, qui ne sont pas capturés par les modèles 1D, soulignant l'importance de la CFD pour garantir la sécurité et la précision des prédictions dans des systèmes fortement exothermiques.

Conclusions et perspectives

Les travaux de cette thèse démontrent que l'EGM constitue un outil puissant pour la conception de HER durables. Les réacteurs profilés permettent des réductions significatives de la génération d'entropie dans les systèmes fortement exothermiques, tandis que les géométries tubulaires simples sont suffisantes pour des réactions faiblement exothermiques. L'approche multi-échelle couplant modèles 1D et CFD combine rapidité, précision et compréhension des phénomènes physiques et constitue une base solide pour la validation expérimentale future et le développement de modèles de substitution assistés par intelligence artificielle.

Pour l'avenir, plusieurs perspectives se dégagent afin d'étendre et d'affiner le cadre de minimisation de la génération d'entropie développé dans cette thèse. Un axe d'amélioration concerne la validation expérimentale, en particulier pour le cas de l'hydrolyse de l'anhydride acétique, pour lequel un réacteur pilote a été construit mais non testé en raison de contraintes de temps. Les travaux futurs devraient viser la réalisation de ces expériences dans des conditions d'écoulement contrôlées. Une telle validation permettrait de confirmer indirectement les prédictions de génération d'entropie en vérifiant les estimations fournies par les différentes modélisations.

L'amélioration des modèles constitue un autre axe clé. Pour surmonter les temps de calcul élevés dans les optimisations basées sur le CFD, l'utilisation de modèles substituts plus entrainés pilotés par intelligence artificielle et entraînés sur des données CFD pourrait accélérer les recherches multi-objectifs tout en conservant une précision représentative. Le développement de corrélations améliorées pour les nombres de Nusselt et les coefficients de friction dans des géométries non conventionnelles et des écoulements réactifs est également essentiel. Cela renforcerait la fiabilité des modèles 1D et réduirait les écarts observés dans cette thèse. Par ailleurs, l'incorporation de modèles à deux températures dans les systèmes

hétérogènes, distinguant les phases gazeuse et solide, bien que nécessitant une calibration expérimentale de coefficients spécifiques, améliorerait la précision des calculs de génération d'entropie.

La question de la fabricabilité des réacteurs profilés reste un défi, mais les progrès en fabrication additive offrent la possibilité de produire des formes complexes de manière économique, facilitant ainsi leur mise en œuvre pratique.

Enfin, l'extension de l'EGM à des systèmes plus complexes présente un potentiel prometteur. L'étude de réacteurs avec refroidissement ou chauffage ponctuel, tels que des HER segmentés avec échangeurs de chaleur localisés, pourrait permettre de minimiser davantage la génération d'entropie dans les procédés fortement exothermiques et de prévenir plus efficacement les points chauds. Les configurations en contre-courant, non étudiées ici, pourraient également améliorer l'efficacité du transfert thermique et réduire les irréversibilités. Au-delà de l'optimisation d'un seul réacteur, adopter une perspective à l'échelle du procédé, incluant d'autres unités telles que des échangeurs de chaleur, compresseurs et pompes, serait particulièrement pertinent. En effet, minimiser la génération d'entropie dans un équipement peut parfois transférer les irréversibilités à d'autres unités, donnant une impression trompeuse de réduction globale. Étendre l'EGM au niveau procédé permettrait donc de détecter cette « entropie cachée » et d'assurer l'optimisation de la performance globale.

Dans l'ensemble, ces perspectives, combinées à la validation expérimentale, favoriseront une application plus large de l'EGM à un éventail étendu de réacteurs chimiques complexes. À plus long terme, ces développements offrent un potentiel significatif pour réduire l'empreinte environnementale de l'industrie chimique, contribuant à des pratiques de production durable et aux efforts globaux de lutte contre le changement climatique.